© Copyright 2025

Hao Anh Nguyen

Designing Huge Colloidal Quantum Dots for Scalable & Deterministic Placement of Single-Photon Emitters

Hao Anh Nguyen

A dissertation

submitted in partial fulfillment of the

requirements for the degree of

Doctor of Philosophy

University of Washington

2025

Reading Committee:

Brandi M Cossairt, Chair

Arka Majumdar

Daniel R. Gamelin

David S. Ginger

Program Authorized to Offer Degree:

Chemistry

University of Washington

Abstract

Designing Huge Colloidal Quantum Dots for Scalable & Deterministic Placement of Single-Photon Emitters

Hao Anh Nguyen

Chair of the Supervisory Committee:
Brandi M. Cossairt
Department of Chemistry

Colloidal quantum dots (QDs) have been widely explored as light-emitting materials due to their tunable optical properties, high quantum yield, and solution-processability. In quantum photonics, individual QDs can serve as single-photon emitters that are critical for quantum technologies, including communication, computing, cryptography, and metrology, where discrete photons function as qubits. However, conventional emissive QDs, including Cd-, In-, Pb-, and Hg-based materials, typically have diameters below 10 nm due to the Bohr radius limitation and synthetic feasibility. Even with core/shell architectures, where materials like CdS or ZnS encapsulate the core QDs to enhance stability and emission, they rarely exceed 20 nm. This size constraint creates a fundamental challenge in integrating QDs into photonic devices, as optical

cavities and resonant structures often have mode volumes on the micrometer scale, leading to poor spatial overlap and limiting efficient light-matter interaction.

To address this size mismatch while maintaining desirable optical properties, this dissertation explores three complementary approaches. First, a machine learning framework is developed to refine CdSe and InP QD syntheses by extracting synthetic parameters from literature, addressing data inconsistencies, and predicting optimized reaction conditions. Using data augmentation and predictive modeling, this method enables precise control over emission wavelengths and sizes, complementing experimental efforts to design QDs with targeted properties (Chapter 3).

Next, Chapter 4 explores silica encapsulation as a method to enlarge QDs and enhance their stability in air. By coating QDs with a protective silica shell, the particle size increases to around 90 nm. This enlargement enables deterministic patterning of emissive particles onto planar substrates while preserving single-photon emission. Finally, a stepwise CdS shelling strategy is introduced in Chapter 5 to synthesize colossal CdSe/CdS QDs with diameters exceeding 100 nm, significantly expanding the range of QD-based light emitters. Using electrohydrodynamic inkjet printing, these QDs are patterned into large arrays and deterministically positioned into nanobeam cavities for scalable quantum light sources. Beyond their advantages for particle placement, colossal QDs exhibit exceptional stability under ambient excitation, making them well-suited for studies requiring sustained high excitation conditions. Their large size also provides a platform for investigating nanocrystal growth mechanisms, as structural evolution can be directly visualized using electron microscopy with greater clarity than smaller QDs allow.

Together, the approaches presented herein advance the synthesis and integration of QDs for scalable quantum photonics by combining data-driven synthesis optimization, silica shelling for size enlargement, and the development of colossal core/shell QDs. These approaches address

key challenges in QD-based single-photon emitters and provide strategies for improving stability, deterministic placement, and scalability. Beyond photonics, the findings contribute to a deeper understanding of QD growth and stability, supporting their broader application in quantum information science and next-generation optoelectronics.

TABLE OF CONTENTS

LIST OF FIGURES

LIST OF TABLES

ACKNOWLEDGEMENTS

These past four and a half years have been some of the most meaningful of my life. I've laughed, struggled, grown, and been constantly amazed by the people I've met and the support I've received. Writing this dissertation feels like closing a chapter that was once just a dream, and I couldn't have done it without so many of you who walked alongside me, sometimes without even realizing it.

I grew up in Tân Hiệp, Kiên Giang, a quiet town in the Mekong Delta of Vietnam. Life there was simple, and dreams often felt distant. But that's also where I learned what resilience and humility look like. It was my parents who first gave me the courage to look beyond the familiar. They sent me to summer school in another city when I was 15 just so I could learn English. Later, they let me spend my senior year of high school away from home so I could pursue my own path. That kind of trust shaped me more than I can express.

To my brother Danh, thank you for always challenging me. You were never afraid to argue with me, to push back, and that constant back-and-forth forced me to sharpen my thinking. To my sister Vân Anh, thank you for asking me endless science questions, even if they were a little naïve. You helped me learn how to explain things clearly, and without realizing it, you helped me become a better teacher. My cousin Duy An was the first person who taught me chemistry. I still remember those summer afternoons in 2012, sitting on the couch while he explained the basics. That was the beginning.

To my childhood friends—Kiều My, Đức Quí, Nhật Anh, Lan, and Việt Anh—thank you for sticking by me since we were kids. Even now, your encouragement still reaches me. And to my high school friends, especially Hương, Thư, Hưng, Trí, Dương, Dìn, Tuyền, Nhi, Khang, Duy,

Tuấn, Phương, Ly, and Thanh, you made one of the hardest but most exciting years of my life unforgettable.

To the teachers who saw something in me before I saw it in myself, thank you. Ms. Thư, my high school literature teacher, you helped shape not just how I learn but how I carry myself. Your influence goes far beyond the classroom.

My time at Pierce College in Washington was my first step in the U.S., and I owe so much to the people who helped me adjust and thrive. Minh Anh, Bảo Trân, and Khoa Lê, thank you for being my first Vietnamese family in America. My English 102 professor Ms. Alison Walker-Stromdahl, my organic chemistry professor Ms. Aly Snow, and my boss at the Writing Center Mr. Keith Kirkworth, thank you for your guidance, warmth, and encouragement. You helped turn a terrifying new beginning into something exciting and manageable.

At Texas A&M, I found my footing in science. Mr. Trung Le and Professor Brian Dolinar were the first people to take a chance on me as a researcher. Brian, you were my first real research mentor and taught me what scientific curiosity looks like in action. Trung, thank you for believing in me enough to help me publish my first paper. I'm also grateful to Professor Marcetta Darensbourg, Professor Holly Gaede, Dylan Denton, Eric Shrader, Mona Fattahi, Rachel Watts, Megan Welch, Ella Mo, Haley Naumann, Kyle Bordovsky, Yunuen Avila Martinez, Karan Hooda, and Danielle Burget. Each of you made College Station feel like home in your own way.

In 2020, I joined the Cossairt Lab at the University of Washington, and everything changed. Brandi, thank you for being the most supportive advisor I could have asked for. You gave me the freedom to explore ideas, the encouragement to speak up, and the confidence to keep going when things didn't work. You gave me the chance to go to so many conferences, gave me space to grow not just as a scientist, but as a person. Thank you for building a lab where people feel they belong.

To all my lab mates, thank you for making research feel less lonely. Emily Nishiwaki, thank you for being my adventure buddy from Ong Lam to Xian Noodle and to every random coffee shop in Seattle. Emily Miura-Stempel, thank you for always agreeing to go on walks any time during work. Professor Samantha Harvey, I can't count how many ~~gossips~~ career development conversations we had circling the fountain and at Sstarbucks. Max Friedfeld, thank you for mentoring me in those first chaotic months. Dr. Hunter Ripberger, you always had the best karaoke performance. Dr. Ding-Yuan Kuo, thanks for catching me roaming around CHB in goggles way too often. Madison Monahan, thank you for taking TEM images of my first ever quantum dots. Nayon Park, thank you for being my hot pot friend, snack supplier, and job search advisor all in one. Florence Dou, somehow you and I share a ridiculous number of things in common. Still mad that you photobombed my selfie with John Isner but OK. You're the only one in the lab who met my little sister in person. Micaela Homer, thank you for sharing your first Uwajimaya experience with me, it's a core memory now. Helen Larson, thank you for being someone I could talk to about science or anything else. Chris Lowe, I still laugh every time you call me "boss"; your kindness and humor are contagious. Soren Sandeno, I have no idea what score you got on the SAT in 2025, but who cares because you crystalized those InAs clusters so fast, bada bing bada boom. Grant Dixon, thank you for the cows; I'm always jealous with all the cool shirts you have. Pedro Pliego, thank you for quietly checking in on me every time I was trying to be alone at Sip House. Reed Worland, thank you for picking up the project I was reluctant to take and making it better. Elise Skytte, I know you'll write the next great chapter of this research. You're a brilliant scientist, a kind human, and, yes, a Swiftie. To my mentees, Shenwei Wu and Griffin Schwartz, working with you was one of the best parts of my time at UW. You reminded me why I love research, and I'm so excited to see where your paths lead.

xx

Outside of the lab, I'm grateful for friends who reminded me that there's more to life than deadlines. Brian Sun, thank you for dragging me to Pike Place at 1 a.m. during our first year when the pressure felt like too much. Phuong Le, Thao Kim, and Corvo from the Vietnamese Chemical Society—thank you for all our "science" discussions, hangouts, and cookouts. You made Seattle feel like home.

To my collaborators: David Sharp, Greg Guymon, Jessica Kline, Ben Hammel, Dr. Yi-Yu Cai, Dr. Johannes Froch, and Tommy Nguyen—thank you for your time, your brilliance, and your patience. I truly couldn't have done this without you. To the professors who supported my work, Arka Majumdar, David Ginger, Devin MacKenzie, Kaimei Fu, Gordana Dukovic, Sadegh Yazdi, and Cherie Kagan, thank you for your guidance. And to IMOD, thank you for creating a collaborative research environment that helped my science grow.

To my committee, Professors Daniel Gamelin, David Ginger, Arka Majumdar, and Matthew Yankowitz, thank you for your thoughtful questions, your time, and your support throughout this process.

And to Baha Okten. Thank you for being there through everything. You supported my work, my decisions, my uncertainty, and my ambitions without hesitation. You listened to me talk about quantum dots, walked with me when I needed quiet, and reminded me that life outside of science matters too. I don't know how I would have done this without you.

This dissertation carries the fingerprints of every single person mentioned here, and many more I couldn't fit into these pages. Thank you, all of you, for walking with me on this path.

DEDICATION

To everyone who supported me to accomplish this work.

PREFACE

When I started my Ph.D. in 2020, quantum computing felt like its own version of the Space Race in the 20th century. The U.S. had just launched the National Quantum Initiative to advance quantum research. Google claimed "quantum supremacy" with its superconducting Sycamore processor, whose performance no classical computer could match in 2019. A year later, Chinese researchers released Jiuzhang, a quantum system based on light. Meanwhile, companies like IBM, Honeywell, Xanadu, Microsoft, and Rigetti were racing to replace traditional bits with quantum bits (qubits), which could completely transform computing. I spent a lot of time learning about different qubit platforms and following which company would build a processor with more qubits than the previous ones. But my interest actually started for a more practical reason, as I was tasked with making CdSe quantum dot (QD) nanocrystals in solution and isolating individual crystals on a flat substrate, which my physicist collaborators needed to extract single photons, each acting as a qubit.

In 2023, colloidal QDs received long-overdue recognition when the Nobel Prize in Chemistry was awarded to Moungi G. Bawendi, Louis E. Brus, and Aleksey Yekimov. A year later, I attended the 2024 Gordon Research Conference on Colloidal Semiconductor Nanocrystals in Les Diablerets, Switzerland. QDs are already widely used in display technology, bioimaging, and solar cells, but what excited me most was that Professor Bawendi focused his event-closing talk on QDs as single-photon sources for quantum information science.

Just as the Space Race pushed the boundaries of exploration, my journey has been about pushing colloidal QD chemistry closer to quantum information science, which may seem like

distant fields, but are steadily converging. This dissertation reflects my efforts to bring the two field together through synthetic chemistry and some engineering.

Chapter 1. BACKGROUND

This chapter aims to provide an introduction to relevant topics in this dissertation. Section 1.1 introduces the history of our understanding of the nature of light and a deep dive into photon statistics to classify light sources. Section 1.2 provides relevant background on colloidal quantum dots. Section 1.3 explains why a QD-cavity integrated system is important. Parts of this chapter are inspired by the book *Quantum Optics: An Introduction* by Mark Fox and Components of this chapter were republished with permission of the American Chemical Society, from "Design Rules for Obtaining Narrow Luminescence from Semiconductors Made in Solution", Hao A. Nguyen, Grant Dixon, Florence Y. Dou, Shaun Gallagher, Stephen Gibbs, Dylan M. Ladd, Emanuele Marino, Justin C. Ondry, James P. Shanahan, Eugenia S. Vasileiadou, Stephen Barlow, Daniel R. Gamelin, David S. Ginger, David M. Jonas, Mercouri G. Kanatzidis, Seth R. Marder, Daniel Morton, Christopher B. Murray, Jonathan S. Owen, Dmitri V. Talapin, Michael F. Toney, Brandi M. Cossairt; Chemical Reviews 2023, 123, 12, 7890–7952; Copyright 2025 American Chemical Society.

1.1 LIGHT

Light has always been central to human experience. From the earliest days, humans used fire not only for heat and cooking, but as a vital source of light to extend activity beyond sunset. Torches, oil lamps, and eventually candles enabled movement, craftsmanship, and communication in the dark. Sunlight marked the passage of time and the changing of seasons, becoming essential for agriculture and early calendars. Light also played a role in signaling through smoke, flame, and later, mirrors and lenses which showed the beginning of light-based technologies.

Our perception or understanding of light has progressed greatly throughout history. From "Let there be light" in the Genesis or the ancient Egyptian Sun God Ra, where light was seen as a symbolic and philosophical mystery, we first made deeper inquiry for behaviors of light through the geometrical optics studies by Euclid and Ptolemy, and later through the *Book of Optics* by Ibn al-Haytham in the classical era. The identity or origin of light was first suggested by Issac Newton in the 17th century, where he proposed that light was made of particles, or "corpuscles", which could explain its straight-line propagation and refraction through prisms. Around the same time, Christiaan Huygens introduced the wave theory of light, offering an alternative explanation for reflection, refraction, and diffraction. The debate continued into the 19th century, when Thomas Young's double-slit experiment demonstrated interference, which is clear evidence of wave-like behavior. Augustin-Jean Fresnel and James Clerk Maxwell expanded this view, with Maxwell ultimately formulating the theory of electromagnetism that defined light as a transverse electromagnetic wave.

Despite the success of the wave theory, certain phenomena could still not be explained. At the turn of the 20th century, Max Planck introduced the idea of energy quantization to explain blackbody radiation, which laid the foundation for quantum theory. Soon after, Albert Einstein proposed that light itself was made of discrete packets of energy, or photons, to explain the photoelectric effect, where light ejects electrons from a metal surface only above a certain frequency. This particle-like behavior of light introduced a duality: light could behave both as a wave and as a particle, depending on the context. The concept of photon energy, given by

$$E = h\nu \tag{1}$$

where E is the photon energy, h is the Planck constant, and ν is the photon frequency. This equation became central to understanding how light (photon) interacts with matter (electron),

which unlocked a new realm of understanding of chemical reactions, electrons, or probing molecular structure. The rigor of the quantum framework in our understanding of light allows us to treat a beam of light as a stream of individual photons rather than as a classical wave, which is important for later chapters in this dissertation, where photon statistics, different types of photon sources, and applications of photonic quantum bits (qubits) are introduced.

Aside from the wave-particle duality, photons are unique among elementary particles as they have no rest mass, always travel at the speed of light of 299 792 458 m/s in a vacuum, and carry both energy and momentum. As bosons with a spin of 1, photons can occupy the same quantum state. Under specific generation conditions, photons can exhibit coherence, which means that photons maintain their monochromaticity, well-defined temporal phase, spatial phase, and polarization. The degree of coherence is a fundamental characteristic that distinguishes different types of photon sources.

1.1.1 *Light Sources*

Most common light sources we encounter in our daily lives are classical light sources, such as thermal light or black-body radiation from the sun, fire, or incandescent light bulbs. These light sources emit photons that are incoherent, meaning photons are emitted in random directions, with varying wavelengths, polarizations, and phases. In contrast, when the emitted photons are coherent, the light sources are classified as coherent light sources, such as lasers. A defining feature of a laser is amplified emission, where the light intensity is high due to the stimulated emission of many photons. This results in the emission of large numbers of photons over a unit of time, typically after a trigger event. However, when only a single photon is emitted after a trigger event, the light source transitions from being a coherent source to a single-photon source, a more specialized and sophisticated light emitter. The distinction between classical, coherent, and single-

photon sources is crucial for understanding the use cases, characterization, and designing light-emitting materials. The following sections aim to provide a simplified classification of these three types of light sources from the perspective of photon statistics.

1.1.2 *Photon Detection*

Counting the number of light particles or photons over a unit of time or space is not a trivial measure. Intuitive approaches include the use of photoconductive, Einstein's photoelectric, photothermal, or photochemical effects that monitor the change in electrical conductivity, the release of electromagnetic radiation, the generation of heat, or the difference in chemical composition, respectively, of a material in a detection device. Taking a photomultiplier (PMT) as an example, this device utilizes Einstein's photoelectric effect (despite being first demonstrated by Heinrich Hertz roughly 18 years before the photoelectric effect was introduced). A PMT converts the incident light intensity into electrical signals or voltage pulses, which go to an electronic counter for readout.

In the case of a monochromatic beam with constant intensity I and an exposed area A, this beam is treated as a stream of photons, and the average photon flux Φ represents the average number of photons passing through a cross-section of the beam per unit time. Photodetectors are characterized by their quantum efficiency η, which defines the ratio of detected photons to incident photons. The number of photons being detected over a unit of time T can be calculated as:

$$N(T) = \eta \Phi T = \eta \frac{IA}{\hbar\omega} T = \eta \frac{P}{\hbar\omega} T \tag{2}$$

where P is the beam power. The detector's average count rate $\mathcal{R}$ is then:

$$\mathcal{R} = \frac{N(T)}{T} = \eta \frac{P}{\hbar\omega} \tag{3}$$

Modern photon detectors have an upper bound of count rate about 10^6 counts/s with $\eta > 10$ %, which limits the beam power P to less than $10^{-12}\ W$. This limitation stems from the finite recovery time required by the detector following each detection event.

There are two main issues with using the well-defined equations above to count photons. The first stems from the inevitable fluctuations in photon number within a given segment due to the discrete nature of photons. On short time scales, the number of photons can vary significantly from the average, and this randomness grows as the observation window narrows. These fluctuations reflect the statistical nature of light and are tied to the Heisenberg uncertainty principle, which suggests that measuring one property precisely, like photon number or location, introduces uncertainty in others, such as phase. The second issue is more technical. While detecting individual voltage signals seems to suggest detection of discrete energy packets, the reality is more complicated due to the small energy of photons. For instance, the energy of a visible photon ($\lambda = 500\ nm$), which is about $3.98 \times 10^{-19}\ J$, can be mistaken by noises and false signals from the detectors. There are ongoing studies in optical physics about whether the events recorded by photon counters truly reflect photon statistics or are simply artifacts of the detection process. Therefore, photon statistics, which is the theoretical and experimental study of the statistical distributions produced in photon counting experiments, is essential for distinguishing true quantum signals from noise and understanding the underlying nature of light.

1.1.3 *Photon Statistics Crash Course*

This brief section serves as an attempt to simplify photon statistical approaches and probability calculus to classify types of light sources. An ideal coherent light beam with constant power has a Poisson distribution of photons because the number of photons here should be

considered as an integer. The average number of photons $\bar{n}$ in a given beam segment with length L can be calculated as

$$\bar{n} = \frac{\Phi L}{c} \tag{4}$$

Since the exact number of photons in the segment with L cannot be measured, it is necessary to estimate the probability $\mathcal{P}(n)$ of finding n photons in L. With the goal of counting single photons, it is also necessary to divide L into N subsegments with length $\frac{L}{N}$ that have a high probability p of finding only one single photon and a negligible probability of finding more than one photon (**Figure 1.1**). Hence, $p = \frac{\bar{n}}{N}$ for any of the N subsegments with length $\frac{L}{N}$. The probability $\mathcal{P}(n)$ of finding n photons in a segment with length L that contain N subsegments is given by the binomial distribution:

$$\mathcal{P}(n) = \frac{N!}{n!\,(N-n)!} p^n (1-p)^{N-n} \tag{5}$$

which can then, with lengthy math, be written in the Poisson distribution form:

$$\mathcal{P}(n) = \frac{\bar{n}^n}{n!} e^{-\bar{n}}, n = 0, 1, 2, \ldots \tag{6}$$

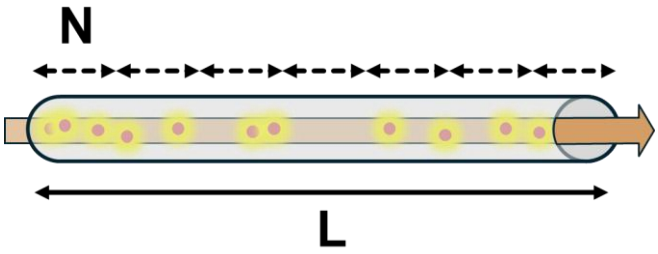

Figure 1.1. Illustration of a stream of photons passing through a tube.

With Poisson statistics, a perfect distribution with a mean value $\bar{n}$ has a variance given by

$$(\Delta n)^2 = \bar{n} \tag{7}$$

and a standard deviation

$$\Delta n = \sqrt{\bar{n}} \tag{8}$$

The two other possibilities are when $\Delta n > \sqrt{\bar{n}}$ (super- Poissonian distribution) and $\Delta n < \sqrt{\bar{n}}$ (sub- Poissonian distribution) (**Figure 1.2**).

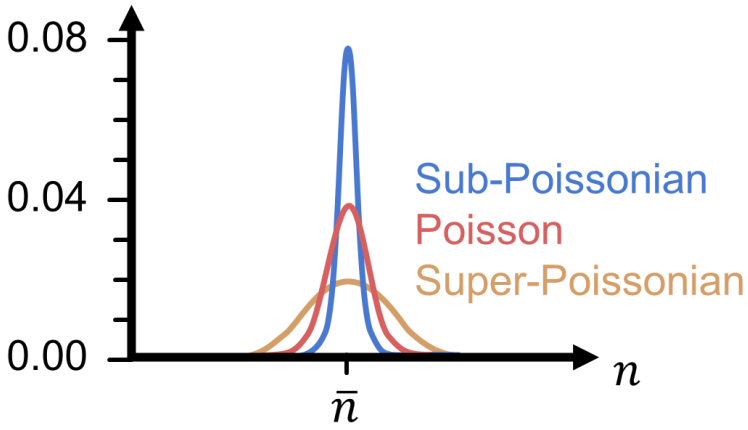

Figure 1.2. Poissonian, sub-Poissonian, and super-Poissonian distributions.

1.1.4 *Types of Light Sources.*

When applying Poissonian statistics to characterize light sources, one key consideration is the mean photon number $\bar{n}, n \in \mathbb{N}_0$ (**Figure 1.3**). A perfectly coherent light source, such as an ideal laser, exhibits a Poisson distribution of photon counts. In contrast, thermal or classical light sources show greater intensity fluctuations over time, leading to a broader distribution that follows super-Poissonian statistics—more accurately described by the Bose-Einstein distribution. On the other hand, an ideal single-photon source demonstrates sub-Poissonian behavior, characterized by a sharply peaked photon number distribution centered at $\bar{n} = n = 1$. This narrow distribution reflects the suppression of multi-photon events, which is a hallmark of true quantum light.

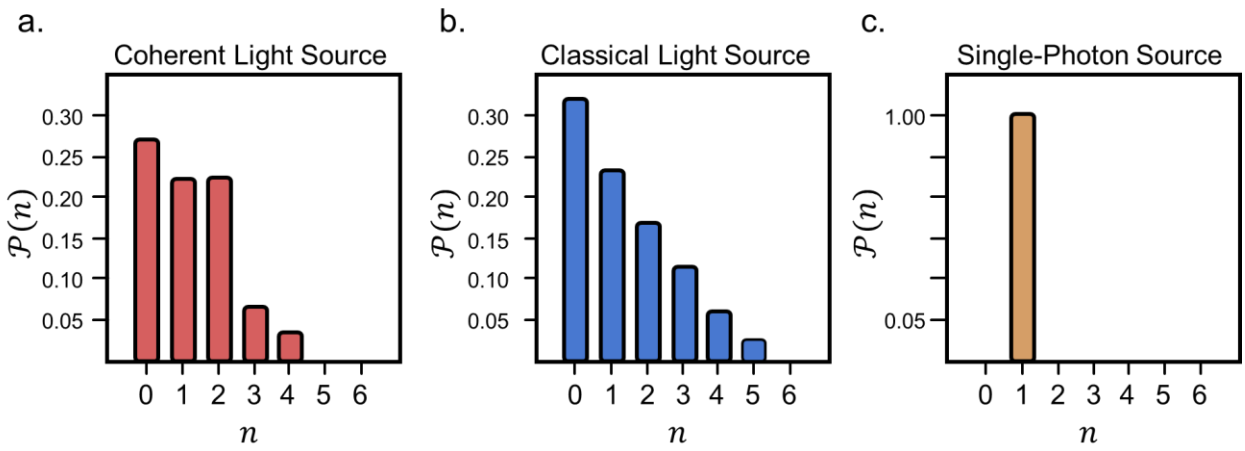

Figure 1.3. Classification of light sources from photon statistics.

1.1.5 *The Hanbury Brown and Twiss Experiment*

The practical development of single-photon sources originated from the Hanbury-Brown and Twiss (HBT) experiment by Robert Hanbury Brown and Richard Q. Twiss, which was originally designed in 1956 to study the spatial coherence of starlight and was successful in measuring the size of Sirius.[1] The need for generating true single photons became more urgent after 1964, when Bell's inequality showed that the predictions of quantum mechanics could not be explained by any theory based on hidden variables and local realism. This initiated experimental test of the Einstein-Podolsky-Rosen (EPR) paradox.[2,3] The paradox argues that if quantum mechanics is correct, then measuring one particle of an entangled pair instantly affects the other, no matter how far apart they are. Einstein and colleagues found this deeply troubling, because it seems to imply "spooky action at a distance," which violates the idea that nothing can travel faster than light. Hence, they proposed that quantum mechanics must be incomplete, and that there might be hidden variables that determine the outcomes of measurements.[3]

Bringing the focus back to single-photon sources, the first successful observation of sub-Poissonian statistics for photons was demonstrated by John Clauser in 1974[4], making it possible

to perform experiments that test whether entangled photons influence each other instantaneously. This marked an important step toward verifying the quantum nature of light at the single-photon level. Moreover, Harry Kimble in 1977 first showed the phenomenon of photon antibunching, meaning photons coming out of a source one at a time.[5] Kimble's experiment was also the first time the HBT setup was used to statistically justify whether a photon source behaves as a true single-photon source. Since then, the HBT experiment has become a central tool for identifying and verifying single-photon emission.

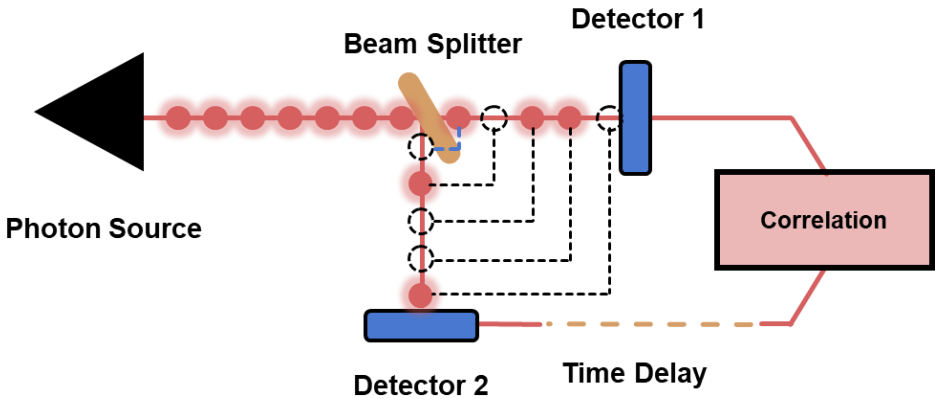

Figure 1.4. A simplified HBT experiment setup

In its basic form **(Figure 1.4)**, the experiment splits the output of a photon source using a 50:50 beam splitter to direct the two resulting paths toward two separate photon detectors. Each detection event is time-stamped and coincidences (instances when both detectors register a photon within a defined time window) are recorded. For a classical or coherent source that produces bunched photons, simultaneous detections occur frequently, resulting in a nonzero coincidence rate when delay time is 0 ($\tau = 0$). In contrast, an ideal single-photon source cannot emit two photons at once, so no coincidences should be observed when $\tau = 0$. In practice, the experiment is conducted over several minutes to hours with 10^5 to 10^7 photon detection events to get meaningful data.

Th results of the HBT effect are quantitatively described by the second-order correlation function of the coincidence events as a function of time delay ($g^{(2)}(\tau)$). It is worth noting that first-order correlation does not capture the temporal spacing between individual photons and therefore cannot reveal photon antibunching, which is fundamentally a second-order intensity correlation effect. The $g^{(2)}(\tau)$ function measures how likely two photons are to be detected with a time separation τ, relative to what would be expected from completely random (Poissonian) arrivals. Conceptually, $g^{(2)}(\tau)$ answers the question: "A photon was detected at time t, what is the probability of detecting another photon at time $t + \tau$?". The most important case is $g^{(2)}(\tau = 0)$ or $g^{(2)}(0)$, which corresponds to simultaneous detection events. Different types of light sources exhibit characteristic values of $g^{(2)}(0)$. Classical light sources exhibiting bunching photons have $g^{(2)}(0) > 2$. Coherent light sources such as lasers with Poissonian photon statistics show $g^{(2)}(0) = 1$. Single-photon sources emitting anti-bunched photons are characterized by $g^{(2)}(0) \ll 1$ or $g^{(2)}(0)$ approaching 0 (**Figure 1.5**).

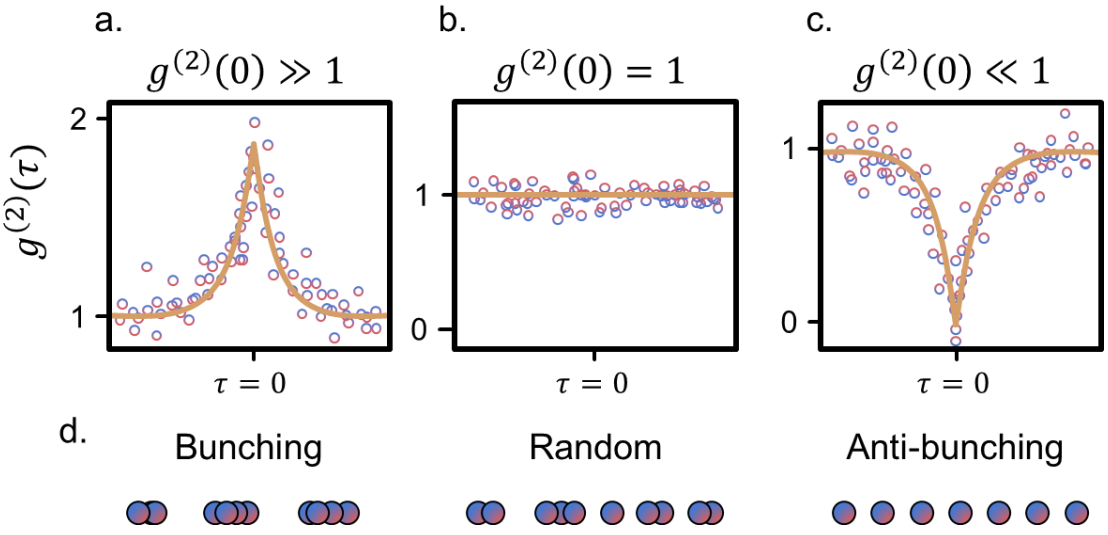

Figure 1.5. $g^{(2)}(\tau)$ graphs for **a.** classical, **b.** coherent, and **c.** quantum light sources. **d.** Illustration of photon bunching behaviors from different class of light sources.

Achieving a perfect single-photon source that emit on demand anti-bunched, indistinguishable photons with well-defined quantum state, one photon at a time, and with a high repetition rate is difficult in practice because photons, which are bosons, tend to congregate in the same quantum state. In simpler terms, photons tend to occupy the same physical space. Furthermore, a perfect single-photon source and detecting perfect single-photon emission are, in fact, unrealistic or even unphysical due to the quantum attributes of photons, Heisenberg uncertainty principle, and photon detection limits.[6] Fortunately, in practical applications, additional components can be integrated to compensate for imperfections in non-ideal single-photon sources to enable the integrated system to reliably photon single photons on demand.[7,8]

1.1.6 *Applications for Single-Photon Sources*

In recent years, the ability to generate single photons has advanced rapidly alongside discoveries of how to use photons in different applications beyond theoretical interests.[7–10] Unlike classical light sources, single-photon sources give rise to the manipulation and uses of single photons, which exhibit inherently quantum properties such as antibunching, coherence, superposition, and entanglement, making them ideal carriers of quantum science information (**Figure 1.6**). In quantum communication, single photons are used in quantum key distribution (QKD) that allows secure transmission of information that is fundamentally immune to eavesdropping.[11] In quantum computing, they serve as quantum bits or qubits in photonic processors, enabling logic operations through interference and entanglement.[9,12] Single photons also form the foundation of emerging quantum networks, where they mediate long-distance entanglement between nodes.[13] Beyond communication and computation, single-photon sources play a role in quantum imaging and sensing with resolution and sensitivity beyond classical limits.[14] Applications include single-molecule detection, low-light biological imaging, and high-

precision metrology.[7,14,15] As single-photon sources become more efficient and accessible, they are poised to revolutionize the way information is transmitted, processed, and measured.

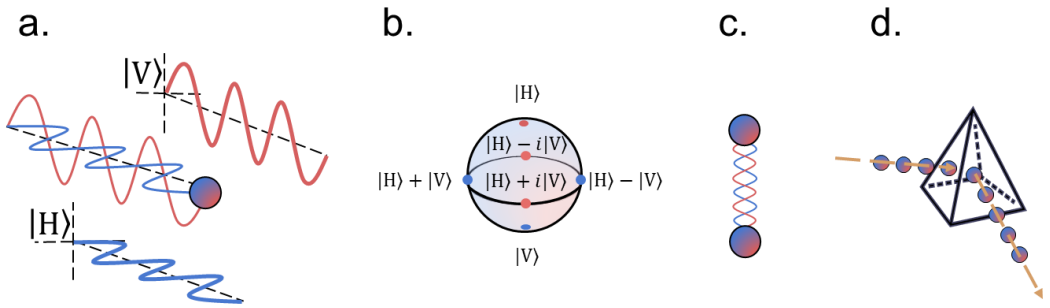

Figure 1.6. a. An example of a photonic qubit that encodes information using the horizontal (H) and vertical (V) polarization of a single photon. **b.** An arbitrary Bloch sphere that shows different quantum states in a single photon. **c.** An illustration of the entanglement effect in a pair of photons, where quantum information is stored across two photons in a shared and distanced state. **d.** An illustration of a stream of anti-bunched photons being redirected through a crystal.

1.1.7 *Materials for Single-Photon Sources*

Single-photon sources are generally classified into two types: probabilistic and deterministic. In both early research and most current commercial devices, probabilistic sources remain the most widely used, typically based on spontaneous parametric down-conversion or four-wave mixing (**Figure 1.7.a-b**). They are termed probabilistic because, following a pump or trigger pulse, there is only a certain probability that a single photon will be generated and successfully emitted, rather than a guaranteed outcome. The other alternative type is deterministic singe-photon sources, which produce single photons on demand. This can be achieved mainly by using an atom-like, two-level system emitter (**Figure 1.7.c)**. Typically, a laser excitation pulse is used to put the emitter into a higher-energy electronic state, from which it relaxes to a lower-energy state and

release a single photon through spontaneous emission. While probabilistic single-photon sources are favored for their relatively simple operation and compatibility with existing optical platforms, deterministic single-photon sources from solid-state materials are much more attractive for quantum applications due to the mesoscopic size, versatility in device integration, and recent advances in synthesis and characterizations in materials science and chemistry to produce high-quality and flexible materials.

Extensive interdisciplinary research conducted over the past two decades has identified a variety of materials that can be used as single-photon sources, including trapped ions,[16,17] diamond color centers,[18,19] two-dimensional materials,[20] small molecules,[21–23] epitaxial quantum dots (QDs),[24–26] and single colloidal QDs.[27] Each class of materials presents advantages and limitations in single-photon emission performance and device integration. For the rest of this dissertation, the focus is on single colloidal QDs as a promising single-photon emitting system for scalable device integration.

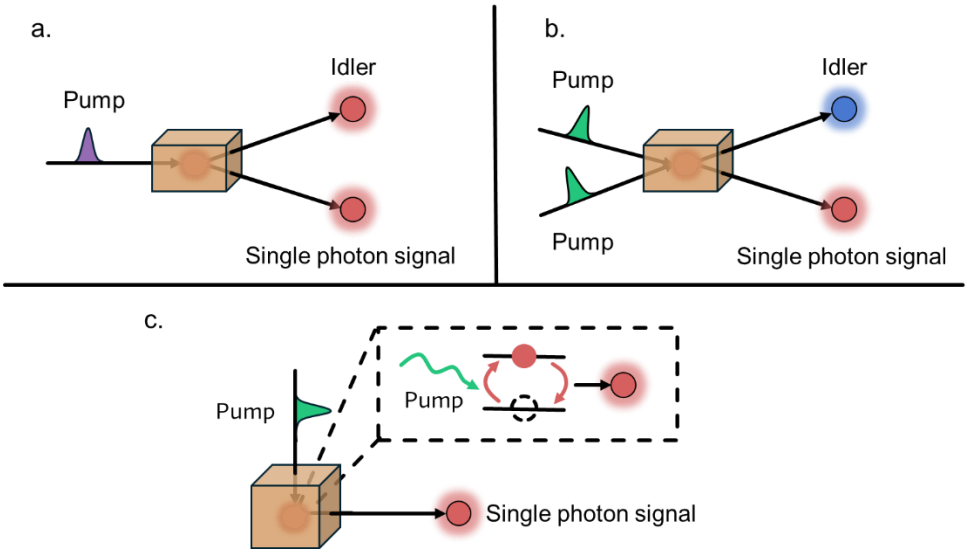

Figure 1.7. Single-photon source from **a.** spontaneous parametric down-conversion, **b.** four-wave mixing, and **c.** a two-level atom-like photon source.

1.2 COLLOIDAL QUANTUM DOTS

"What is the size of colloidal particles? Are they molecules or aggregates of molecules? How many atoms approximately does a single gold particle contain?" These very questions were asked exactly a century ago during the Nobel Lecture delivered by the 1925 Chemistry Nobel Laureate Richard A. Zsigmondy. His most groundbreaking development of the ultramicroscope enabled the direct observation of colloidal particles, first with colloidal gold particles in purple of Cassius and cranberry glass. Given that colloidal QDs are a special class of colloidal particles, distinguished by their size-dependent electronic properties and especially, solution processibility through the colloidal nature, it is fitting to begin this section with a brief historical perspective on colloids, tracing back to Zsigmondy's and others' contributions and the early stages of nanostructured matter.

1.2.1 *Colloids*

Colloids are heterogeneous systems in which particles with dimensions typically between 1 and 1000 nanometers are dispersed within a continuous medium. These particles are large enough to scatter light but small enough to remain suspended due to thermal motion. The intermediate scale gives colloidal particles their distinct optical, kinetic, and thermodynamic behaviors. The scientific foundations of colloid research were laid in the 19th century. In 1857, Michael Faraday famously prepared a stable dispersion of ruby-red colored gold in liquid media, noted "the cone was well defined in the fluid by the illuminated particles", and started thinking about the connection between its optical behavior to particle size. Thomas Graham later introduced the term "colloid" in 1861, emphasizing their resistance to diffusion and crystallization. Building on these early insights, Zsigmondy's ultramicroscope enabled direct visualization of colloidal

particles and demonstrated their discrete, particulate nature. Subsequent advances came from scientists such as Wolfgang Ostwald, who helped formalize colloid chemistry as a discipline, and Theodor Svedberg, whose development of the analytical ultracentrifuge provided quantitative insights into particle size and distribution. Further important contributions included Jean Perrin's work on Brownian motion, which confirmed the molecular nature of colloids and supported atomic theory, and Irving Langmuir's studies on monolayers, which introduced a molecular-level understanding of colloid and particle surface interactions.

Colloidal systems span a wide range of material types and phases, including sols (solid particles in liquid), emulsions (liquid in liquid), foams (gas in liquid or solid), and aerosols (solid or liquid in gas). Their dispersed particles can be composed of metals, oxides, polymers, or biological macromolecules, stabilized by electrostatic or steric interactions. The rest of this chapter will focus on a very special type of colloid, colloidal semiconducting nanocrystals, where nano-size crystallites with semiconducting properties are dispersed in solutions.

1.2.2 *Colloidal Semiconducting Nanocrystals – Colloidal QDs*

The Nobel Prize in Chemistry in 2023 was awarded for the discovery and development of colloidal QDs. This prize has three facets: the experimental discovery of size-dependent quantum effects in nanocrystals by Alexey Ekimov, the theoretical explanation of these effects in colloidal solutions by Louis Brus, and the development of precise synthetic methods by Moungi Bawendi. These landmark contributions collectively transformed quantum dots from a fundamental curiosity into a versatile platform for applications in imaging, optoelectronics, and quantum technologies.

When crystalline solids are reduced to the nanometer scale, their physical and electronic properties begin to deviate significantly from those of the bulk. In this mesoscopic regime, nanocrystals possess too few atoms to exhibit fully delocalized band structures yet are too large to

be treated as discrete molecules. This transition gives rise to quantum confinement, surface-dominated reactivity, and other size-dependent phenomena. For semiconductors, these effects result in tunable optical absorption and emission, allowing the bandgap to be engineered by controlling particle size. Additionally, the high surface-to-volume ratio of nanocrystals leads to unique interfacial properties, often distinct from those of the bulk material.

The emergence of modern nanoscience centered around nanocrystals began in earnest in the early 1980s and continues to evolve today. In fact, Ekimov's early work in glass matrices provided the first experimental evidence that shrinking semiconductors into nanocrystals could shift their optical absorption, now recognized as the hallmark of quantum confinement.[28] But before that, initial efforts largely focused on synthesizing oxide nanocrystals such as TiO_2, ZrO_2, and ThO_2, primarily as additives to improve the mechanical and thermal properties of silica-based solids and fibers, often without full recognition of their semiconducting nature.[29,30] A significant shift occurred in the wake of the 1970s oil crisis, which spurred interest in alternative energy technologies. This led to pioneering studies in colloidal photochemistry, particularly involving CdS and TiO_2 nanocrystals for solar energy conversion.[31,32]

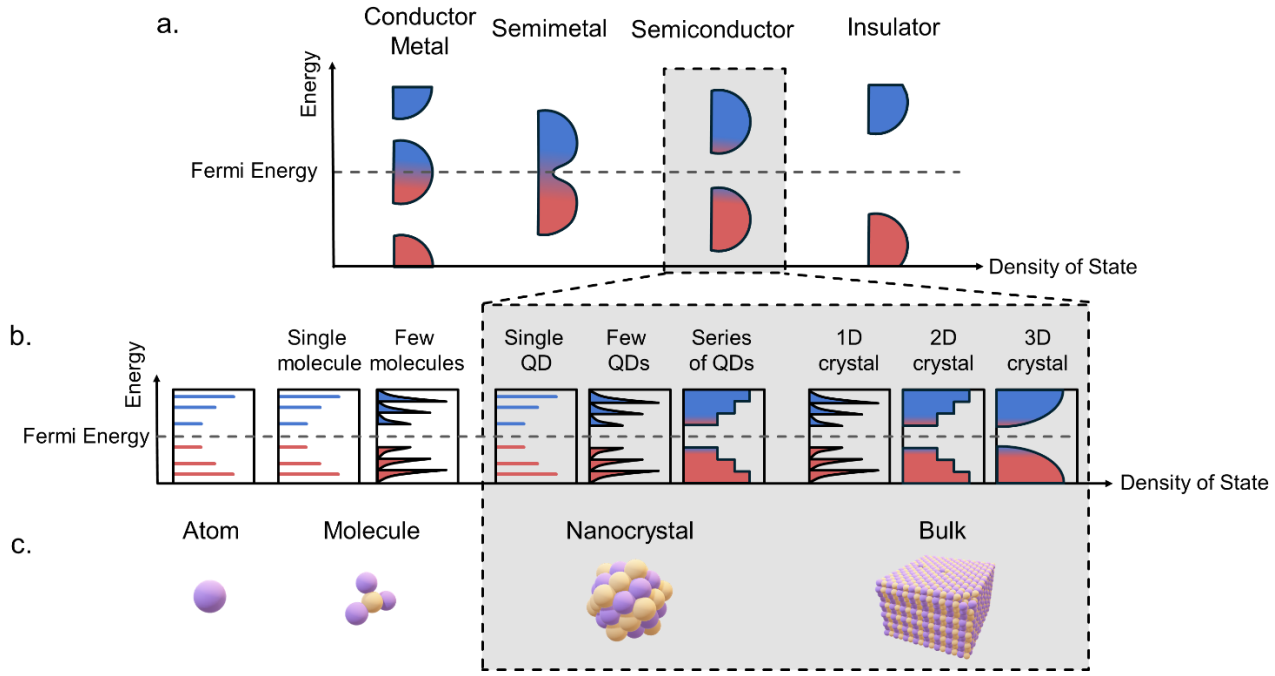

Figure 1.8. a. Schematic illustration of the density of states metal, semimetal, semiconductor, and insulator. **b.** Simplified illustration of the density of states of an atom, molecules, nanocrystal semiconductors, and bulk semiconductors with different degrees of dimensionality. **c.** Atomic view illustrations of an atom, a molecule, a nanocrystal, and a bulk solid.

The electronic properties of solids originate from the atomic orbitals of their constituent atoms. As individual atoms assemble into a molecule and a crystal, their discrete orbitals overlap and split into bands of closely spaced energy levels. In extended solids or bulks, these bands form continuous energy regions known as the valence band (derived from filled bonding orbitals) and the conduction band (derived from empty antibonding orbitals). The energy separation between these bands, which is called the bandgap, determines whether a material behaves as a conductor, semiconductor, or insulator. In semiconductors, the bandgap is small enough to allow thermal or optical excitation of electrons from the valence band to the conduction band, enabling electrical conductivity and light–matter interactions. The Fermi level, the highest occupied energy level at

absolute zero, lies within this gap and serves as a reference point for electron occupancy and excitation. In the context of band theory, the density of states (DOS) describes the number of available electronic states at each energy level within a material. In bulk semiconductors, the DOS is continuous within the conduction and valence bands and increases with energy due to the increasing number of allowed momentum states. However, in quantum-confined systems like nanocrystals, the DOS becomes discretized into sharp energy levels, resembling atomic or molecular spectra. This discretization is a direct consequence of spatial confinement and reduced dimensionality (**Figure 1.8**).

When the dimensions of a semiconductor crystal are confined to the nanometer scale, its band structure no longer remains continuous. Instead, quantum confinement causes the energy bands to break into discrete, atom-like energy levels. This behavior can be understood through the "particle in a box" model, which is a foundational quantum mechanical thought experiment in which a particle is confined within an infinitely deep potential well. Solving the Schrödinger equation for a particle of mass m in a box of length L yields discrete energy levels:

$$E_n = \frac{n^2 h^2}{8mL^2} \tag{9}$$

where n is a positive integer and h is Planck's constant. This result illustrates several key quantum principles: the energy is quantized, it cannot be zero, and it increases as the confinement length L decreases. In the context of nanocrystals, this means that as the crystal size becomes smaller, the electronic energy levels shift higher, effectively widening the bandgap. This simplified model, however, does not yet account for the nature of charge carriers (an electron and a lack of electron or hole) in a QD.

When a photon excites an electron from the valence band to the conduction band, it leaves behind a positively charged hole. The resulting electron–hole pair, bound by Coulombic attraction,

is known as an exciton. In QDs, if the radius R is smaller than twice the exciton Bohr radius (a material-specific value), the exciton becomes confined in all three spatial dimensions, further modifying its energy. This situation is more accurately described by considering a particle in a three-dimensional potential well and incorporating the electron and hole's effective masses and their mutual interaction. Louis Brus introduced a model that captures these effects, which provides the first theoretical framework for understanding how quantum confinement governs the optical and electronic properties of colloidal quantum dots.[33,34] The resulting expression for the size-dependent energy of a QD is:

$$E_{QD} = E_{bulk} + \frac{h^2}{8R^2}\left(\frac{1}{m_e^*} + \frac{1}{m_h^*}\right) - \frac{1.8e^2}{4\pi\varepsilon_0\varepsilon_r R^2} \quad (10)$$

The first term represents the bandgap of the bulk semiconductor (E_{bulk}), the second accounts for quantum confinement of both carriers with m_e^* and m_h^* being the effective mass of the electron and the hole respectively, and the third term captures the Coulombic attraction between the electron and hole with ε_0 and ε_r being the permittivity of vacuum and the material. This model laid the theoretical foundation for understanding and predicting the size-dependent optical and electronic properties of semiconductor nanocrystals.

The third laureate, Moungi Bawendi, later transformed the field by establishing synthetic methods for producing highly uniform and high-quality colloidal quantum dots, which will be discussed in detail in **Chapter 2**.[35]

1.2.3 *Ligands*

When nanocrystals, which are typically composed of inorganic atoms, are dispersed in a solvent, they are subject to a complex web of interactions between the particles themselves and with the surrounding solvent molecules. This interplay governs their motion, stability, and ability

to remain as individual colloids. Jean Perrin's experiments on Brownian motion provided the first quantitative evidence for the molecular nature of matter, showing that tiny particles suspended in fluid exhibit erratic motion due to collisions with solvent molecules.[36] In colloidal QDs, the presence of an organic layer of molecules, called ligand, surrounding each particle fundamentally alters these interactions. When a ligand binds to the surface of a QD, it can weaken the bonds between the surface atoms and the atoms inside the core of the crystal. By binding to the QD surface, ligands can prevent aggregation, modulate interactions with the solvent, and are important for achieving colloidal stability.[37,38]

Ligands typically consist of two parts: a head group that binds directly to surface atoms of the nanocrystal, and a tail group that interfaces with the surrounding medium (**Figure 1.9**). Common head groups include carboxylates, phosphonates, thiols, amines, and halides. These groups vary in their binding strength, reactivity, and selectivity toward different crystal facets.

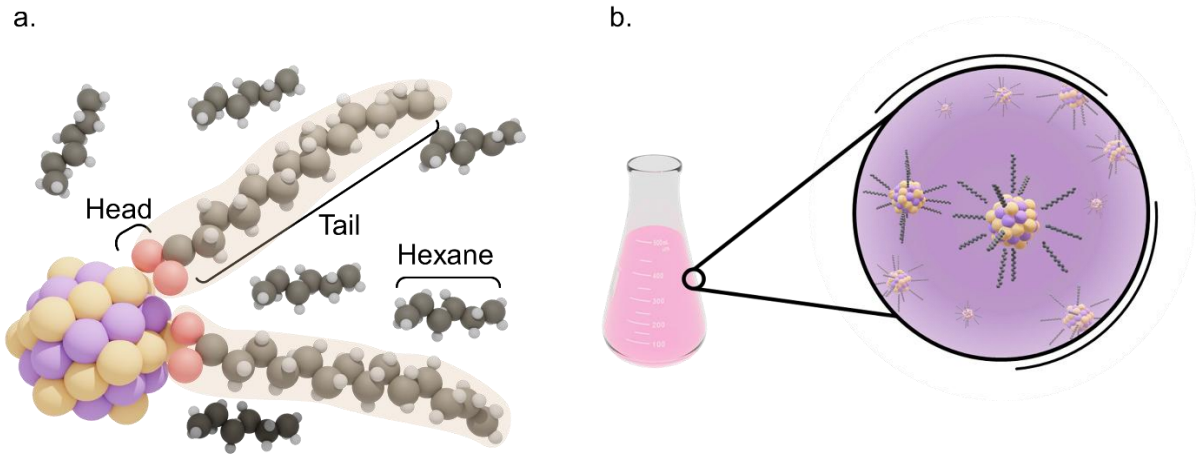

Figure 1.9. a. Illustration of a QD with two attaching oleate ligands and 6 surrounding hexane solvent molecules. The red, black, and white balls represent oxygen, carbon, and hydrogen atoms. **b.** illustration of a solution of QDs containing many QDs with ligands.

Roles of ligands in QD chemistry are not limited to just colloidal stability but also in directing key aspects of their nucleation, growth, and final properties. During synthesis, ligands adsorb to the QD surface, where the head group anchors to undercoordinated surface atoms and the tail group extends outward into the solvent. This dynamic interface regulates precursor access, influences surface energy, and affects growth kinetics.[37,38] As a result, the amount, type, length, and identity of ligands play central roles in determining nanocrystal size, shape, crystal phase, and facet expression. For example, mixed-ligand systems enable facet-selective binding that promotes shape anisotropy, while variations in chain length and steric bulk can modulate the rate of monomer diffusion to the surface.[39]

Since QD chemistry is dominated on the QD surface, where ligands reside, the ligand shell strongly impacts the optical and electronic properties of QDs. Effective passivation by appropriate head groups can minimize (or increase) trap states and improve photoluminescence quantum yield. Meanwhile, tail groups influence interparticle interactions, colloidal stability, and the degree of ligand shell ordering.[40,41] Longer or more entropically disordered tails can enhance solubility but may reduce surface packing density, which leads to electronic heterogeneity. Thus, both the chemical nature and physical structure of the ligand shell must be carefully engineered. Post-synthetic ligand exchange further extends the tunability of surface chemistry, decoupling synthetic requirements from device integration needs.[37,38,40,41]

1.2.4 *Composition and Morphologies of QDs*

QDs can synthesized from a broad range of semiconducting materials, including II–VI, III–V, and IV–VI compounds, as well as emerging perovskite and metal-chalcogenide systems. The scope of this dissertation focuses on cadmium- and indium-based QDs. CdSe, CdS, and CdTe QDs, as representatives of II–VI materials, exhibit high-quality crystallinity, tunable bandgaps,

and well-developed colloidal synthesis protocols. In contrast, III–V QDs such as InP and InAs have received attention due to their distinct covalent bonding nature, electronic structure, and surface chemistry. The core composition may also be modified through shell growth, alloying, or doping to tailor quantum confinement and surface passivation. More specific discussion on shelling QDs is detailed in the later section. Advances in precursor design, ligand control, and reaction conditions have enabled precise control over size, composition, and crystallinity, allowing access to nanocrystals with narrow size distributions and well-defined surface terminations.

Also with colloidal synthesis, QDs can be designed to adopt different morphologies, which play a central role in determining the physical properties and applications. Although most theoretical work on QDs assumes the shape of QD to be spherical for simplification, precisely controlled shapes including isotropic (spherical) and anisotropic geometries, or more specifically one-dimensional morphologies such as nanorods and nanowires, two-dimensional platelets, and branched structures like tetrapods have been realized (**Figure 1.10**). These diverse morphologies arise from kinetic and thermodynamic control during nucleation and growth, often guided by surface ligand interactions and crystal facet selectivity. Shape engineering adds another layer of tunability to quantum dot systems, influencing their electronic structure, confinement regime, and interfacial behavior.

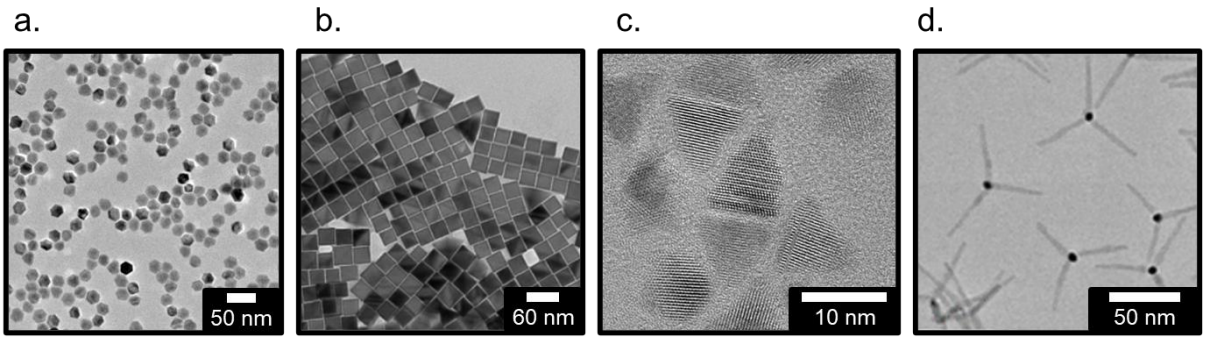

Figure 1.10. Transmission electron microscopic images of **a.** hexagonal, **b.** cube,[42] **c.** tetrahedral, and **d.** tetrapod QDs.[43]

1.2.5 *Imaging QDs with Electron Microscopies*

You might ask how the images in **Figure 1.10** are taken. It is only possible to visually discern the different sizes and shapes of QDs by electron microscopes. "*You see an object when light from it hits your eyes*" is a famous saying from my 5th grade teacher that has stuck in my head since I first heard it. But what we are trying to see now are nanoparticles or even atoms. With optical microscopes that use visible light to form images through refraction and magnification, we run into a fundamental barrier: the diffraction limit, first described by Ernst Abbe in the 19th century. According to this principle, the smallest resolvable detail is approximately half the wavelength of the illuminating light, which for visible light sets a resolution limit near 200 nanometers. For structures smaller than this, optical microscopes cannot produce clear images.

The optical microscope itself has a long and rich history, originating in the late 16th century with early compound designs by Hans and Zacharias Janssen, and later improved by pioneers like Robert Hooke and Antonie van Leeuwenhoek, who first observed living cells and microorganisms. However, when scientists like Michael Faraday and Richard Zsigmondy sought to study colloidal particles, which are far smaller than what these instruments could resolve, new approaches were

needed. Zsigmondy's invention of the ultramicroscope in the early 1900s, which illuminated particles from the side and visualized them via light scattering, allowed researchers to detect nanoparticles as small as 10 nm, even though their shapes and structures remained unresolved because edges and corners of nanoparticles can be only a few atoms thick.

To overcome these limitations and directly image particles at the nanoscale, the field turned to a different kind of "light" – the electron. The invention of the electron microscope was not the work of a single individual, but rather the result of key developments in electron optics from the late 19th to early 20th century. Heinrich Hertz demonstrated electron deflection in 1883, Emil Wiechert focused beams using magnetic fields in 1899, and Hans Busch developed the electromagnetic lens in 1926. In 1931, Ernst Ruska and Max Knoll built the first electron microscope to achieve magnification using magnetic lenses, which laid the foundation for transmission electron microscopy (TEM). This is a significant advance because unlike photons, electrons cannot be bent with glass lenses for image focusing. Independently, Reinhold Rüdenberg filed patents for a similar concept in 1932. By 1933, Ruska and Knoll's design surpassed the resolution of optical microscopes, and Siemens began producing commercial instruments by the late 1930s. Subsequent advancements, including field emission sources and aberration correction, eventually enabled direct imaging of QDs and other nanoscale objects at atomic resolution.

The two types of electron microscopes that are most heavily used in QD research and also in this dissertation are TEM and scanning electron microscopy (SEM). TEM provides high-resolution internal structural and crystallographic information by transmitting a high-energy electron beam through an ultrathin sample. In contrast, SEM scans a focused electron beam across the surface of a sample and collects secondary or backscattered electrons to generate detailed topographical images (**Figure 1.11**).

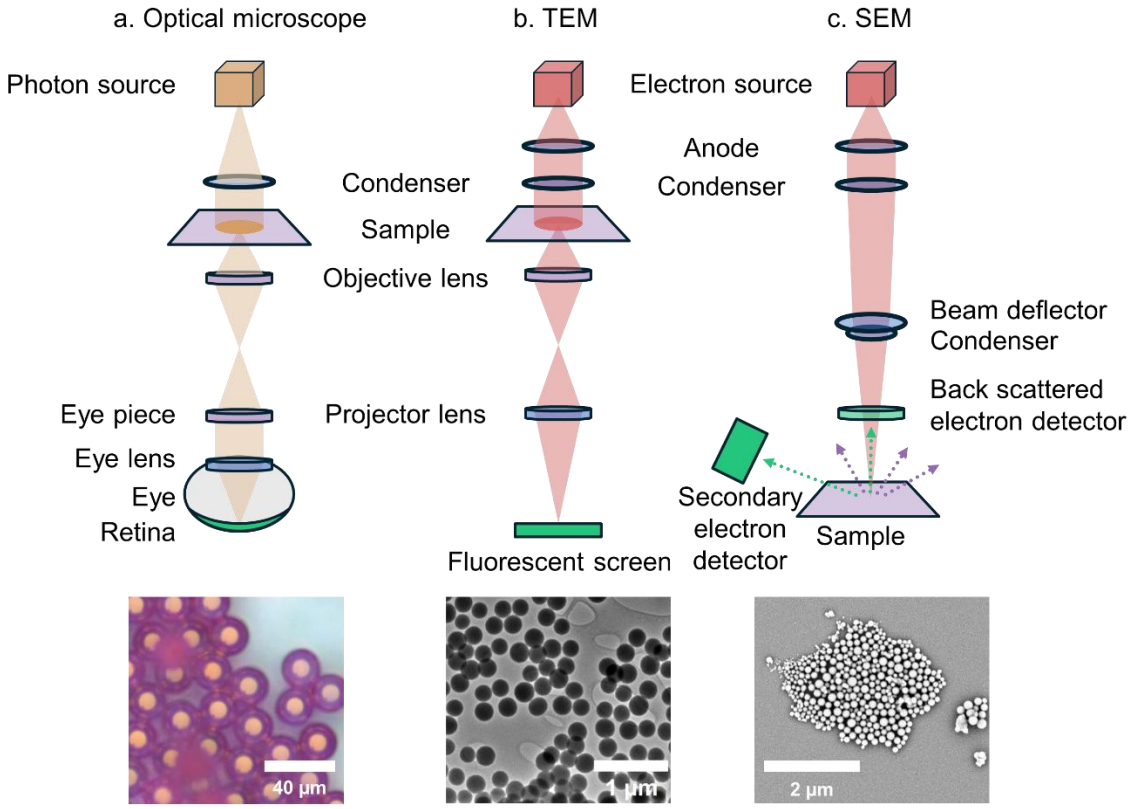

Figure 1.11. Simplified setups of an **a.** optical microscope, **b.** TEM, and **c.** SEM. The images at the bottom are different silica particle samples taken by the three techniques, where the particles in **a.** are tagged with a fluorescent dye for visibility.[44]

1.2.6 *Photophysical Properties of QDs*

The most attractive properties of QDs are their emission and absorption. It is an oversimplification but useful to think about these two processes as just photon and electron interactions. This section does not provide a holistic overview of QD photophysics but rather introduces the specific photophysical processes relevant to this dissertation. For simplicity, these interactions in QDs are usually depicted via single QD band gap diagrams, which is an atom-like two level system (**Figure 1.12**). It is important to (1) differentiate between single QD and QD ensemble (a solution of many QDs or a solid of many QDs) photophysical processes and (2)

consider the environment where the QD measurement is carried out. For the former point, many observations in QD photophysical behaviors are the average of process from many slightly different QDs in a QD sample (**Figure 1.14**). For the latter point, the environment of the QDs is critical as temperature, pressure, ligands, solvent, and excitation power have effects on the properties of QDs.

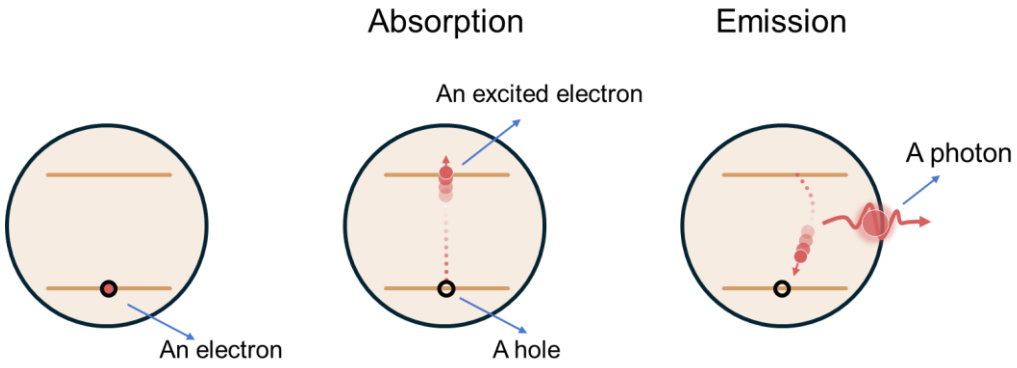

Figure 1.12. A QD two-level diagram showing a simple absorption-emission process, where an electron gets excited then relaxes to release a photon.

1.2.6.1 QD Absorption.

When a QD absorbs a photon with energy equal to or greater than its bandgap, an electron is excited from the valence band to the conduction band, leaving behind a hole. This electron–hole pair forms an exciton (**Figure 1.12** middle). Due to the quantum confinement effect, the absorption spectrum is size-dependent and features discrete transitions rather than continuum (**Figure 13**).

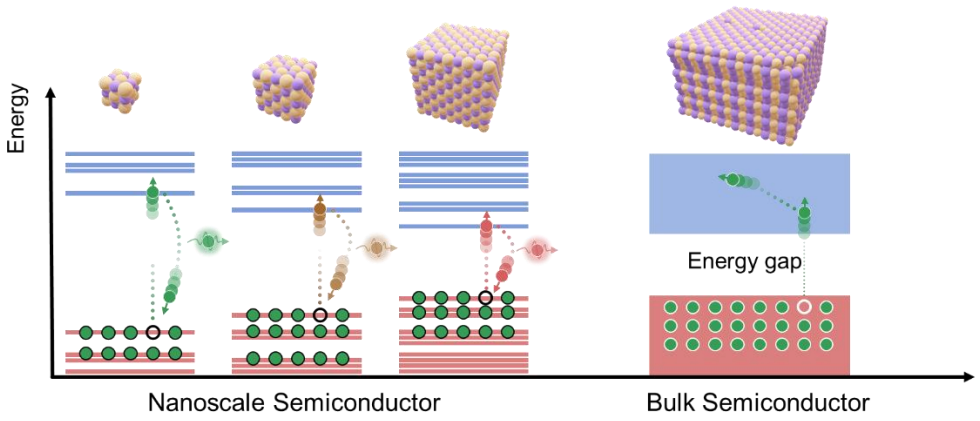

Figure 1.13. Quantum confinement effect shows size-dependent emission wavelength of QDs compared to bulk semiconductors.

1.2.6.2 Photoluminescence – QD Emission.

After excitation either through optical or electrical pump, the electron can relax to the lowest energy state in the conduction band and recombine with the hole, emitting a photon in the process. This radiative recombination is known as photoluminescence (PL) when the excitation is optical. The efficiency of this process is analytically quantified by the photoluminescence quantum yield (PLQY), defined as the ratio of emitted photons (N_{em}) to absorbed photons (N_{abs}).

$$PLQY(\%) = \frac{N_{em}}{N_{abs}} \times 100\% \tag{11}$$

Photophysically, PLQY is quantified by the ratio of the radiative rate (k_r) to all other radiative processes of an exciton.

$$PLQY(\%) = \frac{k_r}{k_r + k_{nr}} \times 100\% \tag{12}$$

where k_{nr} is the nonradiative rate. A high PLQY indicates minimal non-radiative losses and efficient light emission. PLQY can exceed 90% in well-passivated QDs with optimized surface chemistry, where surface trap states are effectively minimized. In contrast, poorly passivated QDs

often exhibit lower PLQYs due to competing non-radiative pathways such as surface recombination or Auger processes. The emission wavelength is determined by the bandgap, which is tunable with QD size, while the spectral linewidth reflects both the homogeneity of the sample and intrinsic electronic structure. **Figure 1.14** shows a typical absorption spectrum and a PL spectrum of a solution of many QDs.

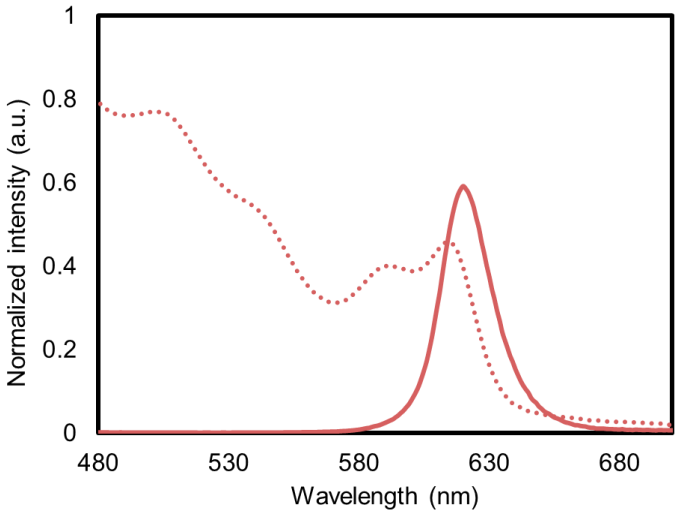

Figure 1.14. Representative of a QD absorption (dashed) and PL (solid) spectra.

1.2.6.3 Exciton Lifetime.

The time between absorption and emission defines the exciton lifetime, typically in the range of nanoseconds. This timescale depends on the QD composition, surface chemistry, and environment. Measuring lifetime can reveal non-radiative processes such as surface trap states or Auger recombination.

1.2.6.4 Auger Recombination.

Auger recombination is a non-radiative process in which the energy released by an electron–hole recombination is not emitted as a photon but is instead transferred to a third charge carrier (another electron or hole) which is subsequently excited to a higher energy state. Unlike radiative recombination, Auger processes do not produce light, and the excited carrier typically

relaxes through thermal dissipation. This process is especially pronounced in QDs due to the spatial confinement of charge carriers and the enhanced Coulombic interactions within the nanocrystal volume. Auger recombination becomes dominant under high excitation conditions, such as multiexciton generation, and is a key factor limiting the quantum efficiency of QDs in applications requiring high brightness or optical gain.

1.2.6.5 Emission Spectral Broadening.

Linewidth is an important attribute of QD emission that defines the spectral purity and performance of QDs as light emitters. The broadness of the emission profile is typically quantified by the full width at half maximum (FWHM) or, alternatively, the half width at half maximum (HWHF = $\frac{1}{2}$ FWHM). The sources of linewidth broadening in QDs can be classified into three categories (**Figure 1.15**). The first is homogeneous broadening, which arises from dynamic processes intrinsic to an individual quantum dot. These include population relaxation, decoherence (including contributions from pure dephasing), orientational relaxation, ligand vibrations, and solvent fluctuations. The second is inhomogeneous (also referred to as heterogeneous or static) broadening, which results from ensemble averaging across a distribution of QDs with variations in size, shape, and composition. Finally, a third class involves environmentally induced spectral diffusion, which captures slower fluctuations in the local dielectric environment or charge landscape that shift the emission energy over time, even for a single QD.

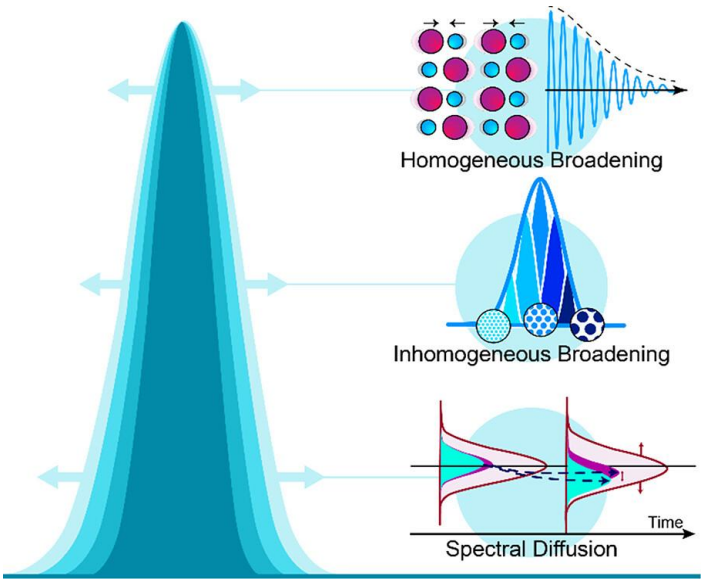

Figure 1.15. Three categories of PL linewidth broadening in colloidal QDs

1.2.6.6 Photo Intermittency – QD Blinking.

Single QDs often exhibit fluorescence intermittency, or "blinking," in which photoluminescence stochastically switches between emissive ("on") and non-emissive ("off") states under continuous excitation, first observed by Bawendi and coworkers.[45] This behavior is generally attributed to transient charging events and surface-related trap states (**Figure 1.16**). Two distinct types of blinking have been identified.[46] Type A blinking (charging) is characterized by a correlation between PL intensity and lifetime, commonly associated with charged exciton (trion) emission. In this regime, the "dim" state corresponds to trion recombination, which typically exhibits shorter lifetimes due to enhanced non-radiative Auger processes. Type B blinking (trapping), on the other hand, shows no correlation between PL intensity and lifetime and is thought to result from reversible trapping of high-energy holes at surface states. These surface traps suppress emission without significantly altering the recombination dynamics. Blinking presents a major challenge in single-particle imaging and time-resolved spectroscopy.

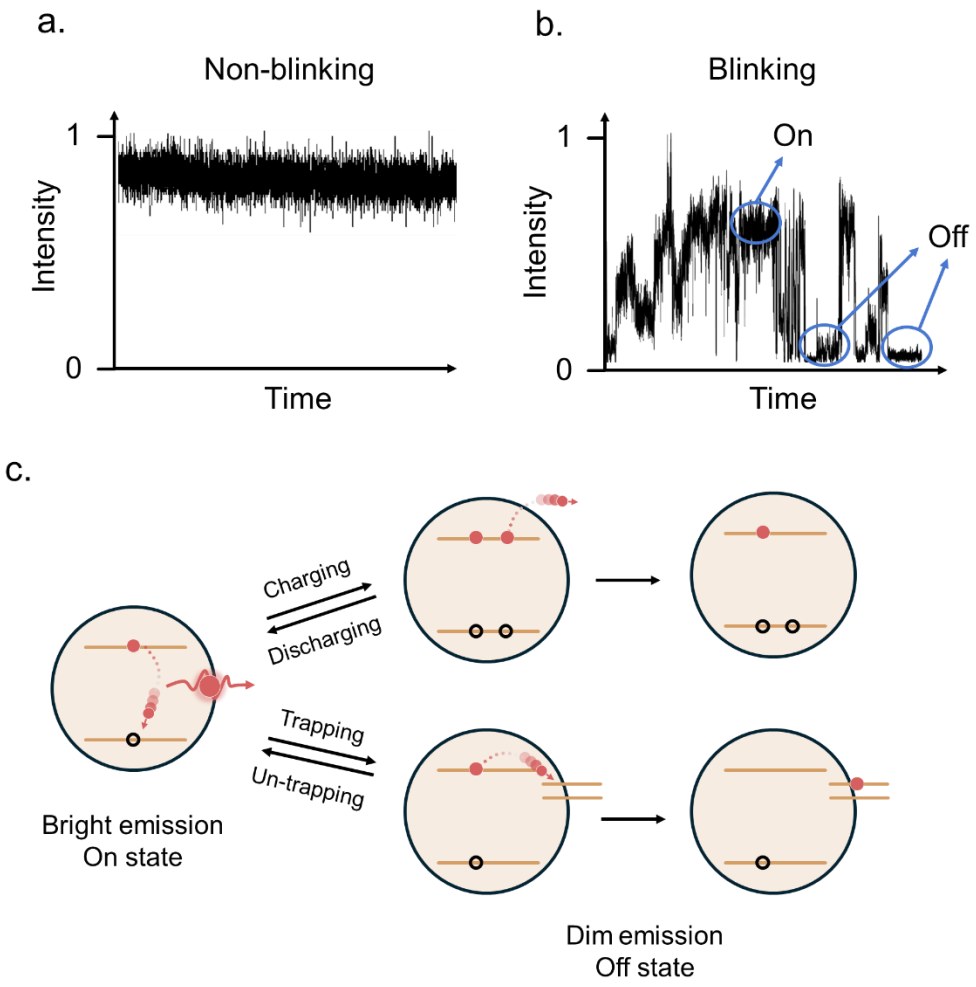

Figure 1.16. Spectra of non-blinking (a) and blinking (b) a single QD. c. Diagram for the mechanism of the two types of blinking.

1.2.7 *Core/Shell QDs*

A strategy to improve almost all aspects of optical stability and performance is inorganic shelling, first done by Hines & Guyot-Sionnest.[47] This can be achieved by adding layers of another crystalline material to encapsulate the QD core, forming a core–shell heterostructure. Electronically, the shell introduces band alignments that can confine charge carriers within the core, effectively reducing the probability of non-radiative processes such as Auger recombination.

By spatially separating the exciton from surface trap states and the surrounding environment, shelling minimizes exposure to defects and fluctuations in dielectric surroundings that typically lead to blinking and spectral diffusion.

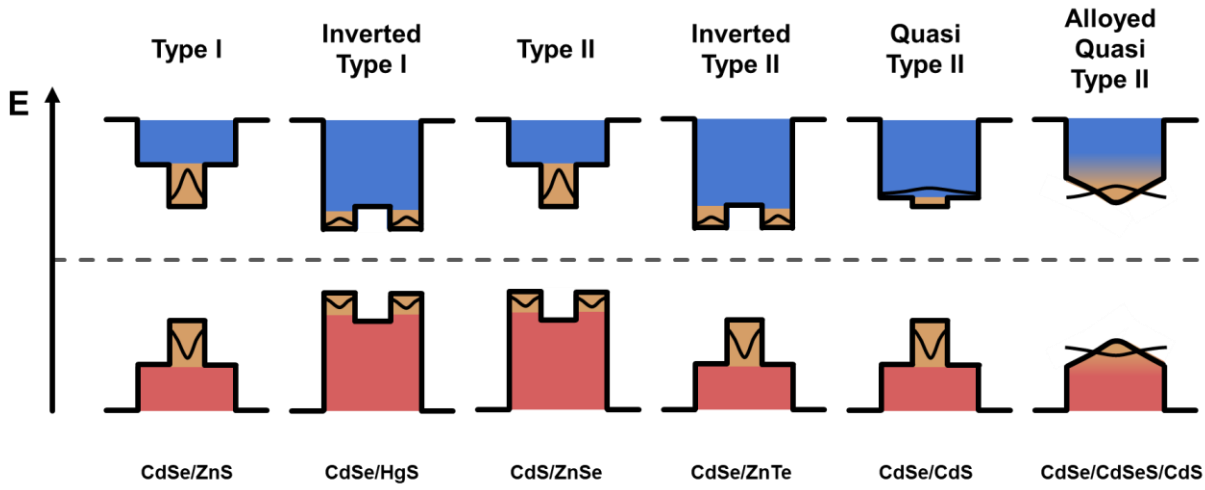

Figure 1.17. Band alignments of typical core/shell CdSe-based QDs

Thick or well-passivated shells significantly enhance PLQY by suppressing non-radiative recombination pathways, leading to brighter and more stable emission.[48,49] Shelling also reduces fluorescence intermittency, or blinking, by stabilizing the charge environment around the QD and reducing surface-mediated charging events. In addition to passivating surface defects and improving optical properties, the shell can also serve several other roles: it protects the core from chemical degradation, improves thermal and colloidal stability, and provides a versatile surface for further chemical functionalization or ligand exchange. The choice of shell material, thickness, and lattice match with the core is critical in determining the extent of these enhancements.

A well-studied example of core–shell quantum dots is CdSe/ZnS, where a CdSe core is shelled with a wider bandgap ZnS shell. This type-I band alignment confines both the electron and hole within the CdSe core, hence, enhancing radiative recombination and suppressing surface-related non-radiative losses. The ZnS shell, with its wide bandgap (~3.7 eV), acts as an effective

barrier to charge carrier leakage and environmental quenching. However, CdSe and ZnS have a relatively large lattice mismatch (~12%), which can introduce interfacial strain and defects if the shell is too thick or abruptly grown. To mitigate this, graded or intermediate shell materials such as CdS or ZnSe are often used to form alloyed or multi-shell structures (e.g., CdSe/CdS/ZnS) that reduce lattice strain while maintaining favorable band alignment. Shelling CdSe with optimized structures can increase PLQY from <10% in bare cores to >90%, depending on synthesis quality. Fluorescence blinking is significantly suppressed in thick-shelled structures, particularly those known as "giant" QDs with shells exceeding 5–10 monolayers.[50] These improvements are attributed to reduced surface trapping and diminished Auger recombination due to spatial separation of charge carriers.

1.2.8 *Applications of Colloidal QD Emitters and Challenges*

1.2.8.1 Displays and Light-Emitting Diodes (LEDs)

Current liquid crystal displays (LCDs) suffer from low color saturation due to the broad emission of traditional phosphors like Ce:YAG. Replacing them with red and green QDs in QD-LCDs significantly improves gamut coverage and energy efficiency by better matching emission with color filters. QDs also serve as color converters, increasing light throughput by removing lossy color filters. In fully electroluminescent QD-LED displays, QDs directly emit red, green, and blue light, removing the need for a backlight. These systems benefit from the fast response times and narrow emission linewidths of QDs compared to organic LEDs. However, challenges remain in patterning, charge injection, and ensuring stability under operating conditions. Continued progress in QD synthesis, ligand engineering, and device integration will be essential to fully realize their potential in commercial displays.

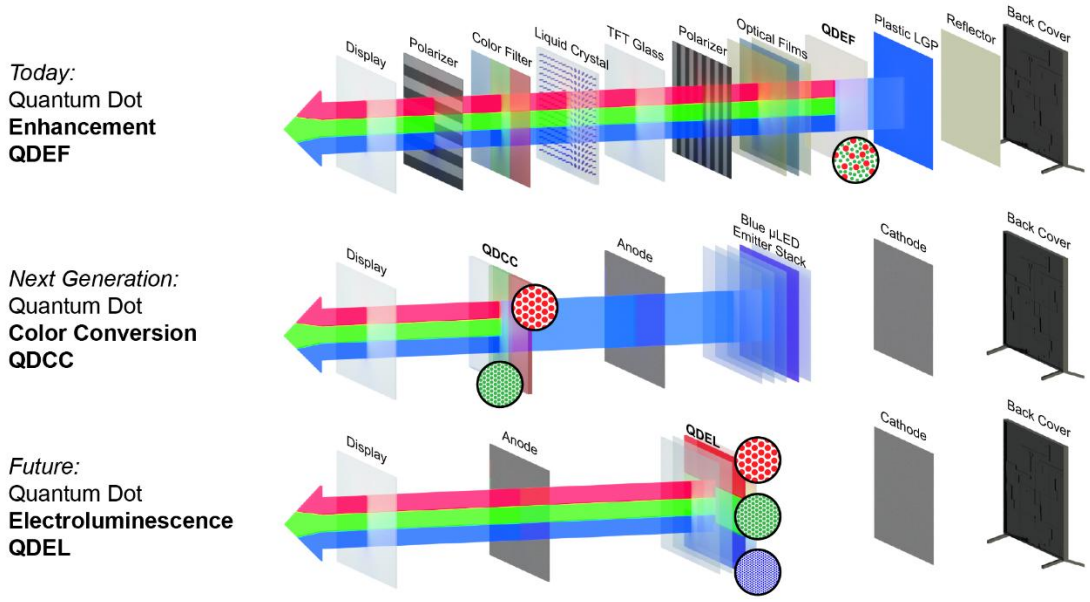

Figure 1.18. Diagram showing the development of QD displays from QD enhancement films to color conversion and beyond to electroluminescent implementations.

1.2.8.2 Photodetection.

QD are promising materials for infrared (IR) photodetectors due to their size-tunable absorption, allowing filterless, narrow-band detection across the 0.75–12 µm range. Unlike traditional single-crystal semiconductors like HgCdTe or InGaAs, which are expensive and require cryogenic cooling, QDs offer low-cost, solution-processable alternatives that can be integrated on various substrates at room temperature. Narrow emission linewidth is not essential for photodetectors, but sharp absorption edges, often correlated with narrow size distributions, are crucial for efficient and spectrally selective response. Leading QD materials for IR detection include PbS for near-IR and HgTe for mid-IR, though both raise concerns due to toxicity and limited stability. Performance issues such as slow response speed, poor charge mobility, and instability under harsh conditions still limit their broader application. Nonetheless, advances in synthetic control, especially in narrowing QD size distributions, have shown promise in improving

spectral selectivity and reducing dark current. QDs also allow advanced architectures, including plasmonic coupling, bilayer heterojunctions, and multispectral pixel arrays. Future work must address toxicity, long-wavelength performance, and environmental robustness to fully realize QD-based IR photodetectors.

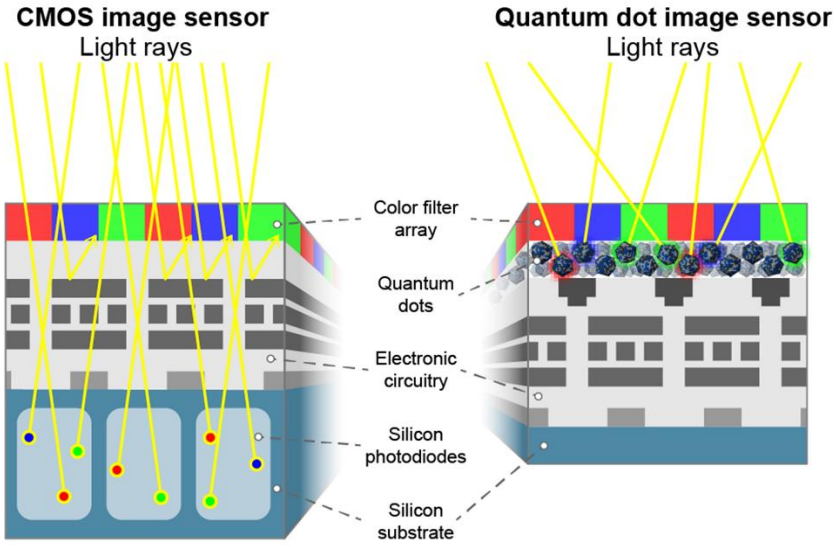

Figure 1.19. CMOS image sensor versus a QD image sensor in a photodetector.

1.2.8.3 Nanolasers.

Since the discovery of colloidal QDs, their uses as solution laser have caught a lot of attention due to their high oscillator strengths, solution processability, and spectral tunability. Lasers with narrow linewidths are particularly valuable for applications such as spectroscopy, holography, and optical communication, where high coherence and low-phase noise are required. QD nanolasers can operate under optical or electrical pumping, and their performance can be tuned through core/shell engineering, surface chemistry, or doping strategies. Achieving optical gain in QDs often relies on biexciton generation, but this is complicated by fast Auger recombination, which increases lasing thresholds and shortens gain lifetimes. Strategies such as facet-selective epitaxy and electrochemical charging have been developed to suppress Auger losses and enable

gain at lower excitation levels. Recent advances have even demonstrated sub-one-exciton gain thresholds, where charging bleaches the ground-state absorption. QDs with larger volume, like nanoplatelets, offer ultranarrow linewidths due to extreme confinement and reduced inhomogeneous broadening. Together, these developments make colloidal QDs increasingly viable for scalable, wavelength-tunable laser sources liquid.

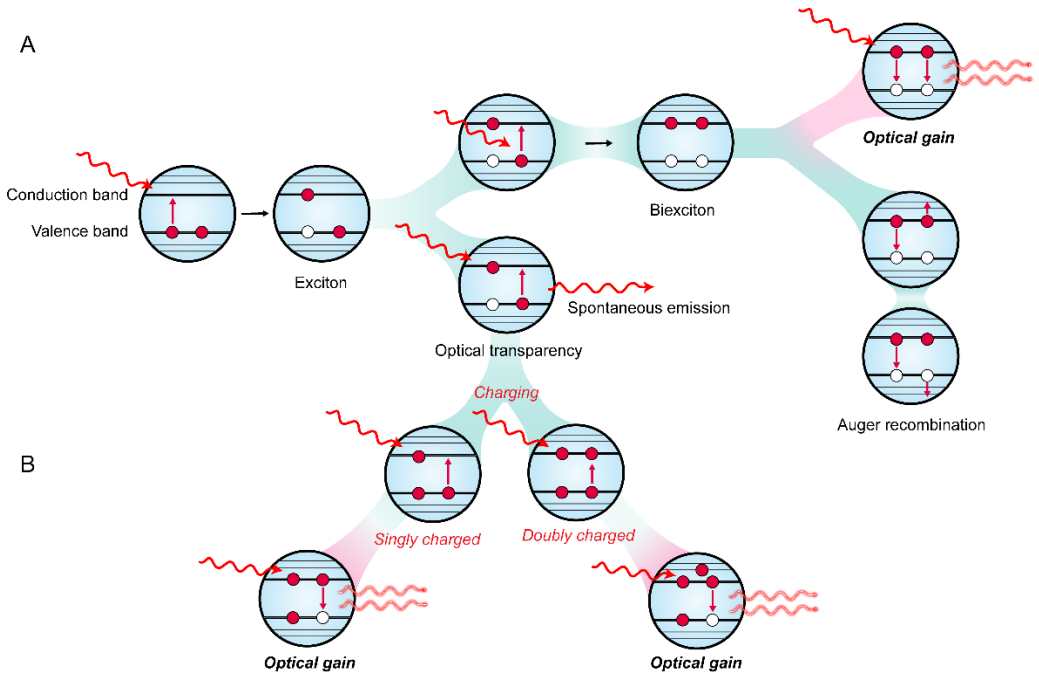

Figure 1.20. Diagram showing the mechanism to achieve optical gain through **a.** biexciton and **b.** sub-single-exciton mechanisms.

1.2.8.4 Quantum Information Science.

As **Chapter 1** and sections above might have hinted, the focused application of this dissertation is the use of QDs as single-photon sources. Colloidal QDs offer a scalable, solution-processable approach for integrating single-photon emitters into quantum photonic circuits. Demonstrations of QDs with high single-photon purity have been achieved, but challenges remain, including random spatial positioning, blinking, photobleaching, and short coherence times. To

realize practical devices, individual QDs must be precisely positioned and coupled to optical cavities, where narrow linewidths improve performance via the Purcell effect. While blinking and bleaching reduce photon generation reliability, these effects can be suppressed through surface passivation and shell engineering. A key limitation for colloidal QDs is their short exciton coherence time (~100 fs), which is insufficient for quantum interference. Lead halide perovskites have shown promise with narrower linewidths and longer coherence, though they require cryogenic temperatures. The development of stable, room-temperature, solution-processable QDs with long coherence times remains an open challenge for scalable quantum photonic technologies.

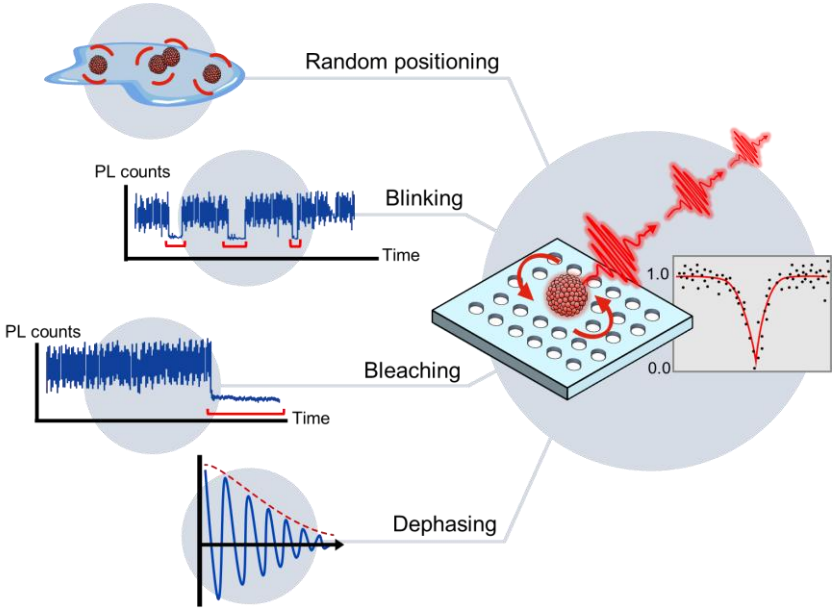

Figure 1.21. Challenges in making scalable photonic platforms with colloidal QD single-photon sources.

1.2.9 *QD Single-Photon Emitters*

We have established that a single colloidal QD can produce single photons. The first observation of anti-bunched photon emission from single colloidal QDs was done by Buratto and coworkers on CdSe/ZnS QDs.[27] Since then, many QD systems have been realized as single-photon

emitters, mostly with core/shell QDs including CdSe[51], InP,[52] PbS[53] cores, CdSe/ZnS nanoplatelets,[54] and perovskites[55] QDs. However, their potential for practical applications as single-photon sources, even for very high-quality QDs, is intrinsically limited due to ensemble inhomogeneity and batch-to-batch variation, nondirectional emission, photon losses in the substrate, distinguishable photons emitted from the same QD, and low single-photon generation rates.

Arguably, the most challenging task to use single colloidal QDs as single-photon sources is to integrate them into photonic devices. **Section 1.3** will discuss this challenge in more detail.

1.3 Integrated System of QDs and Optical Cavities

Besides shelling, placing colloidal QDs in optical cavities offers a powerful strategy to enhance their performance as light emitters. This section introduces QD–cavity integrated systems by first providing background on light–matter interactions and the foundational concepts of cavity quantum electrodynamics (cQED) from a pedagogical approach for chemists. It then outlines recent progress in deterministic QD placement techniques and concludes with key optical observations that demonstrate the interplay between individual QDs and resonant photonic structures.

1.3.1 *Engineered Light-Mater Interactions*

A closer examination of the hydrogen emission spectrum reveals that each spectral line is not singular but rather split into finer components, which is a phenomenon known as fine structure. This splitting arises from relativistic corrections and spin-orbit coupling, and its explanation requires the introduction of the fine-structure constant (α), a dimensionless quantity approximately

equal to $\frac{1}{137}$. The constant α governs the strength of the electromagnetic interaction and sets the scale for how photons interact with charged particles such as electrons. In this context, the probability of photon absorption and emission is not arbitrary but fundamentally constrained by α, which highlights a deep connection between quantum electrodynamics and observable spectral features. This intrinsic limit invites further inquiry: to what extent can light-matter interactions be shaped by external factors if the underlying coupling strength remains fixed?

This question motivated Edward Purcell's pioneering work in 1946, which demonstrated that the spontaneous emission rate of an atom is not an immutable property but can be modified by changing its surrounding electromagnetic environment.[56] In his experiment, Purcell studied nuclear magnetic resonance (NMR) in hydrogen atoms placed within a resonant cavity created by an electrical circuit. He showed that in this coupled system, the spontaneous emission probability is increased and the relaxation time is reduced, which directly challenged the prevailing notion that spontaneous emission was solely determined by intrinsic atomic properties. Purcell computed the enhancement rate (F), which later adopted the name "Purcell enhancement" as:

$$F = \frac{3Q\lambda^3}{4\pi^2 V} \tag{13}$$

where Q is the quality factor of the resonator, which represents how many optical cycles the photon can survive before decaying in the resonator, λ is the resonance frequency, and V is the volume of the resonator. The theoretical framework underlying this observation is provided by Fermi's Golden Rule, which states that the transition rate between quantum states is proportional to both the square of the interaction matrix element and the density of final states. In the case of spontaneous emission, this implies that the local photonic environment can modulate emission rates by changing the density of photonic states at the transition frequency.

Purcell's insight arrived at a time when the foundations of quantum electrodynamics (QED) were being solidified through the work of Feynman, Schwinger, and Tomonaga, and when experimental techniques were becoming sufficiently precise to probe quantum systems with unprecedented control. The idea that the electromagnetic vacuum could be engineered, in other words, the density of states could be manipulated to enhance or suppress atomic transitions, which opened a new direction in quantum optics. This concept not only bridged the emerging fields of cavity quantum electrodynamics (cQED) and spectroscopy, but also laid the groundwork for subsequent developments such as the enhancement of fluorescence in microcavities, control of radiative lifetimes in photonic crystals, and, decades later, the integration of single-photon emitters with nanophotonic structures.

1.3.2 *Optical Cavities*

Purcell's original experiment with an electrical LC circuit demonstrated that modifying the photonic environment can significantly influence spontaneous emission rates. This insight led to the development of resonators capable of enhancing light–matter interactions, with a focus on achieving small mode volumes V and high quality factors Q. A foundational example is the Fabry–Pérot interferometer, which uses two partially reflective mirrors to create resonance through constructive interference. As optical cavity design progressed, high-index dielectric materials such as Si, GaAs, and Si_3N_4 were adopted for their ability to tightly confine light with minimal loss. Beyond material choice, the geometry of cavities evolved to include micropillars, bullseye gratings, and nanobeam photonic crystal cavities (**Figure 1.17**), which confine light through index contrast and periodic structures.

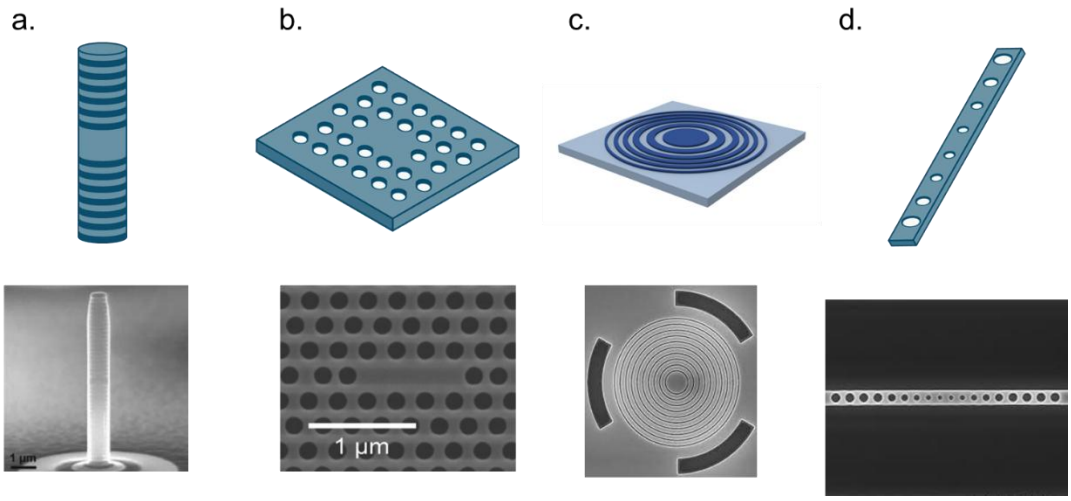

Figure 1.22. Illustrations and SEM images of different types of optical cavities.

The strength of this interaction is characterized by the coupling constant g, which determines whether the system operates in the weak or strong coupling regime. In the weak-coupling regime, g is smaller than the decay rates of the emitter and cavity; while spontaneous emission can still be enhanced via the Purcell effect, energy is lost before coherent exchange occurs. In contrast, the strong-coupling regime (SC), first demonstrated by Haroche in 1983 with Rydberg atoms in a microwave cavity,[57] occurs when g exceeds losses, leading to reversible energy exchange known as vacuum Rabi oscillations. This regime was later realized with single atoms in optical cavities and extended to solid-state systems in 1992 with Wannier excitons in quantum wells coupled to semiconductor microcavities, giving rise to cavity polaritons.[58] These developments laid the foundation for solid-state cavity QED, now extended to include quantum dots and superconducting qubits, enabling scalable platforms for single-photon sources, quantum networks, and integrated photonics.

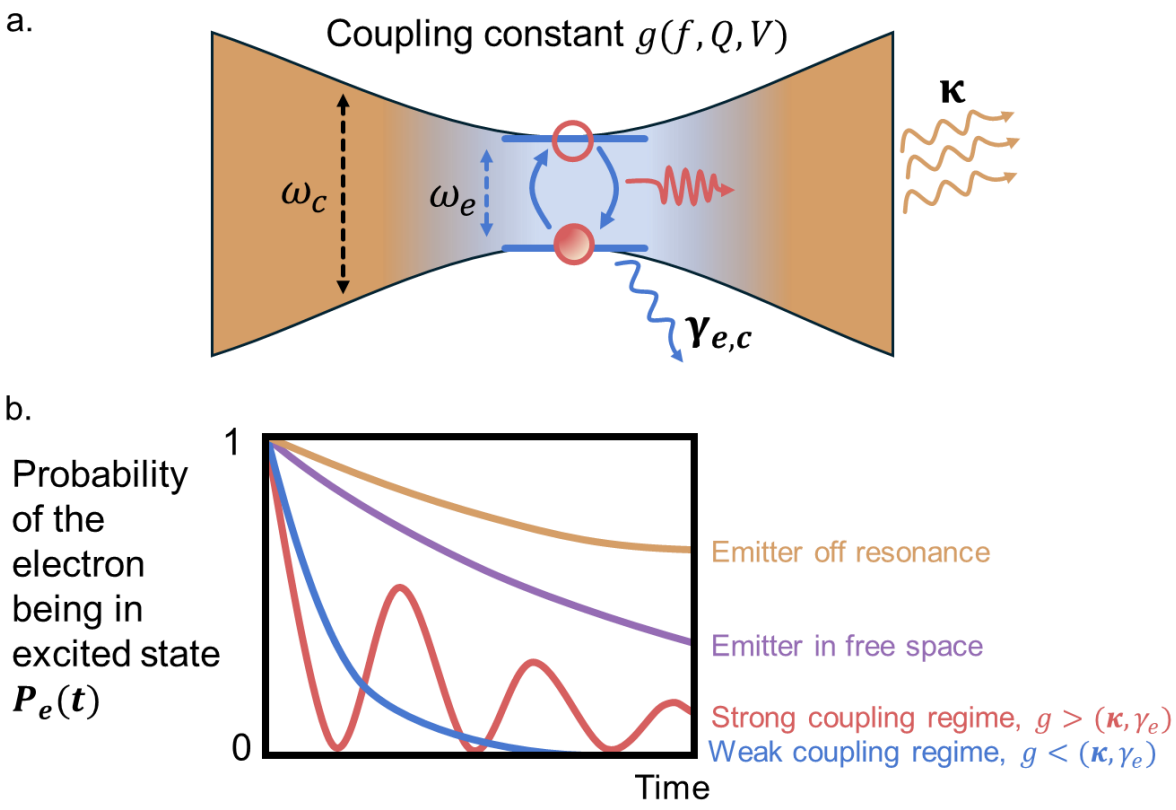

Figure 1.23. a. Illustration of a two-level emitter inside an optical cavity where κ is the cavity decay rate, ω_e is the resonance frequency, $\gamma_{e,c}$ is the emitter decay rate, g is the coupling factor that is dependent on the emitter oscillating strength f, cavity quality factor Q, and volume mode V. **b.** Probability of finding the electron in the excited state when an emitter is coupled to a cavity.

1.3.3 *Colloidal QDs in Optical Cavities*

In free space, atom-like two-level emitters radiate photons into all directions, making efficient collection difficult. This isotropic emission limits their practical use in quantum photonic devices, where photons must be routed into well-defined modes such as waveguides. Colloidal QDs, while promising due to their solution-processability and spectral tunability, present additional challenges. These include long radiative lifetimes, spectral diffusion, and

inhomogeneous emission, all of which compromise photon indistinguishability, a critical requirement for quantum information processing. Furthermore, variations in size, surface chemistry, and crystal quality within the same batch result in significant emitter-to-emitter variability.

To mitigate these limitations, QDs can be coupled to optical cavities, which reshape the photonic density of states to enhance emission via the Purcell effect. When the QD emission is spectrally aligned with a cavity mode and spatially positioned near the field maximum, the spontaneous emission rate can be significantly increased, reducing the excited-state lifetime and improving brightness (**Figure 1.24**).[60] Moreover, the cavity promotes emission into a single optical mode, improving photon collection and coherence. This coupling is typically achieved in the weak coupling regime, suitable for boosting emission rates without introducing vacuum Rabi splitting. While this strategy addresses many of the inherent limitations of colloidal QDs, it also introduces new demands such as precise emitter placement, dipole orientation control, and spectral tuning that must be overcome for scalable, high-performance single-photon sources.

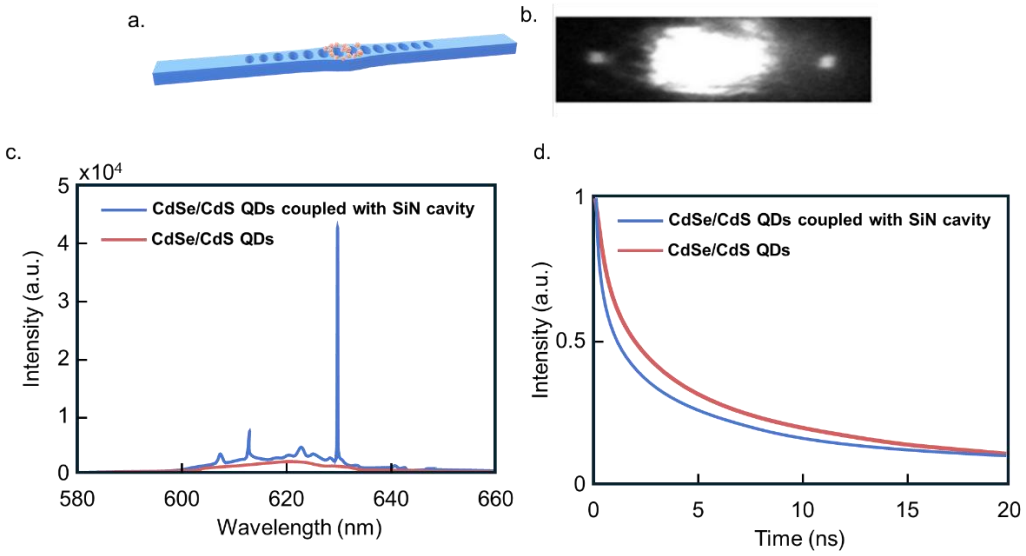

Figure 1.24. a. Illustration of many QDs on a nanobeam cavity**. b.** SEM image of many QDs on a nanobeam cavity. **c.** PL spectra of CdSe/CdS QDs on a planar substrate (red) and on a nanobeam cavity (blue). The peak around 630 nm is the enhanced PL emission from the QD-cavity coupled system. **d.** Lifetime measurement: the red and blue curves are the fits to the time-resolved PL signal from the QDs on the substrate and the QDs coupled with the cavity, respectively.

Despite significant progress in integrating QDs with optical cavities, two major challenges remain. First, achieving precise placement of a single QD at the cavity's resonance region is inherently difficult due to the size mismatch between the small QDs and the large resonance area on cavity. Early methods typically employed a masking process, where a resist layer such as PMMA was patterned by electron-beam lithography to expose the cavity region. After spin-coating a QD solution and performing a lift-off step, QDs were localized to the cavity area (more details in the Introduction of **Chapter 4** and **5**). However, due to the stochastic nature of colloidal deposition, this approach typically resulted in hundreds of QDs within each cavity, even when the exposed area was minimized[59,60]. Second, although post-deposition techniques such as AFM-based nanomanipulation have demonstrated the ability to position individual QDs with nanometer-scale precision, these methods are not scalable for large-scale device fabrication.[10,61] Other approaches,

including inkjet printing and microfluidic delivery, offer improved control but still face limitations in throughput, repeatability, and uniformity across devices.[62] As a result, most current systems contain multiple QDs per cavity, making it difficult to achieve deterministic single-photon emission. Nevertheless, these efforts have enabled observation of QD–cavity coupling, evidenced by shortened emission lifetimes and enhanced photoluminescence intensity at the cavity resonance.[59,60]

1.4 REFERENCES

(1) Brown, R. H.; Twiss, R. Q. Correlation between Photons in Two Coherent Beams of Light. *Nature* **1956**, *177*, 27–29. https://doi.org/10.1038/177027a0.

(2) Bell, J. S. On the Einstein Podolsky Rosen Paradox. *Phys. Phys. Fiz.* **1964**, *1*, 195–200. https://doi.org/10.1103/PhysicsPhysiqueFizika.1.195.

(3) Einstein, A.; Podolsky, B.; Rosen, N. Can Quantum-Mechanical Description of Physical Reality Be Considered Complete? *Phys. Rev.* **1935**, *47*, 777–780. https://doi.org/10.1103/PhysRev.47.777.

(4) Clauser, J. F. Experimental Distinction between the Quantum and Classical Field-Theoretic Predictions for the Photoelectric Effect. *Phys. Rev. D* **1974**, *9*, 853–860. https://doi.org/10.1103/PhysRevD.9.853.

(5) Kimble, H. J.; Dagenais, M.; Mandel, L. Photon Antibunching in Resonance Fluorescence. *Phys. Rev. Lett*. **1977**, *39*, 691–695. https://doi.org/10.1103/PhysRevLett.39.691.

(6) Khalid, S.; Laussy, F. P. Perfect Single-Photon Sources. *Sci. Rep*. **2024**, *14*, 2684. https://doi.org/10.1038/s41598-023-47585-9.

(7) O'Brien, J. L.; Furusawa, A.; Vučković, J. Photonic Quantum Technologies. *Nat. Photonics* **2009**, *3*, 687–695. https://doi.org/10.1038/nphoton.2009.229.

(8) Aharonovich, I.; Englund, D.; Toth, M. Solid-State Single-Photon Emitters. *Nat. Photonics* **2016**, *10*, 631–641. https://doi.org/10.1038/nphoton.2016.186.

(9) Madsen, L. S.; Laudenbach, F.; Askarani, M. Falamarzi.; Rortais, F.; Vincent, T.; Bulmer, J. F. F.; Miatto, F. M.; Neuhaus, L.; Helt, L. G.; Collins, M. J.; et al. Quantum Computational Advantage with a Programmable Photonic Processor. **Nature 2022**, *606*, 75–81. https://doi.org/10.1038/s41586-022-04725-x.

(10) Chen, Y.; Sharp, D.; Saxena, A.; Nguyen, H.; Cossairt, B. M.; Majumdar, A. Integrated Quantum Nanophotonics with Solution-Processed Materials. *Adv. Quantum Technol*. **2022**, *5*, 2100078. https://doi.org/10.1002/qute.202100078.

(11) Zahidy, M.; Mikkelsen, M. T.; Müller, R.; Da Lio, B.; Krehbiel, M.; Wang, Y.; Bart, N.; Wieck, A. D.; Ludwig, A.; Galili, M.; et al. Quantum Key Distribution Using Deterministic Single-Photon Sources over a Field-Installed Fibre Link. *Npj Quantum Inf*. **2024**, *10*, 2. https://doi.org/10.1038/s41534-023-00800-x.

(12) Maring, N.; Fyrillas, A.; Pont, M.; Ivanov, E.; Stepanov, P.; Margaria, N.; Hease, W.; Pishchagin, A.; Lemaître, A.; Sagnes, I.; et al. A Versatile Single-Photon-Based Quantum Computing Platform. *Nat. Photonics* **2024**, *18*, 603–609. https://doi.org/10.1038/s41566-024-01403-4.

(13) Kimble, H. J. The Quantum Internet. *Nature* **2008**, *453*, 1023–1030. https://doi.org/10.1038/nature07127.

(14) Pirandola, S.; Bardhan, B. R.; Gehring, T.; Weedbrook, C.; Lloyd, S. Advances in Photonic Quantum Sensing. *Nat. Photonics* **2018**, *12*, 724–733. https://doi.org/10.1038/s41566-018-0301-6.

(15) Moreva, E.; Cimini, V.; Gianani, I.; Bernardi, E.; Traina, P.; Degiovanni, I. P.; Barbieri, M. Quantum Photonics Sensing in Biosystems. *APL Photonics* **2025**, *10*, 010902. https://doi.org/10.1063/5.0232183.

(16) Darquié, B.; Jones, M. P. A.; Dingjan, J.; Beugnon, J.; Bergamini, S.; Sortais, Y.; Messin, G.; Browaeys, A.; Grangier, P. Controlled Single-Photon Emission from a Single Trapped Two-Level Atom. *Science* **2005**, *309*, 454–456. https://doi.org/10.1126/science.1113394.

(17) Higginbottom, D. B.; Slodička, L.; Araneda, G.; Lachman, L.; Filip, R.; Hennrich, M.; Blatt, R. Pure Single Photons from a Trapped Atom Source. *New J. Phys*. **2016**, *18*, 093038. https://doi.org/10.1088/1367-2630/18/9/093038.

(18) Abe, N.; Mitsumori, Y.; Sadgrove, M.; Edamatsu, K. Dynamically Unpolarized Single-Photon Source in Diamond with Intrinsic Randomness. *Sci. Rep*. **2017**, *7*, 46722. https://doi.org/10.1038/srep46722.

(19) Booker, E. P.; Thomas, T. H.; Quarti, C.; Stanton, M. R.; Dashwood, C. D.; Gillett, A. J.; Richter, J. M.; Pearson, A. J.; Davis, N. J. L. K.; Sirringhaus, H.; et al. Formation of Long-Lived Color Centers for Broadband Visible Light Emission in Low-Dimensional Layered Perovskites. *J. Am. Chem. Soc.* **2017**, *139*, 18632–18639. https://doi.org/10.1021/jacs.7b10223.

(20) Gupta, S.; Wu, W.; Huang, S.; Yakobson, B. I. Single-Photon Emission from Two-Dimensional Materials, to a Brighter Future. *J. Phys. Chem. Lett*. **2023**, *14*, 3274–3284. https://doi.org/10.1021/acs.jpclett.2c03674.

(21) Caldeira, A. O.; Leggett, A. J. Influence of Damping on Quantum Interference: An Exactly Soluble Model. *Phys. Rev. A* **1985**, *31*, 1059–1066. https://doi.org/10.1103/PhysRevA.31.1059.

(22) Kiraz, A.; Ehrl, M.; Hellerer, Th.; Müstecaplıoğlu, Ö. E.; Bräuchle, C.; Zumbusch, A. Indistinguishable Photons from a Single Molecule. *Phys. Rev. Lett*. **2005**, *94*, 223602. https://doi.org/10.1103/PhysRevLett.94.223602.

(23) Lombardi, P.; Emadi, R.; Duquennoy, R.; Murtaza, G.; Colautti, M.; Toninelli, C. Organic Dye Molecules as Single Photon Sources for Optical Quantum Technologies. In Quantum Information and Measurement VI 2021; Sciarrino, F., Treps, N. ,. Giustina, M. ,. and Silberhorn, C., Ed.; Technical Digest Series; Optica Publishing Group: Washington, DC, **2021**; p Tu2B.3. https://doi.org/10.1364/QIM.2021.Tu2B.3.

(24) Somaschi, N.; Giesz, V.; De Santis, L.; Loredo, J. C.; Almeida, M. P.; Hornecker, G.; Portalupi, S. L.; Grange, T.; Antón, C.; Demory, J.; et al. Near-Optimal Single-Photon Sources in the Solid State. *Nat. Photonics* **2016**, *10*, 340–345. https://doi.org/10.1038/nphoton.2016.23.

(25) Liu, F.; Brash, A. J.; O'Hara, J.; Martins, L. M. P. P.; Phillips, C. L.; Coles, R. J.; Royall, B.; Clarke, E.; Bentham, C.; Prtljaga, N.; et al. High Purcell Factor Generation of Indistinguishable On-Chip Single Photons. *Nat. Nanotechnol*. **2018**, *13*, 835–840. https://doi.org/10.1038/s41565-018-0188-x.

(26) Gao, W. B.; Fallahi, P.; Togan, E.; Miguel-Sanchez, J.; Imamoglu, A. Observation of Entanglement between a Quantum Dot Spin and a Single Photon. *Nature* **2012**, *491*, 426–430. https://doi.org/10.1038/nature11573.

(27) Michler, P.; Imamoğlu, A.; Mason, M. D.; Carson, P. J.; Strouse, G. F.; Buratto, S. K. Quantum Correlation among Photons from a Single Quantum Dot at Room Temperature. *Nature* **2000**, *406*, 968–970. https://doi.org/10.1038/35023100.

(28) Ekimov, A.; Onushchenko, A. Quantum Size Effect in Three-Dimensional Microscopic Semiconductor Crystals. *J. Exp. Theor. Phys. Lett.* **1981**, *34*, 345–349.

(29) Kumar, A.; Nasrallah, M.; Douglass, D. L. The Effect of Yttrium and Thorium on the Oxidation Behavior of Ni-Cr-Al Alloys. *Oxid. Met.* **1974**, *8*, 227–263. https://doi.org/10.1007/BF00604042.

(30) Stringer, J.; Wilcox, B. A.; Jaffee, R. I. The High-Temperature Oxidation of Nickel-20 Wt. % Chromium Alloys Containing Dispersed Oxide Phases. *Oxid. Met*. **1972**, *5*, 11–47. https://doi.org/10.1007/BF00614617.

(31) Nozik, A. J. Photoelectrochemistry: Applications to Solar Energy Conversion. *Annual Review of Physical Chemistry*, **1978**, *29*, 189–222. https://doi.org/10.1146/annurev.pc.29.100178.001201.

(32) Huang, S. Y.; Schlichthörl, G.; Nozik, A. J.; Grätzel, M.; Frank, A. J. Charge Recombination in Dye-Sensitized Nanocrystalline TiO2 Solar Cells. *J. Phys. Chem. B* **1997**, *101*, 2576–2582. https://doi.org/10.1021/jp962377q.

(33) Brus, L. E. Electron–Electron and Electron-hole Interactions in Small Semiconductor Crystallites: The Size Dependence of the Lowest Excited Electronic State. *J. Chem. Phys.* **1984**, *80*, 4403–4409. https://doi.org/10.1063/1.447218.

(34) Brus, L. Electronic Wave Functions in Semiconductor Clusters: Experiment and Theory. *J. Phys. Chem.* **1986**, *90*, 2555–2560. https://doi.org/10.1021/j100403a003.

(35) Murray, C. B.; Norris, D. J.; Bawendi, M. G. Synthesis and Characterization of Nearly Monodisperse CdE (E = Sulfur, Selenium, Tellurium) Semiconductor Nanocrystallites. *J. Am. Chem. Soc.* **1993**, *115*, 8706–8715. https://doi.org/10.1021/ja00072a025.

(36) Genthon, A. The Concept of Velocity in the History of Brownian Motion. *Eur. Phys. J. H* **2020**, *45*, 49–105. https://doi.org/10.1140/epjh/e2020-10009-8.

(37) Heuer-Jungemann, A.; Feliu, N.; Bakaimi, I.; Hamaly, M.; Alkilany, A.; Chakraborty, I.; Masood, A.; Casula, M. F.; Kostopoulou, A.; Oh, E.; et al. The Role of Ligands in the Chemical Synthesis and Applications of Inorganic Nanoparticles. *Chem. Rev.* **2019**, *119*, 4819–4880. https://doi.org/10.1021/acs.chemrev.8b00733.

(38) Huang, Y.; Cohen, T. A.; Sperry, B. M.; Larson, H.; Nguyen, H. A.; Homer, M. K.; Dou, F. Y.; Jacoby, L. M.; Cossairt, B. M.; Gamelin, D. R.; et al. Organic Building Blocks at Inorganic Nanomaterial Interfaces. *Mater. Horiz.* **2022**, *9*, 61–87. https://doi.org/10.1039/D1MH01294K.

(39) Yang, Y.; Qin, H.; Jiang, M.; Lin, L.; Fu, T.; Dai, X.; Zhang, Z.; Niu, Y.; Cao, H.; Jin, Y.; et al. Entropic Ligands for Nanocrystals: From Unexpected Solution Properties to Outstanding Processability. Nano Lett. 2016, 16, 2133–2138. https://doi.org/10.1021/acs.nanolett.6b00730.

(40) Calvin, J. J.; Brewer, A. S.; Alivisatos, A. P. The Role of Organic Ligand Shell Structures in Colloidal Nanocrystal Synthesis. *Nat. Synth.* **2022**, *1*, 127–137. https://doi.org/10.1038/s44160-022-00025-4.

(41) Giansante, C. Library Design of Ligands at the Surface of Colloidal Nanocrystals. *Acc. Chem. Res.* **2020**, *53*, 1458–1467. https://doi.org/10.1021/acs.accounts.0c00204.

(42) Lv, L.; Liu, S.; Li, J.; Lei, H.; Qin, H.; Peng, X. Synthesis of Weakly Confined, Cube-Shaped, and Monodisperse Cadmium Chalcogenide Nanocrystals with Unexpected Photophysical Properties. *J. Am. Chem. Soc.* **2022**, *144*, 16872–16882. https://doi.org/10.1021/jacs.2c05151.

(43) Enright, M. J.; Dou, F. Y.; Wu, S.; Rabe, E. J.; Monahan, M.; Friedfeld, M. R.; Schlenker, C. W.; Cossairt, B. M. Seeded Growth of Nanoscale Semiconductor Tetrapods: Generality and the Role of Cation Exchange. *Chem. Mater.* **2020**, *32*, 4774–4784. https://doi.org/10.1021/acs.chemmater.0c01407.

(44) Bchellaoui, N.; Hayat, Z.; Mami, M.; Dorbez-Sridi, R.; El Abed, A. I. Microfluidic-Assisted Formation of Highly Monodisperse and Mesoporous Silica Soft Microcapsules. *Sci. Rep.* **2017**, *7*, 16326. https://doi.org/10.1038/s41598-017-16554-4.

(45) Nirmal, M.; Dabbousi, B. O.; Bawendi, M. G.; Macklin, J. J.; Trautman, J. K.; Harris, T. D.; Brus, L. E. Fluorescence Intermittency in Single Cadmium Selenide Nanocrystals. *Nature* **1996**, *383*, 802–804. https://doi.org/10.1038/383802a0.

(46) Yuan, G.; Gómez, D. E.; Kirkwood, N.; Boldt, K.; Mulvaney, P. Two Mechanisms Determine Quantum Dot Blinking. *ACS Nano* **2018**, *12*, 3397–3405. https://doi.org/10.1021/acsnano.7b09052.

(47) Hines, M. A.; Guyot-Sionnest, P. Synthesis and Characterization of Strongly Luminescing ZnS-Capped CdSe Nanocrystals. *J. Phys. Chem.* **1996**, *100*, 468–471. https://doi.org/10.1021/jp9530562.

(48) Hanifi, D. A.; Bronstein, N. D.; Koscher, B. A.; Nett, Z.; Swabeck, J. K.; Takano, K.; Schwartzberg, A. M.; Maserati, L.; Vandewal, K.; van de Burgt, Y.; et al. Redefining Near-Unity Luminescence in Quantum Dots with Photothermal Threshold Quantum Yield. *Science* **2019**, *363*, 1199–1202. https://doi.org/10.1126/science.aat3803.

(49) Chen, D.; Zhao, F.; Qi, H.; Rutherford, M.; Peng, X. Bright and Stable Purple/Blue Emitting CdS/ZnS Core/Shell Nanocrystals Grown by Thermal Cycling Using a Single-Source Precursor. *Chem. Mater.* **2010**, *22*, 1437–1444. https://doi.org/10.1021/cm902516f.

(50) Chen, Y.; Vela, J.; Htoon, H.; Casson, J. L.; Werder, D. J.; Bussian, D. A.; Klimov, V. I.; Hollingsworth, J. A. "Giant" Multishell CdSe Nanocrystal Quantum Dots with Suppressed Blinking. *J. Am. Chem. Soc.* **2008**, *130*, 5026–5027. https://doi.org/10.1021/ja711379k.

(51) Nguyen, H. A.; Hammel, B. F.; Sharp, D.; Kline, J.; Schwartz, G.; Harvey, S.; Nishiwaki, E.; Sandeno, S. F.; Ginger, D. S.; Majumdar, A.; et al. Colossal Core/Shell CdSe/CdS Quantum Dot Emitters. *ACS Nano* **2024**, *18*, 20726–20739. https://doi.org/10.1021/acsnano.4c06961.

(52) Proppe, A. H.; Berkinsky, D. B.; Zhu, H.; Šverko, T.; Kaplan, A. E. K.; Horowitz, J. R.; Kim, T.; Chung, H.; Jun, S.; Bawendi, M. G. Highly Stable and Pure Single-Photon Emission with 250 Ps Optical Coherence Times in InP Colloidal Quantum Dots. *Nat. Nanotechnol.* **2023**, *18*, 993–999. https://doi.org/10.1038/s41565-023-01432-0.

(53) Krishnamurthy, S.; Singh, A.; Hu, Z.; Blake, A. V.; Kim, Y.; Singh, A.; Dolgopolova, E. A.; Williams, D. J.; Piryatinski, A.; Malko, A. V.; et al. PbS/CdS Quantum Dot Room-Temperature Single-Emitter Spectroscopy Reaches the Telecom O and S Bands via an Engineered Stability. *ACS Nano* **2021**, *15*, 575–587. https://doi.org/10.1021/acsnano.0c05907.

(54) D'Amato, M.; Fu, N.; Glorieux, Q.; Giacobino, E.; Le Jeannic, H.; Ithurria, S.; Lhuillier, E.; Bramati, A. Room-Temperature Efficient Single-Photon Generation from CdSe/ZnS Nanoplatelets. *ACS Nano* **2025**. https://doi.org/10.1021/acsnano.5c01971.

(55) Utzat, H.; Sun, W.; Kaplan, A. E. K.; Krieg, F.; Ginterseder, M.; Spokoyny, B.; Klein, N. D.; Shulenberger, K. E.; Perkinson, C. F.; Kovalenko, M. V.; et al. Coherent Single-Photon Emission from Colloidal Lead Halide Perovskite Quantum Dots. *Science* **2019**, *363*, 1068–1072. https://doi.org/10.1126/science.aau7392.

(56) Purcell, E. M. Spontaneous Emission Probabilities at Radio Frequencies. *Phys. Rev.* **1946**, *69*.

(57) Kaluzny, Y.; Goy, P.; Gross, M.; Raimond, J. M.; Haroche, S. Observation of Self-Induced Rabi Oscillations in Two-Level Atoms Excited Inside a Resonant Cavity: The Ringing Regime of

Superradiance. *Phys. Rev. Lett.* **1983**, *51*, 1175–1178. https://doi.org/10.1103/PhysRevLett.51.1175.

(58) Weisbuch, C.; Nishioka, M.; Ishikawa, A.; Arakawa, Y. Observation of the Coupled Exciton-Photon Mode Splitting in a Semiconductor Quantum Microcavity. *Phys. Rev. Lett.* **1992**, *69*, 3314–3317. https://doi.org/10.1103/PhysRevLett.69.3314.

(59) Gupta, S.; Waks, E. Spontaneous Emission Enhancement and Saturable Absorption of Colloidal Quantum Dots Coupled to Photonic Crystal Cavity. *Opt. Express* **2013**, *21*, 29612–29619. https://doi.org/10.1364/OE.21.029612.

(60) Chen, Y.; Ryou, A.; Friedfeld, M. R.; Fryett, T.; Whitehead, J.; Cossairt, B. M.; Majumdar, A. Deterministic Positioning of Colloidal Quantum Dots on Silicon Nitride Nanobeam Cavities. *Nano Lett.* **2018**, *18*, 6404–6410. https://doi.org/10.1021/acs.nanolett.8b02764.

(61) Choi, M.; Lee, M.; Park, S.-Y. L.; Kim, B. S.; Jun, S.; Park, S. I.; Song, J. D.; Ko, Y.-H.; Cho, Y.-H. Single Quantum Dot Selection and Tailor-Made Photonic Device Integration Using a Nanoscale-Focus Pinspot. *Adv. Mater.* **2023**, *35*, 2210667. https://doi.org/10.1002/adma.202210667.

(62) Guymon, G. G.; Sharp, D.; Cohen, T. A.; Gibbs, S. L.; Manna, A.; Tzanetopoulos, E.; Gamelin, D. R.; Majumdar, A.; MacKenzie, J. D. Electrohydrodynamic Printing-Based Heterointegration of Quantum Dots on Suspended Nanophotonic Cavities. *Adv. Mater. Technol*. **2024**, 2301921. https://doi.org/10.1002/admt.202301921.

Chapter 2. COLLOIDAL SYNTHESIS OF QUANTUM DOTS AND NANOPLATELETS

In this chapter, the discussion will focus on the synthesis of CdSe QDs and CdSe nanoplatelets, including their core/shell heterostructures, that I have done in the Cossairt lab. These systems will serve as model platforms for understanding key optoelectronic behaviors and measurement techniques. To provide context for the methods used in this work, the chapter begins with a brief overview of the historical development of QD synthesis.

2.1 Evolution of QD Synthetic Methods

The development of QD synthesis methods has progressed from serendipitous discoveries in traditional materials to highly controlled chemical techniques grounded in modern nanoscience. Semiconductor nanocrystallites are not a purely contemporary innovation; rather, they have been observed for centuries in colored glasses prepared by artisans who unknowingly created dilute dispersions of nanoscale Cd- and Zn-based chalcogenides. As noted by Koch,[1,2] the incorporation of CdS, ZnS, and related compounds into molten glass produced rich hues attributable to the optical properties of embedded nanocrystallites. However, these early materials lacked precise size or compositional control, and the observed optical effects largely originated from inhomogeneous broadening and compositional fluctuations, rather than true quantum confinement effects.

More systematic approaches to QD synthesis emerged in the late 20th century. Pioneering work by Ekimov and colleagues established that semiconductor nanocrystallites could be intentionally grown in glass matrices through a two-step thermal treatment process.[3] In this method, precursors such as CdSe were dissolved into a high-temperature glass melt (~1500 °C),

rapidly quenched, and then reheated to promote nucleation and growth of crystalline domains within the viscous matrix. This approach enabled the formation of crystalline, nearly spherical particles with narrow size distributions and diameters tunable via the annealing temperature, time, and precursor concentration. Despite the high stability and monodispersity of the resulting nanocrystallites, the glass matrix imposed significant limitations, particularly the inability to further process or modify the QDs after synthesis and the poorly understood nature of the glass-crystal interface, which often resulted in low quantum yields and persistent trap states.

To overcome the rigidity of glass-based systems, researchers turned to low-temperature, solution-phase methods in the 1980s and 1990s. Early aqueous routes relied on the uncontrolled precipitation of Cd-based QDs, often yielding polydisperse, poorly crystalline materials. Henglein introduced polymeric stabilizers such as hexametaphosphate to moderate nucleation and growth, resulting in colloidally stable dispersions.[1,2,4] Further refinement involved controlling the surface chemistry through pH adjustment, which enabled formation of passivating surface layers like $Cd(OH)_2$ and modest enhancement of luminescence. A significant advance came with the development of inverse micelle techniques, which created nanoscale reaction vessels within which Cd^{2+} and chalcogenide precursors could be combined to yield QDs with improved, though still imperfect, size and dispersity control. The micellar environment enabled surface passivation through secondary reactions, and the use of surfactants and capping agents such as aryl thiols allowed for redispersion in organic solvents.

Recognizing the need for higher crystallinity and better control over growth, lyothermal and high-temperature organometallic methods were introduced. In 1993, Moungi Bawendi, who was Louis Brus's postdoc and his students (Chris Murray and David Norris) developed a synthetic route involving the separation of nucleation and growth phases.[5] Small CdSe seed QDs prepared

by micelle methods were isolated and then annealed at elevated temperatures (e.g., 200 °C) in coordinating solvents such as tributylphosphine oxide. This protocol enabled Ostwald ripening and crystal annealing, resulting in highly monodisperse, nearly defect-free QDs with sharp excitonic features and strong near band-edge emission. Subsequent advances extended these principles to other Cd-based materials and paved the way for the development of reproducible, scalable synthetic protocols. Recent innovations have included hydrothermal synthesis under pressure and the integration of automated, machine-learning-guided platforms to further refine and accelerate QD discovery and optimization. The historical trajectory of QD synthesis thus reflects an ongoing convergence of chemical insight, material control, and process engineering, aimed at mastering the structure and uniformity of colloidal semiconductor nanocrystals. As of 2025, the synthesis of Cd-, Pb-, and In- based colloidal QDs have been commercialized by many companies including Nanosys, UbiQD, Quantum Solutions, and Nanoco, who serve as manufacturers for the display, energy conversion, and sensor industries.

2.2 SYNTHESIS OF CDSE QDS

Two common crystal phases of CdSe are hexagonal wurtzite and cubic zinc blende. Most of my CdSe procedures produce the wurtzite. However, the subtle difference between these two phases is only in their closed packed stacking sequence, where wurtzite has ABABAB stacking along and 0001zinc blende adopts the ABCABC stacking along 111. While the amount of precursors and ligands can dictate the final crystal phase, nucleation temperature is the most important parameter, where higher temperature (> 350 ℃) yields wurtzite crystals and lower temperature (< 300 ℃) yields zincblende crystals.[6]

2.2.1 *Synthesis of Wurtzite CdSe QDs*

The wurtzite CdSe hot-injection synthesis follows Chen & Bawendi's method.[7] TOPO (3 g), CdO (0.06 g), ODPA (0.28 g), and a magnetic stir bar were loaded into a 15-mL three-neck round bottom flask secured with a septum, a thermowell equipped with a thermometer, and a condenser. The flask was also wrapped with glass wool and aluminum foil to ensure efficient heating. The flask was heated to 110 ℃ and put under vacuum for 30 min. The flask was then refilled with N_2 gas and was heated to 375 ℃. All the reaction precursors were dissolved to yield a colorless solution at above 290 ℃. While the temperature was ramping up from 320 ℃ to 370 ℃, TOP (1.5 mL) was added slowly into the reaction. When the temperature was stabilized around 372–375 ℃, a solution of Se powder (0.058 g) completely dissolved in TOP (0.4 mL) was quickly injected into the reaction. The reaction temperature fluctuated around 368–370 ℃. After a certain after the Se injection amount of time (45, 60, or 90 s) the heating was stopped. The flask was quickly cooled down to room temperature with forced. To avoid the reaction solution from solidifying at room temperature, 2 mL of anhydrous toluene was injected into the reaction when the temperature was 90 ℃. The product was purified in a glovebox with methyl acetate as antisolvent and hexane as solvent as follows. Anhydrous methyl acetate (5 mL) was added, and the reaction solution was centrifuged at 7800 rpm for 10 min. The supernatant was discarded, and the red, emissive precipitate was dissolved in 5 mL of hexane, then was centrifuged at 4000 rpm for 3 min. The white or gray precipitate was discarded. The transparent scarlet hexane solution of QDs was washed 3 times by addition of methyl acetate following by centrifugation. The final product of CdSe QDs in hexane was stored in a N_2 gas-filled glovebox.

It is important to emphasize, for the sake of reproducibility, that the synthesis described above is highly sensitive to temperature. While the nucleation time generally determines the

position of the lowest electronic energy transition (LEET) feature in the absorption spectrum, since longer nucleation times typically yield larger, red-shifted QDs, the precise timing in this synthesis is difficult to control due to the rapid onset of nucleation at temperatures above 370 ℃. Variations in synthetic setup, glassware, and temperature measurement methods can all affect the thermal profile, potentially leading to differences in the tunability and final color of the QDs.

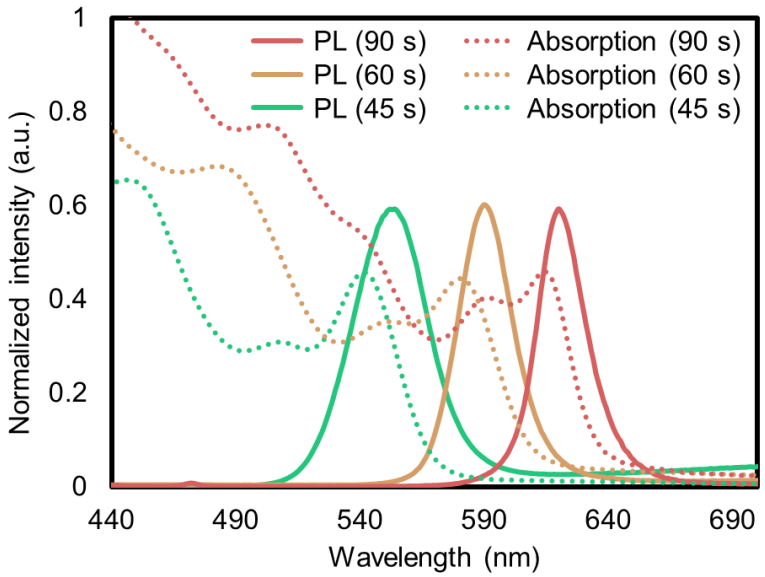

Figure 2.1. Absorption (dotted traces) and PL (solid traces) spectra of three wurtzite CdSe QD samples with different sizes.

2.2.2 *Synthesis of Zincblende CdSe QDs*

The heat-up synthesis of zincblende CdS follows the procedure from David Kelley and coworkers.[8] CdO (0.256 g, 0.2 mmol), oleic acid (1 mL) and 4 mL ODE were loaded into a 25 mL three-neck round bottom flask secured with a septum, a thermowell equipped with a thermometer, and a condenser. The flask was put under vacuum for 30 min and then refilled with N_2 before it was heated to 250 ℃ to form a transparent solution and then cooled to 40 ℃. Se powder (0.0079 g, 0.1 mmol) was loaded into the flask, which was subsequently heated to 240 ℃. The synthesis

was quenched by rapid cool down with air after 20 min of heating. The product was purified in a glovebox with methyl acetate as antisolvent and hexane as solvent as follows. Anhydrous methyl acetate (5 mL) was added, and the reaction solution was centrifuged at 7800 rpm for 10 min. The supernatant was discarded, and the red, emissive precipitate was dissolved in 5 mL of hexane, then was centrifuged at 4000 rpm for 3 min. The white or gray precipitate was discarded. The transparent scarlet hexane solution of QDs was washed 3 times by addition of methyl acetate following by centrifugation. The final product of CdSe QDs in hexane was stored in a N_2 gas-filled glovebox.

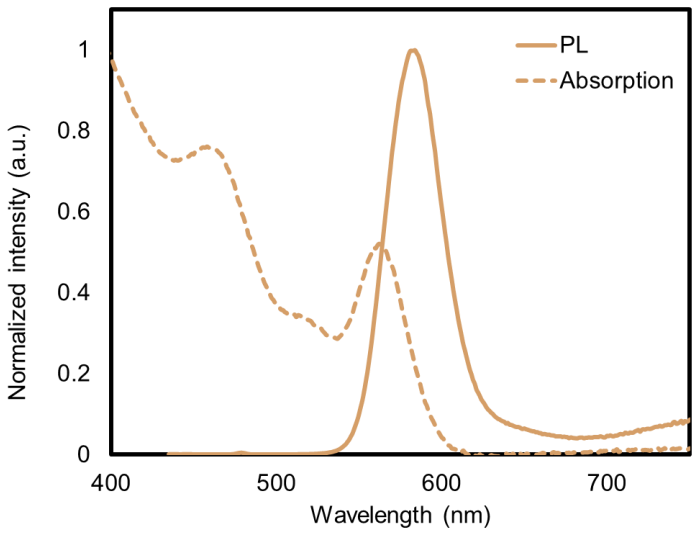

Figure 2.2. Absorption (dotted traces) and PL (solid traces) spectra of zinc blend CdSe QDs

2.2.3 *Absorption Behavior of Different Crytal Phases*

After years of making CdSe QDs, I still find it intriguing that instead of doing an XRD powder diffraction experiment (which would require me to walk to a different building), I can simply look at the absorbance traces (which I can do right in my lab) to differentiate their crystal structures. As shown in **Figure 2.3** for two CdSe samples with similar absorption profiles, the first valley after the LEET feature (in wavelength) is always higher in absorption than the second valley

for wurtzite CdSe crystals, while the opposite is true for zincblende. This effect is even clearer with highly monodisperse samples. You can look up any CdSe absorption spectrum and fact-check this. What if the two valleys have equal absorption? I suppose in that case, the crystal may contain a mixture of both phases or the sample is too polydisperse in size for the effect to be clearly observed. I do not have a definitive explanation, please take this with a grain of salt.

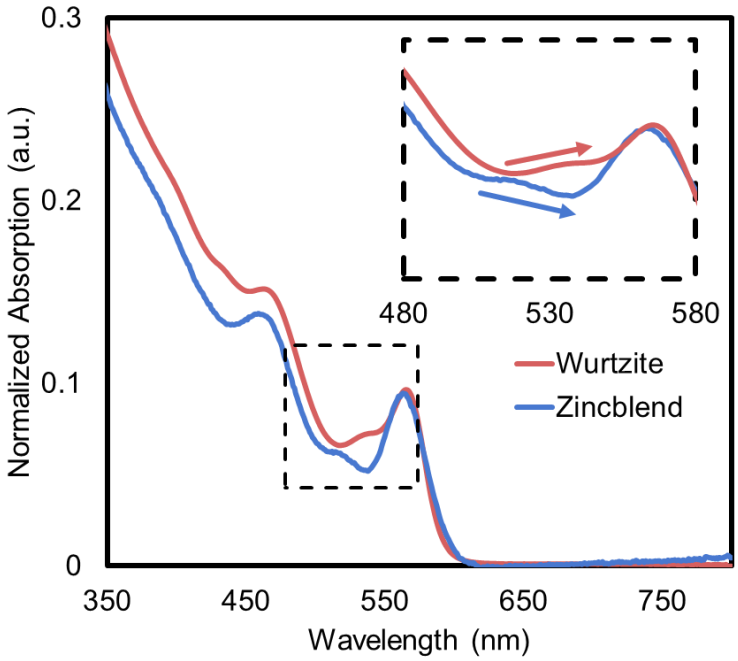

Figure 2.3. Comparison of absorption spectra between wurtzite and zinc blend CdSe QDs.

2.3 Synthesis of CdSe/CdS, CdSe/ZnS, and CdSe/CdS/ZnS QDs

2.3.1 *Synthetic Considerations Before Shelling*

There are three main methods to colloidally shell CdSe cores with CdS or ZnS: Successive ionic layer adsorption and reaction (SILAR), high-temperature continuous injection (HTCI), and colloidal atomic layer deposition (cALD). The SILAR method involves alternately adding precursors for the cation ($Cd(oleate)_2$ for example) and anion (S-TOP for example) at controlled

concentrations, which allows shell growth to proceed one layer at a time in a relatively mild, diffusion-limited manner. This approach offers good control over shell thickness and reduces unwanted homogeneous nucleation. The HTCI method, by contrast, introduces precursors slowly and continuously into a hot reaction mixture, which allows shell growth under kinetically controlled conditions. This method promotes rapid deposition but might also initiate secondary nucleation or core diffusion. The cALD mimics semiconductor gas-phase atomic layer deposition in solution. It relies on self-limiting surface reactions between highly reactive precursors (such as dimethyl cadmium) added sequentially under inert conditions. This technique offers precise control over shell composition and thickness at the atomic level. The main disadvantage of SILAR and c-ALD for shelling thick shells is their labor-intensive nature since attention is needed after every single layer. In most of my synthesis for thick-shelled QDs, I used the HTCI method.

Four important parameters when doing a shelling synthesis with HTCI are the core size, core concentration, the desired amount of shell monolayers or final size, and injection rate. The core size can be determined very accurately by TEM, but estimation can also be done through fitting the absorption trace of the core to a sizing curve, which also gives the core concentration through molar coefficient. Jasieniak, van Embden, Mulvaney, and Califano have a very nice article explaining how sizing curves are made and how they work for CdSe.[9] For size estimation, the sizing equation is given by:

$$\mathrm{D\ (nm)} = 59.60816 - 0.54736\lambda + 1.8873 \times 10^{-3}\lambda^2 - 2.85743 \times 10^{-6}\lambda^3 + 1.62974 \times 10^{-9}\lambda^4 \quad (14)$$

where λ is the LEET wavelength. The molar extinction coefficient (ε_{1S}) can also be extracted from the equation:

$$\varepsilon_{1S} = 155507 + 6.67054 \times 10^{13} \times e^{\frac{E_{1S}}{0.10551}} \quad (15)$$

where $E_{1S} = 1239.8/\lambda$ is the energy of the LEET wavelength in eV. The concentration of the core CdSe QD solution can then be calculated by Beer's law:

[CdSe] (M) = (Absorbance) / ($\varepsilon_{1S} l$) × (HWHM / 0.06) = 1.00×10^{-4} M

$$[CdSe](M) = \frac{(absorbance_{1S})}{l \times \varepsilon_{1S}} \tag{16}$$

where l is the light path. Since any QD solution contains many sizes, which result in a broaden absorption linewidth at LEET, the concentration estimation can be further corrected:

$$[CdSe]_{corrected}(M) = [CdSe] \times \frac{HWHM_{1S}}{0.06} \tag{17}$$

where $HWHM_{1S}$ is the HWHM of the LEET absorption peak in eV.

For the case of CdS, the number of shell MLs can be chosen depending the purpose of shelling. Since the thickness of one CdS ML is about 0.0375 nm, if small core/shell QDs are needed, about 1-5 CdS MLs can be targeted to achieve the final particle diameter about 3-5 nm. For highest PLQY of CdSe/CdS QDs, the optimal CdS shell MLs is about 7-10 MLs.[7,10]

In a HTCI shelling setup, two syringes containing equal molar concentrations and volumes of shelling precursors are simultaneously injected into a reaction flask containing CdSe cores using a digitally controlled syringe pump, enabling precise regulation of the injection rate. This rate plays a critical role in determining the quality of the resulting particles.[11] If the injection is too fast, particularly into a solution with low core concentration, secondary nucleation can occur, leading to the formation of small CdS particles independent of the CdSe cores. Conversely, a slow injection rate prolongs the exposure of the particles to high temperatures, which can promote ripening and priming, ultimately reducing the crystallinity of the final product. At a reaction temperature of

310 °C, an optimized injection rate for a 0.2 M solution of Cd and S precursors has been established at 0.3 mL/h to balance shell growth and minimize unwanted side reactions.

2.3.2 *Shelling CdSe with CdS and ZnS*

M-oleate and octanethiol (M = Cd or Zn) were selected as shell precursors for CdSe/CdS synthesis due to their relatively low reactivity, which allows for controlled shell growth.[7] The long alkyl chain of M-oleate reduces its reactivity and also matches the ligand environment of the CdSe cores, promoting compatibility during shell formation. Octanethiol, with its strong carbon-sulfur covalent bond, requires elevated temperatures (310 ℃ for CdS shells and 270 ℃ for ZnS shells) to react, enabling slow precursor release that facilitates defect annealing and minimizes structural imperfections at the core–shell interface.

To begin the shelling reaction, 6 mL of ODE was added to a 50 mL three-neck round-bottom flask equipped with a septum, a thermometer inserted through a thermowell, and a condenser. The solution was heated to 110 ℃ and placed under vacuum for 1 hour to remove residual moisture and oxygen. After refilling the flask with nitrogen, a desired amount of CdSe cores dispersed in hexane (typically 5–100 nmol of QDs, corresponding to 0.0048–0.96 mL of stock solution) was introduced into the reaction vessel. The mixture was degassed under vacuum for an additional 30 minutes to ensure complete removal of hexane, then refilled with nitrogen. The temperature was then raised to 310 ℃ (or 270 ℃ for ZnS). Once the temperature reached 260 ℃, solutions of 0.2 M $Cd(oleate)_2$ (or $Zn(oleate)_2$) and 0.2 M 1-octanethiol in ODE, precalculated based on the amount of CdSe cores and the desired shell thickness in monolayers, were simultaneously injected into the reaction mixture using a dual-syringe pump at a rate of 3 mL/h. Typically, the target temperature of 310 °C (or 270 ℃ for ZnS) was reached within 5 minutes of initiating the injection. After the injection was completed, the reaction was held at

310 ℃ for 10 minutes, followed by a 4-hour annealing step at 280 °C (or 240 ℃ for ZnS) to promote shell crystallinity and minimize interfacial defects. The reaction was then rapidly cooled to room temperature using forced air and transferred into a glovebox for purification. To isolate the product, 5 mL of methyl acetate was added to the reaction mixture. The mixture was centrifuged at 7800 rpm for 5 minutes. The resulting precipitate was collected and redispersed in 5 mL of hexane. More centrifugation steps can be done with methyl acetate as the anti-solvent and hexane as the solvent. The final product was dissolved in hexane and stored in a N_2-filled glovebox. It should be noted that this procedure is a standard procedure for CdS shelling, which I adopted for ZnS to generalize the process, therefore, it might not give the best results for CdSe/ZnS core/shell QDs.

The procedure described above can be adapted to synthesize core/shell/shell CdSe/CdS/ZnS QDs by replacing Cd-oleate with Zn-oleate after a desired shell thickness of CdS has been deposited. This modification is motivated by the electronic structure of the heterostructure: while CdSe/CdS exhibits a quasi-type II band alignment, the addition of a ZnS outer shell shifts the system toward a type I band alignment. In this configuration, the electron wavefunction becomes more strongly confined within the CdSe core, which can enhance radiative recombination and improve the overall optical performance of the QDs.

To illustrate the versatility of this shelling procedure, I systematically targeted a final QD diameter of approximately 10–11 nm while varying both the core size and shell architecture. Specifically, three core sizes, designated here by their emission maxima as CdSe(560), CdSe(590), and CdSe(620), were paired with three different shell structures, including single-shell and core/shell/shell configurations (see **Table 2.1**). Core sizes were estimated from their absorption

spectra and denoted by emission peak wavelengths for clarity. The number of shell monolayers (MLs) was carefully controlled and is indicated for each case.

Table 2.1. Number of MLs of CdS and ZnS on three CdSe cores.

	CdSe (560)	CdSe (590)	CdSe (620)
CdS/ZnS Shell MLs	5 CdS / 4 ZnS	4 CdS / 4 ZnS	3 CdS / 4 ZnS
ZnS Shell MLs	11	9	8
CdS Shell MLs	10	9	7

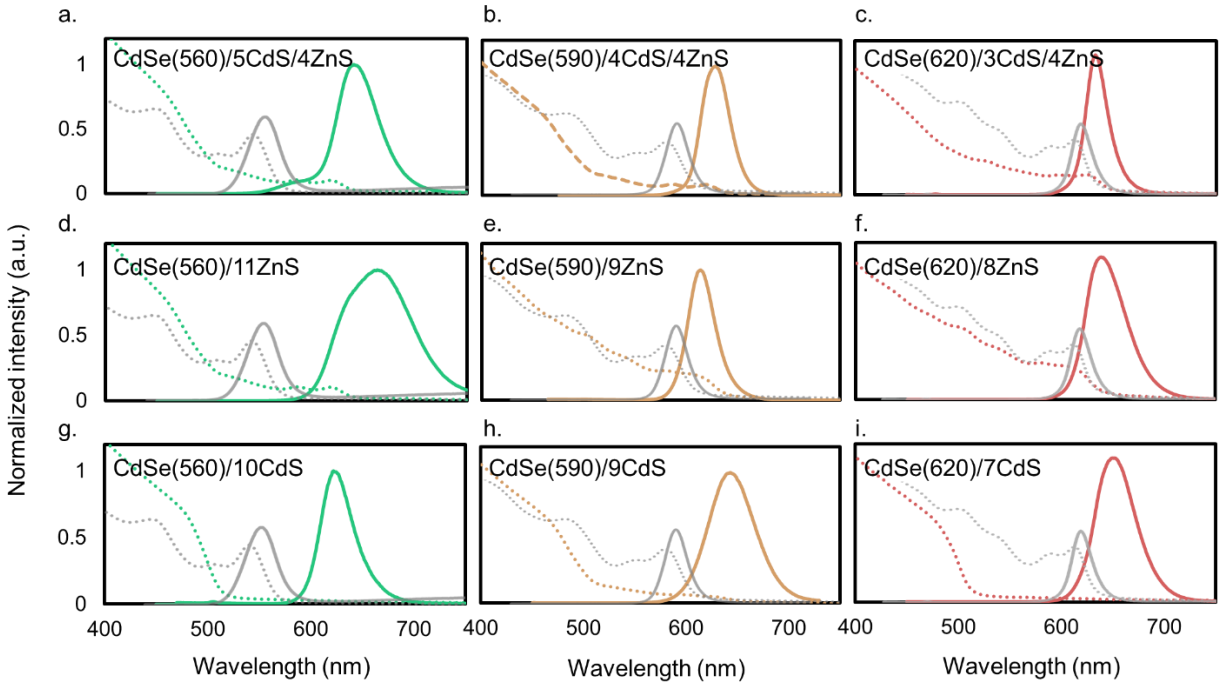

Figure 2.4. Absorption (dotted traces) and PL (solid traces) spectra of cores (grey) and core/shell samples in hexane.

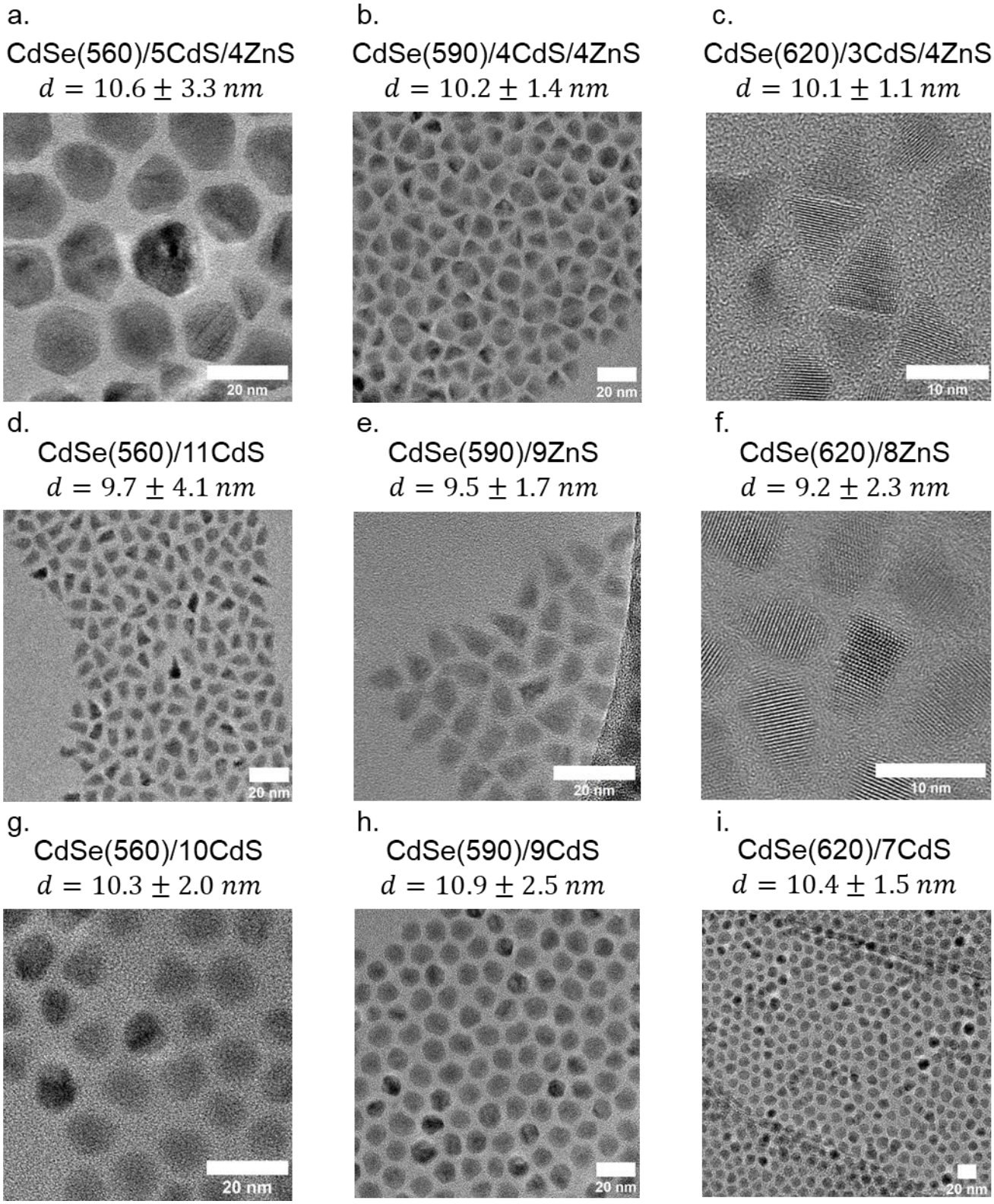

Figure 2.5. TEM images of 9 core/shell samples.

Figure __ presents the photoluminescence (PL) and absorption spectra of the resulting core/shell QDs. As expected, the absorption profiles of the final heterostructures are dominated by the shell material, with the characteristic features of the CdSe cores largely obscured. In contrast, PL spectra provide insight into size distribution and emission uniformity. For smaller cores, particularly CdSe(560)11ZnS and CdSe(560)/5CdS/4ZnS, broader and often multimodal PL profiles suggest incomplete or uneven shelling, a known challenge of high-temperature continuous injection (HTCI) methods in this size regime. This issue becomes less pronounced for the medium and larger cores, indicating that core size plays a key role in maintaining monodispersity during shell growth. Half-width-at-half-maximum (HWHM) values are generally narrower for samples containing ZnS, consistent with type-I band alignment in both CdSe/ZnS and CdSe/CdS/ZnS systems, which promotes emission from the CdSe bandgap regardless of shell thickness.

In addition to emission profiles, the data also reveals insights into atomic diffusion during shell growth. A comparison of core-only and core/shell emission peaks shows greater redshifts in the smaller cores, suggesting more significant Se diffusion into the shell layers, particularly into CdS compared to ZnS. This observation aligns with the expected behavior based on bond dissociation energies and lattice compatibility: Cd–S bonds are energetically more favorable for Se substitution than Zn–S, leading to more pronounced intermixing at the CdSe/CdS interface. Band alignment further supports this interpretation; quasi-type II behavior in CdSe/CdS can allow partial carrier delocalization, while type-I alignment in CdSe/ZnS helps confine both carriers within the core, limiting diffusion-driven emission shifts.

Morphological analysis by TEM reveals a clear dependence of particle shape on shell composition. QDs containing ZnS tend to exhibit triangular or bullet-like shapes, while those with CdS shells remain more spherical and faceted. Notably, samples with fixed ZnS shell thickness

but decreasing CdS shell layers show progressively more faceted and anisotropic shapes, with the most pronounced triangular morphology observed in CdSe(620)/3CdS/4ZnS (**Figure 2.5**).

Finally, PLQYs correlate with both core size and shell composition (**Figure 2.6**). Smaller QDs consistently yield lower PLQYs, reflecting their higher surface-to-volume ratios and the more significant impact of lattice mismatch. Across all core sizes, CdS-shelled QDs exhibit higher PLQYs than those shelled solely with ZnS, with mixed CdS/ZnS shells falling in between. This trend is consistent with lattice mismatch considerations: CdSe and CdS differ by 3.9%, while the mismatch between CdSe and ZnS is a much larger 12.3%, leading to increased strain and defect formation, particularly problematic in smaller QDs. Together, these findings highlight the importance of core size, shell composition, and interface quality in determining the optical and structural characteristics of core/shell nanocrystals synthesized via HTCI.

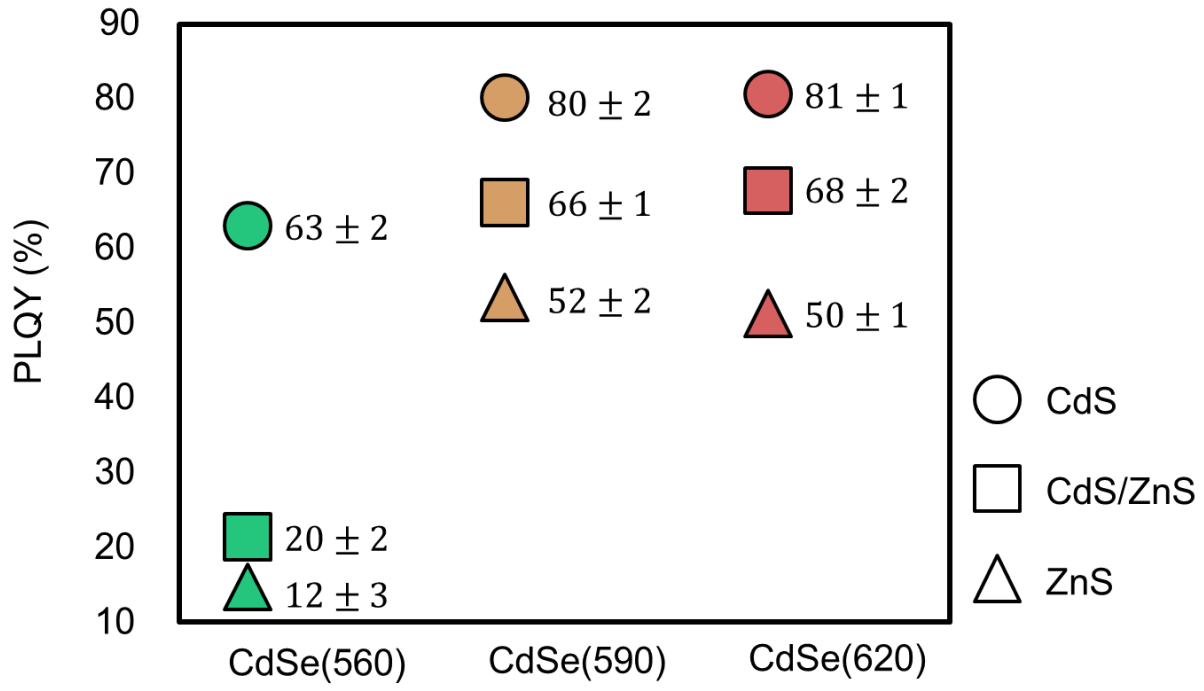

Figure 2.6. Comparison of PLQY from 9 core/shell samples

2.4 SYNTHESIS OF CDSE NANOPLATELETS

CdSe nanoplatelets (NPLs) represent a striking advancement in colloidal nanocrystal design, offering atomic-level control over thickness and remarkably uniform optical properties. Unlike QDs, whose three-dimensional confinement introduces size-dependent inhomogeneity, NPLs confine carriers in just one dimension, producing optical features as sharp as those found in epitaxial quantum wells—but accessible through solution-phase chemistry.[12] The initial motivation behind synthesizing CdSe NPLs was to combine the structural precision of epitaxially grown heterostructures with the chemical flexibility and scalability of colloidal synthesis. Although both the cubic zinc blende (first synthesized by Hyeon and coworkers in 2006)[13] and hexagonal wurtzite (first synthesized by Sandrine Ithurria, Benoit Dubertret in 2008)[14] phases are not inherently predisposed to two-dimensional growth, specific synthetic conditions, such as anisotropic surface energies and ligand-directed facet stabilization, favor lateral extension over vertical stacking. Kinetic models suggest that early symmetry breaking during nucleation, coupled with facet-selective monomer addition, drives the formation of thin, planar structures with sub-nanometer thickness control.

Structurally, CdSe NPLs grow along the [001] direction of the zinc blende lattice, where alternating atomic planes define the number of monolayers. Because the thickness is discretized at the atomic scale and can be tuned with high fidelity, NPL ensembles are free from the size dispersion that typically broadens emission in spherical QDs. This precise control leads to photoluminescence linewidths often narrower than 40 meV at room temperature, nearly half that of the best-prepared QDs of equivalent bandgap. The narrow linewidth arises not only from uniform thickness but also from strong exciton confinement and suppressed spectral diffusion, making NPLs uniquely suited for spectrally demanding applications. These characteristics have

positioned CdSe NPLs as ideal candidates for technologies requiring intense, spectrally pure emission, such as light-emitting diodes, lasers, and color displays. Their large exciton binding energies, high oscillator strengths, and rapid radiative recombination also make them promising platforms for nonlinear optics and ultrafast spectroscopy. More than a structural novelty, NPLs serve as precision-engineered systems for probing the fundamentals of low-dimensional quantum confinement and for constructing optoelectronic devices with tailored optical responses.

Building on the established synthetic strategies for CdSe NPLs, I prepared a series of samples with discrete monolayer thicknesses 3, 4, and 6MLs, to investigate how their optical features evolve with thickness. The syntheses closely followed previously reported procedures with minor adjustments for reproducibility and purification.[15] The resulting samples exhibited characteristic emission peaks centered at 462 nm for 3 MLs (~1.9 nm thick), 512 nm for 4 MLs (~2.2 nm), 550 nm for 5 MLs, and 585 nm for 6 MLs (~2.5 nm). As shown in **Figure 2.7**, the photoluminescence spectra of the 3, 4, and 6 ML CdSe NPLs display sharp, well-defined peaks, with the 6 ML sample containing a minor population of 5 ML NPLs as a synthetic byproduct.

For the 3 ML NPLs, cadmium acetate, oleic acid, and ODE were degassed and heated under vacuum before rapid injection of 1 M TOP-Se at 180 °C, followed by a 20-minute growth period. The 4 ML NPLs were synthesized from $Cd(myristate)_2$, elemental Se, and $Cd(acetate)_2$ under rapid heating to 240 °C, producing clean platelets after a short 5-minute reaction.

The 6 ML NPL synthesis required tighter control over precursor timing and purification. The synthesis was adopted from a direct method adapted from Cho et al.,[16] with minor modifications. In a 50 mL three-neck round-bottom flask equipped with a condenser, temperature probe, and septum, 170 mg of cadmium myristate was mixed with 14 mL of octadecene and degassed under vacuum at 110 °C for 15 minutes. The flask was then filled with nitrogen and

heated to 250 °C. Once the temperature stabilized, 12 mg of selenium powder (pre-dispersed in 1 mL of octadecene by sonication) was injected rapidly. After 20 seconds, 60 mg of freshly ground cadmium acetate dihydrate was added, followed 60 seconds later by the dropwise addition of 0.15 mL of 0.5 M aqueous cadmium chloride solution over 2 minutes. The reaction mixture was maintained at 250 °C for an additional 3 minutes before being rapidly cooled to room temperature using forced air. At 120 °C, a mixture of 2 mL oleic acid and 15 mL methylcyclohexane was added to aid dispersion. The NPLs were isolated by centrifugation at 11,000 rpm for 7 minutes and redispersed in methylcyclohexane or toluene for further use.

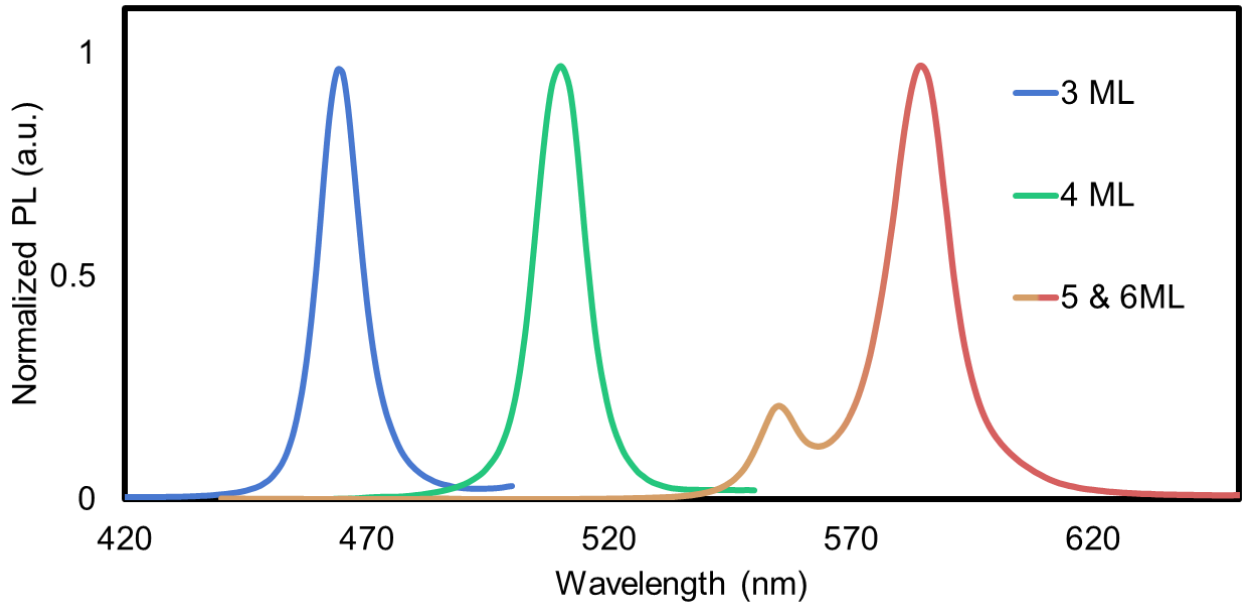

Figure 2.7. PL spectra of CdSe NPLs with 3 (blue), 4 (green), 5 (yellow), and 6 (red) MLs.

While the number of MLs dictates the thickness of NPLs, the lateral sizes or aspect ratio can be tuned by changing reaction conditions. In 2016, Bertrand et al.[17] investigated how the use of $Cd(acetate)_2$ precursors and their degree of hydration influences the aspect ratio of 4 ML CdSe NPLs. They proposed that thermal decomposition of hydrated $Cd(acetate)_2$ at elevated temperatures generates hydroxide ions in situ, which may adsorb onto specific NPL surfaces and

promote lateral growth along the <100> direction, leading to the formation of more isotropic, square-like NPLs, as reported by Moreels and co-workers.[18] In my syntheses, I used $Cd(acetate)_2 \cdot 2H_2O$ as the cadmium source without additional water injection or explicit control over hydroxide concentration. Instead, I varied the Cd-to-Se precursor ratio and observed a clear correlation with aspect ratio: at a 1:1 ratio, the NPLs were elongated with aspect ratios exceeding 4; at 1:2, the aspect ratio decreased to approximately 2; and at 1:6, the NPLs appeared nearly square with aspect ratios close to 1 (**Figure 2.8**). These results diverge from prior reports,[17] possibly due to differences in hydroxide availability or other uncontrolled variables, suggesting that both precursor chemistry and stoichiometry may influence lateral growth behavior. Further studies are needed to systematically disentangle these effects.

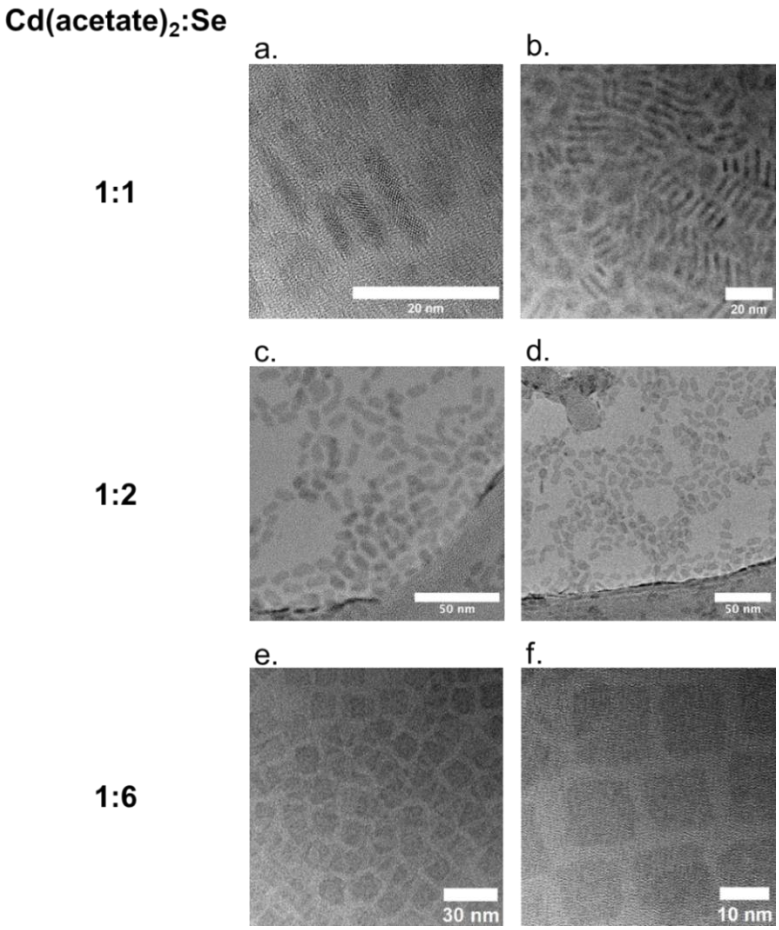

Figure 2.8. TEM images of 4 ML CdSe NPLs synthesized with different Cd(acetate)$_2$:Se ratios

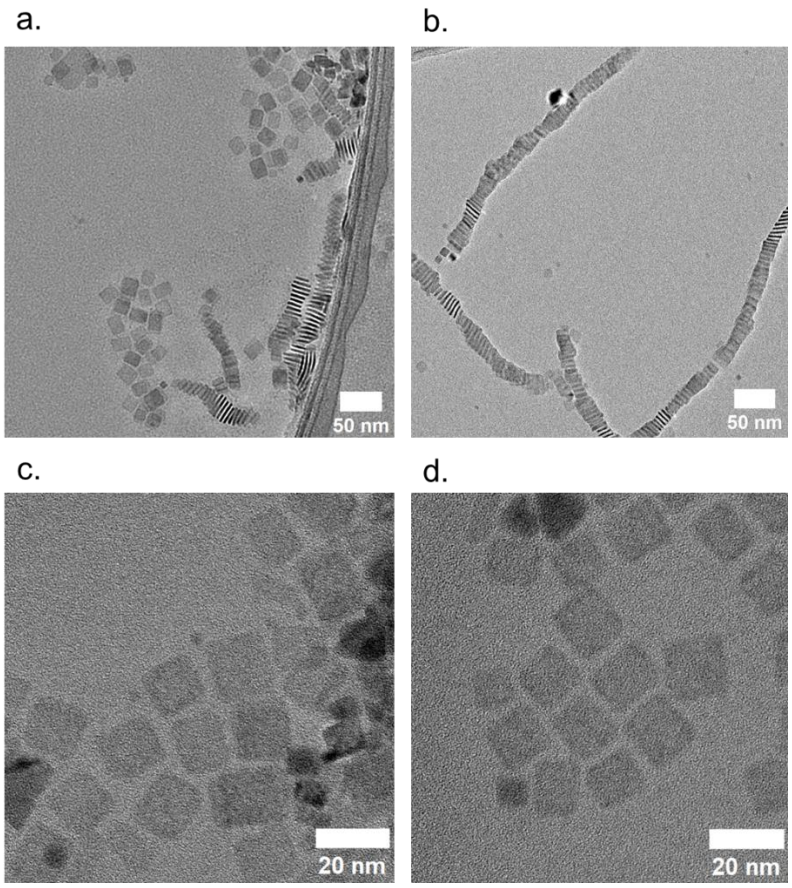

Figure 2.9. TEM images of 6 ML CdSe NPLs.

Another interesting thing about NPLs is that they can stack![19] CdSe NPLs, especially ones with large lateral dimensions, are prone to cofacial stacking due to strong van der Waals interactions and limited steric stabilization by short ligands. Although stacking can be exploited for self-assembly, it often indicates reduced colloidal stability. In my synthesis, stacking was not intentional but was observed after extensive purification, which likely stripped surface ligands and triggered aggregation. To mitigate stacking in the synthesis of 6 ML CdSe NPLs, I injected 1.5 mL

of 1 M Cd-oleate in ODE, which was preheated to 100 °C, prior to cooling the reaction mixture, which improved colloidal stability and suppressed stacking by replenishing surface ligands.

2.5 Synthesis of Core/Shell CdSe/CdS Nanoplatelets

Building core/shell structures on CdSe NPLs presents an opportunity to combine their spectrally sharp emission with improved photoluminescence quantum yield through surface passivation. However, shell growth on these 2D materials requires circumventing challenges such as thermal instability and the limited accessibility of the well-passivated {100} facets. To address this, I employed colloidal atomic layer deposition (c-ALD), a low-temperature, layer-by-layer method that enables monolayer-precision shelling by alternately introducing chalcogen and metal precursors.[20,21] The flat, atomically defined surfaces of NPLs are especially suited for this approach, making them ideal systems to explore precise heterostructure formation without the need for epitaxial techniques.

In my synthesis, 4 ML CdSe NPLs were shelled with two monolayers of CdS to form a symmetric 2CdS/4CdSe/2CdS structure. Li_2S and anhydrous $Cd(formate)_2$ were used as the sulfide and cadmium sources, respectively. All steps were performed inside a nitrogen glovebox using rigorously dried solvents because Li_2S is sensitive to air and polysufides/polyselenides. For each cycle, ~15 mg of CdSe NPLs dispersed in 100 µL MCH was combined with 15 mg Li_2S, 500 µL ODE, and 100 µL OAm, stirred at 150 °C for 1.5 minutes. After removing excess solids and washing with ethanol, the sulfide-treated NPLs were added to $Cd(formate)_2$, 500 µL ODE, and 100 µL OAm, and stirred at 150 °C for 3 minutes to complete one monolayer. This cycle was repeated to achieve the final 2CdS/4CdSe/2CdS structure.

Several noteworthy trends emerged from the shelling experiments. First, the purity of the starting CdSe cores plays a critical role in determining the quality of the final core/shell product. As shown in **Figure 2.10**, when the initial NPL sample contains impurities, particularly unshelled quantum dots, these species also undergo shell growth due to the high reactivity of both sulfur and cadmium precursors, resulting in broadened emission profiles with shoulders at longer wavelengths. Second, insufficient precursor quantities during shelling lead to incomplete coverage of the NPL surfaces. This yields products with emission peaks intermediate between those of the bare cores and fully shelled structures, likely corresponding to CdSe/CdS core–crown heterostructures rather than the intended CdS/CdSe/CdS sandwiched NPLs. Third, S-capped NPLs exhibited significantly quenched photoluminescence, which could be largely restored by the subsequent addition of a Cd layer, indicating the importance of balanced surface passivation. Finally, TEM analysis revealed that the sharp, well-defined edges of the original 4 ML CdSe cores became less distinct after shelling. This morphological change may arise from thermal effects during shell growth or from the reactivity of undercoordinated edge and corner atoms, which could promote surface reconstruction or local diffusion.

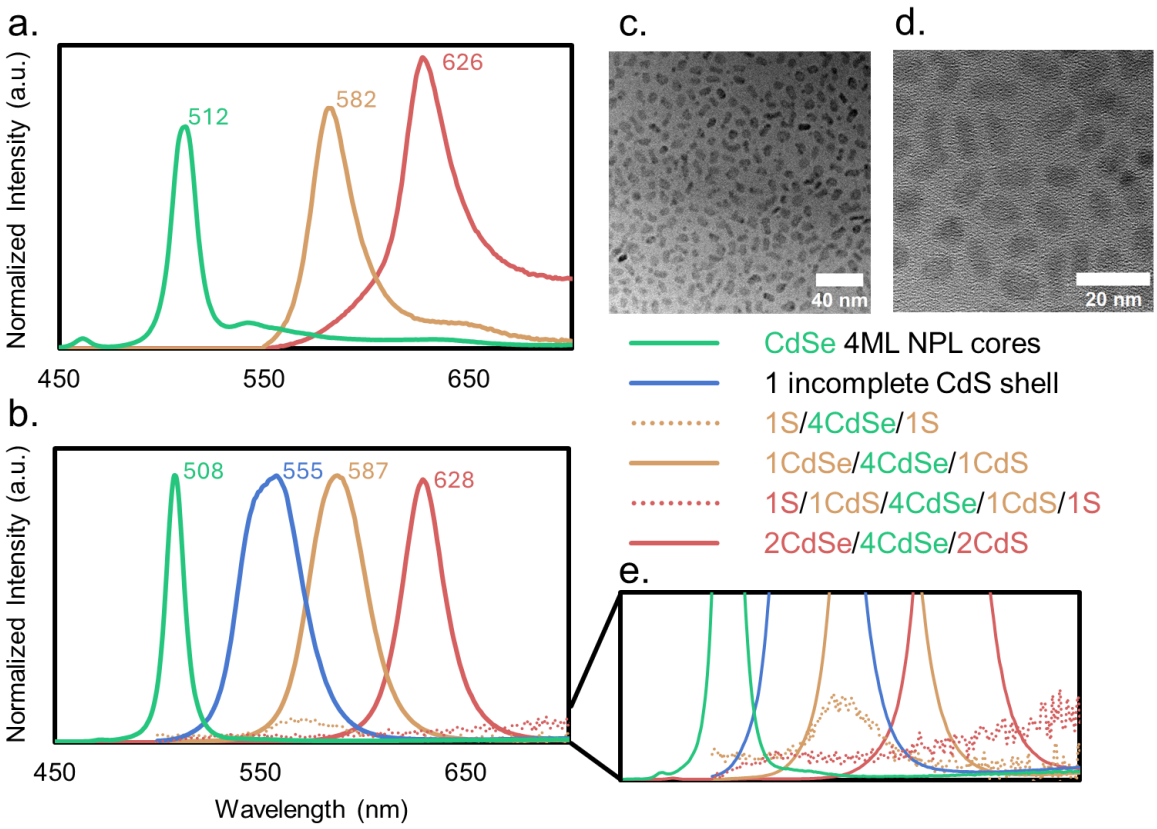

Figure 2.10. PL spectra of core 4 ML CdSe and core/shell 2CdS/4CdSe/2CdS NPLs

2.6 CONCLUSION

This chapter highlights a series of exploratory syntheses that are built upon, but also diverge from, very established methods for preparing CdSe QDs and NPLs. By making deliberate adjustments to standard procedures, I was able to probe how small changes in precursor identity, injection timing, and purification impact the structural and optical properties of the resulting nanocrystals. The work includes not only synthesis of discrete-thickness CdSe NPLs, but also their shelling via c-ALD to form well-defined core/shell heterostructures. Along the way, I encountered phenomena such as lateral growth tuning, stacking behavior, and shelling-induced defects, each offering insights into surface chemistry and colloidal stability. While some results aligned with

prior literature, others raised new questions and highlighted the need for further study. Together, these experiments lay the foundation for the optical studies presented in the next chapter.

2.7 REFERENCES

(1) Koch, U.; Fojtik, A.; Weller, H.; Henglein, A. Photochemistry of Semiconductor Colloids. Preparation of Extremely Small ZnO Particles, Fluorescence Phenomena and Size Quantization Effects. *Chem. Phys. Lett.* **1985**, *122*, 507–510. https://doi.org/10.1016/0009-2614(85)87255-9.

(2) Fojtik, A.; Weller, H.; Koch, U.; Henglein, A. Photo-Chemistry of Colloidal Metal Sulfides 8. Photo-Physics of Extremely Small CdS Particles: Q-State CdS and Magic Agglomeration Numbers. Berichte Bunsenges. *Für Phys. Chem.* **1984**, *88*, 969–977. https://doi.org/10.1002/bbpc.19840881010.

(3) Ekimov, A.; Onushchenko, A. Quantum Size Effect in Three-Dimensional Microscopic Semiconductor Crystals. *J. Exp. Theor. Phys. Lett.* **1981**, *34*, 345–349.

(4) Henglein, A. Photochemistry of Colloidal Cadmium Sulfide. 2. Effects of Adsorbed Methyl Viologen and of Colloidal Platinum. *J. Phys. Chem.* **1982**, *86*, 2291–2293. https://doi.org/10.1021/j100210a010.

(5) Murray, C. B.; Norris, D. J.; Bawendi, M. G. Synthesis and Characterization of Nearly Monodisperse CdE (E = Sulfur, Selenium, Tellurium) Semiconductor Nanocrystallites *J. Chem. Am. Soc.* **1993**, *115*, *19*, 8706–8715. https://doi.org/10.1021/ja00072a025.

(6) Nan, W.; Niu, Y.; Qin, H.; Cui, F.; Yang, Y.; Lai, R.; Lin, W.; Peng, X. Crystal Structure Control of Zinc-Blende CdSe/CdS Core/Shell Nanocrystals: Synthesis and Structure-Dependent Optical Properties. *J. Am. Chem. Soc.* **2012**, *134*, 19685–19693. https://doi.org/10.1021/ja306651x.

(7) Chen, O.; Zhao, J.; Chauhan, V. P.; Cui, J.; Wong, C.; Harris, D. K.; Wei, H.; Han, H.-S.; Fukumura, D.; Jain, R. K.; et al. Compact High-Quality CdSe–CdS Core–Shell Nanocrystals with Narrow Emission Linewidths and Suppressed Blinking. *Nat. Mater.* **2013**, *12*, 445–451. https://doi.org/10.1038/nmat3539.

(8) Gong, K.; Martin, J. E.; Shea-Rohwer, L. E.; Lu, P.; Kelley, D. F. Radiative Lifetimes of Zincblende CdSe/CdS Quantum Dots. *J. Phys. Chem. C* **2015**, *119*, 2231–2238. https://doi.org/10.1021/jp5118932.

(9) Jasieniak, J.; Smith, L.; van Embden, J.; Mulvaney, P.; Califano, M. Re-Examination of the Size-Dependent Absorption Properties of CdSe Quantum Dots. *J. Phys. Chem. C* **2009**, *113*, 19468–19474. https://doi.org/10.1021/jp906827m.

(10) Hanifi, D. A.; Bronstein, N. D.; Koscher, B. A.; Nett, Z.; Swabeck, J. K.; Takano, K.; Schwartzberg, A. M.; Maserati, L.; Vandewal, K.; van de Burgt, Y.; et al. Redefining Near-Unity Luminescence in Quantum Dots with Photothermal Threshold Quantum Yield. *Science* **2019**, *363*, 1199–1202. https://doi.org/10.1126/science.aat3803.

(11) Christodoulou, S.; Vaccaro, G.; Pinchetti, V.; De Donato, F.; Grim, J. Q.; Casu, A.; Genovese, A.; Vicidomini, G.; Diaspro, A.; Brovelli, S.; et al. Synthesis of Highly Luminescent Wurtzite CdSe/CdS Giant-Shell Nanocrystals Using a Fast Continuous Injection Route. *J. Mater. Chem. C* **2014**, *2*, 3439–3447. https://doi.org/10.1039/C4TC00280F.

(12) Diroll, B. T.; Guzelturk, B.; Po, H.; Dabard, C.; Fu, N.; Makke, L.; Lhuillier, E.; Ithurria, S. 2D II–VI Semiconductor Nanoplatelets: From Material Synthesis to Optoelectronic Integration. *Chem. Rev.* **2023**, *123*, 3543–3624. https://doi.org/10.1021/acs.chemrev.2c00436.

(13) Joo, J.; Son, J. S.; Kwon, S. G.; Yu, J. H.; Hyeon, T. Low-Temperature Solution-Phase Synthesis of Quantum Well Structured CdSe Nanoribbons. *J. Am. Chem. Soc.* **2006**, *128*, 5632–5633. https://doi.org/10.1021/ja0601686.

(14) Ithurria, S.; Dubertret, B. Quasi 2D Colloidal CdSe Platelets with Thicknesses Controlled at the Atomic Level. *J. Am. Chem. Soc*. **2008**, *130*, 16504–16505. https://doi.org/10.1021/ja807724e.

(15) She, C.; Fedin, I.; Dolzhnikov, D. S.; Dahlberg, P. D.; Engel, G. S.; Schaller, R. D.; Talapin, D. V. Red, Yellow, Green, and Blue Amplified Spontaneous Emission and Lasing Using Colloidal CdSe Nanoplatelets. *ACS Nano* **2015**, *9*, 9475–9485. https://doi.org/10.1021/acsnano.5b02509.

(16) Cho, W.; Kim, S.; Coropceanu, I.; Srivastava, V.; Diroll, B. T.; Hazarika, A.; Fedin, I.; Galli, G.; Schaller, R. D.; Talapin, D. V. Direct Synthesis of Six-Monolayer (1.9 Nm) Thick Zinc-Blende CdSe Nanoplatelets Emitting at 585 Nm. *Chem. Mater*. **2018**, *30*, 6957–6960. https://doi.org/10.1021/acs.chemmater.8b02489.

(17) Bertrand, G. H. V.; Polovitsyn, A.; Christodoulou, S.; Khan, A. H.; Moreels, I. Shape Control of Zincblende CdSe Nanoplatelets. *Chem. Commun.* **2016**, *52*, 11975–11978. https://doi.org/10.1039/C6CC05705E.

(18) Moreels, I.; Lambert, K.; De Muynck, D.; Vanhaecke, F.; Poelman, D.; Martins, J. C.; Allan, G.; Hens, Z. Composition and Size-Dependent Extinction Coefficient of Colloidal PbSe Quantum Dots. *Chem. Mater.* **2007**, *19*, 6101–6106. https://doi.org/10.1021/cm071410q.

(19) Abécassis, B.; Tessier, M. D.; Davidson, P.; Dubertret, B. Self-Assembly of CdSe Nanoplatelets into Giant Micrometer-Scale Needles Emitting Polarized Light. *Nano Lett.* **2014**, *14*, 710–715. https://doi.org/10.1021/nl4039746.

(20) Ithurria, S.; Talapin, D. V. Colloidal Atomic Layer Deposition (c-ALD) Using Self-Limiting Reactions at Nanocrystal Surface Coupled to Phase Transfer between Polar and Nonpolar Media. *J. Am. Chem. Soc.* **2012**, *134*, 18585–18590. https://doi.org/10.1021/ja308088d.

(21) Hazarika, A.; Fedin, I.; Hong, L.; Guo, J.; Srivastava, V.; Cho, W.; Coropceanu, I.; Portner, J.; Diroll, B. T.; Philbin, J. P.; et al. Colloidal Atomic Layer Deposition with Stationary Reactant Phases Enables Precise Synthesis of "Digital" II–VI Nano-Heterostructures with Exquisite Control of Confinement and Strain. *J. Am. Chem. Soc.* **2019**, *141*, 13487–13496. https://doi.org/10.1021/jacs.9b04866.

Chapter 3. PREDICTING INDIUM PHOSPHIDE QUANTUM DOT PROPERTIES FROM SYNTHETIC PROCEDURES USING MACHINE LEARNING

This chapter aims to show an approach of using machine learning to predict outcomes of InP and CdSe QDs syntheses and how to work around small datasets from the literature. Components of this chapter were republished with permission of the American Chemical Society, from "Predicting Indium Phosphide Quantum Dot Properties from Synthetic Procedures Using Machine Learning", Hao A. Nguyen, Florence Y. Dou, Nayon Park, Shenwei Wu, Harrison Sarsito, Benedicte Diakubama, Helen Larson, Emily Nishiwaki, Micaela Homer, Melanie Cash, and Brandi M. Cossairt; *Chemistry of Materials* **2022**, *34*, *14*, 6296–6311; Copyright 2025 American Chemical Society.

3.1 INTRODUCTION

Indium phosphide quantum dots (QDs) are a promising alternative to traditional Cd- and Pb-based materials for lighting, displays, and optoelectronic technologies.[1-3] However, due to its increased covalency, limitations in easily accessible precursors, and inherent distinctions in precursor reactivity and valency, the synthesis of InP has been met with more challenges compared to their II–VI and IV–VI counterparts in terms of extracting generalizable design principles and targeted properties.[4] Since the first InP QD synthesis in 1994 that reported the use of chloroindium oxalate combined with tris(trimethylsilyl)phosphine ($P(TMS)_3$) in a mixture of trioctylphosphine (TOP) and trioctylphosphine oxide (TOPO) using a heat-up method,[5] intense effort has been devoted to exploring new synthetic methodologies and new precursors (**Figure 3.1**). The most

important synthetic developments include the hot injection method that typically produces ensembles with a high degree of monodispersity,[6] the magic-sized cluster-mediated method that exploits our understanding of the nonclassical growth mechanisms observed under certain reaction conditions,[7,8] and the microwave-assisted method that uses inductive heating and in situ fluoride generation to develop a scalable InP synthetic platform that results in luminescent InP cores directly out of the synthesis.[9] Efforts to replace the highly reactive and challenging to handle tris(trimethylsilyl)phosphine ($P(TMS)_3$) precursor to better separate nucleation and growth have resulted in a variety of new phosphorus precursors such as aminophosphines,[10] tris(trimethylgermyl)phosphine,[11] phosphine gas,[12] and white phosphorus.[13] In general, synthetic development has focused on narrowing size distributions, increasing quantum yields, and exploring more environmentally benign reagents. Other important considerations in this regard are tunability and reproducibility in particle size and emission wavelength, which are governed by different synthetic factors including but not limited to nucleation temperature, reaction time, precursor conversion kinetics, additives, and postsynthetic manipulations. Often, QDs with distinct sizes and excitonic emission wavelengths are isolated by taking aliquots from the reaction mixture at different reaction times. However, maximizing material yield and achieving precise synthetic control and reproducibility over particle size and emission wavelengths of InP QDs still remain a challenge.

In recent years, machine learning (ML) has emerged as a powerful tool to accelerate chemical reaction design and materials discovery. ML techniques are effective at inferring patterns and uncovering trends from complex chemical processes or mechanisms when a database of a reasonable size is available. In the field of nanomaterials, ML has been used to extract data,[14–16] discover novel materials,[17–19] optimize chemical reactions,[20–22] reveal underlying mechanisms,[23,24]

and predict synthetic outcomes.[25] For example, support vector machine classification and regression models were used to synthetically control layer thickness of perovskite halide nanoplatelets.[26] In another application, Bayesian optimization was applied to improve monodispersity of PbS QDs, leading to the narrowest reported half-width at half-maximum of absorbance of this material.[27] In 2020, Santos and co-workers published a study wherein different ML algorithms were applied to identify influential synthetic parameters and to predict the final size of a variety of metal chalcogenide QDs, including CdSe, CdS, PbS, PbSe, and ZnSe.[25] The Gradient Boosting Machine algorithm used in that study resulted in a high R^2 value and revealed that growth temperature and time are the most influential synthetic parameters. In addition, several groups have used automated technology with feedback learning mechanisms to generate their own synthesis parameter space to create nanocrystals, including InP,[28] with desired characteristics.[20,29] The accuracy of predictions is typically limited by the size, completeness, and quality of the dataset. While there are many valuable materials databases such as the Inorganic Crystal Structure Database, NREL Materials Database, Materials Project, Stanford Catalysis-Hub, and PubChem in the field of nanomaterials, there are a limited number of adequate datasets largely due to inconsistencies in reporting and the lack of an organized, centralized data repository.

In this work, we employ different predictive ML algorithms to gain insights into reaction condition control over particle diameter, absorption, and emission wavelength of InP QDs from reported data. ML methods are appropriate to help us gain a deeper understanding of InP QD synthesis because of the complexity of factors that affect the physical and electronic structures of the QDs. In principle, particle diameter, excitonic absorption, and band-edge emission should be connected, but from experimental observations, nuances related to surface chemistry, stoichiometry, and size and morphological heterogeneity make direct correlations less obvious.

We demonstrate a dataset preprocessing technique to overcome the challenge of having limited data from the literature. Different approaches to define input descriptors and machine learning model types are explored to find the best strategy for reaction prediction. Finally, we deploy an accessible user interface for external users and apply this interface to compare the results of new experiments with predicted results obtained from the ML models.

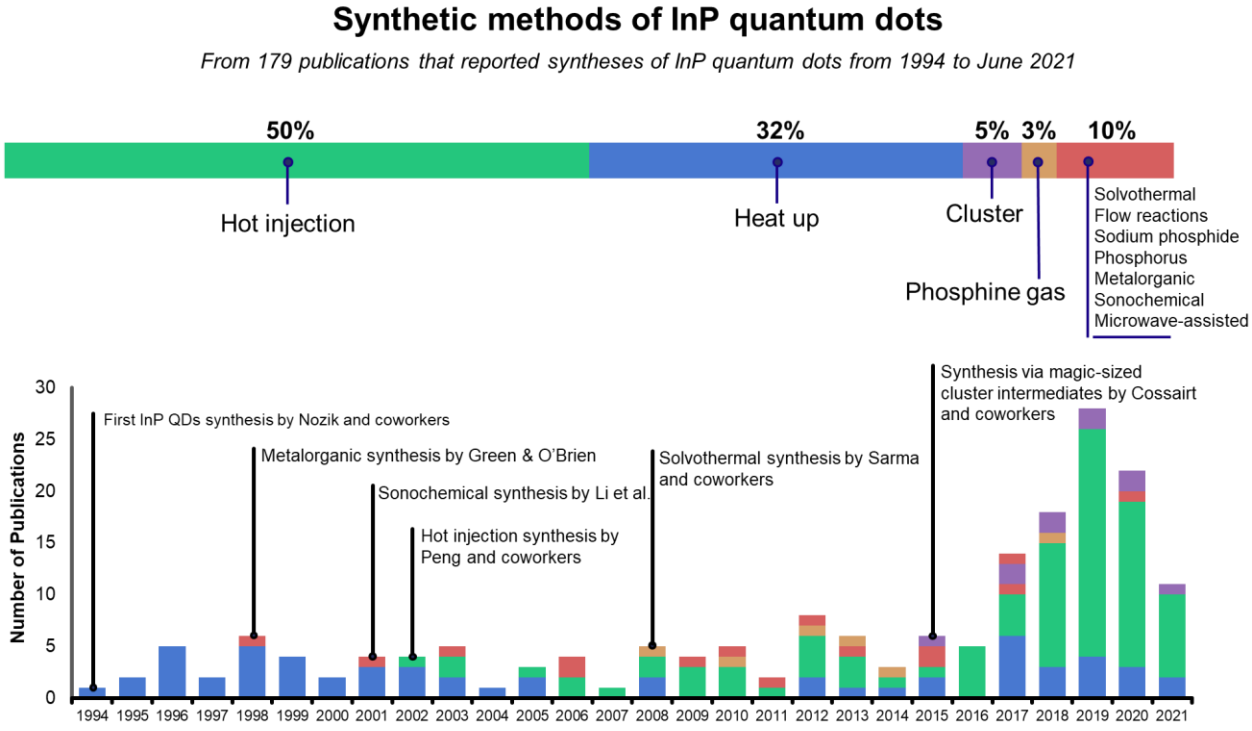

Figure 3.1. Timeline and number of publications on the synthesis of InP QDs.

3.2 Machine Learning Methods

3.2.1 *Data Acquisition.*

The dataset was created by manually extracting reaction conditions and resultant size and optical properties reported in the literature using Web of Science and Scifinder with search terms: "indium phosphide", "indium phosphide quantum dots", "InP", and "III–V quantum dots". We identified 179 articles from 1994 to June 2021 that reported syntheses of InP QDs. We then

classified the articles by synthetic methods (e.g., heat-up, hot injection, magic-sized cluster-mediated, etc.). Since there are significant practical differences among these synthetic methods that can affect the accuracy of the predictions, only similar methods, where the reaction is performed using batch-type techniques with molecular indium and phosphorus precursors, were used for further data extraction. We also excluded syntheses that did not include any size, absorption, or emission data. This process resulted in an initial dataset that included 219 syntheses from 72 different articles, in which the hot injection method, heat-up method, reactions using phosphine gas, reactions using white phosphorus, and reactions using sodium phosphide make up 73, 19, 5, 2, and 1% of the syntheses, respectively. An illustration of how the data extraction was done can be found in **Figure 3.2**.

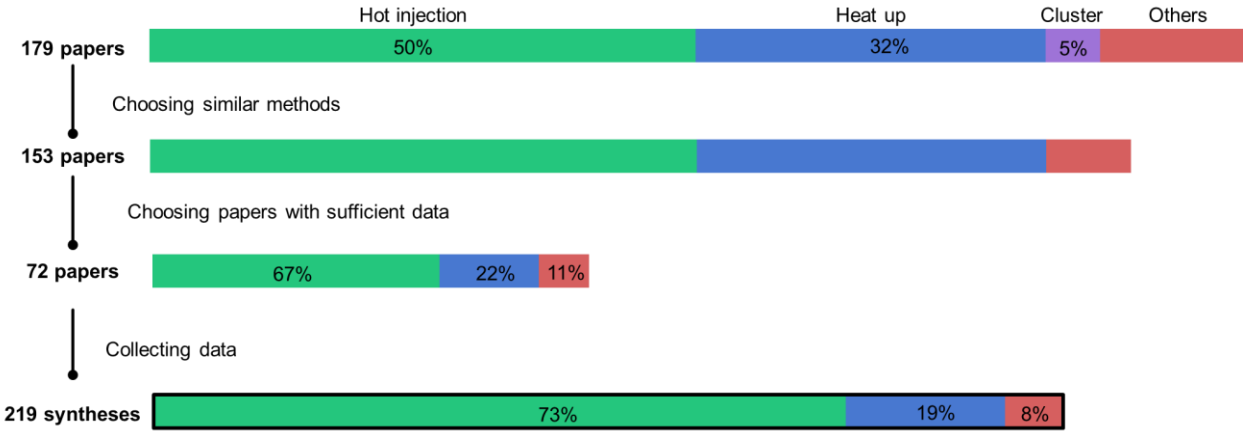

Figure 3.2. Data extraction and selection process

3.2.2 *Datasets.*

The data extracted from the 219 syntheses were split into input features and output targets. With the goal of predicting the properties of QDs, the output targets contained particle diameter in nanometers measured directly from transmission electron microscopy (TEM), absorption wavelength in nanometers, and photoluminescence (PL) emission wavelength in nanometers.

Although the three chosen outputs are physically related, e.g., QD size can be theoretically determined by the excitonic peak from absorption spectra, we wanted to investigate the ability of the ML models to recognize these relationships.

While defining the output set was straightforward, determining the input features required more consideration. In general, the performance of a predictive model depends on finding representative input features.[30-31] Furthermore, using too many input features may lead to overfitting. This becomes challenging, especially for predictive chemical synthesis models, where the outcomes of syntheses are nontrivially affected by unknown, unreported, and/or seemingly trivial parameters. Therefore, to evaluate the effect of feature selection on our models, we defined two sets of input features (**Figure 3.3.a**) and compiled two datasets: an extended dataset with 22 features and a condensed dataset with 18 features (**Figure 3.3.b**). In the extended dataset, the additives beyond the indium and phosphorus sources were categorized by their functional groups (e.g., carboxylic acid, amine, thiol), while the condensed dataset grouped chemicals by their primary assumed role in the synthesis (e.g., ligands, solvents). Using the extended dataset, we hoped to uncover trends of additives based on chemical identity such as fatty amines, zinc salts, and thiol-containing ligands that may play more than one role in the synthesis.[32-35] For example, since thiols and fatty amines are sometimes used as both coordinating solvents and capping ligands that directly affect the optical properties of QDs, it is more reasonable to separate these features from each other and from other features (solvents and acids) in the dataset with the risk of having a high dimensionality. On the other hand, features in the condensed dataset were chosen to reduce the number of input variables for better ML performance with the tradeoff of not observing unique behaviors of some additives. Prior to training machine learning models, the continuous values (In amount, P amount, reaction time, etc.) in the input set were scaled and the categorical features (In

source, P source, etc.) were transformed to numerical features using one-hot encoding and the scikit-learn software package (sklearn).[36]

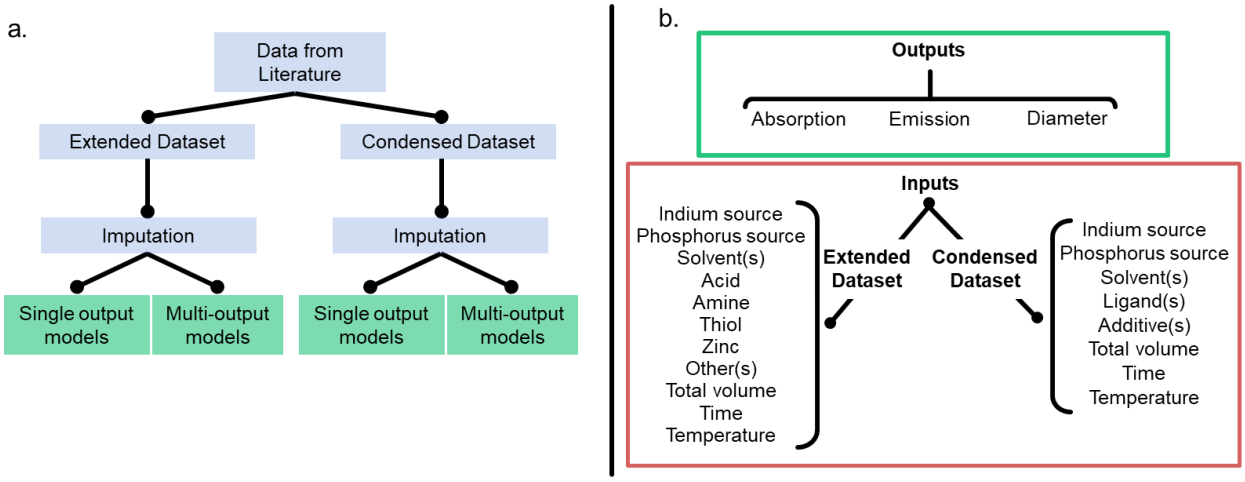

Figure 3.3. a. Workflow and b. output and input feature selection

3.2.3 *Data Imputation.*

After defining the two datasets, we applied a data imputation process to both datasets. One of the biggest challenges when applying machine learning to materials chemistry is the lack of sufficient data. In our initial dataset, only 35 out of 219 syntheses had a complete set of output target values because only a few articles reported all three targeted properties of InP QD (**Figure 3.4.a**) To "fill in" the output target values, we performed a data imputation process. Data imputation, or imputing, is a technique used for filling in missing entries in the dataset, when values are not measured or reported.[37,38] This method is simple when only a small fraction of the output set is missing and when the missing values can be calculated or easily predicted.

In our study, we imputed the missing values by training a predictive model for each output feature, using the initial input set and the available output entries as training data. Since absorption was the most frequently reported output in the initial dataset (205 syntheses), data imputation was

performed on absorption first, followed by emission, and finally diameter. Each imputative model was tuned by an exhaustive grid search to find the best parameters.

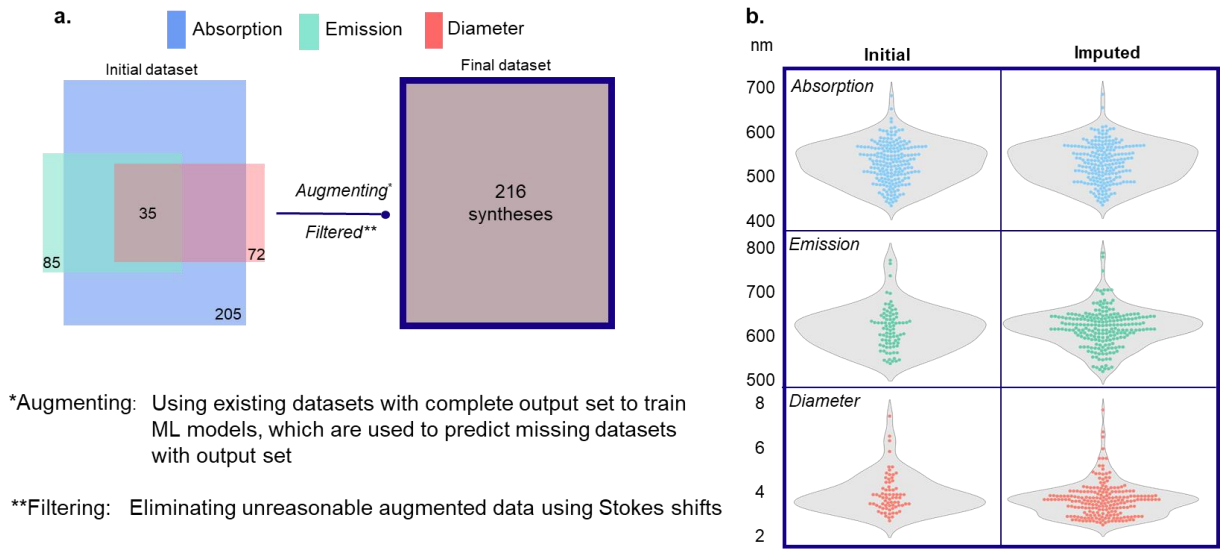

Figure 3.4. a. Data imputation process and **b.** descriptions of the initial and imputed datasets.

In the initial dataset with 219 syntheses, 97 syntheses only include absorption, 7 syntheses only include emission; 7 syntheses only include diameter, 43 syntheses include absorption and emission, 30 syntheses include absorption and diameter, and 35 syntheses include all three outputs. The data imputation process was done similarly for both condensed and extended datasets. First, 205 syntheses that have absorption in the output set were used to train and validate the absorption predicting models. The best models were then used to predict the missing absorption values for the rest of the dataset. In the Abs-imputed dataset, syntheses that include emission were used to train and validate the emission predicting models. The best models were then used to predict missing emission values for the rest of the dataset. The same process was done to predict diameter using data from the Abs-Emi-imputed dataset. The fully imputed dataset includes 219 syntheses with a complete output set. The best model and its MAE for each case are shown in the table in **Figure 3.5**.

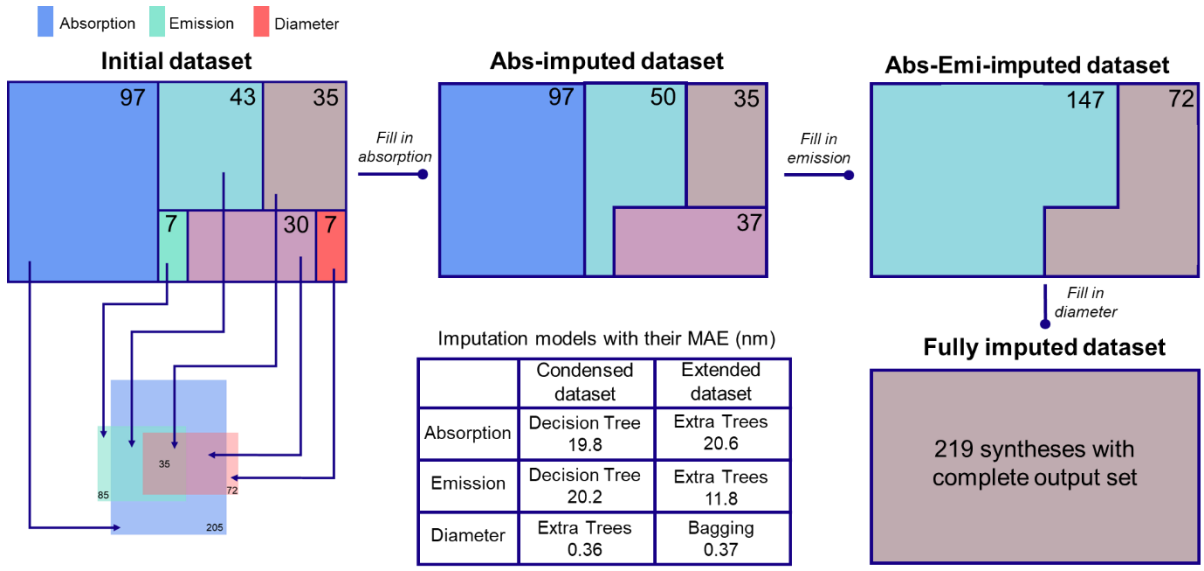

Figure 3.5. Summary of the data imputation process.

We then eliminated any syntheses that gave negative Stokes shift values, resulting in a final dataset of 216 syntheses, where excitonic absorption maxima ranged between 397 and 729 nm, band-edge PL emission ranged between 470 and 775 nm, and diameters ranged between 1.5 and 8.3 nm **Figure 3.4.b**.

3.2.4 *Machine Learning Models and Metrics.*

After filling in the missing output targets, we trained our datasets by both single- and multi-output regressors. Single-output models predict each target individually, and the features do not depend on each other. Multi-output models predict all output targets simultaneously, and the output targets depend on each other and on the input features.[39] We tested six regression algorithms suitable for small datasets: Extra Trees, Decision Tree, Random Forest, k-NN, Bagging, and Gradient Boosting using sklearn. To create representative samples for testing and training, we performed random sampling and stratified sampling methods for our datasets; and used Extra Trees and Decision Tree models to evaluate which train/test partitions give better pretraining

performance. For the stratified sampling method, we sorted our data based on the values in the "emission_nm" column and put them into six "bins": [450, 500), [500, 550), [550, 600), [600, 650), [650, 700), and [700, 800). Then, we sampled uniformly from each bin. Dividing this dataset by these bins avoids clustering of data since some specific QD sizes are more common synthetically than others. For all models, the datasets were split into 85% for training and 15% for testing. We optimized the hyperparameters for each model using grid search. The final hyperparameters used for each model are listed in the Supporting Information S11. We used the mean absolute error (MAE), the coefficient of determination (R^2), and relative absolute errors (RAE) as metrics to assess the performance of all models. MAEs are sensitive to outliers since it is a linear score, in which all differences are weighted equally. Using MAEs also helps compare performances across datasets and models for three different output targets in a direct and intuitive manner. R^2 indicates the proportion of variance for a dependent variable determined by an independent variable. RAEs consider all errors equally important and provide informative metrics to nonexperts in the field of QDs. For each model in this study, we reported the MAE, R^2, and RAE of the predicted set versus the test set.

3.3 Quantum Dot Syntheses.

We conducted eight new syntheses of InP QDs to test the prediction accuracy of our models. The experiments were designed based on four procedures found in the literature[40-43] with minor adjustments such that all reaction parameters were not already included as entries in the dataset used to train machine learning models. The reaction parameters were also selected such that they were not easily extrapolated from the parent procedures.

3.3.1 *Materials.*

All glassware was dried in an oven overnight at 160 °C before use. All manipulations were performed by using standard Schlenk or glovebox techniques under dry N_2 unless otherwise noted. Zinc acetate (99.99%), zinc chloride (99.99), indium acetate (99.99%), indium chloride (98%), tris(diethylamino)phosphine ($P(DEA)_3$, 97%), trioctylphosphine (TOP, 97%), oleic acid (OA, 90%), lauric acid (98%), and oleylamine (70%) were purchased from Sigma-Aldrich and used as received without further purification. 1- Octadecene (ODE, 90%) was purchased from Sigma-Aldrich and distilled prior to use. Methanol, ethanol, 2-propanol, acetonitrile, ethyl acetate, toluene, and pentane were purchased anhydrous and/or dried over CaH2 and stored over 3 Å molecular sieves prior to use. $((TMS)_3)P$ was synthesized as reported previouslyI. Indium oleate was synthesized as reported previously. Caution: $((TMS)_3)P$ is a very toxic and highly pyrophoric liquid that may form toxic phosphine gas upon reaction with air or water.

3.3.2 *Synthesis of InP QDs.*

For InP_1, indium chloride (0.1 mmol), zinc chloride (0.3 mmol) and oleylamine (1 mL) were mixed in a 25 mL three-neck round bottom flask, followed by degassing at 120 ℃ for 30 min and then heating to 180 ℃ under a N_2 flow. When the temperature was stable at 180 ℃, $P(DEA)_3$ (0.15 mmol) was swiftly injected into the reaction mixture. The flask was removed from the heating mantle after 2 min and let cool down to room temperature. The flask was then transferred to a nitrogen-filled glovebox. The resulting InP particles were removed from the solvent by precipitation with anhydrous ethyl acetate, followed by three cycles of washing with anhydrous ethyl acetate, centrifugation at 7800 rpm for 6 min, and redispersion in anhydrous toluene.

For InP_2, the procedure of this synthesis is similar to the synthesis of InP_1, except that the reaction flask was removed from the heating mantle 20 min after the injection of $P(DEA)_3$.

For InP_3, the procedure of this synthesis is similar to the synthesis of InP_1, except that the initial mixture did not have zinc chloride and the reaction flask was removed from the heating mantle 10 min after the injection of $P(DEA)_3$.

For InP_4, indium chloride (0.12 mmol) and zinc chloride (0.7 mmol) were added to a 25 mL three-neck round bottom flask containing oleylamine (2.5 mL). The mixture was degassed under reduced pressure at 120 ℃ for 1 h and then refilled with N_2 gas before heating to 180 ℃. When the temperature was stable at 180 °C, $P(DEA)_3$ (0.15 mmol) was swiftly injected into the reaction mixture. The flask was removed from the heating mantle after 5 min and let cool down to room temperature. The resulting InP particles were removed from the solvent by precipitation with anhydrous ethyl acetate, followed by three cycles of washing with anhydrous ethyl acetate, centrifugation at 7800 rpm for 6 min, and redispersion in anhydrous toluene.

For InP_5, the procedure of this synthesis is similar to the synthesis of InP_4, except that the reaction flask was removed from the heating mantle 40 min after the injection of $P(DEA)_3$.

For InP_6, indium oleate (0.1 mmol), and OA (0.1 mmol) were added to a 25 mL three-neck round bottom flask containing 6 mL of ODE. The mixture was degassed under reduced pressure at 120 ℃ for 1 h and then refilled with N_2 gas. $(TMS)_3P$ (0.1 mmol) was injected into the solution at room temperature, followed by a rapid heating to 220 ℃. The flask was removed from the heating mantle 20 min after the temperature was stable at 220 ℃ and let cool down to room temperature. The resulting InP particles were removed from the solvent by precipitation with anhydrous ethyl acetate, followed by three cycles of washing with anhydrous ethyl acetate, centrifugation at 7800 rpm for 6 min, and redispersion in anhydrous toluene.

For InP_7, the procedure of this synthesis is similar to the synthesis of InP_6, except that the reaction flask was removed from the heating mantle 30 min after the temperature was stable at 220 ℃.

For InP_8, indium oleate (0.3 mmol), zinc acetate (0.6 mmol), and OA (2.4 mmol) were added to a 25 mL three-neck round bottom flask containing 5 mL of ODE. The mixture was degassed under reduced pressure at 120 ℃ for 1 h and then refilled with N_2 gas before heating up to 150 oC. $(TMS)_3P$ (0.2 mmol) was injected into the solution at room temperature, followed by a rapid heating to 200 ℃. The flask was removed from the heating mantle 20 min after the temperature was stable at 200 ℃ and let cool down to room temperature. The resulting InP particles were removed from the solvent by precipitation with anhydrous ethyl acetate, followed by three cycles of washing with anhydrous ethyl acetate, centrifugation at 7800 rpm for 6 min, and redispersion in anhydrous toluene.

3.3.3 *Characterization Details.*

UV−vis absorption spectra were obtained by using an Agilent Cary 5000 spectrophotometer, and fluorescence measurements were obtained on a Horiba Jobin Yvon FluoroMax-4 fluorescence spectrophotometer. All TEM samples were prepared in a nitrogen glovebox by drop-casting 5 μL of a diluted solution of InP QDs in toluene onto an ultrathin carbon film on a lacey carbon support film, 400 mesh, copper grids purchased from Ted Pella Inc, and then allowed to dry for 30 min. TEM images were obtained on an FEI Technai G2 F20 microscope operated at 200keV. Analysis of TEM images was performed using ImageJ software with an average of 150 diameter measurements per average value reported.

3.4 Results and Discussion

3.4.1 *Data Description.*

After the data extraction process the dataset contained 219 syntheses of InP QDs from 72 papers. However, the dataset is biased toward hot injection syntheses, with 71% of entries from this method. This bias reflects the widespread use of the hot injection method, which has been proposed to assist the formation of monodisperse InP QDs due to rapid nucleation at elevated temperatures.[44] Despite this bias, we also included comparable methods in the dataset to maximize the size and diversity of inputs in our dataset, even though every synthetic parameter (e.g., temperature ramp rate) could not be captured due to limited and inconsistent reporting. As can be seen, the most common In and P precursors were indium acetate, indium chloride, and $P(TMS)_3$ (**Figure 3.6**). The addition of zinc salts is known to increase the photoluminescence quantum yield and the stability of the InP QDs;[45] around 41% of the syntheses in the dataset include a Zn additive, with $ZnCl_2$ being the most common. The reaction temperatures ranged from 130 to 310 °C, among which the lowest temperatures correspond to reactions using chloroindium oxalate, and the highest temperatures correspond to reactions using indium tris(*N*,*N*′-diisopropylacetamidinato), indium trifluoroacetate, indium oxalate, indium palmitate, and indium myristate. Across the dataset, the reaction times were concentrated below 1 h, again related to the widespread use of the hot injection method. In contrast, the heat-up procedure requires much longer reaction times, due to progressive heating and typically lower precursor reactivity, resulting in long supersaturation times.[46]

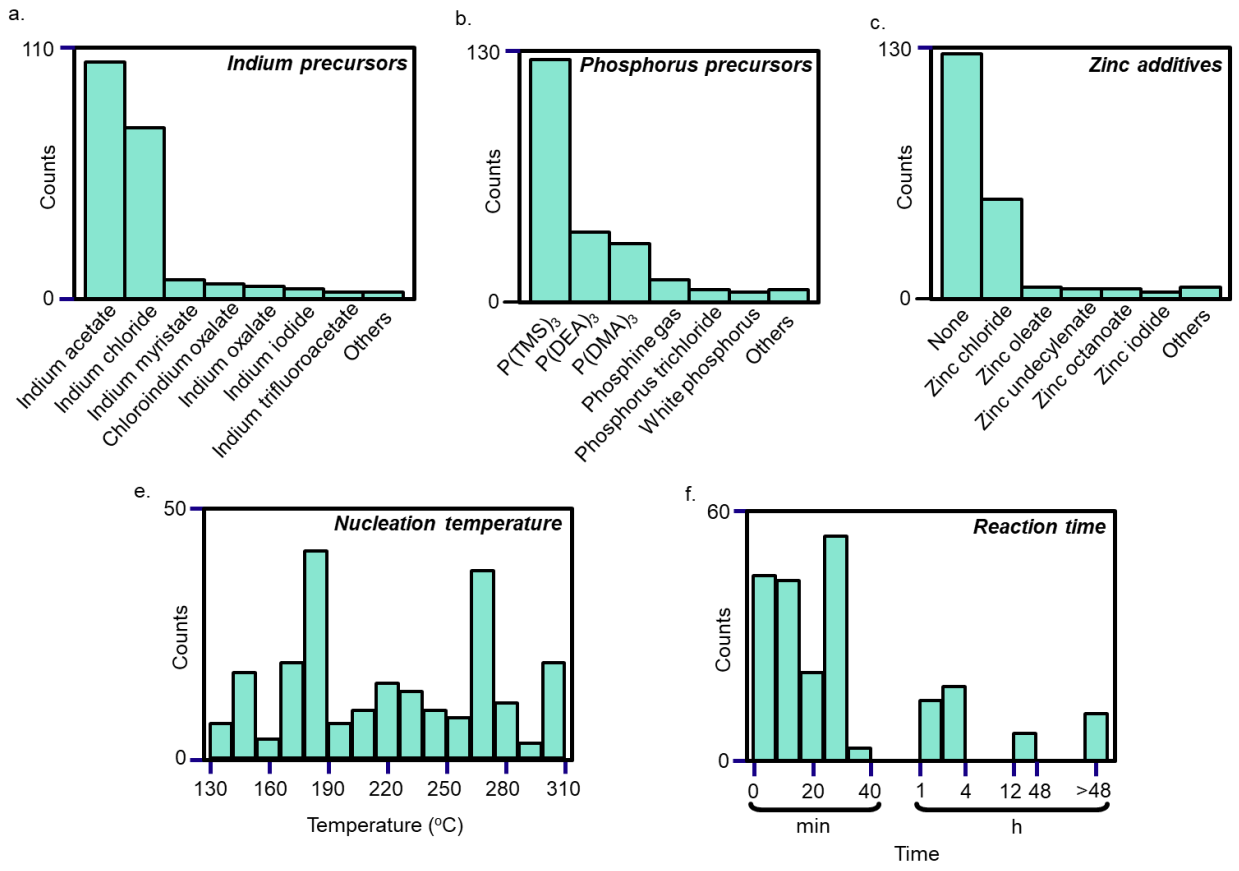

Figure 3.6. Description of the input set. Histograms of indium precursors, phosphorus precursors, zinc additives, nucleation temperature, and reaction time of the syntheses in the initial dataset.

Principal component analysis (PCA, **Figure 3.7.a**) was performed using continuous features in the extended dataset (In amount, P amount, etc.). The scree plot (**Figure 3.7.b**) identifies the three directions (PC1, PC2, and PC3 capturing 29.68, 10.01, and 15.95% of the dataset, respectively) along which the data have the largest spread. The features contributing the most to PC1 are total volume of reaction, solvent amount, and Indium precursor amount; while reaction temperature and phosphorus precursor amount contribute the most to PC2, and reaction time contributes the most to PC3 (**Figure 3.7.c**). When shown as coefficients of PC1 vs PC2 and PC1 vs PC3, no clear relationship between these PCs and absorption wavelengths is observed. The

spanning of syntheses along PC1 indicates that most InP QD syntheses in the dataset were conducted on a similar scale, while there are three syntheses that have a significantly larger scale than the rest of the dataset. The spanning of syntheses along PC3 indicates that most of the syntheses in the dataset were run for a similar duration, owing to their use of the hot injection method (typically less than 1 h), while a portion of the syntheses was run for a much longer time.

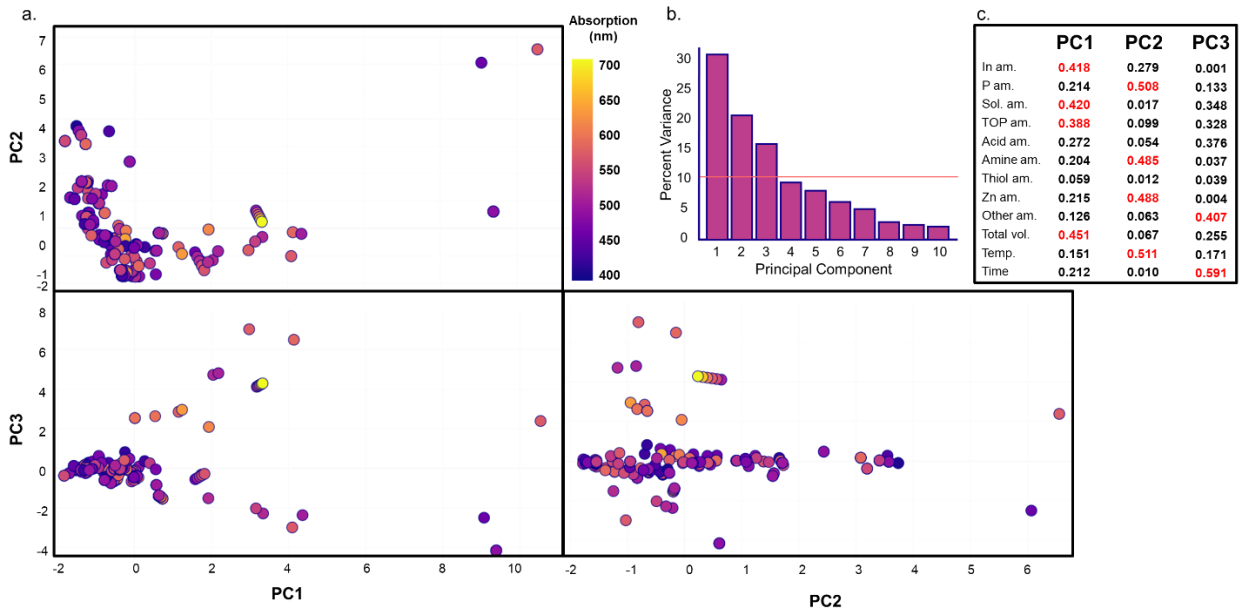

Figure 3.7. Principal component analysis (PCA) of the extended dataset before imputation, where continuous features are considered. **a.** PCA biplots with syntheses plotted in two dimensions using their projections onto the first three principal components (PC). The syntheses are colored according to the absorption wavelength (nm) of the synthetic outcomes. **b.** Scree plot indicating the variance of the PCs when PCA is applied to the dataset. **c.** Table of loadings showing which features contribute the most to the PCs.

The plot of absorption peak versus the emission peak from the datasets before and after imputation (**Figure 3.8.a**) suggests a linear relationship between these two output targets. **Figure 3.8.b** displays the dependence of the Stokes shift on the first excitonic absorption peak. Our

observation from the dataset before imputation (e.g., only reported values) agrees with the size-dependent behavior of Stokes shifts in InP QDs in that Stokes shift increases as QD size decreases or as absorption peak energy increases.[47]

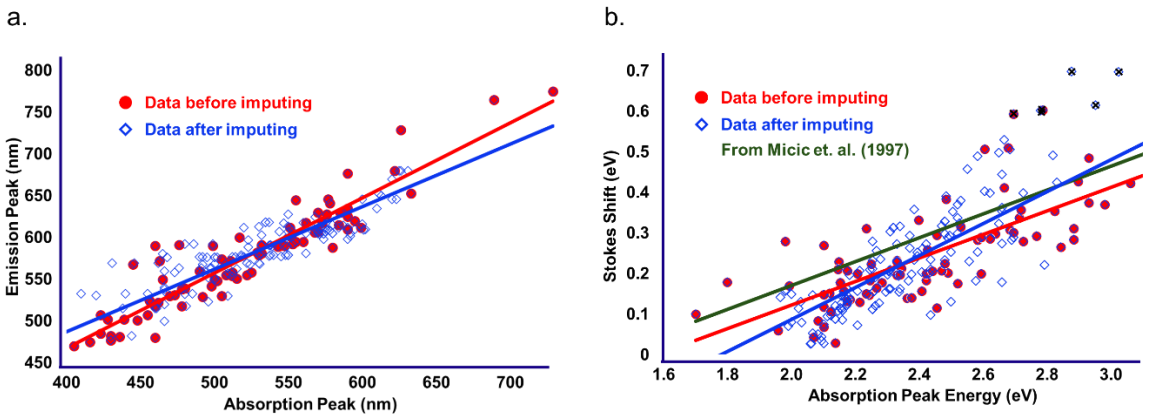

Figure 3.8. Plots and best-fit lines after excluding outliers (indicated by black crosses) for datasets before and after imputation. **a.** Emission peak versus the first excitonic absorption peak in nanometers. **b.** First excitonic absorption energy peak versus Stokes shift (energy difference between emission peak and absorption peak). The green line is from Mićić et al.[47]

In **Figure 3.9**, we plotted the band gap energy versus InP QD size and generated sizing curves from both the initial dataset and the imputed dataset. In the small particle size range (2–4 nm), both curves fit reasonably well with the empirical sizing curve developed by Mićić et al.,[5] the calculated sizing curves from Cho et al.[48] and Baskoutas and Terzis,[49] but the curve after imputing deviates in the larger size range. The inverse square fitted sizing curve for the data before imputing is

$$E_0 = 1.69 + \frac{1}{0.206 \times d^2} \tag{3.1}$$

and the curve for the data after imputing is

$$E_0 = 1.94 + \frac{1}{0.343 \times d^2} \tag{3.2}$$

where E_0 is the band gap in eV and d is the QD diameter in nanometers. The most likely reason for the deviation in the curves at larger sizes is the limited available data for high-quality InP QDs larger than 4 nm. However, challenges associated with sample size polydispersity and surface oxidation may also be convoluting the reported data. It is also interesting to see the difference in the sizing curves before and after imputing in comparison to the empirically derived sizing curve from Mićić. The imputed dataset seems to fit better than the raw dataset in the smallest size regime, but imputation appears to overestimate the band gap in the 2.5–3.5 nm regime in some cases leading to a higher degree of curvature in the line of best fit.

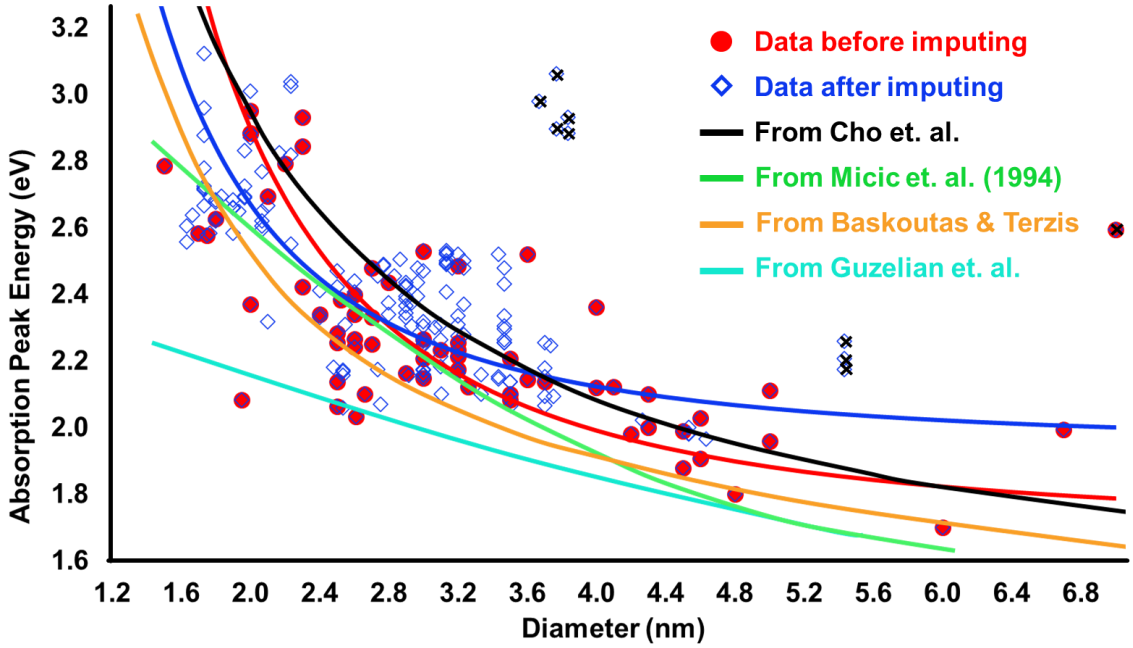

Figure 3.9. Band gap energy (eV) versus InP QD diameter determined by TEM. Red circles represent datapoints from the initial dataset, blue diamonds represent datapoints after the imputation step, and red and blue lines represent the sizing curves for InP QDs using the dataset before and after imputation, respectively, after excluding outliers (indicated by black crosses). The cyan and green lines represent empirical sizing curves developed by Guzelian et al.[50] and

Mićić et al.,[5] respectively. The black line represents the sizing curve calculated using density functional theory by Cho et al.[48] The orange line represents the sizing curved calculated by the potential-morphing method on the effective mass approximation by Basloutas and Terzis.[49]

3.4.2 *Model Performance*

Figure 3.10 shows the performance of the best model for each output in each study case. For most cases, the Extra Trees algorithm outperformed other algorithms. Considering that the datasets in this study are small, unbalanced, and contain noise, randomized tree-based algorithms such as Extra Trees would be expected to perform better than other methods, such as single decision tree or boosting algorithms. The Extra Trees algorithm uses the entire set of learning entries to develop the tree, and the decision rule is selected randomly; therefore, bias in the datasets is minimized.[51]

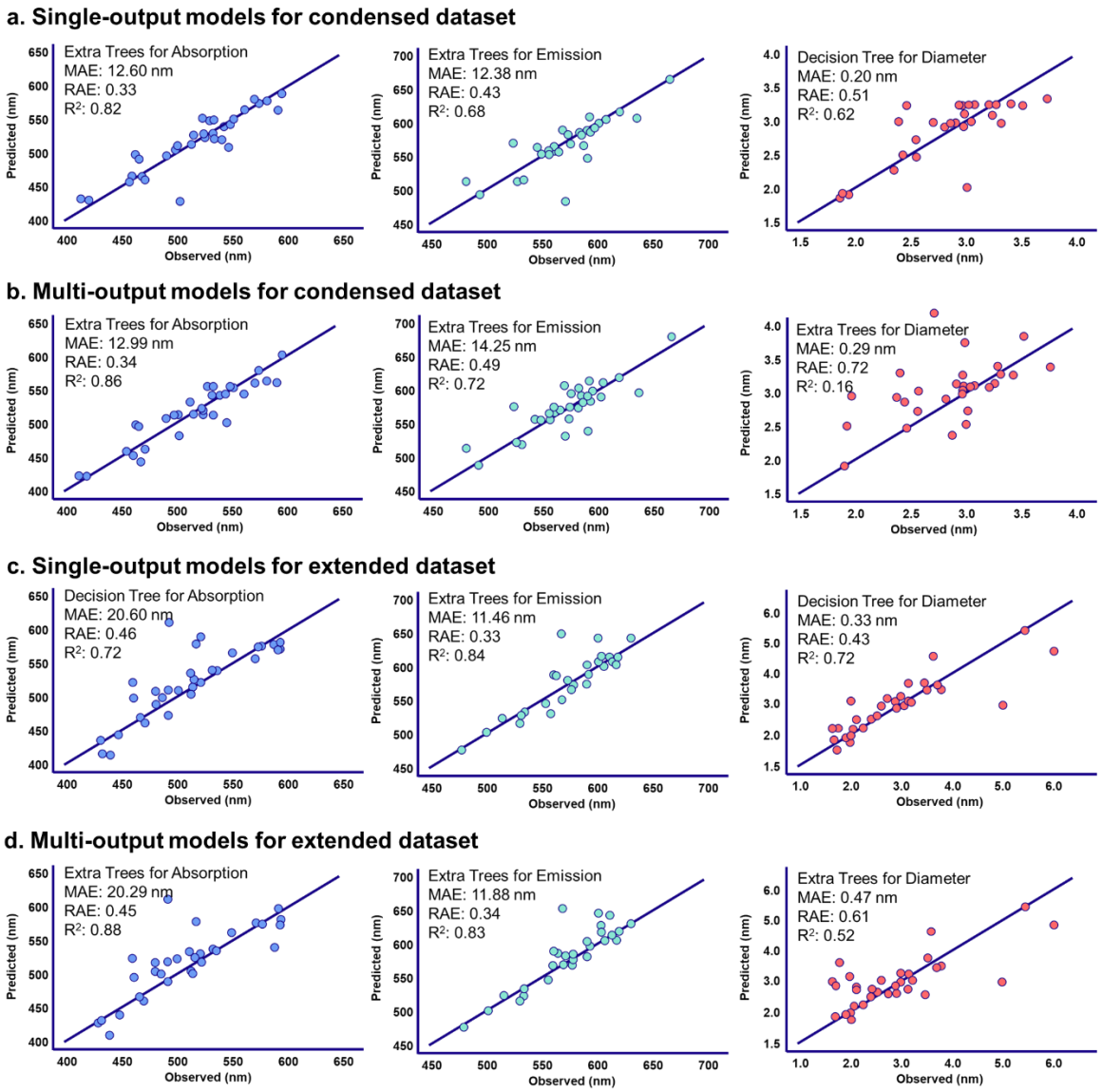

Figure 3.10. Parity plots of observed vs predicted values and error metrics for single-output and multi-output models using the condensed and extended datasets.

Among the three output targets, predictions of emission were the best, followed by absorption, and finally diameter. The differences in predictions among different synthetic outcomes might be attributed to the correlation between the reported outcome values and reported synthetic conditions. Emission and absorption peaks are often used to monitor QD reactions, while particle diameter, determined by TEM, must be done many hours after the synthesis finishes and

most often following purification. Further, the size measurements are usually done manually without established best practices in the community. Therefore, data on particle size is not consistent and hence, more prone to poor correlations with synthetic conditions, leading to poor predictions when synthetic conditions are used as the descriptors.

Although multi-output models were expected to give better predictions due to the strong correlation between the three output targets, single-output models showed better performance for both the condensed and the extended datasets, indicating that assuming a relationship among the output targets did not improve but worsened the predictions. While there seems to be a linear relationship between emission and absorption wavelength (**Figure 3.8.a**), the datasets failed to reflect the expected relationship between particle size and absorption. Thus, for these datasets, using different model selections for each output, would give a better prediction performance.

When comparing the performance of the two descriptor sets using the models that gave the lowest MAEs, models that used the condensed dataset were expected to show better performance since they have lower dimensionality from manually combining some input features while retaining the same information. **Figure 3.10** shows that models using the condensed dataset gave better predictions for absorption wavelength and diameter than models using the extended dataset, while emission prediction accuracy seemed to be similar in both cases. However, for the single-output Decision Tree model for diameter that used the condensed dataset, we saw that many predictions were centered around 3.3 nm for the observed range of 3–4 nm (**Figure 3.10.a**, right). This might be caused by the low complexity of the model and/or oversimplification of the descriptor set, leading to inaccurate predictions when a few input features have a significantly higher influence on the model than others. When the Decision Tree model was applied to the extended dataset with similar complexity, this behavior seemed to be eliminated (**Figure 3.10.c**,

right). Thus, we note that to improve ML model performance for QD synthesis, oversimplification of feature engineering must be carefully considered as it may directly affect the prediction accuracy.

3.4.3 *Validation*

Applying a complex algorithm to a small dataset can result in significant overfitting that leads to misleading predictions. Here, we used different methods, statistically and experimentally, to detect overfitting and test the accuracy of our ML models.

3.4.3.1 Stratified k-Fold Validation

We first used the stratified k-fold validation method on both the condensed dataset and the extended dataset to justify the accuracy of our ML models. The datapoints were divided into five groups based on their emission wavelength output to ensure that test sets are uniformly sampled across the dataset (**Figure 3.11**). Then, a stratified test/train split of the dataset was performed to achieve a ratio of 15/85, consistent with the ratio used in this study. For the four cases, we applied the same ML algorithms as shown in **Figure 3.10** and evaluated their performance by MAEs. **Figure 3.12** indicates that the accuracy of all models was consistent over five iterations, and no considerable overfitting was observed. It should be noted that the hyperparameters used in the models for this validation step were adopted from the models in **Figure 3.10**.

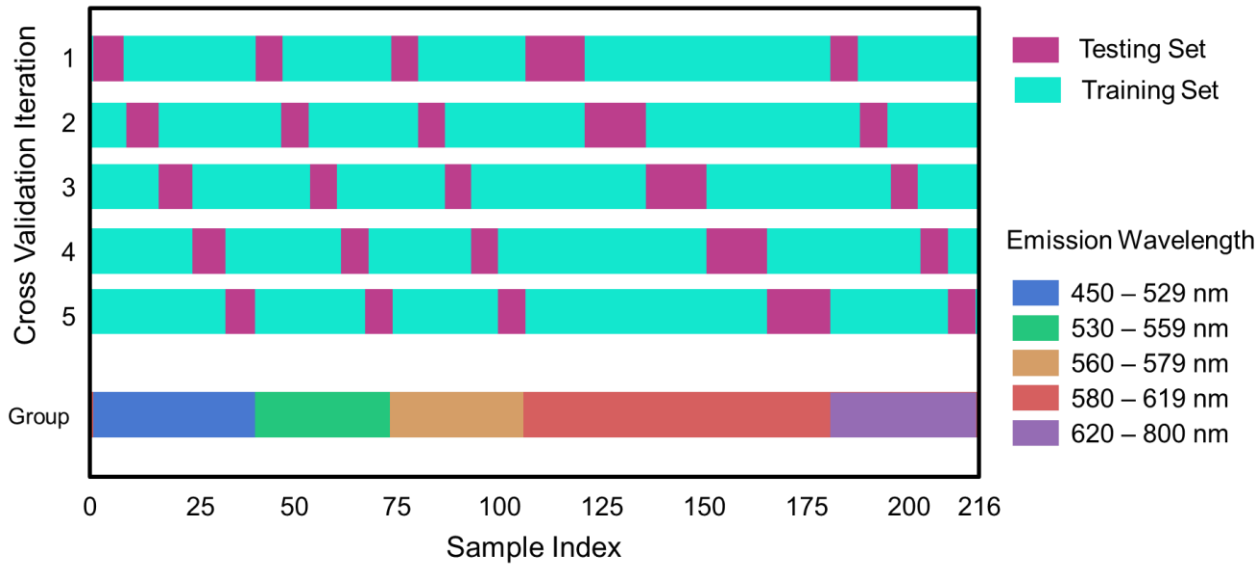

Figure 3.11. Visualization of the stratified k-fold validation.

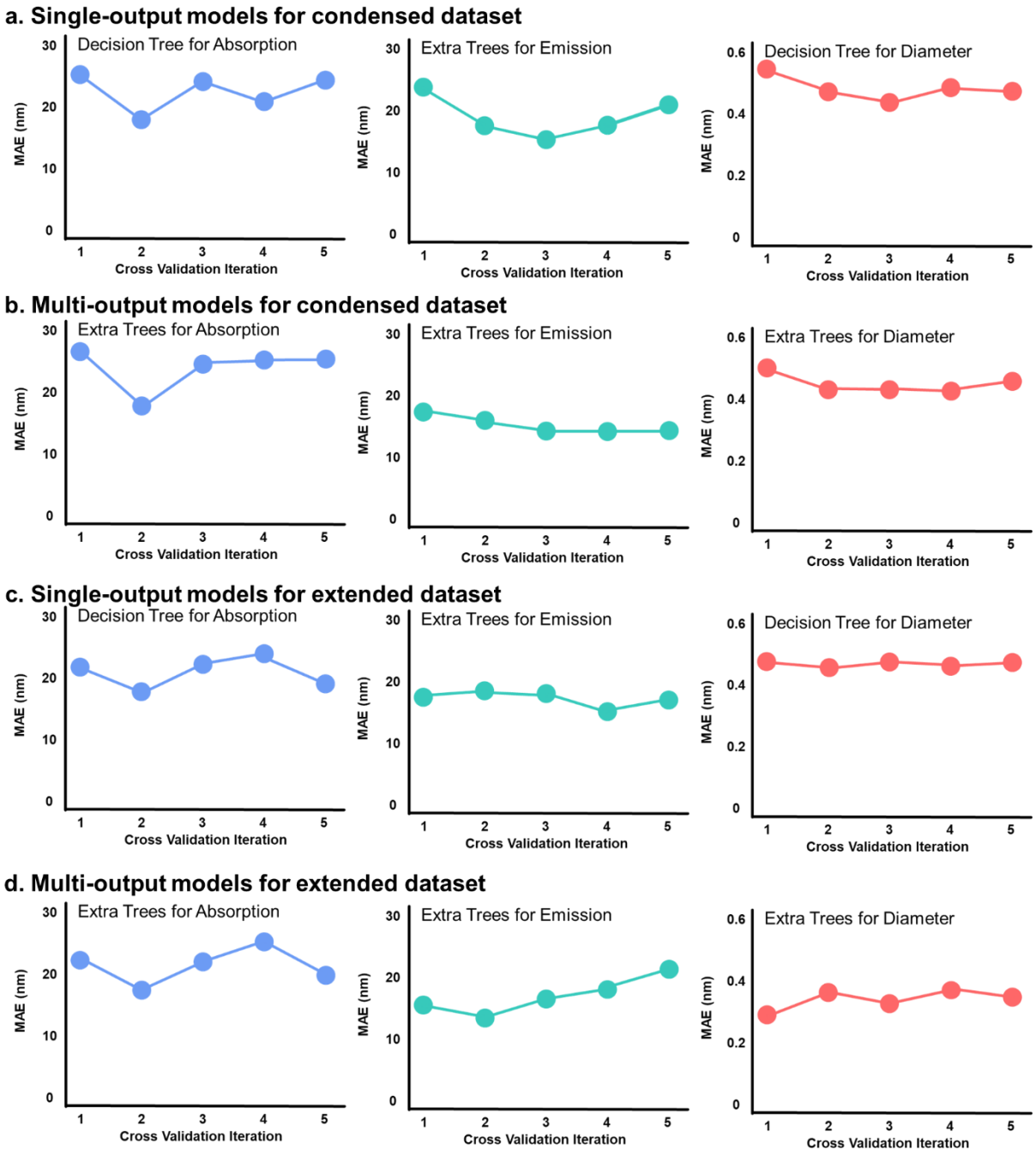

Figure 3.12. Mean absolute errors over five iterations of stratified k-fold validation.

3.4.3.2 Comparison with Nonimputed Models.

Next, we trained and tested models with the initial or nonimputed datasets. Due to the small dataset size (205 datapoints for absorption, 85 datapoints for emission, and 72 datapoints for

diameter), predictions using the nonimputed datasets gave higher errors especially for emission and diameter targets (**Figure 3.13**). This result indicates that it is necessary to effectively impute the missing data to improve the performance of predictive models for QD synthesis when the available datasets are limited.

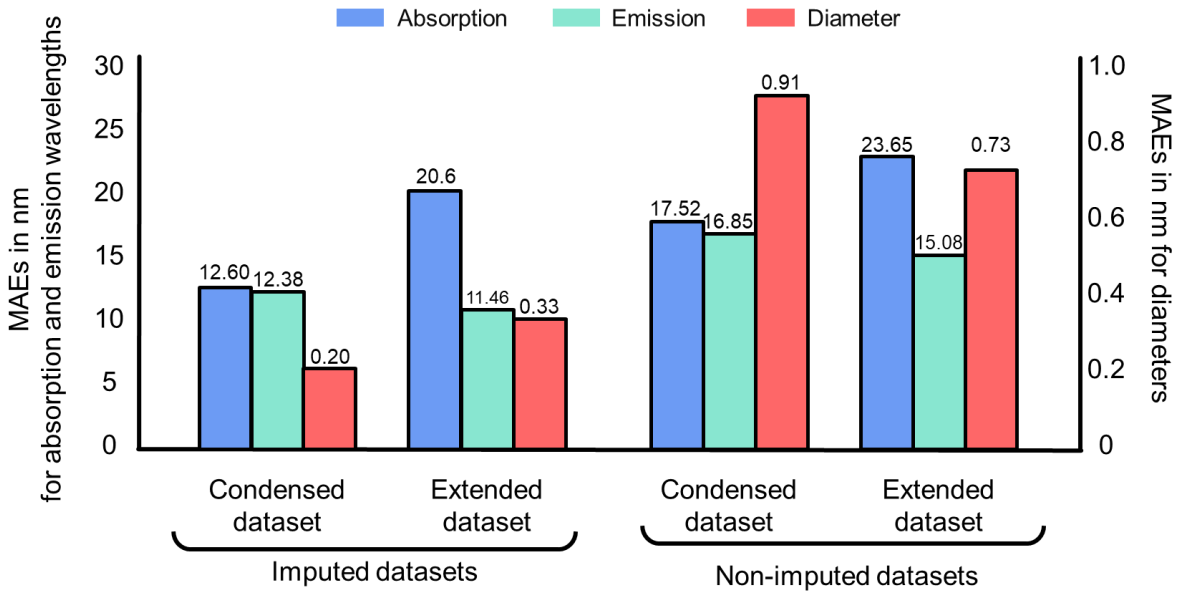

Figure 3.13. Performance comparison of models using the imputed datasets and the nonimputed datasets.

3.4.3.3 Comparison with Experimental Data.

To further test the practical accuracy of the models, we conducted a series of eight InP QD syntheses. The synthetic procedures were designed by varying the reaction conditions of existing syntheses of InP QDs found in the literature such that they would not be entries in the initial dataset and not be easily extrapolated from the original reports. The QDs from each synthesis were characterized by UV–vis and photoluminescence spectroscopy, and the particle sizes were determined by TEM analysis. Only five out of eight batches of InP QDs showed strong luminescence because as-prepared InP NCs generally exhibit poor luminescence due to

nonradiative channels originating from surface states. The parity plots in **Figure 3.14** show that the models correctly predicted the actual synthetic outcomes in many cases. While predictions of experimental absorption and particle size had similar accuracy as the test sets, MAEs for emission predictions were high because there were only five datapoints for emission and MAEs are sensitive to large errors. It should be noted that models using the extended dataset had a much better performance than the models using the condensed dataset for prediction of particle size.

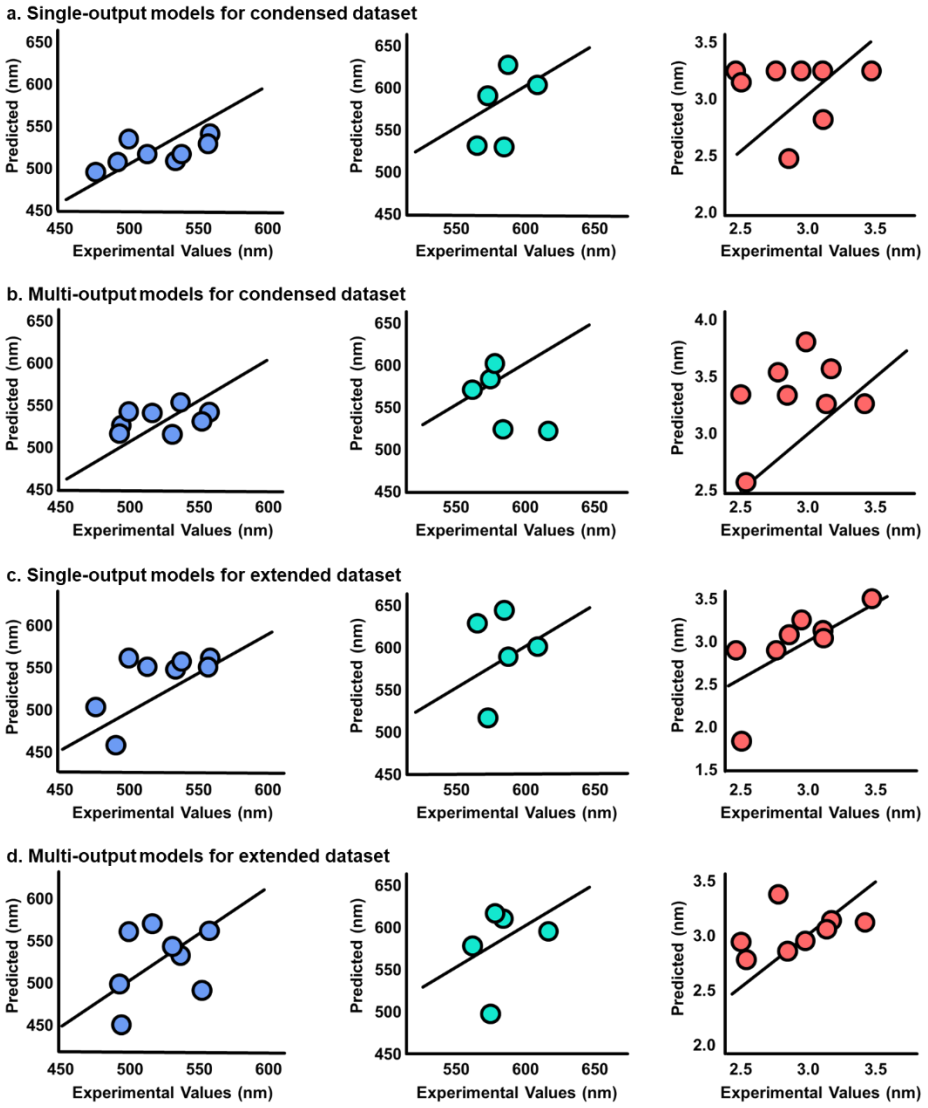

Figure 3.14. Parity plots of experimental values vs. predicted values from the ML models.

3.4.4 *Interactive User Interface.*

To allow external users, including researchers with no background in machine learning, to use our model to predict InP QDs synthesis outcomes and explore new synthetic methods, we deployed a user interface using an open-source Python library provided by Streamlit.[52] Streamlit is a framework for building interactive web applications with user-friendly components such as buttons, sliders, and plots. From the best ML models in this study, we deployed a Streamlit web app that enabled real-time reaction analysis and prediction https://share.streamlit.io/cossairt-lab/indium-phosphide/Hot_injection/hot_injection_prediction.py. The web app includes sections where users answer questions about QD synthetic conditions to get a prediction of diameter, emission, and the first excitonic absorption peak with a prediction interval as uncertainty. We anticipate that this web app will enable more chemical insights into InP synthesis from machine learning. Although the best models from this study were used, inaccurate predictions, i.e., absorption wavelength higher than emission wavelength, can sometimes be seen from the web app due to inconsistency and low synthesis variety in the dataset. We expect the performance of the web app to improve when a larger dataset becomes available.

3.4.5 *Synthetic Insights.*

Using the best model for our four study cases, we calculated the feature importance of each model. Feature importance reflects the extent to which a variable is used for accurate predictions (i.e., the more a model uses a variable, the more important it is). Specifically in the case of Extra Trees and Decision Tree algorithms, feature importance is computed as the normalized total reduction of the criterion brought by that feature, which is also known as the Gini importance. As expected, temperature and time were found to be most important in all cases as they directly

influence nucleation and growth kinetics. Interestingly, the presence of zinc additives also played an important role (**Figure 3.15**), consistent with the reported observations of spectral shifts and size changes when a zinc salt is present in the synthesis.[45, 53]

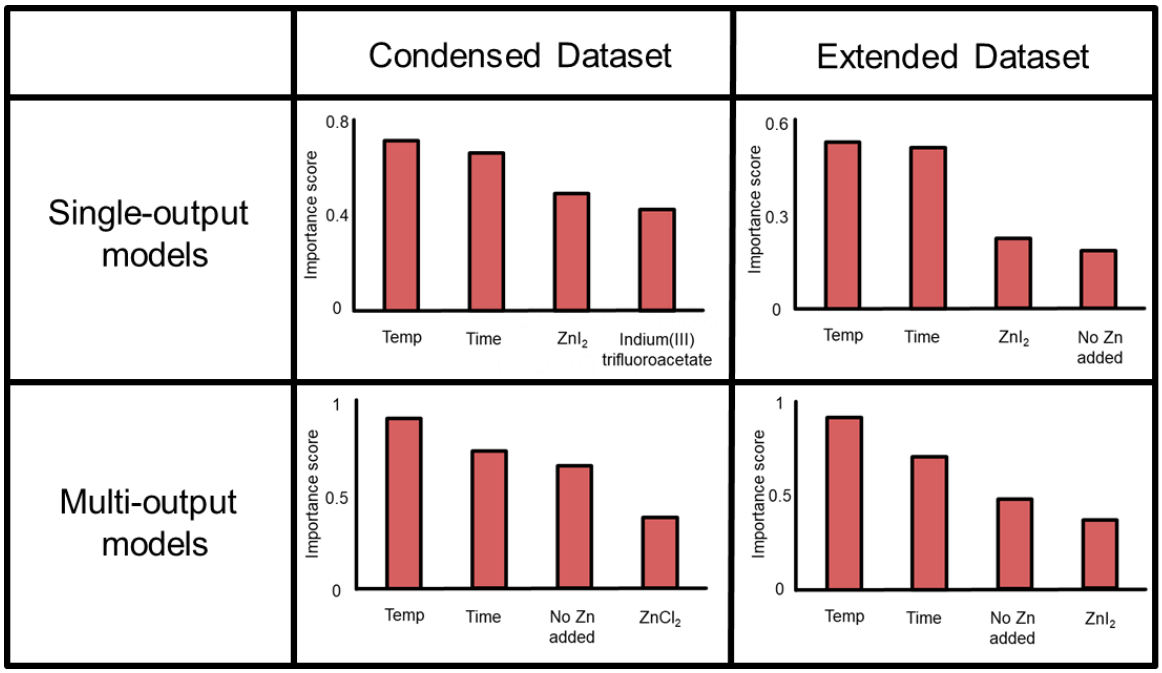

Figure 3.15. Feature importance charts for the best model in each study case.

As discussed in the above section, the web app allowed us to explore the chemical intuition of our algorithms beyond basic statistical metrics and discover synthetic trends without conducting actual experiments. For example, predicted outcomes from the web app suggested that for a typical hot injection synthesis where $InCl_3$ reacts with tris(diethylamino)phosphine, the presence of TOP red-shifts the emission and absorption maxima, while the presence of a zinc halide salt results in spectral blueshifts (**Figure 3.16**). These observations are consistent with the reported literature.[45, 54]

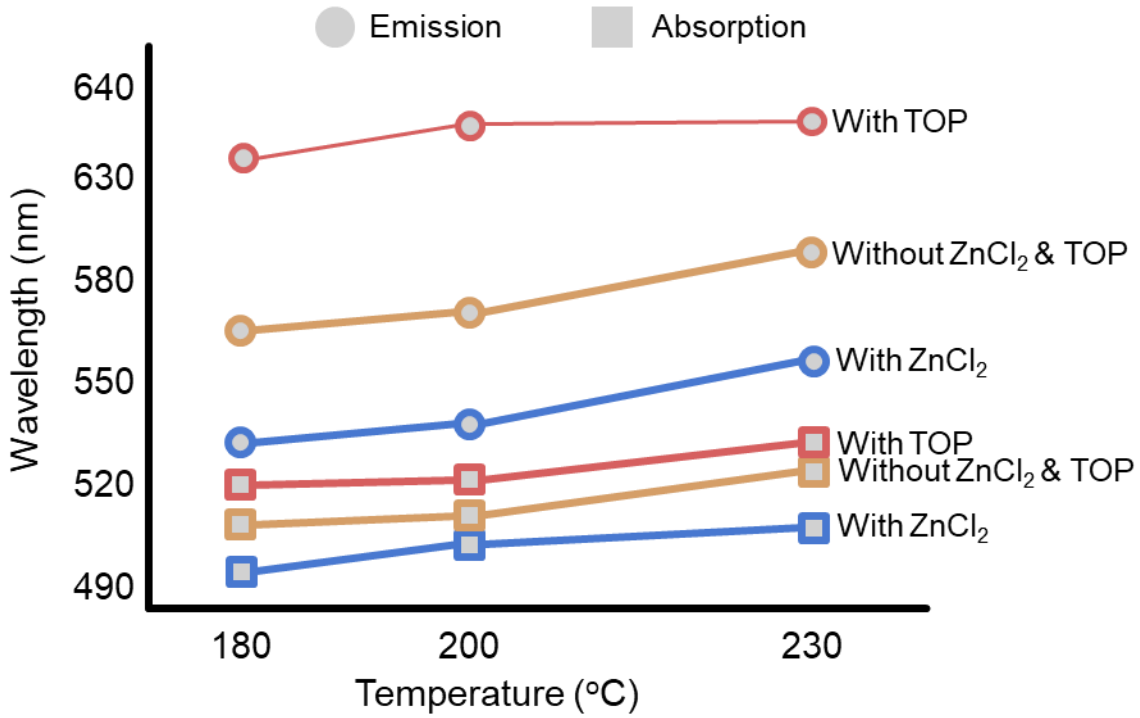

Figure 3.16. Predicted emission (circles) and absorption (squares) wavelengths from the Streamlit web app using single-output algorithms and the condensed dataset with all methods. Reaction conditions include 0.1 mmol of $InCl_3$, 1 mL of oleylamine, 0.15 mmol of $P(DEA)_3$, nucleation temperature at 180 °C, reaction time of 2 min, with 0.3 mmol of $ZnCl_2$ (blue outlines), or with 0.2 mL TOP (red outlines), or without both $ZnCl_2$ and TOP (yellow outlines).

3.4.6 *Limitations.*

Despite their accuracy, there are several inevitable limitations of the ML models that arise from the available data and the nature of QD synthesis. The novelty of this study is based on the collection, imputation, and ML training of reported data in the literature; however, the presence of unknown or unreported contaminants and the related lack of standardization in reporting data in the literature heavily influence these ML results. Many publications did not report details of the synthesis, which significantly decreases the size of the dataset despite the large number of

published reports of InP QD synthesis in the past decades. Other synthetic parameters that also affect the synthetic outcomes but are often not mentioned include injection rate,[55] solvent and precursor purity,[56,57] and QD purification status and methods.[58-60] Moreover, heterogeneity of experimental conditions in different labs also impacts synthetic outcomes. For example, it has been shown that the presence of trace water can affect the size of InP QDs.[61,62] Another inconsistency in reporting synthetic results comes from uncertainties associated with using TEM to determine particle size and size distribution. As discussed in detail by Pyrz and Buttrey,[63] many decisions during image acquisition and size determination can lead to over- and underestimation of particle size, especially for smaller particles. Those decisions include optimization of measurement resolution, limiting electron beam damage, proper determination of particle boundaries, and reliable quantification of particle size distributions. Data diversification plays an important role in the performance of ML models. In this study, a diverse dataset that consists of many syntheses of a variety of particle sizes or emission peaks would help improve ML model performance. However, since the synthesis of blue-emitting (< 480 nm) or small InP QDs is still challenging, and current applications of InP often make use of QDs in the size range of 2–4 nm, the data inevitably concentrated around a small range of particle sizes, leading to less accurate predictions for the synthesis of QDs outside of that range. Furthermore, at this time, our system does not allow for exploration of new precursors or reagents.

3.5 Applications.

3.5.1 *Predicting InP QD Hot Injection Synthesis Outcomes*.

We applied the process of data preparation, data imputation, and ML training from this study to other datasets with similar size. First, we prepared new condensed and extended datasets

that have only hot injection syntheses by filtering our initial datasets. These new datasets contained 157 syntheses. The results (**Table 3.1**) showed improvement in R^2 values for all outputs and lower MAEs for emission predictions but demonstrated modest differences in MAEs for diameter and absorption wavelength. Similar to the previous observation, models using the condensed dataset and single-output algorithms have better performance than models using the extended dataset and multi-output algorithms, respectively. It should be noted that single-output algorithms using the hot injection dataset could achieve MAEs as low as 0.13 nm for diameter and 6.39 nm for emission wavelength predictions (**Figure 3.17**). The algorithms were also able to identify temperature and time as the most influential parameters that affect the synthetic outcomes (**Figure 3.18**).

Table 3.1. Performance of the Best Algorithms Using the Hot Injection Dataset (Output: Model/MAE in nm/R^2)

	Condensed dataset	**Extended dataset**
Single-output models	absorption: Extra Trees/15.61/0.83	absorption: Decision Tree/15.89/0.86
	emission: Extra Trees/6.39/0.86	emission: Decision Tree/9.88/0.82
	diameter: Decision Tree/0.23/0.79	diameter: Extra Trees/0.13/0.85
Multi-output models	absorption: Extra Trees/17.91/0.85	absorption: Extra Trees/18.22/0.82
	emission: Extra Trees/7.27/0.88	emission: Extra Trees/12.09/0.72
	diameter: Extra Trees/0.50/0.25	diameter: Extra Trees/0.16/0.61

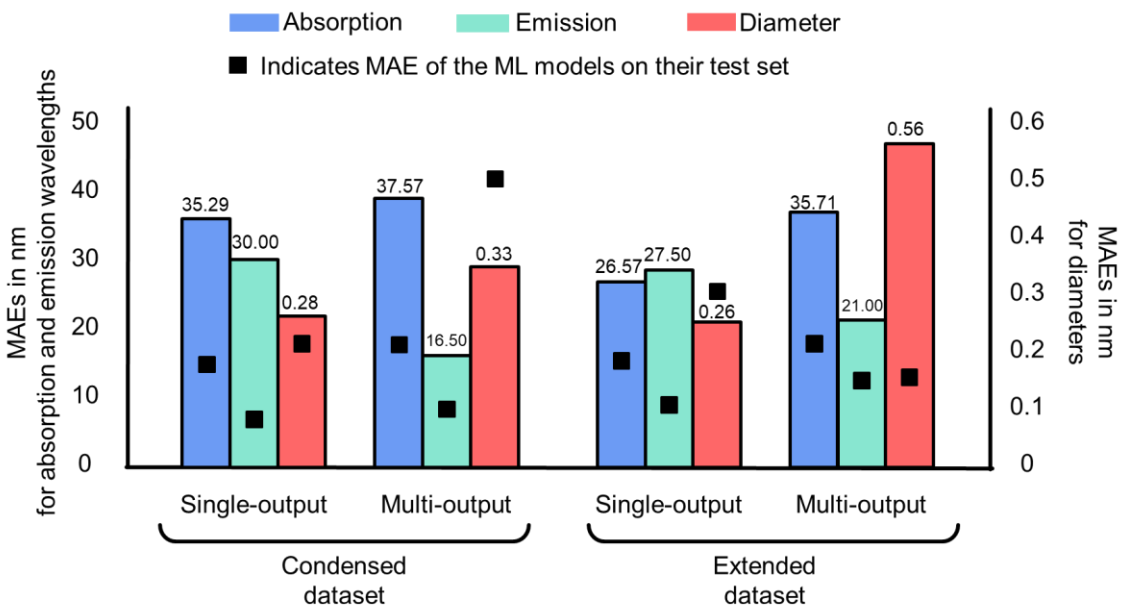

Figure 3.17. Mean absolute errors (MAE) in nm of model predictions vs experimental results. Algorithms used the datasets with only hot injection method. Black squares indicate MAEs of the models on their test set.

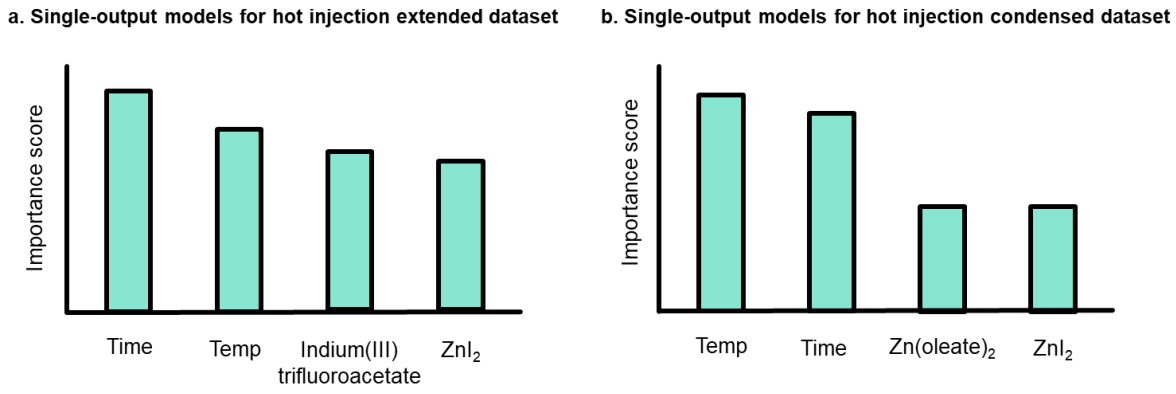

Figure 3.18. Feature importance of the best model for single-output models using the hot injection datasets.

3.5.2 *Predicting CdSe QD Hot Injection Synthesis Outcomes*.

To further evaluate the reliability and show the utility of the imputing method for small datasets, we revised and extended the CdSe QD dataset from Baum et al.[25] to include absorption and emission wavelengths in the output set. The revised dataset contained 233 hot injection syntheses of CdSe QDs, in which the absorption wavelength is absent in 38 syntheses (16%) and the emission wavelength is absent in 77 syntheses (33%). The dataset preprocessing, data imputation, model tuning, model training, and user interface creation were done in the same manner as the InP study. For feature selection, we reduced the number of input features from 27 to 15 since models with fewer input variables typically give better performance.[30] Compared to the InP models for the hot injection dataset, the CdSe models showed better performance for all three output features, especially for diameter. This is likely a result of the original study's focus on diameter, whose values were not limited to TEM measurements but were also calculated from absorption spectra. Further, a much smaller portion of the dataset was missing absorption and emission entries, perhaps reflecting the inherent poor emissivity of InP QDs, thus reducing prediction bias. Results from the hot injection models also showed that single-output models outperformed multi-output models with MAEs as low as 14.67, 8.37, and 0.18 nm for absorption wavelength, emission wavelength, and particle diameter, respectively. R^2 values for diameter from the Extra Trees and Decision Tree algorithms are comparable to the value from the reported Gradient Boosting Machine algorithm (**Figure 3.19**).[25] Examining feature importance in our study showed that reaction time and growth temperature are the most influential factors in the synthesis of CdSe QDs. This is consistent with the Gradient Boosting Machine model from Baum et al.; however, in this study, the two most important variables have a significantly higher influence on the synthesis than other variables (**Figure 3.20**).

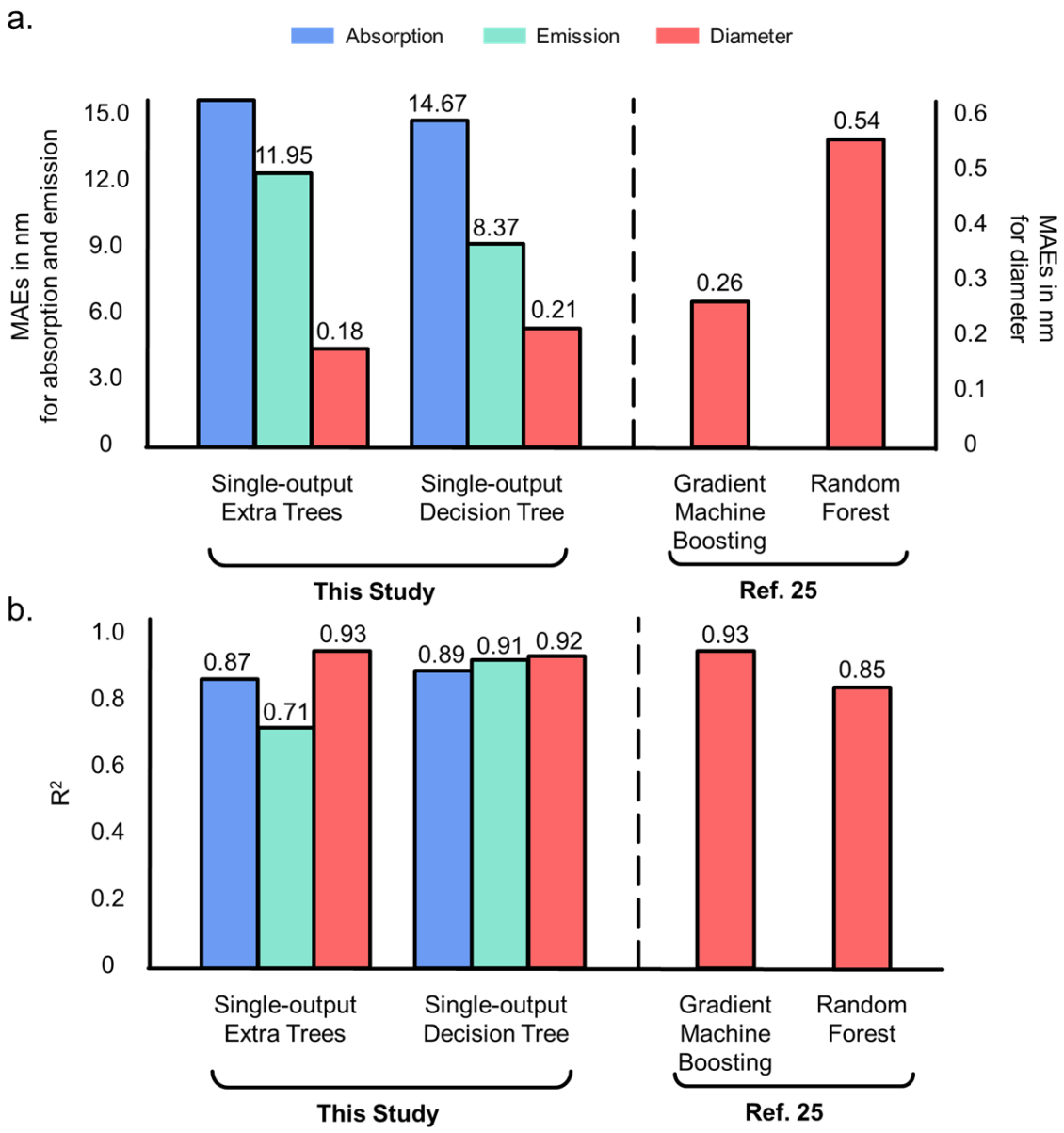

Figure 3.19. a. MAEs and **b.** R^2 values comparison of the two models between this study and ref 25.[25]

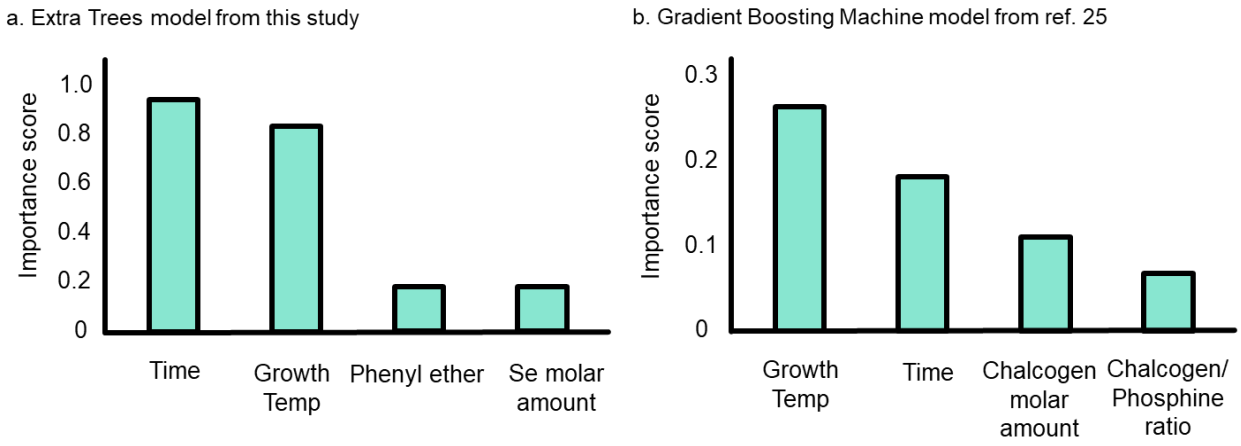

Figure 3.20. Feature importance charts of the **a.** Extra Trees model from this study and **b.** Gradient Boosting Machine model from ref 25.[25]

3.5.3 *Inverse Design Using the Streamlit User Interface*.

Finally, we targeted 600 nm–absorbing InP QDs using synthetic conditions and precursors from an existing procedure.[64] Using the Streamlit web app, we entered the synthetic conditions from the procedure, modified chemicals to what were available to us, and adjusted the reaction temperature and time to achieve the desired synthetic outcome. We conducted the experiment and were able to synthesize InP QDs with desired optical properties with high accuracy (**Figure 3.21**). For absorption and emission wavelengths, we also found that there was a noticeable difference between samples before and after purification. This observation justifies our previous hypotheses that the inconsistency from reported values from the literature can strongly affect the accuracy of prediction, that our syntheses were a mix of purified and in situ data entries, and that there are many unreported factors that can also play a role in achieving precise optical properties.

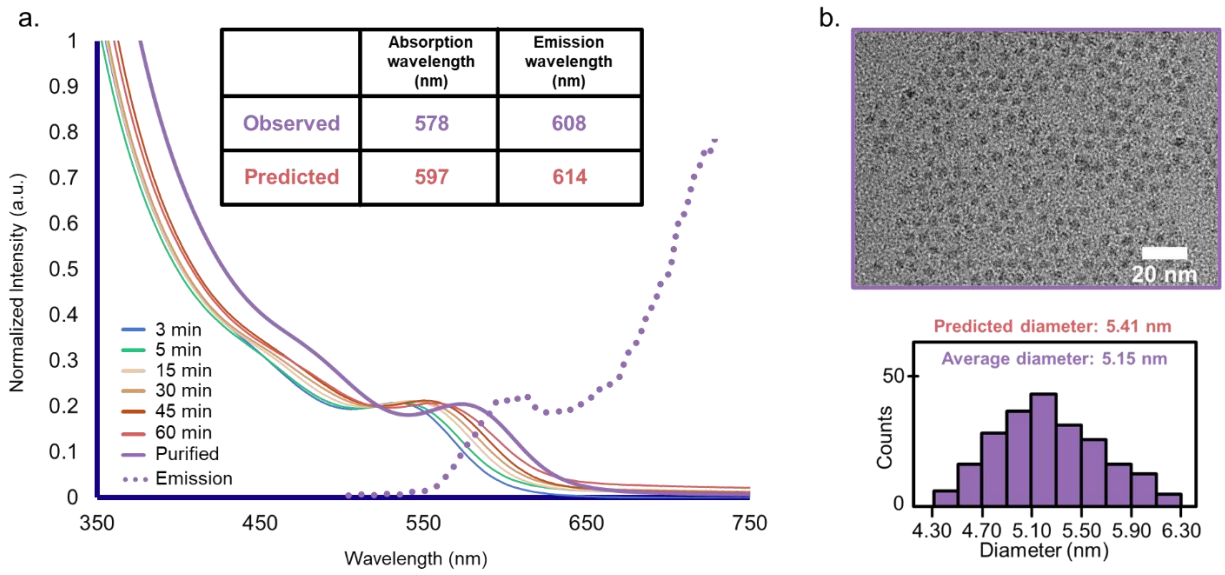

Figure 3.21. **a.** UV–vis spectra of timed aliquots and emission spectrum of the purified product from the reaction using 0.40 mmol of indium acetate, 1.45 mmol of myristic acid, and 0.20 mmol of $P(SiMe_3)_3$ injected at 315 °C. The nucleation temperature was 310 °C. **b.**TEM image of the purified particles with an average diameter of 5.15 nm.

3.6 CONCLUSION

We have trained and used ML models to predict the properties of InP QDs based on synthetic conditions. The descriptor space was defined in two ways (condensed and extended) to study the best approach for predicting QD synthesis outcomes where the available data is limited. We tested single-output and multi-output ML algorithms and found that single-output models showed enhanced performance over the multi-output models despite the physical relationships among the output targets (diameter, absorption and emission wavelengths). The performance of the models was validated in different ways, including stratified *k*-fold validation, comparison with nonimputed datasets, and comparison with newly collected experimental data. From the model estimation errors, we found that reaction temperature, time, and the addition of zinc salts were the

most influential synthetic parameters. The same dataset preprocessing, imputation, and ML training were applied to both InP and CdSe hot injection datasets, resulting in accurate predictions for these two cases. Furthermore, we deployed a web app that employs our best algorithms so that external users can use them to predict InP and CdSe synthetic outcomes. Using this web app, we were able to test our models with newly adapted InP syntheses that targeted and achieved desired optical properties. The web apps also allowed us to investigate the limitations of the ML approach in this study. Because the algorithms cannot recognize new precursors, reaction conditions need to be closely based on existing procedures to obtain accurate predictions. Overall, this work provides a procedure to preprocess datasets, train ML models, and implement models for public users in the field of nanocrystal synthesis, especially where available datasets are small and incomplete.

3.7 REFERENCES

(1) Eren, G. O.; Sadeghi, S.; Bahmani Jalali, H.; Ritter, M.; Han, M.; Baylam, I.; Melikov, R.; Onal, A.; Oz, F.; Sahin, M.; Ow-Yang, C. W.; Sennaroglu, A.; Lechner, R. T.; Nizamoglu, S. Cadmium-Free and Efficient Type-II InP/ZnO/ZnS Quantum Dots and Their Application for LEDs. *ACS Appl. Mater. Interfaces* **2021**, *13*, 32022–32030. https://doi.org/10.1021/acsami.1c08118.

(2) Sadeghi, S.; Bahmani Jalali, H.; Melikov, R.; Ganesh Kumar, B.; Mohammadi Aria, M.; Ow-Yang, C. W.; Nizamoglu, S. Stokes-Shift-Engineered Indium Phosphide Quantum Dots for Efficient Luminescent Solar Concentrators. *ACS Appl. Mater. Interfaces* **2018**, *10*, 12975–12982. https://doi.org/10.1021/acsami.7b19144.

(3) Saeboe, A. M.; Nikiforov, A. Yu.; Toufanian, R.; Kays, J. C.; Chern, M.; Casas, J. P.; Han, K.; Piryatinski, A.; Jones, D.; Dennis, A. M. Extending the Near-Infrared Emission Range of Indium Phosphide Quantum Dots for Multiplexed In Vivo Imaging. *Nano Lett.* **2021**, *21*, 3271–3279. https://doi.org/10.1021/acs.nanolett.1c00600.

(4) Kim, Y.; Chang, J. H.; Choi, H.; Kim, Y.-H.; Bae, W. K.; Jeong, S. III–V Colloidal Nanocrystals: Control of Covalent Surfaces. *Chem. Sci.* **2020**, *11*, 913–922. https://doi.org/10.1039/C9SC04290C.

(5) Mićić, O. I.; Curtis, C. J.; Jones, K. M.; Sprague, J. R.; Nozik, A. J. Synthesis and Characterization of InP Quantum Dots. *J. Phys. Chem. A* **1994**, *98*, 4966–4969. https://doi.org/10.1021/j100070a004.

(6) Battaglia, D.; Peng, X. Formation of High Quality InP and InAs Nanocrystals in a Noncoordinating Solvent. *Nano Lett.* **2002**, *2*, 1027–1030. https://doi.org/10.1021/nl025687v.

(7) Gary, D. C.; Flowers, S. E.; Kaminsky, W.; Petrone, A.; Li, X.; Cossairt, B. M. Single-Crystal and Electronic Structure of a 1.3 Nm Indium Phosphide Nanocluster. *J. Am. Chem. Soc.* **2016**, *138*, 1510–1513. https://doi.org/10.1021/jacs.5b13214.

(8) Cossairt, B. M. Shining Light on Indium Phosphide Quantum Dots: Understanding the Interplay among Precursor Conversion, Nucleation, and Growth. *Chem. Mater.* **2016**, *28*, 7181–7189. https://doi.org/10.1021/acs.chemmater.6b03408.

(9) Gerbec, J. A.; Magana, D.; Washington, A.; Strouse, G. F. Microwave-Enhanced Reaction Rates for Nanoparticle Synthesis. *J. Am. Chem. Soc.* **2005**, *127*, 15791–15800. https://doi.org/10.1021/ja052463g.

(10) Tessier, M. D.; Dupont, D.; De Nolf, K.; De Roo, J.; Hens, Z. Economic and Size-Tunable Synthesis of InP/ZnE (E = S, Se) Colloidal Quantum Dots. *Chem. Mater.* **2015**, *27*, 4893–4898. https://doi.org/10.1021/acs.chemmater.5b02138.

(11) Harris, D. K.; Bawendi, M. G. Improved Precursor Chemistry for the Synthesis of III–V Quantum Dots. *J. Am. Chem. Soc.* **2012**, *134*, 20211–20213. https://doi.org/10.1021/ja309863n.

(12) Vinokurov, A. A.; Dorofeev, S. G.; Znamenkov, K. O.; Panfilova, A. V.; Kuznetsova, T. A. Synthesis of InP Quantum Dots in Dodecylamine from Phosphine and Indium(III) Chloride. *Mendeleev Commun.* **2010**, *20*, 31–32. https://doi.org/10.1016/j.mencom.2010.01.012.

(13) Bang, E.; Choi, Y.; Cho, J.; Suh, Y.-H.; Ban, H. W.; Son, J. S.; Park, J. Large-Scale Synthesis of Highly Luminescent InP@ZnS Quantum Dots Using Elemental Phosphorus Precursor. *Chem. Mater.* **2017**, *29*, 4236–4243. https://doi.org/10.1021/acs.chemmater.7b00254.

(14) Schmidt, J.; Marques, M. R. G.; Botti, S.; Marques, M. A. L. Recent Advances and Applications of Machine Learning in Solid-State Materials Science. *Npj Comput. Mater.* **2019**, *5*, 83. https://doi.org/10.1038/s41524-019-0221-0.

(15) Jensen, Z.; Kim, E.; Kwon, S.; Gani, T. Z. H.; Román-Leshkov, Y.; Moliner, M.; Corma, A.; Olivetti, E. A Machine Learning Approach to Zeolite Synthesis Enabled by Automatic Literature Data Extraction. *ACS Cent. Sci.* **2019**, *5*, 892–899. https://doi.org/10.1021/acscentsci.9b00193.

(16) Mukaddem, K. T.; Beard, E. J.; Yildirim, B.; Cole, J. M. ImageDataExtractor: A Tool To Extract and Quantify Data from Microscopy Images. *J. Chem. Inf. Model.* **2020**, *60*, 2492–2509. https://doi.org/10.1021/acs.jcim.9b00734.

(17) Li, Z.; Najeeb, M. A.; Alves, L.; Sherman, A. Z.; Shekar, V.; Cruz Parrilla, P.; Pendleton, I. M.; Wang, W.; Nega, P. W.; Zeller, M.; Schrier, J.; Norquist, A. J.; Chan, E. M. Robot-

Accelerated Perovskite Investigation and Discovery. *Chem. Mater*. **2020**, *32*, 5650–5663. https://doi.org/10.1021/acs.chemmater.0c01153.

(18) Masood, H.; Toe, C. Y.; Teoh, W. Y.; Sethu, V.; Amal, R. Machine Learning for Accelerated Discovery of Solar Photocatalysts. *ACS Catal*. **2019**, *9*, 11774–11787. https://doi.org/10.1021/acscatal.9b02531.

(19) Vasylenko, A.; Gamon, J.; Duff, B. B.; Gusev, V. V.; Daniels, L. M.; Zanella, M.; Shin, J. F.; Sharp, P. M.; Morscher, A.; Chen, R.; Neale, A. R.; Hardwick, L. J.; Claridge, J. B.; Blanc, F.; Gaultois, M. W.; Dyer, M. S.; Rosseinsky, M. J. Element Selection for Crystalline Inorganic Solid Discovery Guided by Unsupervised Machine Learning of Experimentally Explored Chemistry. *Nat. Commun.* **2021**, *12*, 5561. https://doi.org/10.1038/s41467-021-25343-7.

(20) Epps, R. W.; Bowen, M. S.; Volk, A. A.; Abdel-Latif, K.; Han, S.; Reyes, K. G.; Amassian, A.; Abolhasani, M. Artificial Chemist: An Autonomous Quantum Dot Synthesis Bot. *Adv. Mater.* **2020**, *32*, 2001626. https://doi.org/10.1002/adma.202001626.

(21) Zhou, Z.; Li, X.; Zare, R. N. Optimizing Chemical Reactions with Deep Reinforcement Learning. *ACS Cent. Sci*. **2017**, *3*, 1337–1344. https://doi.org/10.1021/acscentsci.7b00492.

(22) Kim, J. Y.; Steeves, A. H.; Kulik, H. J. Harnessing Organic Ligand Libraries for First-Principles Inorganic Discovery: Indium Phosphide Quantum Dot Precursor Design Strategies. *Chem. Mater*. **2017**, *29*, 3632–3643. https://doi.org/10.1021/acs.chemmater.7b00472.

(23) Meng, F.; Li, Y.; Wang, D. Predicting Atomic-Level Reaction Mechanisms for SN2 Reactions via Machine Learning. *J. Chem. Phys.* **2021**, *155*, 224111. https://doi.org/10.1063/5.0074422

(24) Komp, E.; Valleau, S. Machine Learning Quantum Reaction Rate Constants. *J. Phys. Chem. A* **2020**, *124*, 8607–8613. https://doi.org/10.1021/acs.jpca.0c05992.

(25) Baum, F.; Pretto, T.; Köche, A.; Santos, M. J. L. Machine Learning Tools to Predict Hot Injection Syntheses Outcomes for II–VI and IV–VI Quantum Dots. *J. Phys. Chem. C* **2020**, *124*, 24298–24305. https://doi.org/10.1021/acs.jpcc.0c05993.

(26) Braham, E. J.; Cho, J.; Forlano, K. M.; Watson, D. F.; Arròyave, R.; Banerjee, S. Machine Learning-Directed Navigation of Synthetic Design Space: A Statistical Learning Approach to Controlling the Synthesis of Perovskite Halide Nanoplatelets in the Quantum-Confined Regime. *Chem. Mater.* **2019**, *31*, 3281–3292. https://doi.org/10.1021/acs.chemmater.9b00212.

(27) Voznyy, O.; Levina, L.; Fan, J. Z.; Askerka, M.; Jain, A.; Choi, M.-J.; Ouellette, O.; Todorović, P.; Sagar, L. K.; Sargent, E. H. Machine Learning Accelerates Discovery of Optimal Colloidal Quantum Dot Synthesis. *ACS Nano* **2019**, *13*, 11122–11128. https://doi.org/10.1021/acsnano.9b03864.

(28) Vikram, A.; Brudnak, K.; Zahid, A.; Shim, M.; Kenis, P. J. A. Accelerated Screening of Colloidal Nanocrystals Using Artificial Neural Network-Assisted Autonomous Flow Reactor Technology. *Nanoscale* **2021**, *13*, 17028–17039. https://doi.org/10.1039/D1NR05497J.

(29) Bezinge, L.; Maceiczyk, R. M.; Lignos, I.; Kovalenko, M. V.; deMello, A. J. Pick a Color MARIA: Adaptive Sampling Enables the Rapid Identification of Complex Perovskite Nanocrystal Compositions with Defined Emission Characteristics. *ACS Appl. Mater. Interfaces* **2018**, *10*, 18869–18878. https://doi.org/10.1021/acsami.8b03381.

(30) Kuhn, M.; Johnson, K. *Applied Predictive Modeling*; Springer: New York, 2013.

(31) Guyon, I.; Elisseeff, A. An Introduction to Variable and Feature Selection. *J. Mach. Learn. Res.* **2003**, *3*, 1157–1182. https://doi.org/10.1162/153244303322753616.

(32) Clarke, M. T.; Viscomi, F. N.; Chamberlain, T. W.; Hondow, N.; Adawi, A. M.; Sturge, J.; Erwin, S. C.; Bouillard, J.-S. G.; Tamang, S.; Stasiuk, G. J. Synthesis of Super Bright Indium

Phosphide Colloidal Quantum Dots through Thermal Diffusion. *Commun. Chem.* **2019**, *2*, 36. https://doi.org/10.1038/s42004-019-0138-z.

(33) Suh, Y.-H.; Lee, S.; Jung, S.-M.; Bang, S. Y.; Yang, J.; Fan, X.-B.; Zhan, S.; Samarakoon, C.; Jo, J.-W.; Kim, Y.; Choi, H. W.; Occhipinti, L. G.; Lee, T. H.; Shin, D.-W.; Kim, J. M. Engineering Core Size of InP Quantum Dot with Incipient ZnS for Blue Emission. *Adv. Opt. Mater.* **2022**, *10*, 2102372. https://doi.org/10.1002/adom.202102372.

(34) Jiang, W.; Choi, Y.; Chae, H. Efficient Green Indium Phosphide Quantum Dots with Tris(Dimethylamino)-Phosphine Phosphorus Precursor for Electroluminescent Devices. *J. Mater. Sci. Mater. Electron.* **2021**, *32*, 4686–4694. https://doi.org/10.1007/s10854-020-05206-5.

(35) Riehle, F. S.; Yu, K. Role of Alcohol in the Synthesis of CdS Quantum Dots. *Chem. Mater.* **2020**, *32*, 1430–1438. https://doi.org/10.1021/acs.chemmater.9b04009.

(36) Pedregosa, F. Scikit-Learn: Machine Learning in Python. *J. Mach. Learn. Res.* **2011**, *12*, 2825–2830.

(37) Irwin, B. W. J.; Mahmoud, S.; Whitehead, T. M.; Conduit, G. J.; Segall, M. D. Imputation versus Prediction: Applications in Machine Learning for Drug Discovery. *Future Drug Discovery* **2020**, *2*, FDD38. https://doi.org/10.4155/fdd-2020-0008.

(38) Guo, C.-Y.; Yang, Y.-C.; Chen, Y.-H. The Optimal Machine Learning-Based Missing Data Imputation for the Cox Proportional Hazard Model. *Front. Public Health* **2021**, *9*, 881. https://doi.org/10.3389/fpubh.2021.680054.

(39) Borchani, H.; Varando, G.; Bielza, C.; Larrañaga, P. A Survey on Multi-Output Regression. *WIREs Data Min. Knowl. Discovery* **2015**, *5*, 216–233. https://doi.org/10.1002/widm.1157.

(40) Lee, S. H.; Kim, Y.; Jang, H.; Min, J. H.; Oh, J.; Jang, E.; Kim, D. The Effects of Discrete and Gradient Mid-Shell Structures on the Photoluminescence of Single InP Quantum Dots. *Nanoscale* **2019**, *11*, 23251–23258. https://doi.org/10.1039/C9NR06847C.

(41) Kim, H.-J.; Jo, J.-H.; Yoon, S.-Y.; Jo, D.-Y.; Kim, H.-S.; Park, B.; Yang, H. Emission Enhancement of Cu-Doped InP Quantum Dots through Double Shelling Scheme. *Materials* **2019**, *12*, 2267. https://doi.org/10.3390/ma12142267.

(42) Stein, J. L.; Holden, W. M.; Venkatesh, A.; Mundy, M. E.; Rossini, A. J.; Seidler, G. T.; Cossairt, B. M. Probing Surface Defects of InP Quantum Dots Using Phosphorus Kα and Kβ X-Ray Emission Spectroscopy. *Chem. Mater.* **2018**, *30*, 6377–6388. https://doi.org/10.1021/acs.chemmater.8b02590.

(43) Min, C.-H.; Joo, J. Studies on the Effect of Acetate Ions on the Optical Properties of InP/ZnSeS Core/Shell Quantum Dots. *J. Ind. Eng. Chem.* **2020**, *82*, 254–260. https://doi.org/10.1016/j.jiec.2019.10.021.

(44) Gary, D. C.; Terban, M. W.; Billinge, S. J. L.; Cossairt, B. M. Two-Step Nucleation and Growth of InP Quantum Dots via Magic-Sized Cluster Intermediates. *Chem. Mater.* **2015**, *27*, 1432–1441. https://doi.org/10.1021/acs.chemmater.5b00286.

(45) Kirkwood, N.; De Backer, A.; Altantzis, T.; Winckelmans, N.; Longo, A.; Antolinez, F. V.; Rabouw, F. T.; De Trizio, L.; Geuchies, J. J.; Mulder, J. T.; Renaud, N.; Bals, S.; Manna, L.; Houtepen, A. J. Locating and Controlling the Zn Content in In(Zn)P Quantum Dots. *Chem. Mater.* **2020**, *32*, 557–565. https://doi.org/10.1021/acs.chemmater.9b04407.

(46) van Embden, J.; Chesman, A. S. R.; Jasieniak, J. J. The Heat-Up Synthesis of Colloidal Nanocrystals. *Chem. Mater.* **2015**, *27*, 2246–2285. https://doi.org/10.1021/cm5028964.

(47) Mićić, O. I.; Cheong, H. M.; Fu, H.; Zunger, A.; Sprague, J. R.; Mascarenhas, A.; Nozik, A. J. Size-Dependent Spectroscopy of InP Quantum Dots. *J. Phys. Chem. B* **1997**, *101*, 4904–4912. https://doi.org/10.1021/jp9704731.

(48) Cho, E.; Jang, H.; Lee, J.; Jang, E. Modeling on the Size Dependent Properties of InP Quantum Dots: A Hybrid Functional Study. *Nanotechnology* **2013**, *24*, 215201. https://doi.org/10.1088/0957-4484/24/21/215201.

(49) Baskoutas, S.; Terzis, A. F. Size-Dependent Band Gap of Colloidal Quantum Dots. *J. Appl. Phys.* **2006**, *99*, 013708. https://doi.org/10.1063/1.2158502.

(50) Guzelian, A. A.; Katari, J. E. B.; Kadavanich, A. V.; Banin, U.; Hamad, K.; Juban, E.; Alivisatos, A. P.; Wolters, R. H.; Arnold, C. C.; Heath, J. R. Synthesis of Size-Selected, Surface-Passivated InP Nanocrystals. *J. Phys. Chem. B* **1996**, *100*, 7212–7219. https://doi.org/10.1021/jp953719f.

(51) Geurts, P.; Ernst, D.; Wehenkel, L. Extremely Randomized Trees. *Mach. Learn.* **2006**, *63*, 3–42. https://doi.org/10.1007/s10994-006-6226-1.

(52) https://docs.streamlit.io/library/get-started.

(53) Stein, J. L.; Mader, E. A.; Cossairt, B. M. Luminescent InP Quantum Dots with Tunable Emission by Post-Synthetic Modification with Lewis Acids. *J. Phys. Chem. Lett.* **2016**, *7*, 1315–1320. https://doi.org/10.1021/acs.jpclett.6b00177.

(54) Zhang, X.; Lv, H.; Xing, W.; Li, Y.; Geng, C.; Xu, S. Trioctylphosphine Accelerated Growth of InP Quantum Dots at Low Temperature. *Nanotechnology* **2021**, *33*, 055602. https://doi.org/10.1088/1361-6528/ac3180.

(55) Achorn, O. B.; Franke, D.; Bawendi, M. G. Seedless Continuous Injection Synthesis of Indium Phosphide Quantum Dots as a Route to Large Size and Low Size Dispersity. *Chem. Mater.* **2020**, *32*, 6532–6539. https://doi.org/10.1021/acs.chemmater.0c01906.

(56) Shallcross, R. C.; Graham, A. L.; Karayilan, M.; Pavlopoulous, N. G.; Meise, J.; Pyun, J.; Armstrong, N. R. Influence of the Processing Environment on the Surface Composition and Electronic Structure of Size-Quantized CdSe Quantum Dots. *J. Phys. Chem. C* **2020**, *124*, 21305–21318. https://doi.org/10.1021/acs.jpcc.0c05622.

(57) Wang, F.; Tang, R.; Buhro, W. E. The Trouble with TOPO; Identification of Adventitious Impurities Beneficial to the Growth of Cadmium Selenide Quantum Dots, Rods, and Wires. *Nano Lett.* **2008**, *8*, 3521–3524. https://doi.org/10.1021/nl801692g.

(58) Kowalczyk, B.; Lagzi, I.; Grzybowski, B. A. Nanoseparations: Strategies for Size and/or Shape-Selective Purification of Nanoparticles. *Curr. Opin. Colloid Interface Sci.* **2011**, *16*, 135–148. https://doi.org/10.1016/j.cocis.2011.01.004.

(60) Morris-Cohen, A. J.; Donakowski, M. D.; Knowles, K. E.; Weiss, E. A. The Effect of a Common Purification Procedure on the Chemical Composition of the Surfaces of CdSe Quantum Dots Synthesized with Trioctylphosphine Oxide. *J. Phys. Chem. C* **2010**, *114*, 897–906. https://doi.org/10.1021/jp909492w.

(61) Taylor, D. A.; Teku, J. A.; Cho, S.; Chae, W.-S.; Jeong, S.-J.; Lee, J.-S. Importance of Surface Functionalization and Purification for Narrow FWHM and Bright Green-Emitting InP Core–Multishell Quantum Dots via a Two-Step Growth Process. *Chem. Mater.* **2021**, *33*, 4399–4407. https://doi.org/10.1021/acs.chemmater.1c00348.

(62) Vikram, A.; Zahid, A.; Bhargava, S. S.; Keating, L. P.; Sutrisno, A.; Khare, A.; Trefonas, P.; Shim, M.; Kenis, P. J. A. Mechanistic Insights into Size-Focused Growth of Indium Phosphide

Nanocrystals in the Presence of Trace Water. *Chem. Mater.* **2020**, *32*, 3577–3584. https://doi.org/10.1021/acs.chemmater.0c00781.

(63) Xie, L.; Harris, D. K.; Bawendi, M. G.; Jensen, K. F. Effect of Trace Water on the Growth of Indium Phosphide Quantum Dots. *Chem. Mater.* **2015**, *27*, 5058–5063. https://doi.org/10.1021/acs.chemmater.5b01626.

(64) Pyrz, W. D.; Buttrey, D. J. Particle Size Determination Using TEM: A Discussion of Image Acquisition and Analysis for the Novice Microscopist. *Langmuir* **2008**, *24*, 11350–11360. https://doi.org/10.1021/la801367j.

(65) Gary, D. C.; Cossairt, B. M. Role of Acid in Precursor Conversion During InP Quantum Dot Synthesis. *Chem. Mater.* **2013**, *25*, 2463–2469. https://doi.org/10.1021/cm401289j.

Chapter 4. DETERMINISTIC SINGLE-PHOTON EMITTER ARRAYS FROM GIANT SILICA-SHELLED QDS

This chapter presents a proof of concept demonstrating how ~100 nm emissive particles can be patterned into large-scale arrays for single-photon emission application. Components of this chapter were republished with permission of the American Chemical Society, from "*Deterministic Quantum Light Arrays from Giant Silica-Shelled Quantum Dots*", Hao A. Nguyen, David Sharp, Johannes E. Fröch, Yi-Yu Cai, Shenwei Wu, Madison Monahan, Christopher Munley, Arnab Manna, Arka Majumdar, Cherie R. Kagan, and Brandi M. Cossairt; *ACS Applied Materials & Interfaces* **2023,** *15*, *3*, 4294–4302; Copyright 2025 American Chemical Society.

4.1 INTRODUCTION

Quantum nanophotonics holds great potential for several quantum technologies including quantum sensing, quantum computing, and quantum communication.[1,2] However, poor scalability is a critical hurdle that hinders progress in this field. A scalable nanophotonics platform requires replacing traditional bulky table-top optics with chip-scale photonics. One necessary condition for such a scalable platform is the ability to deterministically position single-photon emitters in an array, and subsequent coupling to nanophotonic structures, such as resonators. Although large arrays of nanophotonic cavities have been demonstrated, finding the ideal material for reliable generation of indistinguishable single photons and their scalable integration still remain outstanding challenges.

Among the many material candidates, including self-assembled quantum dots (QDs),[4,5] defects in hexagonal boron nitride,[6-8] diamond,[9,10] two-dimensional materials,[11,12] trapped ions,[13,14] and molecules,[15,16] colloidal QDs have emerged as promising building blocks for integrated photonic systems that provide a unique approach to solve the challenge of deterministic, scalable integration. Colloidal core–shell Cd- and In-based QDs or halide perovskite QDs can be prepared to exhibit strong antibunching behavior, that is, their second-order intensity correlation at zero-time delay $g^{(2)}(\tau = 0)$ is less than 0.5 and often approaches zero for a single emitter.[17-23] This makes colloidal QDs competitive candidates for solid-state single-photon sources.

Besides their attractive characteristics for photonic applications including emission wavelength tunability, room temperature stability, and low-cost and flexible synthesis, the key advantage of colloidal QDs is their solution processability. Dispersions of colloidal materials are compatible with various solution-phase integration techniques.[21,22,24,25] Straightforward integration methods, such as spin-coating, drop-casting, capillary assembly, and doctor blade coating, are often performed on patterned or templated substrates with nano- or microscale traps generated by electron beam lithography to enable precise positioning of isolated single QDs.[26-33] Deterministic and scalable positioning of one or a few QDs using these approaches can be realized when the QD size is maximized and/or the size of the predefined trap is minimized.[34,35] A different route for precise placement is to manipulate the location of a QD on a substrate with atomic force microscopy and/or scanning electron microscopy (SEM) with a nanomanipulator;[36-38] however, this approach does not offer a feasible path to scaling. Most recently, electrohydrodynamic inkjet printing has been demonstrated to deposit droplets of nanoparticles on an array of nanocavities.[39] For this technique, although the production of small ink droplets containing a few nanoparticles was achieved, targeting one particle per droplet remains difficult due to the small size of the

nanoparticles and the constraints imposed by the nozzle diameter. Furthermore, implementing available techniques for large-scale patterning of QD single-photon emitters is problematic due to the QD's small size, surface chemistry, and/or poor stability in ambient conditions. Overall, despite intense effort, deterministic positioning of QD single-photon emitters with high scalability remains a challenge.

Here, we demonstrate a bottom-up strategy via silica shelling of CdSe/CdS QDs combined with template-assisted self-assembly to deterministically position QD single photon emitters. Applications of silica-shelled QDs are ubiquitous in the biomedical field based on four major advantages: (1) optical transparency, (2) high colloidal, chemical, and optical stability of their dispersions, including in water at different pH values, (3) reduced toxicity of conventional QDs, and (4) versatility of surface modification.[40-45] In this study, we experimentally show that silica shells both increase the physical size of the CdSe/CdS QDs to facilitate device integration and stabilize the QDs to achieve room-temperature single-photon emission. We use the template-assisted self-assembly technique, recently reported for placement of nanoparticles,[46,47] to deterministically deposit single giant silica-shelled CdSe/CdS QDs in ordered arrays wherein they continue to exhibit bright single-photon emission. This synthetic approach provides a scalable and versatile strategy that could be combined with other large-scale placement methods for fabricating quantum nanophotonic devices.

4.2 Synthesis And Characterizations of Giant Silica-Shelled QDs

For core–shell CdSe/CdS QDs, increasing the number of monolayers of the shelling material is a typical approach to achieve larger particle sizes. However, even with the laborious and time-intensive deposition of 19 monolayers of CdS, the QD size only reaches 20 nm in diameter, while a large amount of precursor material is consumed.[48] In addition, an excessively

large CdS shell on a CdSe core leads to a reduction in photoluminescence quantum yield (PLQY) to the formation of interfacial defects caused by lattice strain.[49-51] The optimal PLQY is observed when 8−10 monolayers of CdS are applied to achieve QDs of 10−11 nm in total diameter.[52] Hence, we synthesized wurtzite CdSe/CdS core−shell QDs containing 9 monolayers of CdS with a total diameter of 11 ± 0.4 nm via the dual injection method (**Figure 4.1.b**).[52,53] The synthesized QDs show PL centered around 640 nm with a narrow emission linewidth with a halfwidth-half-maximum of 27 nm and an 82% PLQY. To controllably increase the particle size, we encapsulated the CdSe/CdS QDs in silica shells. Synthesis of silica shells on nanoparticles can be achieved usisng two main techniques: the Stober method and the reverse microemulsion method.[40,54] We used the latter procedure because of its greater degree of control over the particle size and the higher yield for encapsulating one single QD in one silica sphere.[55-57] Generally, the hydrophobic ligands of the initial QDs are replaced by non-ionic surfactant molecules such as IGEPAL CO-520 or Triton X100 in cyclohexane to create a microemulsion. These emulsions act as nanoreactors to control the hydrolysis of the silica precursor, tetraethyl orthosilicate (TEOS), and the resulting silica shell growth using an aqueous ammonia catalyst.

With the reverse microemulsion route, the CdSe/CdS QDs were efficiently encapsulated in silica shells with an average total diameter of 90 ± 18 nm, confirmed by transmission electron microscopy (TEM, **Figure 4.1.b-c**). We also observed a small number of hollow silica particles and non-shelled QDs. After the silica shelling process, the PL of the QDs slightly blue-shifted, resulting in a peak maximum at 635 nm with an improved half-width-half-maximum of 20 nm, which are typical behaviors of silanization of QDs (**Figure 4.1.a**). We also saw an expected drop in PLQY to 34%, which remained the same after 14 months at room temperature as water or ethanol dispersions (**Figure 4.2**). This observation indicates that silica shells are effective at

protecting QDs from PLQY quenching effects arising from the outside environment. On the other hand, considering the surface ligands and the quasi-type II heterostructure of CdSe/CdS QDs where the electron wavefunction is delocalized over the whole QD and the hole wavefunction is localized in the core, we assume the initial drop in PLQY after the silica shelling process may originate from several aspects including the initial ligand exchange step, the formation of oxidic surface trap sites during the silanization, and lattice strain.[57-59] Several PLQY preservation strategies have been reported including phase-transfer treatment,[41] post-synthetic annealing with UV activation,[60] and QD core heterostructure engineering,[57,61] further improve the final PLQY of the SiO_2-shelled QDs.

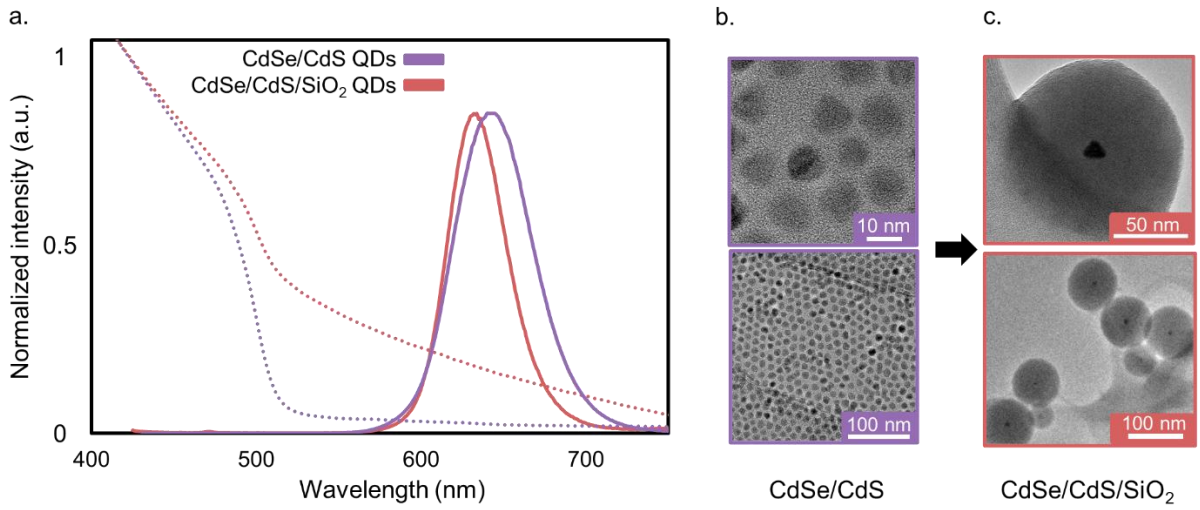

Figure 4.1. Characterization of the synthesized QDs including **a.** photoluminescence (solid curves) and UV–visible absorption spectra (dotted curves), **b.** TEM images of CdSe/CdS QDs, and **c.** CdSe/CdS/SiO_2 QDs.

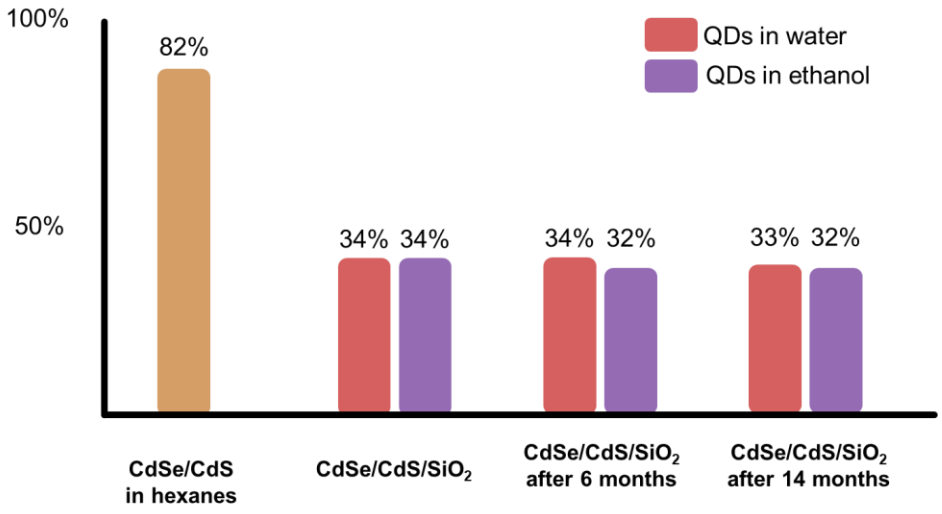

Figure 4.2. Photoluminescence of QDs over time in water and ethanol.

4.3 GIANT QDS ON A PLANAR SUBSTRATE

To test the optical properties of individual giant QDs, we explored spin-coating the colloidal giant QD dispersions on a planar SiO_2 substrate. To avoid aggregation of silica particles caused by interparticle siloxane bonding upon drying, ethanol was used as the solvent. Control over concentration and sonication was also required to achieve either a uniform monolayer or isolated QDs (**Figure 4.3)**. A small amount (10 μL) of the giant QD stock dispersion in ethanol (100 mg of QDs in 5 mL of ethanol) was directly spin-coated on a planar Si substrate resulting in large clusters of agglomerated nanoparticles. A uniform monolayer of giant QDs was achieved when the same solution was sonicated for 10 min prior to spin-coating. To reach the level of isolated QDs, the original dispersion was diluted by a factor of 100 using ethanol, followed by 10 min of sonication prior to spin-coating. To study the single-photon emission of these silica-coated QDs, we performed PL measurements and second-order photon correlation measurements, $g^{(2)}(\tau)$. At room temperature and in air, among 46 measured QDs, 19 QDs bleached rapidly, 7 QDs bleached after 4 min, and 20 QDs bleached after 6 min upon continuous wave laser irradiation

(532 nm, ~3 μW, ~1 kW cm–2). As photobleaching is assumed to originate from photo–chemical reactions on the surface of the QDs under excitation,[62–65] we initially expected that thick silica shells would reduce this unwanted behavior. However, the photobleaching timescales of the silica-shelled QDs are similar to those of single CdSe-based core/shell QDs.[31,34] Therefore, we hypothesize that the photobleaching phenomenon arises from oxides at the silica–CdS interface, which could be mitigated by applying an insulating layer between the CdS and the silica shells.[62] **Figure 4.4.a** shows the distribution of the PL maxima of the measured QDs, with most of the emission peaks centered around 635 nm, consistent with PL results from the ensemble dispersion. The PL intensity time trace measurements showed that 15 QDs had a largely unimodal ON state of emission indicating a low blinking behavior. We measured $g^{(2)}(\tau)$ for 18 QDs and found that the $g^{(2)}(\tau=0)$ value ranged from 0.06 to 0.79 (**Figure 4.4.b**). Among them, 12 QDs had $g^{(2)}(\tau=0)$ below a threshold of 0.5, with the lowest value of 0.06. **Figure 4.4.c–l** displays the outcome of single-particle measurements of three representative QDs. Spectral cutoffs at ~600 and 645 nm appear because a bandpass filter was used to reduce background from non-QD emission. These results from isolated silica-shelled QDs including variations in optical behaviors, blinking, photobleaching, and antibunching are analogous to those of isolated Cd-based core/shell QDs in previous studies.[21,23,31,34,66–68]

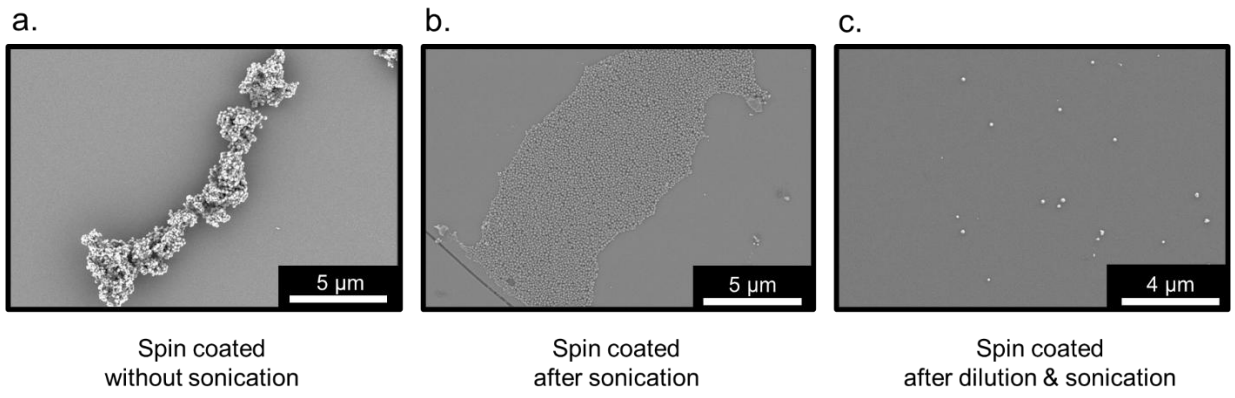

Figure 4.3. SEM images of giant QDs on a planar substrate. **a.** Aggregation of silica coated QDs after spin coating without prior sonication. **b.** Monolayer of silica coated QDs after sonication for 5 min followed by spin coating. **c.** Isolated silica coated QDs from a highly diluted ethanol solution after sonication for 5 min followed by spin coating.

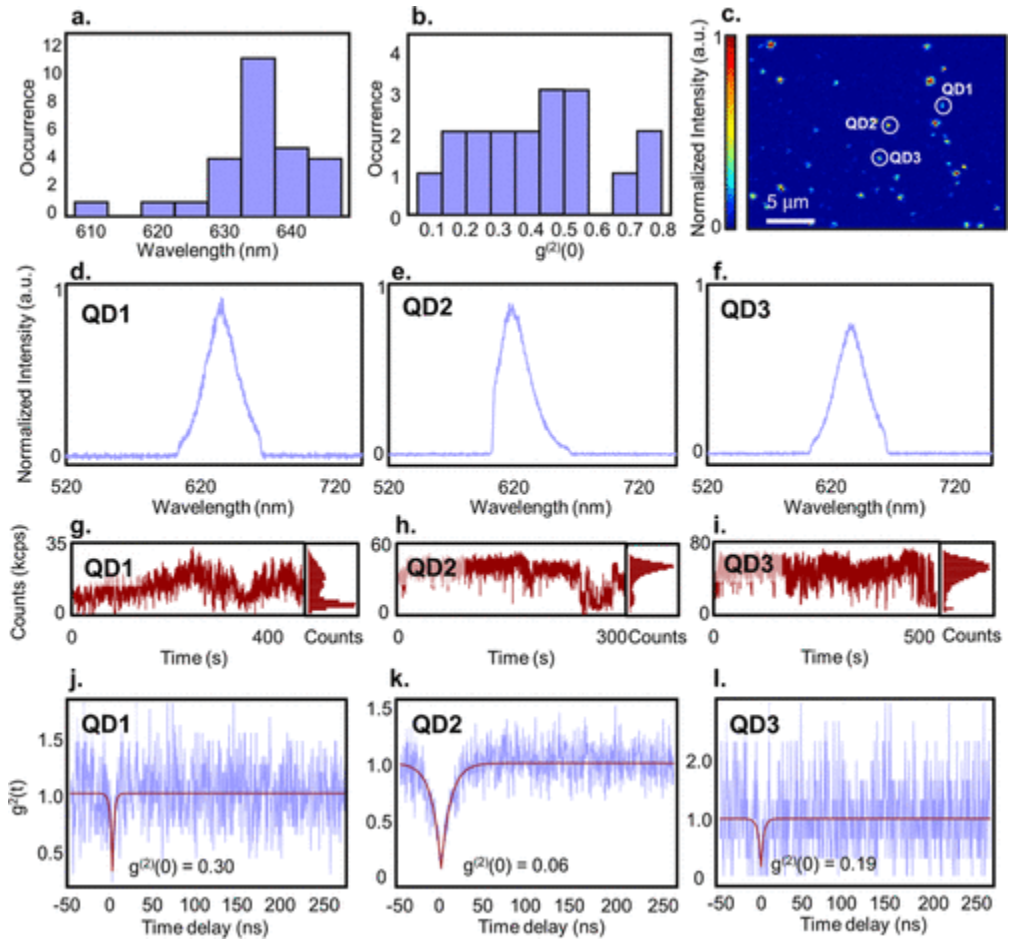

Figure 4.4. Quantum optical characterization of isolated silica-shelled CdSe/CdS QDs. **a.** Distribution of emission maxima of 27 single silica-shelled QDs. **b.** Distribution of outcomes from second-order autocorrelation function $g^{(2)}(\tau)$ of 18 single silica-shelled QDs. **c.** PL image of single silica-coated QDs on a planar SiO_2 substrate. **d–f.** Single particle emission spectra. **g–i.** PL intensity time trace. **j–l.** Second-order autocorrelation function $g^{(2)}(\tau)$ measurements of three representative single silica-shelled QDs.

4.4 Deterministic Positioning of Silica-Shelled QDs into Arrays

To deterministically position the giant silica-coated QDs into arrays, we employed a template-assisted self-assembly technique that has been demonstrated to precisely arrange single nano-diamonds and gold nanoparticles with diameters as small as 40 nm across millimeter-scale areas.[46,47] On a Si/SiO_2 substrate, electron beam lithography was used to define poly(methyl methacrylate) (PMMA) resist templates composed of 9 × 24 rectangular arrays of cylindrical traps with a 10 μm spacing and a depth of 157 nm, equal to the PMMA resist thickness. For every row, to optimize the capture of single 90 nm diameter silica-shelled QDs, the trap diameters were designed to increase from 90 to 170 nm in 10 nm increments, although the actual trap sizes were measured from SEM images to be larger (likely due to overexposure or overdeveloping) and to range from 122 to 238 nm in diameter.

The assembly was performed in a home-built apparatus in which an aqueous dispersion of silica-coated QDs was deposited between a glass slide and the template surface. The QD dispersion was translated across the template surface at a speed of 2 μm/s by a motorized stage (**Figure 4.5**). A strong capillary force at the meniscus of the liquid rear edge drives the particles into the template traps.[28,32,33,46,69–71] During the assembly process, the environmental humidity (ambient dew point around −25 °C) and the substrate temperature (22 °C) were monitored and kept consistent as fluctuations of these factors can affect the assembly yield.[46] Finally, a liftoff step through immersion of the samples in N-methyl-2-pyrrolidone for 1 min and acetone for 1 min was done to remove the PMMA layer and any non-specifically bound QDs outside of the traps.

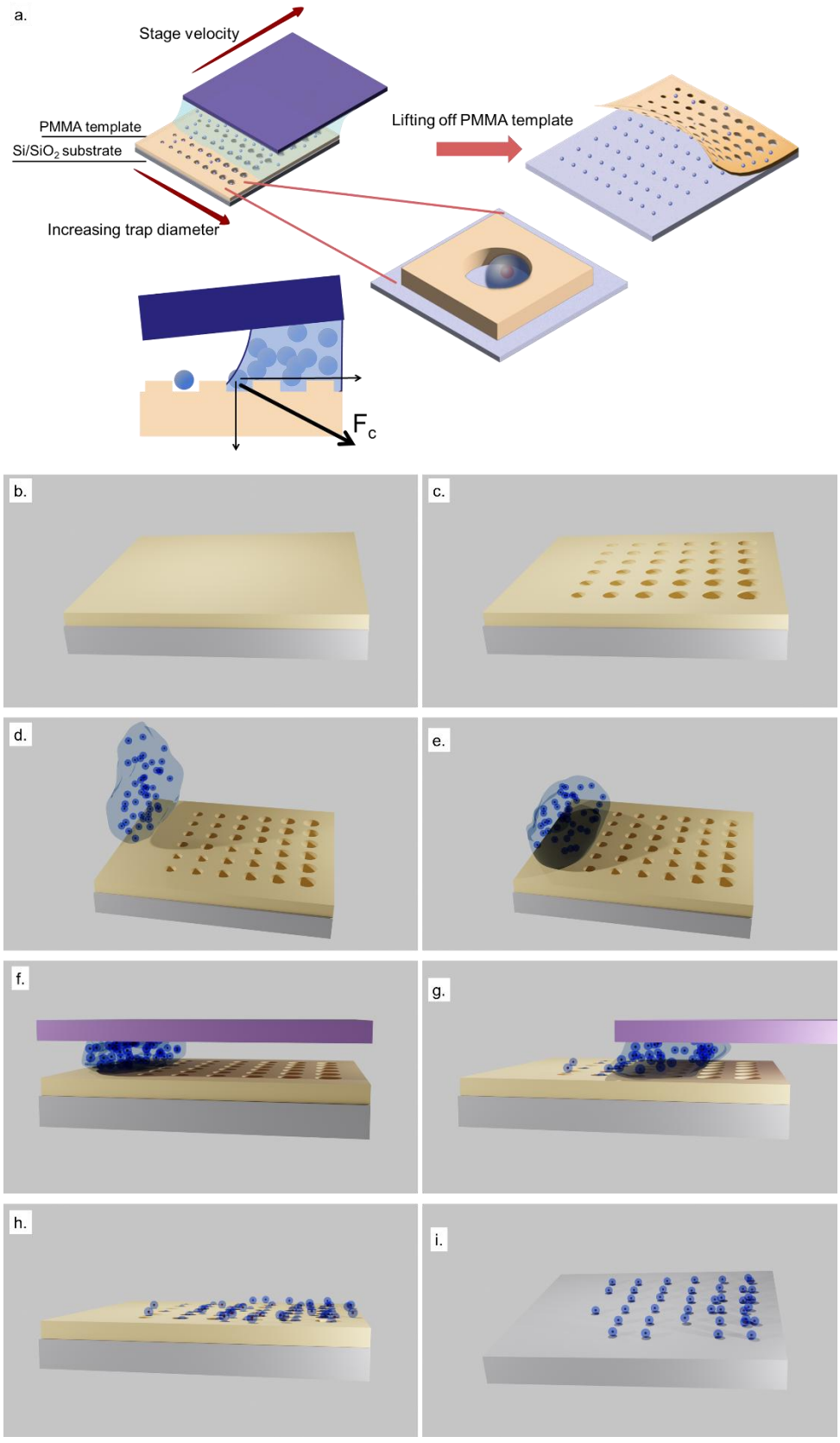
a.
Stage velocity
PMMA template
Si/SiO2 substrate
Increasing trap diameter
Lifting off PMMA template
Fc
b.
c.
d.
e.
f.
g.
h.
i.

Figure 4.5. Schematic process of the template-assisted self-assembly method to deterministically place silica (light blue sphere)-shelled QDs (red sphere) in an array using a PMMA template (yellow) on a Si/SiO_2 substrate (gray).

To obtain the yield for the QD assembly into the patterned array, SEM was used to image all 216 positions of one 9 × 24 array. Positioning of QDs in the entire array was tracked by taking images of subarrays to construct the large array image (**Figure 4.6.a**). Full reconstruction of the array is shown in Section S10 of the Supporting Information. Ordered subarrays of QDs were clearly seen from the SEM images (**Figure 4.6.c**), in which positions with a single QD (**Figure 4.6.d,e**), multiple QDs (**Figure 4.6.f**), and missing QDs could be clearly identified. Statistical characterization of the assembly showed that 75% of the traps were occupied by single QDs, 14% contained multiple QDs, and 11% were empty. **Figure 4.6.b** shows that the optimal assembly yield for the silica-shelled QDs with an average diameter of 90 nm was achieved with a trap diameter of 160 nm, where only one position in the 24-member column was vacant. In addition, a smaller trap size (diameter < 150 nm) resulted in a higher frequency of missing QDs, and a larger trap size (diameter > 190 nm) exhibited a higher frequency of multiple QDs. From the SEM images of the array before the PMMA liftoff step (**Figure 4.6.d**), we found that the single QDs tend to attach to the trap wall after assembling, indicating that the absolute position of single QDs from our technique is influenced heavily by the trap diameter. This leads to a trade-off between assembly yield and precise positioning, where larger traps result in better capturing of QDs, but less precision in the absolute position of the QDs.

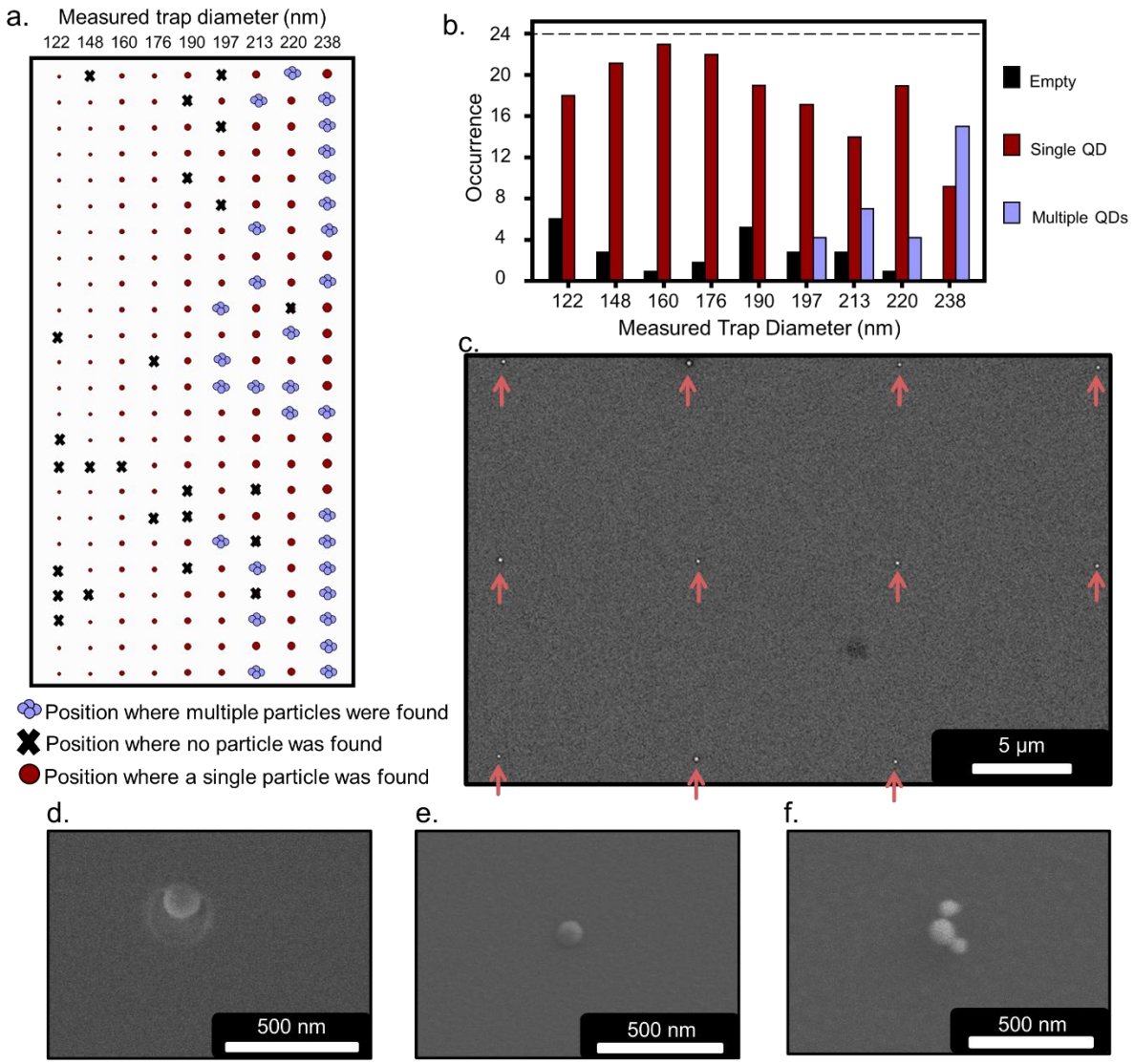

Figure 4.6. a. Schematic construction of one 9 × 24 array showing the assembly yield. **b.** Plot showing the frequency of traps containing multiple, one, or no QDs as a function of trap diameter. SEM images of **c.** sub arrays of QDs, **d.** a single QD in a trap before the PMMA liftoff step, **e.** a single QD in a templated position after the PMMA liftoff step, and **f.** multiple QDs in a templated position after the PMMA liftoff step. The contrast of the SEM images was adjusted after imaging to optimize visibility of particles and the array.

4.5 Optical Characterization of Giant QDs in Arrays

Finally, we studied the optical properties of the giant QDs in the 9 × 24 array to compare with the ones on the planar substrate. It should be noted that measurements of QDs on the planar substrate and QDs in the array were taken 6 months apart. **Figure 4.6.a** shows the distribution of emission maxima for 34 single QDs in the array. The majority of the emission peaks centered around 635 nm, consistent with the ensemble QD emission. To acquire the statistics for single-photon emission of the single giant QDs in the array, the second-order autocorrelation functions, $g^{(2)}(\tau)$, of 32 QDs were collected. **Figure 4.6.b** displays the distribution of $g^{(2)}(\tau = 0)$ values, where 16 QDs show photon antibunching behavior with $g^{(2)}(\tau = 0) < 0.5$. The PL time traces of the measured QDs showed that emission bleaching occurred in less than 3.5 min for 11 QDs, between 3.5 and 10 min for 17 QDs, and after more than 10 min for 4 QDs. Additionally, blinking suppression was observed for 10 QDs. **Figure 4.6.c** displays the PL map of a subarray highlighting three representative QD single-photon emitters with low $g^{(2)}(\tau = 0)$ values. The optical characterization of these three QDs is shown in **Figure 4.6 d-l.**, where blinking suppression was seen in QD5 and QD6 and the $g^{(2)}(\tau = 0)$ value was as low as 0.14 for QD6. These results confirm that the silica-shelled QDs retained their photostability and single-photon emission through the assembly process and over a long period of time, making them suitable for photonic device operation at room temperature. This is an important advance since colloidal materials often become unstable within weeks after their synthesis when left under ambient conditions.

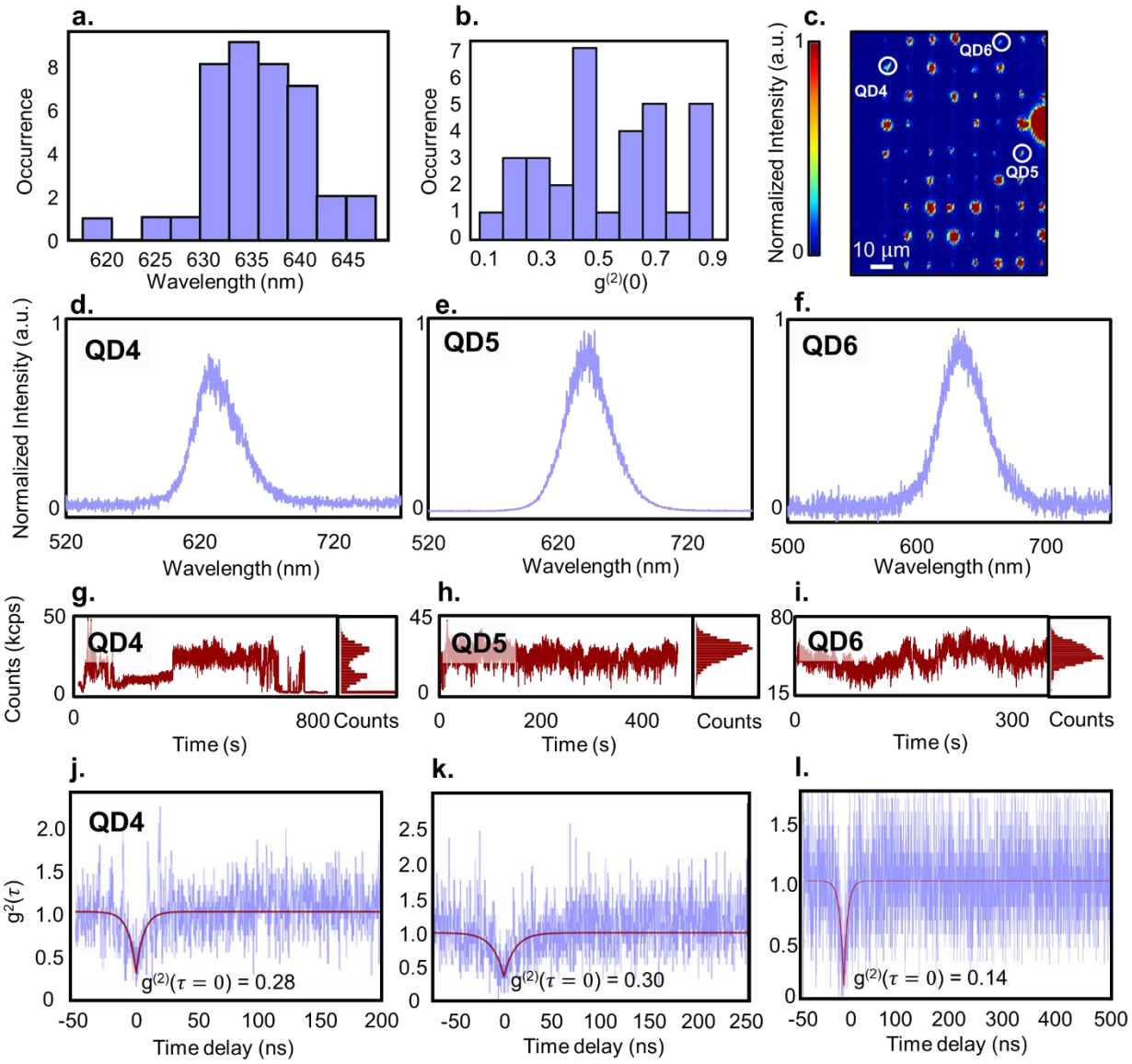

Figure 4.7. Quantum optical characterization of single silica-shelled QDs in a 9 × 24 array. **a.** Distribution of emission maxima of 34 single silica-shelled QDs in array. **b.** Distribution of outcomes from second-order autocorrelation function $g^{(2)}(\tau)$ of 32 single silica-shelled QDs. **c.** PL image of single silica-coated QDs in a representative section of the templated array. **d–f.** Single particle emission, **g–i.** PL intensity time trace, and **j–l.** second-order autocorrelation function $g^{(2)}(\tau)$ measurements of three representative single silica-shelled QDs in an array.

4.6 SINGLE SILICA-SHELLED QDS ON NANOBEAM CAVITY

Using the same method for patterning, we successfully deposit single silica-shelled QDs on nanobeam cavity (**Figure 4.8b**). This process is somewhat different from patterning single QDs on a planar substrate since the surface of the chip is not flat with the presence of the cavities. This created an issue where the PMMA template could not be coated uniformly. The uniformity of the template was problematic since bumps on the surface prevent the QDs from being 'dragged' evenly across the chip, resulting in large aggregates of QDs at the area where the cavities reside (**Figure 4.8a**). After removing the PMMA layer, we were still able to see instances of a single QD at the center of a nanobeam cavity, but the yield is below 10%, and there many QDs sitting next to the cavity resonance region. PL measurements to show coupled emissions were not successful due to the blinking and bleached emission from the silica shelled QDs, and the high background noise from the SiN cavities.

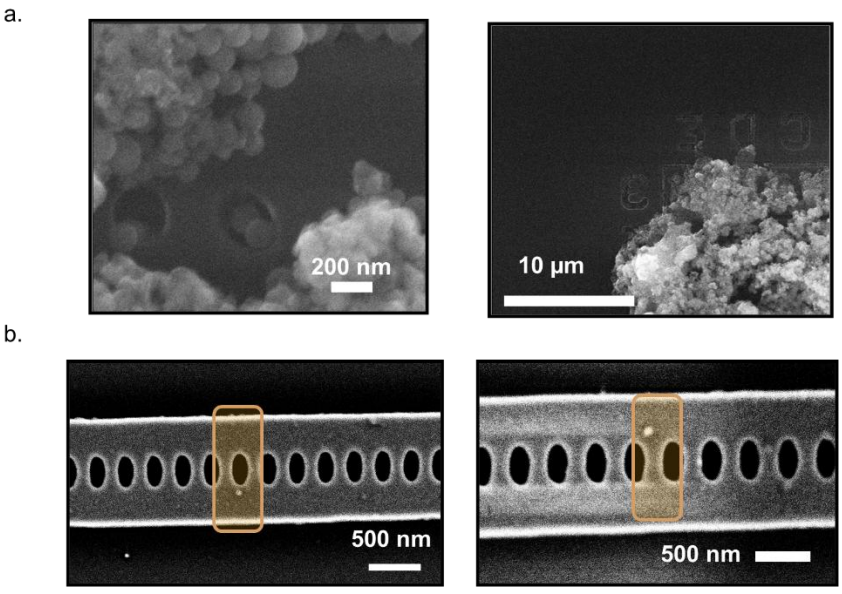

Figure 4.8. SEM images of QDs on top of cavities area on a chip **a.** before lifting of the PMMA layer and **b.** single silica-shelled QDs on nanobeam cavities after lift-off.

4.7 CONCLUSIONS

A practical nanophotonics platform using colloidal materials as quantum emitters requires scalable integration. Our work presents a combination of a synthesis design to increase colloidal QD size through silica shelling with a template-assisted self-assembly technique to deterministically position giant QD single-photon emitters in a large array, which directly demonstrates the scalability advantage of colloidal materials for photonic devices. We have shown that template-assisted self-assembly allows placement of QD single-photon emitters into a large array with high assembly yield. The giant QDs both in the array and on planar substrates showed clear antibunching, characteristic of single-photon generation. It can be expected that optimization of the silica shelling process will maintain the superior PLQY of the starting CdSe/CdS and related core/shell QDs and may mitigate photobleaching issues, thus even further improving the single-photon emission properties of these materials. We envision that the demonstrated method of silica shelling may be applicable to other highly emissive nanomaterials such as halide perovskites or semiconductor QDs emitting in the IR range, which increases their stability and will advance the use of solution processable materials in the field of quantum nanophotonics. Finally, giant silica-shelled QDs are also a flexible class of materials that may be compatible with other device fabrication techniques to achieve deterministic single-particle positioning in complex photonic platforms.

4.8 EXPERIMENTAL SECTION

4.8.1 *Materials*

Syntheses of CdSe/CdS QDs were performed air-free. Silica shelling was done in ambient air in a well-ventilated fume hood or on a benchtop. All glassware was dried overnight in an oven at 160 °C. All chemicals listed below were used without further purification unless stated otherwise. Anhydrous ethanol (99.5%), anhydrous oleic acid (≥99%), anhydrous chloroform (99%), anhydrous toluene (99.5%), anhydrous methyl acetate (99.5%), 2-propanol (≥99.5%), acetone (≥99.5%), selenium powder (99.999%, 100 mesh), cadmium oxide powder (CdO, 99.9%), tri-noctylphosphine oxide (TOPO, 99%), trioctylphosphine (90%), 1-octanethiol (99%), octadence (ODE, 90%), tetraethyl orthosilicate (TEOS, 99.999%), Triton X-100, ammonium hydroxide solution (NH_4OH, 28.0–30.0% w/w), and N-methyl-2-pyrrolidone were purchased from MilliporeSigma and n-octadecylphosphonic acid (ODPA, 99%) was purchased from PCI Synthesis. Cadmium oleate was synthesized following a literature procedure.[52] 18.2 MΩ water was collected from an EMD Millipore purification system. UV–vis spectra were collected on a Cary 5000 spectrophotometer from Agilent. Steady-state PL measurements were taken on a HORIBA Jobin Yvon FluoroMax-4 fluorescence spectrophotometer and quantum yield measurements were taken with a Hamamatsu C9920-12 integrating sphere with a Hamamatsu C10027-01 photonic multi-channel analyzer.

4.8.2 *Synthesis of CdSe/CdS QDs*

Wurtzite core/shell CdSe/CdS QDs were synthesized using an established method with some minor modifications.[52] The synthesis of the CdSe core emitting at 620 nm was stopped 60 s after the injection of the Se-TOP solution. CdS shelling of the CdSe core was performed with 100

nanomole of CdSe QDs. The amounts of Cd- and S-precursors were calculated to achieve 9 monolayers of the CdS shells. To purify the QDs, ethyl acetate (15 mL) was mixed with the reaction solution and the QDs were precipitated by centrifugation at 7800 rpm for 6 min. The colorful precipitate was dissolved in hexane (7 mL) and the solution was centrifuged at 7800 rpm for 6 min to isolate unreacted precursors and byproducts from the QDs. The precipitate was discarded, and the red solution was mixed with ethyl acetate (15 mL), followed by another centrifugation at 7800 rpm for 6 min. The colorful precipitate was dissolved in chloroform (5 mL) and stored in a N_2-filled glovebox.

4.8.3 *Silica shelling of CdSe/CdS QDs*

The CdSe/CdS QDs were shelled in silica spheres via the reverse microemulsion process.[57] To a mixture of 10 mL of cyclohexane, 1.9 mL of Triton X-100, 1.8 mL of hexanol, and 20 nmol of the CdSe/CdS QDs in chloroform were added. The mixture was stirred for 30 min, followed by dropwise addition of 200 μL of TEOS and stirring for another 15 min. Finally, 30 μL of ammonium hydroxide solution and 0.2 mL of water were injected successively. The reaction was stirred in the dark. After 3 days, a mixture (20 mL) of acetone and ethanol (1:1 ratio) was added to the solution followed by 5 min of centrifugation at 5000 rpm. The yellow precipitate was collected and washed with ethanol three times. The final product was dispersed in 5 mL of 18.2 MΩ water or ethanol and stored in air at room temperature.

4.8.4 *Spin Coating*

To avoid aggregation of nanoparticles, a low concentration of the giant QD solution and a sonication step prior to fabrication were necessary. For the dynamic dispense spin-coating technique, 50 μL of the solution of giant QDs was dropped onto a substrate, which was rotating at

1500 rpm. The rotation was stopped after 30 s. For the static dispense spin-coating technique, 50 μL of the solution of giant QDs was dropped at the center of a silicon nitride chip. The rotation at 1500 rpm was started and then stopped after 30 s.

4.8.5 *Template Fabrication and Assembly*

Onto a single-side-polished Si wafer with a 280 nm thermal oxide layer, a PMMA positive resist (950 A4, Kayaku), was spun at 6000 rpm for 60 s followed by a soft bake at 180 °C for 120 s. Circular traps with design diameters ranging from 90 to 170 nm were created by electron beam lithography (Elionix ELS-7500EX) at a 50 kV accelerating voltage and a 50 pA beam current. The PMMA was developed in a 1:3 MIBK and isopropanol solution for 90 s. The substrate was cleaned by 6 s O_2 plasma treatment with 75 W and 20 sccm prior to assembly using a Gatan Solarus plasma cleaner. After the plasma treatment, the thickness of the PMMA layer was approximately 157 nm. The assembly was performed using a custom-built capillary assembly apparatus.[46] An aqueous dispersion of the silica-shelled QDs (about 5 μL) was deposited in between the patterned substrate and a glass slide. The substrate was translated by a motorized linear stage (New Focus Picomotor) at a speed of 2 μm/s. The whole process was performed in a home-built chamber equipped with a humidity-controlled setup. To maintain the temperature around 22 °C during the assembly process, the substrate was mounted on a water-cooled stage and monitored with a thermocouple. The ambient dew point was maintained around −25 °C. The liftoff of the PMMA template was done by immersing the assembled samples in N-methyl-2-pyrrolidone for 1 min, followed by 1 min in acetone.

4.8.6 *Optical Setup*

PL maps were obtained with a home-built confocal scanning PL setup. A 532 nm continuous-wave laser (Laserglow Technologies 532 nm DPSS Laser) was filtered through a 532 nm laser line filter and focused on the sample surface using a 100× (NA 0.95) objective lens to excite the QDs. A nano-positioning piezo stage (Physik Instrumente P-611.3S) was used to control the sample position. The QD PL was collected with the same objective and filtered through a 580 nm long pass filter and coupled into a fiber, which was either sent to an avalanche photodiode to create a PL map or to a spectrometer to obtain spectra of individual QDs. The spectral position and linewidth of the QD PL spectrum was then extracted by fitting the spectra to a Voigt line shape using a custom Python script and the SciPy software package. For $g^{(2)}(\tau)$ measurements, the signal was sent through a 1 × 2 fiber splitter with a 50/50 output ratio. Both output ends were connected to separate avalanche photodiodes (MPD-PDM). Their outputs were time correlated using a time tagger (PicoQuant TimeHarp 260). For all measurements, a custom software was used, which mapped a specific area of the sample first and allowed us to select specific spots. At the same time, the PL counts at that site were displayed live during the measurement. For QDs in arrays, all potential sites of the array were probed and if the single emitter/ensemble did not bleach, then spectra, $g^{(2)}(\tau)$, and PL were collected. For samples, where QDs were spin-coated, we considered emitters that appeared as isolated spots in the PL map and showed a PL count larger than 3k and less than 50k.

4.9 REFERENCES

(1) Madsen, L. S.; Laudenbach, F.; Askarani, M. F..; Rortais, F.; Vincent, T.; Bulmer, J. F. F.; Miatto, F. M.; Neuhaus, L.; Helt, L. G.; Collins, M. J.; Lita, A. E.; Gerrits, T.; Nam, S. W.; Vaidya,

V. D.; Menotti, M.; Dhand, I.; Vernon, Z.; Quesada, N.; Lavoie, J. Quantum Computational Advantage with a Programmable Photonic Processor. *Nature* **2022**, *606*, 75–81. https://doi.org/10.1038/s41586-022-04725-x.

(2) Wang, H.; Qin, J.; Ding, X.; Chen, M.-C.; Chen, S.; You, X.; He, Y.-M.; Jiang, X.; You, L.; Wang, Z.; Schneider, C.; Renema, J. J.; Höfling, S.; Lu, C.-Y.; Pan, J.-W. Boson Sampling with 20 Input Photons and a 60-Mode Interferometer in a 10^{14}-Dimensional Hilbert Space. *Phys. Rev. Lett.* **2019**, *123*, 250503. https://doi.org/10.1103/physrevlett.123.250503.

(3) Majumdar, A.; Rundquist, A.; Bajcsy, M.; Dasika, V. D.; Bank, S. R.; Vučković, J. Design and Analysis of Photonic Crystal Coupled Cavity Arrays for Quantum Simulation. *Phys. Rev. B* **2012**, *86*, 195312. https://doi.org/10.1103/physrevb.86.195312.

(4) Warburton, R. J. Single Spins in Self-Assembled Quantum Dots. *Nat. Mater.* **2013**, *12*, 483–493. https://doi.org/10.1038/nmat3585.

(5) Buckley, S.; Rivoire, K.; Vučković, J. Engineered Quantum Dot Single-Photon Sources. *Rep. Prog. Phys.* **2012**, *75*, 126503. https://doi.org/10.1088/0034-4885/75/12/126503.

(6) Sajid, A.; Ford, M. J.; Reimers, J. R. Single-Photon Emitters in Hexagonal Boron Nitride: A Review of Progress. *Rep. Prog. Phys.* **2020**, *83*, 044501. https://doi.org/10.1088/1361-6633/ab6310.

(7) Nikolay, N.; Mendelson, N.; Özelci, E.; Sontheimer, B.; Böhm, F.; Kewes, G.; Toth, M.; Aharonovich, I.; Benson, O. Direct Measurement of Quantum Efficiency of Single-Photon Emitters in Hexagonal Boron Nitride. *Optica* **2019**, *6*, 1084–1088. https://doi.org/10.1364/optica.6.001084.

(8) Fröch, J. E.; Kim, S.; Mendelson, N.; Kianinia, M.; Toth, M.; Aharonovich, I. Coupling Hexagonal Boron Nitride Quantum Emitters to Photonic Crystal Cavities. *ACS Nano* **2020**, *14*, 7085–7091. https://doi.org/10.1021/acsnano.0c01818.

(9) Dolan, P. R.; Adekanye, S.; Trichet, A. A. P.; Johnson, S.; Flatten, L. C.; Chen, Y. C.; Weng, L.; Hunger, D.; Chang, H.-C.; Castelletto, S.; Smith, J. M. Robust, Tunable, and High Purity Triggered Single Photon Source at Room Temperature Using a Nitrogen-Vacancy Defect in Diamond in an Open Microcavity. *Opt. Express* **2018**, *26*, 7056–7065. https://doi.org/10.1364/oe.26.007056.

(10) Bradac, C.; Gao, W.; Forneris, J.; Trusheim, M. E.; Aharonovich, I. Quantum Nanophotonics with Group IV Defects in Diamond. *Nat. Commun.* **2019**, *10*, 5625. https://doi.org/10.1038/s41467-019-13332-w.

(11) Ren, S.; Tan, Q.; Zhang, J. Review on the Quantum Emitters in Two-Dimensional Materials. *J. Semiconduct.* **2019**, *40*, 071903. https://doi.org/10.1088/1674-4926/40/7/071903.

(12) Zhou, X.; Zhang, Z.; Guo, W. Dislocations as Single Photon Sources in Two-Dimensional Semiconductors. *Nano Lett.* **2020**, *20*, 4136–4143. https://doi.org/10.1021/acs.nanolett.9b05305.

(13) Saha, U.; Siverns, J. D.; Hannegan, J.; Prabhu, M.; Bersin, E.; Bandyopadhyay, S.; Carolan, J.; Quraishi, Q.; Englund, D.; Waks, E. Routing Single Photons from a Trapped Ion with Photonic Integrated Circuits. *Conf. Lasers Electro-Optics*, Optica Publishing Group: San Jose, CA, 2022. FTh5O.1.

(14) Higginbottom, D. B.; Slodička, L.; Araneda, G.; Lachman, L.; Filip, R.; Hennrich, M.; Blatt, R. Pure Single Photons from a Trapped Atom Source. *New J. Phys.* **2016**, *18*, 093038. https://doi.org/10.1088/1367-2630/18/9/093038.

(15) Toninelli, C.; Gerhardt, I.; Clark, A. S.; Reserbat-Plantey, A.; Götzinger, S.; Ristanović, Z.; Colautti, M.; Lombardi, P.; Major, K. D.; Deperasińska, I.; Pernice, W. H.; Koppens, F. H. L.; Kozankiewicz, B.; Gourdon, A.; Sandoghdar, V.; Orrit, M. Single Organic Molecules for Photonic Quantum Technologies. *Nat. Mater.* **2021**, *20*, 1615–1628. https://doi.org/10.1038/s41563-021-00987-4.

(16) Lombardi, P.; Trapuzzano, M.; Colautti, M.; Margheri, G.; Degiovanni, I. P.; López, M.; Kück, S.; Toninelli, C. A Molecule-Based Single-Photon Source Applied in Quantum Radiometry. *Adv. Quantum Technol.* **2020**, *3*, 1900083. https://doi.org/10.1002/qute.201900083.

(17) Aharonovich, I.; Englund, D.; Toth, M. Solid-State Single-Photon Emitters. *Nat. Photonics* **2016**, *10*, 631–641. https://doi.org/10.1038/nphoton.2016.186.

(18) Kagan, C. R.; Bassett, L. C.; Murray, C. B.; Thompson, S. M. Colloidal Quantum Dots as Platforms for Quantum Information Science. *Chem. Rev.* **2021**, *121*, 3186–3233. https://doi.org/10.1021/acs.chemrev.0c00831.

(19) Chen, Y.; Sharp, D.; Saxena, A.; Nguyen, H.; Cossairt, B. M.; Majumdar, A. Integrated Quantum Nanophotonics with Solution-Processed Materials. *Adv. Quantum Technol.* **2022**, *5*, 2100078. https://doi.org/10.1002/qute.202100078.

(20) Zhu, C.; Marczak, M.; Feld, L.; Boehme, S. C.; Bernasconi, C.; Moskalenko, A.; Cherniukh, I.; Dirin, D.; Bodnarchuk, M. I.; Kovalenko, M. V.; Rainò, G. Room-Temperature, Highly Pure Single-Photon Sources from All-Inorganic Lead Halide Perovskite Quantum Dots. *Nano Lett.* **2022**, *22*, 3751–3760. https://doi.org/10.1021/acs.nanolett.2c00756.

(21) Michler, P.; Imamoğlu, A.; Mason, M. D.; Carson, P. J.; Strouse, G. F.; Buratto, S. K. Quantum Correlation among Photons from a Single Quantum Dot at Room Temperature. *Nature* **2000**, *406*, 968–970. https://doi.org/10.1038/35023100.

(22) Chandrasekaran, V.; Tessier, M. D.; Dupont, D.; Geiregat, P.; Hens, Z.; Brainis, E. Nearly Blinking-Free, High-Purity Single-Photon Emission by Colloidal InP/ZnSe Quantum Dots. *Nano Lett.* **2017**, *17*, 6104–6109. https://doi.org/10.1021/acs.nanolett.7b02634.

(23) Sebald, K.; Michler, P.; Passow, T.; Hommel, D.; Bacher, G.; Forchel, A. Single-Photon Emission of CdSe Quantum Dots at Temperatures up to 200 K. *Appl. Phys. Lett.* **2002**, *81*, 2920–2922. https://doi.org/10.1063/1.1515364.

(24) Lin, X.; Dai, X.; Pu, C.; Deng, Y.; Niu, Y.; Tong, L.; Fang, W.; Jin, Y.; Peng, X. Electrically-Driven Single-Photon Sources Based on Colloidal Quantum Dots with near-Optimal Antibunching at Room Temperature. *Nat. Commun.* **2017**, *8*, 1132. https://doi.org/10.1038/s41467-017-01379-6.

(25) Morozov, S.; Pensa, E. L.; Khan, A. H.; Polovitsyn, A.; Cortés, E.; Maier, S. A.; Vezzoli, S.; Moreels, I.; Sapienza, R. Electrical Control of Single-Photon Emission in Highly Charged Individual Colloidal Quantum Dots. *Sci. Adv.* **2020**, *6*, eabb1821. https://doi.org/10.1126/sciadv.abb1821.

(26) Chen, Y.; Ryou, A.; Friedfeld, M. R.; Fryett, T.; Whitehead, J.; Cossairt, B. M.; Majumdar, A. Deterministic Positioning of Colloidal Quantum Dots on Silicon Nitride Nanobeam Cavities. *Nano Lett.* **2018**, *18*, 6404–6410. https://doi.org/10.1021/acs.nanolett.8b02764.

(27) Xu, X.; Jin, S. Strong Coupling of Single Quantum Dots with Low-Refractive-Index/High-Refractive-Index Materials at Room Temperature. *Sci. Adv.* **2020**, *6*, eabb3095. https://doi.org/10.1126/sciadv.abb3095.

(28) Cui, Y.; Björk, M. T.; Liddle, J. A.; Sönnichsen, C.; Boussert, B.; Alivisatos, A. P. Integration of Colloidal Nanocrystals into Lithographically Patterned Devices. *Nano Lett.* **2004**, *4*, 1093–1098. https://doi.org/10.1021/nl049488i.

(29) Yadav, R. K.; Liu, W.; Li, R.; Odom, T. W.; Agarwal, G. S.; Basu, J. K. Room-Temperature Coupling of Single Photon Emitting Quantum Dots to Localized and Delocalized Modes in a Plasmonic Nanocavity Array. *ACS Photonics* **2021**, *8*, 576–584. https://doi.org/10.1021/acsphotonics.0c01635.

(30) Yadav, R. K.; Bourgeois, M. R.; Cherqui, C.; Juarez, X. G.; Wang, W.; Odom, T. W.; Schatz, G. C.; Basu, J. K. Room Temperature Weak-to-Strong Coupling and the Emergence of Collective Emission from Quantum Dots Coupled to Plasmonic Arrays. *ACS Nano* **2020**, *14*, 7347–7357. https://doi.org/10.1021/acsnano.0c02785.

(31) Brokmann, X.; Messin, G.; Desbiolles, P.; Giacobino, E.; Dahan, M.; Hermier, J. P. Colloidal CdSe/ZnS Quantum Dots as Single-Photon Sources. *New J. Phys.* **2004**, *6*, 99. https://doi.org/10.1088/1367-2630/6/1/099.

(32) Holzner, F.; Kuemin, C.; Paul, P.; Hedrick, J. L.; Wolf, H.; Spencer, N. D.; Duerig, U.; Knoll, A. W. Directed Placement of Gold Nanorods Using a Removable Template for Guided Assembly. *Nano Lett.* **2011**, *11*, 3957–3962. https://doi.org/10.1021/nl202276q.

(33) Malaquin, L.; Kraus, T.; Schmid, H.; Delamarche, E.; Wolf, H. Controlled Particle Placement through Convective and Capillary Assembly. *Langmuir* **2007**, *23*, 11513–11521. https://doi.org/10.1021/la700852c.

(34) Eich, A.; Spiekermann, T. C.; Gehring, H.; Sommer, L.; Bankwitz, J. R.; Schrinner, P. P. J.; Preuß, J. A.; Michaelis de Vasconcellos, S.; Bratschitsch, R.; Pernice, W. H. P.; Schuck, C. Single-Photon Emission from Individual Nanophotonic-Integrated Colloidal Quantum Dots. *ACS Photonics* **2022**, *9*, 551–558. https://doi.org/10.1021/acsphotonics.1c01493.

(35) Zhang, Q.; Dang, C.; Urabe, H.; Wang, J.; Sun, S.; Nurmikko, A. Large Ordered Arrays of Single Photon Sources Based on II–VI Semiconductor Colloidal Quantum Dot. *Opt. Express* **2008**, *16*, 19592–19599. https://doi.org/10.1364/oe.16.019592.

(36) Kim, J.-H.; Aghaeimeibodi, S.; Richardson, C. J. K.; Leavitt, R. P.; Englund, D.; Waks, E. Hybrid Integration of Solid-State Quantum Emitters on a Silicon Photonic Chip. *Nano Lett.* **2017**, *17*, 7394–7400. https://doi.org/10.1021/acs.nanolett.7b03220.

(37) Davanco, M.; Liu, J.; Sapienza, L.; Zhang, C.-Z.; De Miranda Cardoso, J. V.; Verma, V.; Mirin, R.; Nam, S. W.; Liu, L.; Srinivasan, K. Heterogeneous Integration for On-Chip Quantum Photonic Circuits with Single Quantum Dot Devices. *Nat. Commun.* **2017**, *8*, 889. https://doi.org/10.1038/s41467-017-00987-6.

(38) Kolchin, P.; Pholchai, N.; Mikkelsen, M. H.; Oh, J.; Ota, S.; Islam, M. S.; Yin, X.; Zhang, X. High Purcell Factor Due To Coupling of a Single Emitter to a Dielectric Slot Waveguide. *Nano Lett.* **2015**, *15*, 464–468. https://doi.org/10.1021/nl5037808.

(39) Cohen, T. A.; Sharp, D.; Kluherz, K. T.; Chen, Y.; Munley, C.; Anderson, R. T.; Swanson, C. J.; De Yoreo, J. J.; Luscombe, C. K.; Majumdar, A.; Gamelin, D. R.; Mackenzie, J. D. Direct Patterning of Perovskite Nanocrystals on Nanophotonic Cavities with Electrohydrodynamic Inkjet Printing. *Nano Lett.* **2022**, *22*, 5681–5688. https://doi.org/10.1021/acs.nanolett.2c00473.

(40) Nann, T.; Mulvaney, P. Single Quantum Dots in Spherical Silica Particles. *Angew. Chem., Int. Ed.* **2004**, *43*, 5393–5396. https://doi.org/10.1002/anie.200460752.

(41) Ma, Y.; Li, Y.; Ma, S.; Zhong, X. Highly Bright Water-Soluble Silica Coated Quantum Dots with Excellent Stability. *J. Mater. Chem. B* **2014**, *2*, 5043–5051. https://doi.org/10.1039/c4tb00458b.

(42) Hu, X.; Zrazhevskiy, P.; Gao, X. Encapsulation of Single Quantum Dots with Mesoporous Silica. *Ann. Biomed. Eng.* **2009**, *37*, 1960–1966. https://doi.org/10.1007/s10439-009-9660-y.

(43) Goftman, V. V.; Aubert, T.; Ginste, D. V.; Van Deun, R.; Beloglazova, N. V.; Hens, Z.; De Saeger, S.; Goryacheva, I. Y. Synthesis, modification, bioconjugation of silica coated fluorescent quantum dots and their application for mycotoxin detection. *Biosens. Bioelectron.* **2016**, *79*, 476–481. https://doi.org/10.1016/j.bios.2015.12.079.

(44) Aubert, T.; Soenen, S. J.; Wassmuth, D.; Cirillo, M.; Van Deun, R.; Braeckmans, K.; Hens, Z. Bright and Stable CdSe/CdS@SiO2 Nanoparticles Suitable for Long-Term Cell Labeling. *ACS Appl. Mater. Interfaces* **2014**, *6*, 11714–11723. https://doi.org/10.1021/am502367b.

(45) Huang, Y.; Cohen, T. A.; Sperry, B. M.; Larson, H.; Nguyen, H. A.; Homer, M. K.; Dou, F. Y.; Jacoby, L. M.; Cossairt, B. M.; Gamelin, D. R.; Luscombe, C. K. Organic Building Blocks at Inorganic Nanomaterial Interfaces. *Mater. Horiz.* **2022**, *9*, 61–87. https://doi.org/10.1039/d1mh01294k.

(46) Shulevitz, H. J.; Huang, T.-Y.; Xu, J.; Neuhaus, S. J.; Patel, R. N.; Choi, Y. C.; Bassett, L. C.; Kagan, C. R. Template-Assisted Self-Assembly of Fluorescent Nanodiamonds for Scalable Quantum Technologies. *ACS Nano* **2022**, *16*, 1847–1856. https://doi.org/10.1021/acsnano.1c09839.

(47) Greybush, N. J.; Pacheco-Peña, V.; Engheta, N.; Murray, C. B.; Kagan, C. R. Plasmonic Optical and Chiroptical Response of Self-Assembled Au Nanorod Equilateral Trimers. *ACS Nano* **2019**, *13*, 1617–1624. https://doi.org/10.1021/acsnano.8b07619.

(48) Chen, Y.; Vela, J.; Htoon, H.; Casson, J. L.; Werder, D. J.; Bussian, D. A.; Klimov, V. I.; Hollingsworth, J. A. "Giant" Multishell CdSe Nanocrystal Quantum Dots with Suppressed Blinking. *J. Am. Chem. Soc.* **2008**, *130*, 5026–5027. https://doi.org/10.1021/ja711379k.

(49) Gong, K.; Kelley, D. F. Lattice Strain Limit for Uniform Shell Deposition in Zincblende CdSe/CdS Quantum Dots. *J. Phys. Chem. Lett.* **2015**, *6*, 1559–1562. https://doi.org/10.1021/acs.jpclett.5b00566.

(50) Pahomi, T. E.; Cheche, T. O. Strain Influence on Optical Absorption of Giant Semiconductor Colloidal Quantum Dots. *Chem. Phys. Lett.* **2014**, *612*, 33–38. https://doi.org/10.1016/j.cplett.2014.07.078.

(51) Rafipoor, M.; Dupont, D.; Tornatzky, H.; Tessier, M. D.; Maultzsch, J.; Hens, Z.; Lange, H. Strain Engineering in InP/(Zn,Cd)Se Core/Shell Quantum Dots. *Chem. Mater.* **2018**, *30*, 4393–4400. https://doi.org/10.1021/acs.chemmater.8b01789.

(52) Hanifi, D. A.; Bronstein, N. D.; Koscher, B. A.; Nett, Z.; Swabeck, J. K.; Takano, K.; Schwartzberg, A. M.; Maserati, L.; Vandewal, K.; van de Burgt, Y.; Salleo, A.; Alivisatos, A. P. Redefining Near-Unity Luminescence in Quantum Dots with Photothermal Threshold Quantum Yield. *Science* **2019**, *363*, 1199–1202. https://doi.org/10.1126/science.aat3803.

(53) Chen, O.; Zhao, J.; Chauhan, V. P.; Cui, J.; Wong, C.; Harris, D. K.; Wei, H.; Han, H.-S.; Fukumura, D.; Jain, R. K.; Bawendi, M. G. Compact High-Quality CdSe–CdS Core–Shell Nanocrystals with Narrow Emission Linewidths and Suppressed Blinking. *Nat. Mater.* **2013**, *12*, 445–451. https://doi.org/10.1038/nmat3539.

(54) Darbandi, M.; Thomann, R.; Nann, T. Single Quantum Dots in Silica Spheres by Microemulsion Synthesis. *Chem. Mater.* **2005**, *17*, 5720–5725. https://doi.org/10.1021/cm051467h.

(55) Yang, Y.; Jing, L.; Yu, X.; Yan, D.; Gao, M. Coating Aqueous Quantum Dots with Silica via Reverse Microemulsion Method: Toward Size-Controllable and Robust Fluorescent Nanoparticles. *Chem. Mater.* **2007**, *19*, 4123–4128. https://doi.org/10.1021/cm070798m.

(56) Selvan, S. T.; Tan, T. T.; Ying, J. Y. Robust, Non-Cytotoxic, Silica-Coated CdSe Quantum Dots with Efficient Photoluminescence. *Adv. Mater.* **2005**, *17*, 1620–1625. https://doi.org/10.1002/adma.200401960.

(57) Wang, N.; Koh, S.; Jeong, B. G.; Lee, D.; Kim, W. D.; Park, K.; Nam, M. K.; Lee, K.; Kim, Y.; Lee, B.-H.; Lee, K.; Bae, W. K.; Lee, D. C. Highly Luminescent Silica-Coated CdS/CdSe/CdS Nanoparticles with Strong Chemical Robustness and Excellent Thermal Stability. *Nanotechnology* **2017**, *28*, 185603. https://doi.org/10.1088/1361-6528/aa6828.

(58) Zhang, A.; Chen, L.; Wang, M.; Li, J.; Chen, L.; Shi, R.; Zhang, N.; Yang, P. Study on the Luminescence Stability of CdSe/CdxZn1-XS Quantum Dots during the Silication Process. *J. Lumin.* **2020**, *219*, 116907. https://doi.org/10.1016/j.jlumin.2019.116907.

(59) Anderson, B. D.; Wu, W.-C.; Tracy, J. B. Silica Overcoating of CdSe/CdS Core/Shell Quantum Dot Nanorods with Controlled Morphologies. *Chem. Mater.* **2016**, *28*, 4945–4952. https://doi.org/10.1021/acs.chemmater.6b01225.

(60) Wang, X.; Li, W.; Zhao, B.; Zhang, D.; Sun, K.; An, X.; Zhang, Z.; Shen, Z. Highly Fluorescent Quantum Dot@silica Nanoparticles by a Novel Post-Treatment for Live Cell Imaging. *RSC Adv.* **2013**, *3*, 3553–3556. https://doi.org/10.1039/c3ra22782k.

(61) Goryacheva, O. A.; Wegner, K. D.; Sobolev, A. M.; Häusler, I.; Gaponik, N.; Goryacheva, I. Y.; Resch-Genger, U. Influence of Particle Architecture on the Photoluminescence Properties of Silica-Coated CdSe Core/Shell Quantum Dots. *Anal. Bioanal. Chem.* **2022**, *414*, 4427–4439. https://doi.org/10.1007/s00216-022-04005-7.

(62) Cao, H.; Ma, J.; Huang, L.; Qin, H.; Meng, R.; Li, Y.; Peng, X. Design and Synthesis of Antiblinking and Antibleaching Quantum Dots in Multiple Colors via Wave Function Confinement. *J. Am. Chem. Soc.* **2016**, *138*, 15727–15735. https://doi.org/10.1021/jacs.6b10102.

(63) Qin, H.; Meng, R.; Wang, N.; Peng, X. Photoluminescence Intermittency and Photo-Bleaching of Single Colloidal Quantum Dot. *Adv. Mater.* **2017**, *29*, 1606923. https://doi.org/10.1002/adma.201606923

(64) van Sark, W. G. J. H. M.; Frederix, P. L. T. M.; Bol, A. A.; Gerritsen, H. C.; Meijerink, A. Blueing, Bleaching, and Blinking of Single CdSe/ZnS Quantum Dots. *ChemPhysChem* **2002**, *3*, 871–879. https://doi.org/10.1002/1439-7641(20021018)3:10<871::aid-cphc871>3.0.co;2-t.

(65) Lee, S. F.; Osborne, M. A. Brightening, Blinking, Bluing and Bleaching in the Life of a Quantum Dot: Friend or Foe?. *ChemPhysChem* **2009**, *10*, 2174–2191. https://doi.org/10.1002/cphc.200900200.

(66) Orfield, N. J.; McBride, J. R.; Wang, F.; Buck, M. R.; Keene, J. D.; Reid, K. R.; Htoon, H.; Hollingsworth, J. A.; Rosenthal, S. J. Quantum Yield Heterogeneity among Single Nonblinking Quantum Dots Revealed by Atomic Structure-Quantum Optics Correlation. *ACS Nano* **2016**, *10*, 1960–1968. https://doi.org/10.1021/acsnano.5b05876.

(67) Yuan, Z.; Kardynal, B. E.; Stevenson, R. M.; Shields, A. J.; Lobo, C. J.; Cooper, K.; Beattie, N. S.; Ritchie, D. A.; Pepper, M. Electrically Driven Single-Photon Source. *Science* **2002**, *295*, 102–105. https://doi.org/10.1126/science.1066790.

(68) Brokmann, X.; Giacobino, E.; Dahan, M.; Hermier, J. P. Highly Efficient Triggered Emission of Single Photons by Colloidal CdSe/ZnS Nanocrystals. *Appl. Phys. Lett.* **2004**, *85*, 712–714. https://doi.org/10.1063/1.1775280.

(69) Yin, Y.; Lu, Y.; Gates, B.; Xia, Y. Template-Assisted Self-Assembly: A Practical Route to Complex Aggregates of Monodispersed Colloids with Well-Defined Sizes, Shapes, and Structures. *J. Am. Chem. Soc.* **2001**, *123*, 8718–8729. https://doi.org/10.1021/ja011048v.

(70) Mehraeen, S.; Asbahi, M.; Fuke, W.; Yang, J. K. W.; Cao, J.; Tan, M. C. Directed Self-Assembly of Sub-10 Nm Particles: Role of Driving Forces and Template Geometry in Packing and Ordering. *Langmuir* **2015**, *31*, 8548–8557. https://doi.org/10.1021/acs.langmuir.5b01696.

(71) Asbahi, M.; Mehraeen, S.; Wang, F.; Yakovlev, N.; Chong, K. S. L.; Cao, J.; Tan, M. C.; Yang, J. K. W. Large Area Directed Self-Assembly of Sub-10 Nm Particles with Single Particle Positioning Resolution. *Nano Lett.* **2015**, *15*, 6066–6070. https://doi.org/10.1021/acs.nanolett.5b02291.

Chapter 5. COLOSSAL CORE/SHELL CDSE/CDS QUANTUM DOTS

This chapter focuses on the shelling approach to grow extremely large core/shell CdSe/CdS particles and how they are printed onto large arrays and deterministically onto nanobeam cavities. Components of this chapter were republished with permission of the American Chemical Society, from "*Colossal Core/Shell CdSe/CdS Quantum Dot Emitters*", Hao A. Nguyen, Benjamin F. Hammel, David Sharp, Jessica Kline, Griffin Schwartz, Samantha Harvey, Emily Nishiwaki, Soren F. Sandeno, David S. Ginger, Arka Majumdar, Sadegh Yazdi, Gordana Dukovic, and Brandi M. Cossairt; *ACS Nano* **2024,** *18, 31,* 20726–20739; and "*Deterministic printing and heterointegration of single colloidal quantum dot photon sources*", Gregory G. Guymon, Hao A. Nguyen, David Sharp, Tommy Nguyen, Henry Lei, David S. Ginger, Kai-Mei C. Fu, Arka Majumdar, Brandi M. Cossairt, and J. Devin MacKenzie; Copyright 2025 American Chemical Society.

5.1 INTRODUCTION

Single-photon sources are key components in advancing next-generation quantum technologies, wherein photons are employed as information carriers.[1–3] Extensive interdisciplinary research conducted over the past several decades has identified a variety of materials that can be used as single-photon sources, including trapped ions,[4,5] diamond color centers,[6,7] two-dimensional materials,[8,9] small molecules,[10,11] and semiconducting QDs. [3,12,13] Each class of materials presents advantages and limitations in single-photon emission performance and device integration. For these materials to be practically applied in quantum devices, a crucial requirement is scalability.[14–16] This involves the deterministic positioning of identical single-photon sources into large arrays, which can then be integrated with functional nanophotonic structures. In this

context, colloidal QDs, especially core/shell and perovskite QDs, are the most promising candidates due to their solution processability, which facilitates large-scale synthesis and integration into nanoscale devices.[14,15,17−19]

While a colloidal QD itself can generate single photons, its potential for practical applications as a single-photon source, even for very high-quality QDs, is intrinsically limited due to ensemble inhomogeneity and batch-to-batch variation,[20] nondirectional emission,[21] photon losses in the substrate,[22] distinguishable photons emitted from the same QD,[23] and low single-photon generation rates, except for lead halide perovskite QDs.[24−26] To improve upon the current state of the art, an integrated system is required.[1,14,23,27] More specifically, a QD single-photon emitter needs to be deterministically placed in the region of maximum electromagnetic field of an optical cavity for enhanced emission through the Purcell effect.[14,28] Current demonstrations of single-photon emission and cavity-coupling from QDs are often limited to random placement of single QDs on solid substrates[29,30] or manipulation of particle position via top-down fabrication tools,[31−34] thus providing no path for scalability. Meanwhile, large-scale placement of single nanoparticles requires substrates with nano- or microscale traps created through electron beam lithography, where the size compatibility between the traps and the particles is crucial.[14,15,30,35] Existing single-particle patterning techniques are typically less efficient with smaller particles. Therefore, increasing the size of the particles offers a promising solution to enhance the efficiency of this process.

QDs are small, with diameters typically ranging from ∼3 to 6 nm. Inorganic shells, typically Cd- and Zn-based, are grown on the cores to improve their chemical stability and PL.[36] These core/shell QDs, composed of materials with different band gaps and band alignments, show a variety of optical properties due to their overall composition and shell thickness. Furthermore,

external silica shells can be grown on core/shell QDs to increase the particle size to near 100 nm.[17,37] Although silica shells provide a path for deterministic positioning of emissive QDs, the single-particle PL of silica-shelled QDs suffers a high degree of blinking due to additional charged states induced by the CdS-SiO_2 interface.[17,38]

The largest emissive QDs without silica shells reported in the literature to date are the traditional quasi-type II giant core/shell CdSe/CdS QDs, with 15–20 CdS MLs and total diameters ranging from 20 to 50 nm.[39−42] The giant CdS shells not only increase the size of the emissive QDs but also reduce blinking through Auger recombination suppression and isolate the exciton from surface interactions.[39,43,44] In these quasi-type II core/shell systems, the electron wave function is delocalized into the CdS shell, while the hole wave function is effectively confined within the CdSe core. This geometric separation of charge carriers results in multiexciton formation that is advantageous for lasing and can affect the single-photon purity.[42,45−48]

The two main methods to grow large core/shell CdSe/CdS are successive ionic layer adsorption and reaction (SILAR) and high-temperature continuous injection (HTCI).[39,40,49] The differences between the two methods and the correlation between synthetic conditions and QD properties have been rigorously studied by Hollingsworth and co-workers.[39,40,50,51] By examining ∼20 nm, truncated octahedral QDs prepared by the two methods, they showed that while both methods result in nonblinking QDs with high stability, QDs prepared by the HTCI method have significantly higher PLQY while QDs prepared by the SILAR method have better optical stability at ambient conditions.[40] Further in-depth analysis revealed that high crystalline quality with high interfacial alloying and low defect concentrations in the CdS shells could be achieved with the HTCI method by postsynthetic annealing and the use of 1-octanethiol, which acts as both S precursor and growth-facilitating ligand.[40] Using the HTCI method but with S dissolved in ODE

(S-ODE) as the sulfur precursor instead of 1-octanethiol, Dubertret and co-workers were also able to grow CdSe/CdS QDs with sizes up to 50 nm.[42] Meanwhile, Chen and co-workers have proposed three key design rules to form large, flat-faceted particles, including (1) slow epitaxial shell growth, (2) avoiding additional oleic acid, and postsynthesis annealing, which smooth out flat facets toward a spherical shape, and (3) intermediate purification steps to remove unreacted materials and byproducts for monodisperse products.[52] Leveraging these insights using the HTCI method enabled consistent syntheses of monodisperse bipyramidal wurtzite CdSe/CdS QDs with a longest dimension of 22 nm. In a different study, Bals and co-workers synthesized bullet-shaped CdSe/CdS QDs with a size of 30 nm using the SILAR method, and S-ODE.[41] These findings delineate the nuanced parameters for large QD synthesis and highlight an open question: what is the maximum QD size achievable without sacrificing the optical emission properties?

Motivated by the need for scalable and deterministic positioning of colloidal QD single-photon emitters in optical cavities, we introduce in this paper a series of "colossal" QDs, an extension of the class of giant QDs, with particle diameters exceeding 100 nm. We show that using a stepwise HTCI method with 1-octanethiol as our S precursor, we can systematically grow ultrathick CdS shells on wurtzite CdSe cores. The particle formation and morphology are studied by synthetic and electron microscopic analyses. The colossal QDs exhibit long PL lifetimes on the order of microseconds and suppressed blinking at room temperature. Surprisingly, high single-photon emission purity with low second-order photon correlation $g^{(2)}(\tau = 0)$ values are observed even for QDs with 80 and 100 CdS ML shells.

5.2 SYNTHESIS OF COLOSSAL QDS

All samples in this study were synthesized by growing CdS shells on 3.5 nm wurtzite CdSe cores using a modified HTCI method.[49,52] Cadmium oleate and 1-octanethiol (both 0.2 M in ODE) were used as the shell growth precursors. The final size and the number of shell MLs of the resultant core/shell CdSe/CdS QD can be estimated by assuming spherical particles and a thickness for one CdS ML of 0.3375 nm. With this estimation, a direct HTCI synthesis of 50 nm core/shell CdSe/CdS QDs, starting from 50 nmol of CdSe cores, would require 350 mL of each precursor solution and a continuous injection period of 114 h at the standard rate of 3 mL/h, an approach that is unfeasible in most research laboratories. Therefore, we sought to grow colossal QDs using a multistep growth strategy, wherein only a fraction of a previously synthesized batch is used for the next growth step.

The stepwise synthesis used to achieve 100 CdS MLs is described here as an example (**Figure 5.1.a**). Using the HTIC method, 30 MLs of CdS were initially grown on CdSe cores (CdSe30CdS), followed by thermal annealing at 280 °C for 4 h to minimize defects.[53,54] A portion of the CdSe30CdS QD batch was then taken into a new reaction flask, to which 20 MLs of CdS were added, followed by thermal annealing at 280 °C for 4 h to achieve CdSe50CdS. Similarly, CdSe80CdS QDs were synthesized from CdSe50CdS, and CdSe100CdS were synthesized from CdSe80CdS. The injection rate was set at 3 mL/h for all syntheses to maintain the growth of large, monodisperse particles.[40,55] In contrast to the syntheses of hexagonal pyramidal and bipyramidal CdSe/CdS QDs by Tan et al.,[52] purification between steps was not performed to allow more accurate calculations of the additional precursor amounts for the targeted number of CdS MLs based on the initial core concentration.

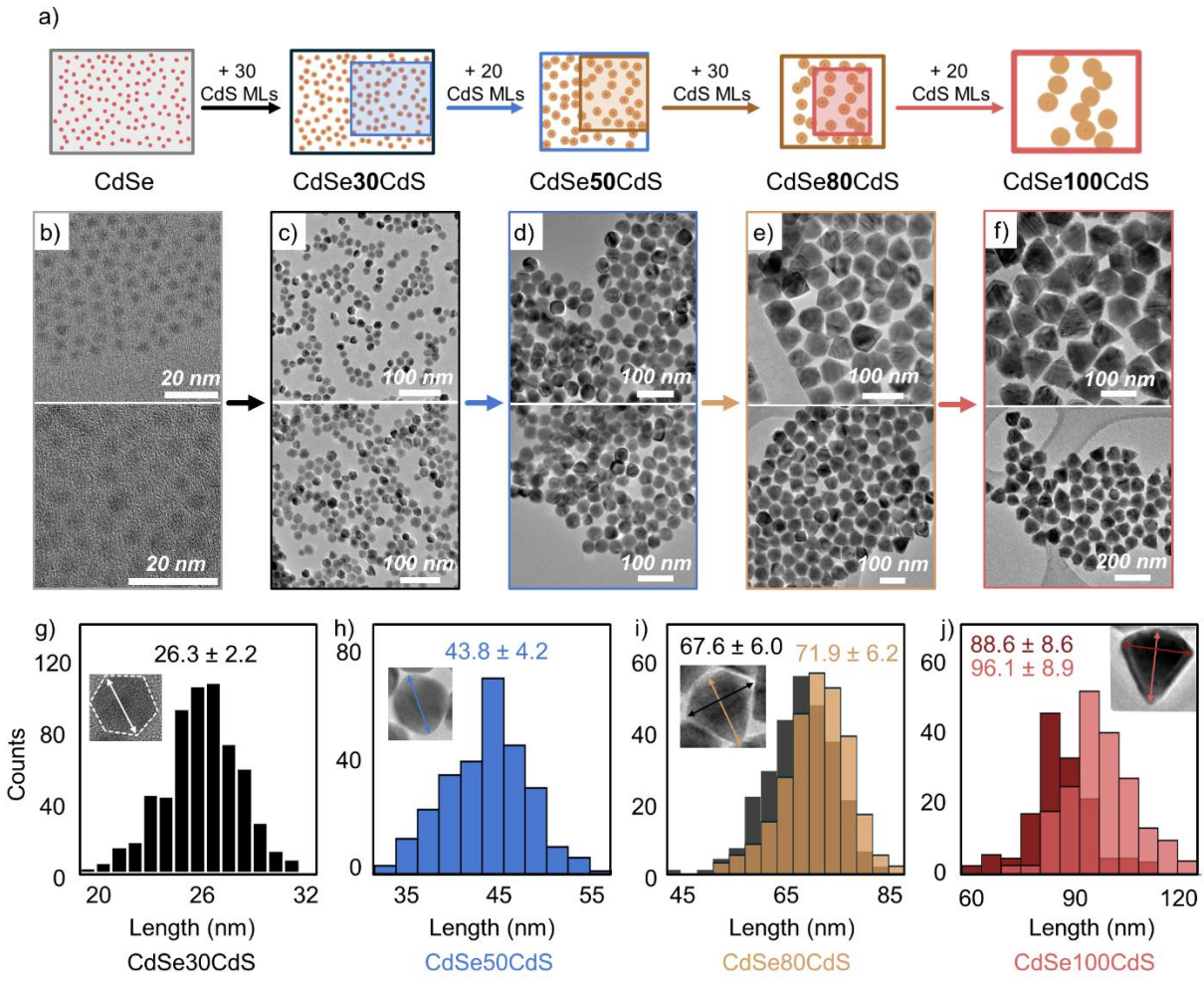

Figure 5.1. **a.** Synthesis scheme for the stepwise CdS shelling of the CdSe cores. TEM images of CdSe cores **b.** and resultant core/shell CdSe/CdS QDs with 30, 50, 80, and 100 CdS MLs **c–f** and their size distributions **g–j**. Insets show a zoomed-in particle, where arrows indicate how measurements were made. In **i.** and **j.** the overlap of the two histograms is shown in the in-between color to represent the distribution of both sets of data.

Figure 5.1.b-j presents TEM images of the CdSe cores and the resultant core/shell QDs, with their relative size distribution as bar graphs. TEM images show that CdSe30CdS QDs have hexagonal projections with sharp corners and flat facets, CdSe50CdS QDs have rounded projections, while the projections of CdSe80CdS and CdSe100CdS QDs are similarly diamond-shaped (the projection distribution for each sample is shown in **Table 5.2**). The QDs with 30, 50,

80, and 100 CdS MLs have average sizes of 26.3 ± 2.2, 43.8 ± 4.2, 69.7 ± 6.5, and 92.4 ± 8.8 nm, respectively, showing a consistent size distribution where the variance does not exceed 10% of the mean size. **Table 5.1** compares the targeted and measured diameters and the number of CdS MLs. The accuracy of size calculations decreases with increasing particle size due to the discrepancy between the spherical particle shape assumption used in the calculations and the actual particle shape.

Table 5.1. Summary of targeted and measured particle diameter and number of CdS MLs. For CdSe80CdS and CdSe100CdS, the listed measured diameters are averages of diagonal and slant height. The number of MLs is calculated using 3.5 nm for the core diameter and 0.3375 nm for the thickness of one ML. For CdSe80CdS and CdSe100CdS, the number of MLs is calculated based on their shorter dimensions.

Samples	**Targeted diameter (nm)**	**Measured size (nm)**	**Targeted number of MLs**	**Measured number of MLs**
CdSe30CdS	23.75	26.3 ± 2.2	30	33.8 ± 3.3
CdSe50CdS	37.25	43.8 ± 4.2	50	59.7 ± 6.2
CdSe80CdS	57.50	69.7 ± 6.5	80	95.0 ± 8.9
CdSe100CdS	71.00	92.4 ± 8.8	100	126.1 ± 12.7

To validate the importance of the stepwise approach, we conducted a series of direct CdS shelling experiments. Without the stepwise approach, direct synthesis with identical conditions

yielded similar particle shapes and sizes only up to 30 CdS MLs (**Figure 5.2**). However, attempts to shell CdSe cores directly with 40 and 50 CdS MLs resulted in a significant amount of twinning, particle instability, and a high level of polydispersity (**Figure 5.2**). This decline in structural integrity can be attributed to the accumulation of unreacted precursors, byproducts, and defects in the shell and at the core–shell interface.[52,53]

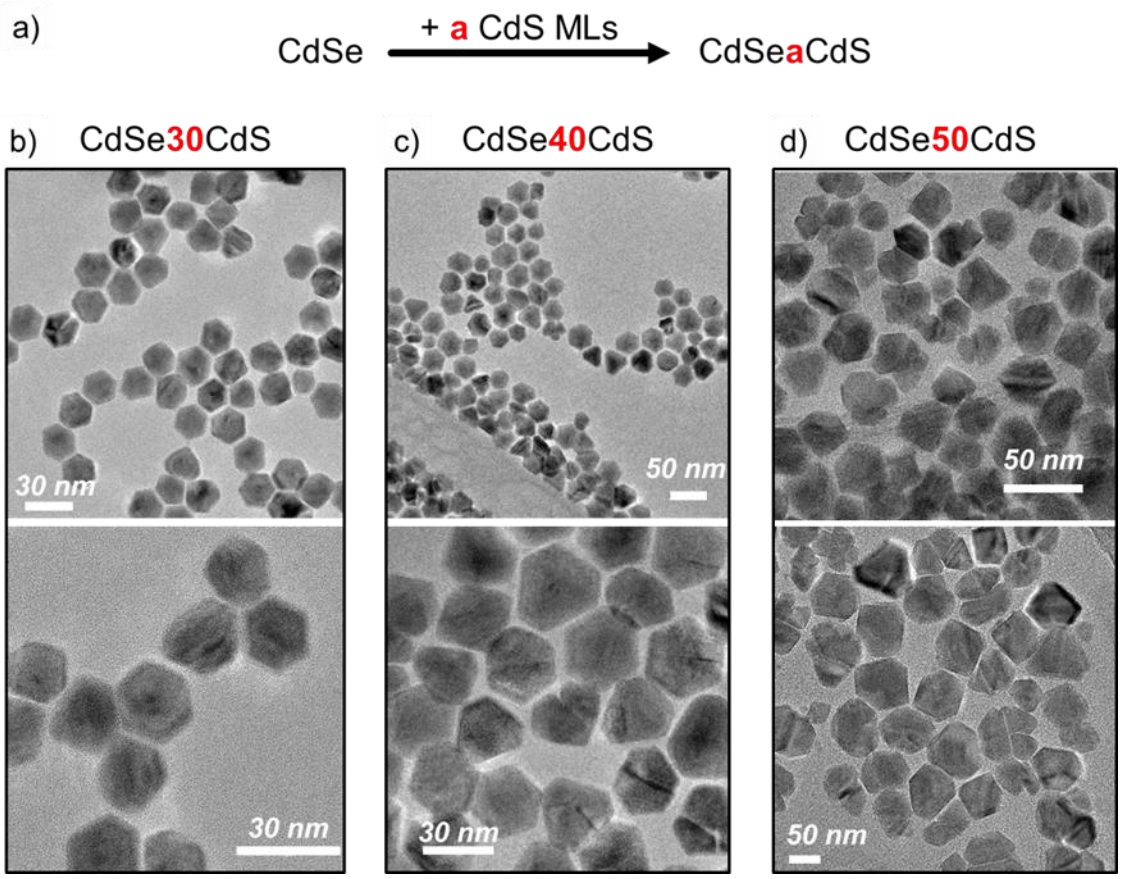

Figure 5.2. a. Synthesis scheme of direct CdS shelling of CdSe cores. TEM images of resultant core/shell CdSe/CdS QDs with 30 **b.**, 40 **c.,** and 50 **d.** CdS MLs.

Following the synthesis of CdSe100CdS QDs using the stepwise shelling strategy, we added calculated amounts of Cd and S precursors to achieve CdSe115CdS (**Figure 5.3.a**, top). However, we observed particle instability (**Figure 5.3.b**). We hypothesize that this instability

stems from the formation of islands on a specific particle facet during the shelling process. Quantitative analysis revealed that 31% of the particles in the CdSe100CdS sample already exhibit island formations (appearing as distinct lumps in the TEM images) exclusively at the base of diamond-shaped projections, the (0001) facet. As known in the literature, the Cd-terminated facets of CdS nanocrystals have higher surface energy than other facets. [56,57] For CdSe100CdS QDs, the large surface area can be substantial enough to facilitate the formation of CdS islands and their subsequent independent growth into larger islands before a new ML uniformly covers the facet. Compared to flat facets, these large islands may generate more considerable surface strain, leading to instability or deformation of the particles at this facet. [58] Additionally, the formation of small nanorods was observed following this shelling step (**Figure 5.3.e**). This is attributed to the gradual dilution of the reaction solution after each step in the stepwise shelling process, which eventually favors the independent nucleation of small particles over shell growth on existing QD seeds. Thus, a higher deposition rate of the precursors and a more concentrated solution are required to achieve uniform deposition of additional shells onto all facets without promoting significant island growth on Cd-rich facets. We carried out two shelling experiments using the same molar amounts of precursors but different concentrations with purified and more concentrated solutions of CdSe100CdS QDs (**Figure 5.3.a**, bottom). Compared with the shelling of a diluted particle sample, minimal particle instability was observed when 0.2 M precursor solutions were used (**Figure 5.3.c**). A total of 95%, or 698 out of 725 particles counted, showed islands at the base of the diamond-shaped particles compared to 31% (142/459) for the CdSe100CdS sample (**Figure 5.3.e**). The hexagon base diagonal and the slant height of the resulting particles increased to 98.6 ± 7.4 and 103.8 ± 7.6 nm, respectively. Conversely, using 0.4 M precursor solutions resulted in almost no islands at the base of the diamond-shaped particles, with more small particles adhering to the

large particles (**Figure 5.3.d**). The diagonal of the hexagon base and the slant height of the resulting particles increased to 95.2 ± 6.5 and 98.5 ± 7.1 nm, respectively. Only 11% or 62 out of 565 counted particles displayed rough surfaces (**Figure 5.3.e**). Additionally, more small nanoparticles were observed around the large particles in this sample, attributed to the higher concentration of the added precursor solutions, which leads to increased independent nucleation and less material being deposited onto the seeds, leading to smaller resulting particles compared to those produced by using the 0.2 M precursor solutions. While it has been demonstrated that CdS particles larger than 200 nm can be synthesized, these methods require the use of highly polar solvent[56] or autoclaves,[59] and the particles produced from these methods are not colloidally stable. Such conditions can undermine the stability of the emissive CdSe cores for shelling. Meanwhile, our findings indicate that growing particles larger than our CdSe100CdS QDs with the current method and conditions becomes increasingly challenging due to complications associated with the relative concentration of precursors and the reaction solution.

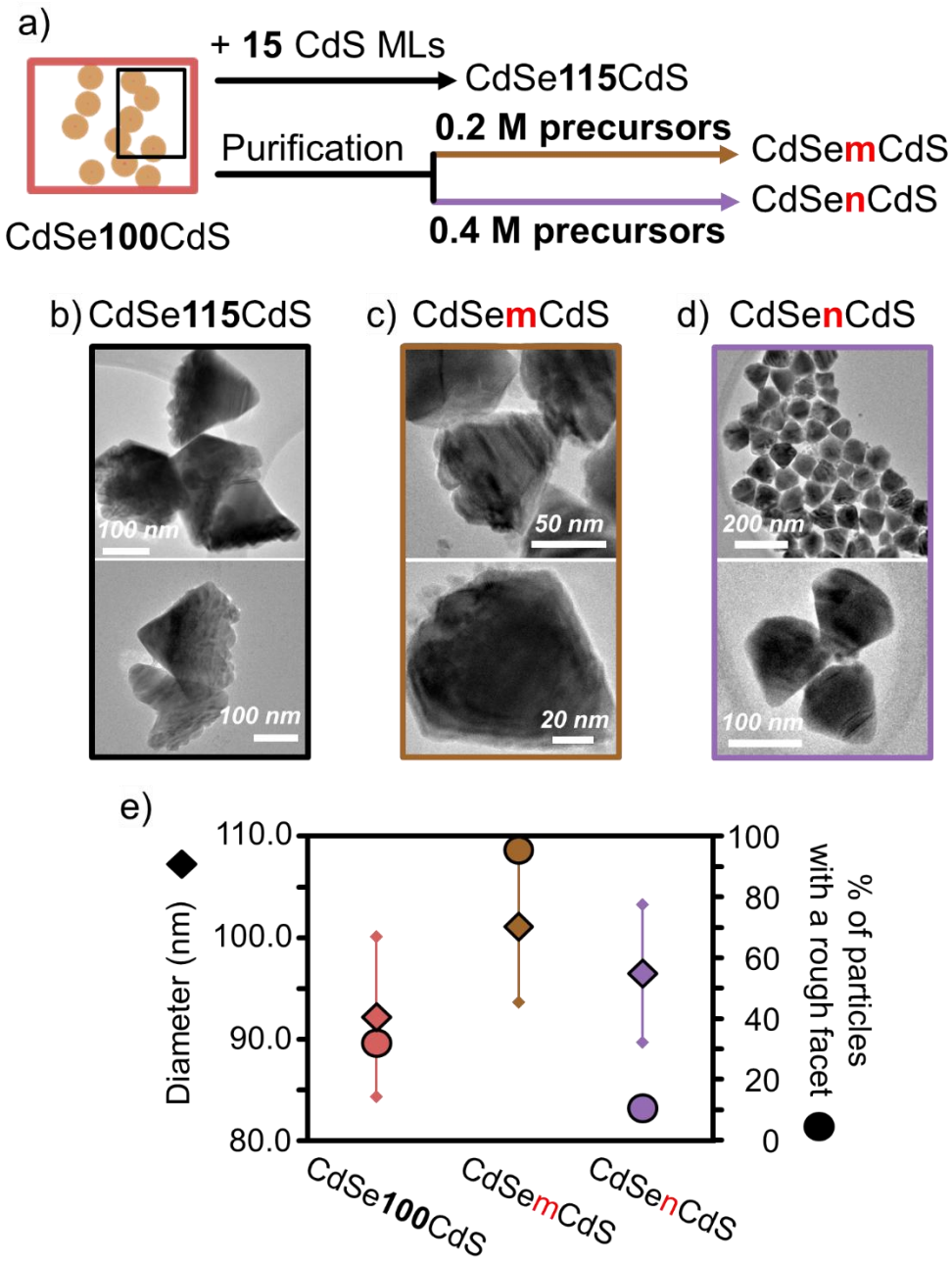

Figure 5.3. a. Synthesis scheme for shelling beyond 100 MLs of CdS from CdSe100CdS. TEM images of resultant core/shell CdSe/CdS QDs with 115 **b.**, m **c.**, and n **d.** CdS MLs, where m, and n are arbitrary numbers of CdS MLs since determination of CdSe100CdS concentration after purification is not possible. **e.** Comparison of particles with a rough facet among CdSe100CdS, CdSe*m*CdS, and CdSe*n*CdS samples.

5.3 Structural Characterization of Colossal QDs

5.3.1 *Shape Analysis and Facet Determination*

Since TEM images only show the particles from one projection, it is ambiguous whether the sample consists of a single-particle morphology observed from many different orientations or is a mixture of different morphologies (**Table 5.2**). To characterize the three-dimensional (3D) shape of the colossal NCs, we performed electron tomography in scanning transmission electron microscopy (STEM) mode on CdSe80CdS and CdSe100CdS QDs. Electron tomography involves acquiring a series of high-angle annular dark-field (HAADF) STEM images of the sample at different tilt angles. This approach allows the same particles to be imaged from multiple orientations. Utilizing the monotonic relationship between the HAADF intensity and projected thickness, the 3D shape of the particles can be reconstructed by processing this series of images. Specifically, we collected roughly 70 images per series from approximately −70 to 70° in 2° increments. We collected a total of five tilt-series on the CdSe80CdS and CdSe100CdS samples. Examination of all five tilt-series provides a nuanced view of the morphology of these colossal CdSe/CdS QDs. Notably, the tilt-series of 17 CdSe80CdS QDs in **Figure 5.4.a** reveals that while the diamond shape is consistent across all the QDs, the overall size and facet dimensions vary between QDs. Tilting the QDs also reveals features not visible from all projections, such as the large crack emerging from the (0001) facet in one CdSe100CdS QD, as shown in **Figure 5.4.e**. **Figure 5.5** shows the tomographic reconstruction of CdSe80CdS and CdSe100CdS QDs, both of which have diamond shapes. This diamond shape resembles the hexagonal pyramidal and bipyramidal CdSe/CdS nanocrystals studied by Tan et al.,[52] who determined the shape to be

defined by (0001) and $\{10\bar{1}1\}$ facets stabilized by phosphonic acid and oleate ligands, respectively. However, unlike the pyramidal nanocrystals, defined by 6 $\{10\bar{1}1\}$ facets and one (0001) facet, or the bipyramidal nanocrystals, defined by 12 $\{10\bar{1}1\}$ facets, the diamond shape we observe appears to be a combination of both cases, being composed of 12 semipolar $\{10\bar{1}1\}$ facets and one polar (0001) facet. This hypothesis was tested with structural modeling in the software VESTA, where we found that the shape of the colossal CdSe/CdS QDs in this study could be approximated by a combination of $\{10\bar{1}1\}$ facets and one (0001) facet. We suspect that the reason there is only one (0001) facet, as opposed to symmetric (0001) and $(000\bar{1})$ facets, is that the particle grows faster in the $[000\bar{1}]$ direction than the [0001] direction as predicted theoretically[61] and observed in wurtzite CdSe nanorods.[52,62]

Table 5.2. Percentage of 2D projections on TEM images.

	Regular hexagon	**Truncated triangle**	**Truncated kite**
CdSe30CdS	25.4	61.7	12.9
CdSe50CdS	-	-	-
CdSe80CdS	17.3	8.2	74.5
CdSe100CdS	18.0	9.9	72.1

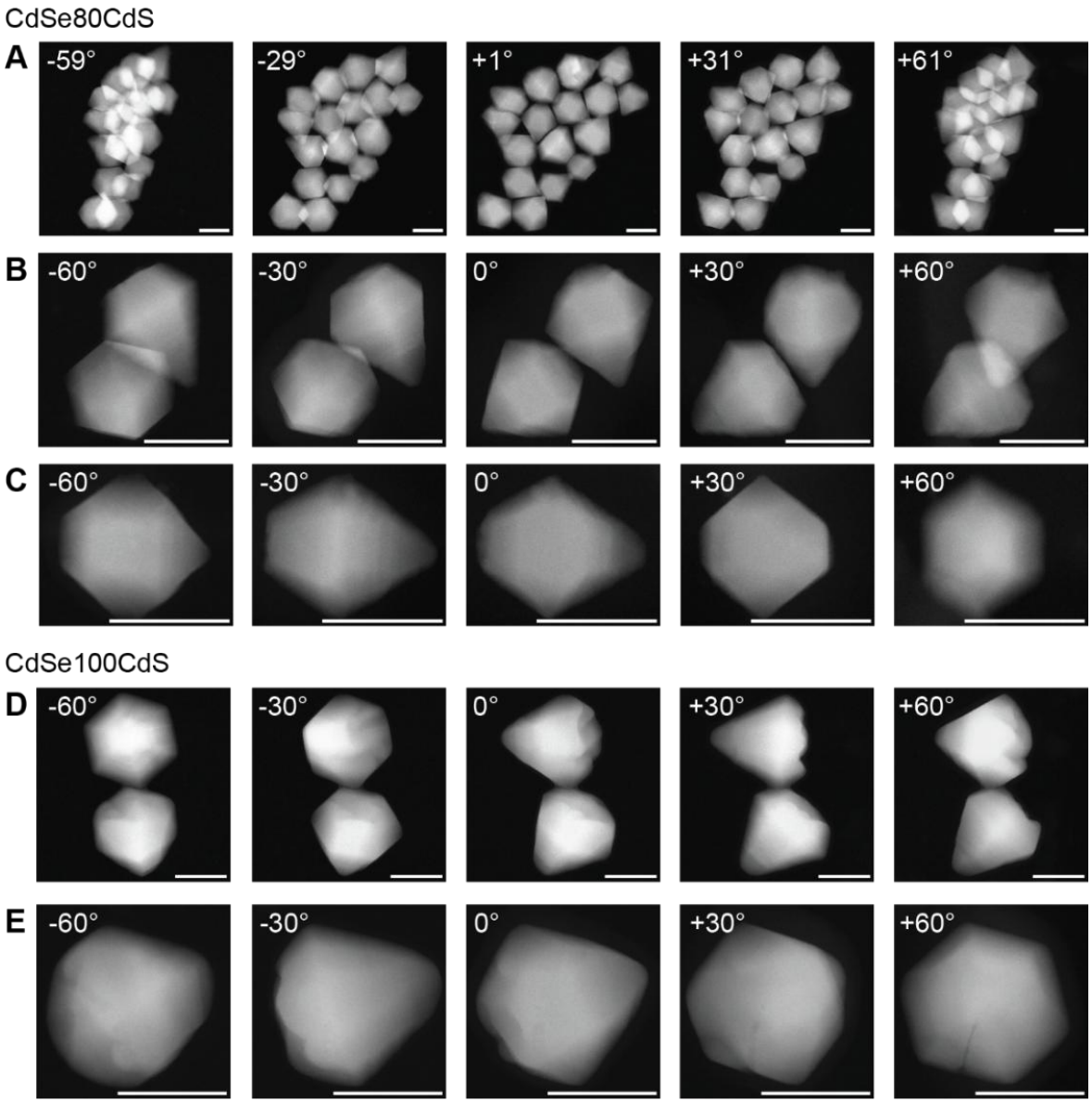

Figure 5.4. Snapshots from the five tilt series collected on CdSe80CdS and CdSe100CdS. Scale bars are 50 nm.

The CdSe80CdS QDs exhibit flat faceting and closely resemble the modeled structure, albeit with some variation in the dimensions and relative size of the facets, as seen in the tilt series snapshots shown in **Figure 5.4**. The CdSe100CdS QDs studied show some deviations from the diamond shape, most notably lumps or ridges at the (0001) facet, as discussed above, which are

resolved by TEM (**Figure 5.1.f**) and STEM (**Figures 5.4 and 5.5**). Overall, tilt series information from multiple particles suggests that while there can be some variation in the dimensions of the particles, the morphology is consistent, defined by semipolar $\{10\bar{1}1\}$ faceting and asymmetric growth on the c-axis, leading to a pointy end in the $[000\bar{1}]$ direction and a flat (0001) facet.

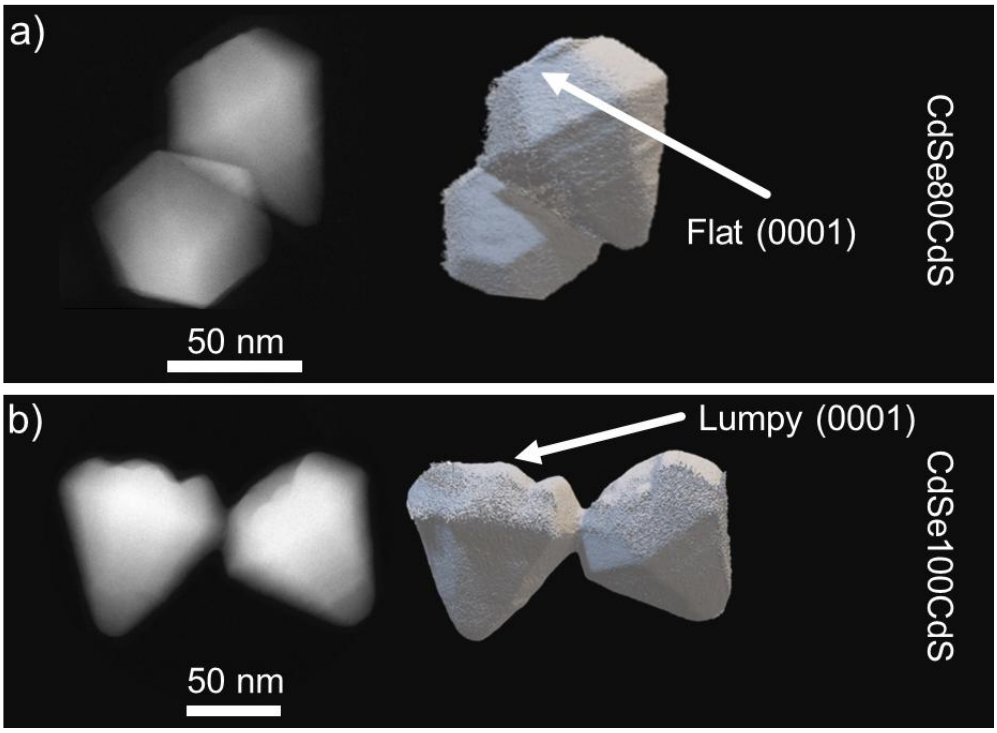

Figure 5.5. a. Left: One image from the tilt series of the CdSe80CdS QDs. Right: Reconstructed tomogram of two CdSe80CdS QDs. **b.** Tilt series and tomogram of two CdSe100CdS QDs.

In the study by Tan et al.,[52] small hexagonal pyramidal core/shell CdSe/CdS particles evolved into a larger, symmetrical hexagonal bipyramidal morphology upon further shelling after purification and the addition of oleylamine to completely remove octadecylphosphonic acid (ODPA) ligands. When more ODPA was added during the shelling of the hexagonal pyramidal CdSe/CdS particles, a large hexagonal pyramidal morphology was formed. In our study, we propose that residual ODPA ligands from the CdSe cores remain strongly bound to the QDs.

Coordination of ODPA to the CdSe cores and core/shell QDs was confirmed by ^{31}P NMR spectroscopy (**Figure 5.6**). This interaction leads to asymmetric shelling in the early stages of the sequential shelling process. As no more ODPA is added, it is significantly diluted at later shelling stages, culminating in a diamond morphology instead of hexagonal pyramidal or bipyramidal morphologies. Together with observations from Tan et al.[52] and Bladt et al.,[41] our results contribute to the library of giant QD morphologies and show that these shapes can be engineered by tuning shelling conditions (**Figure 5.7**). Additionally, the final diamond shape of our particles is similar to large CdS particles grown in polar solvents[56] or autoclave synthesis[59].

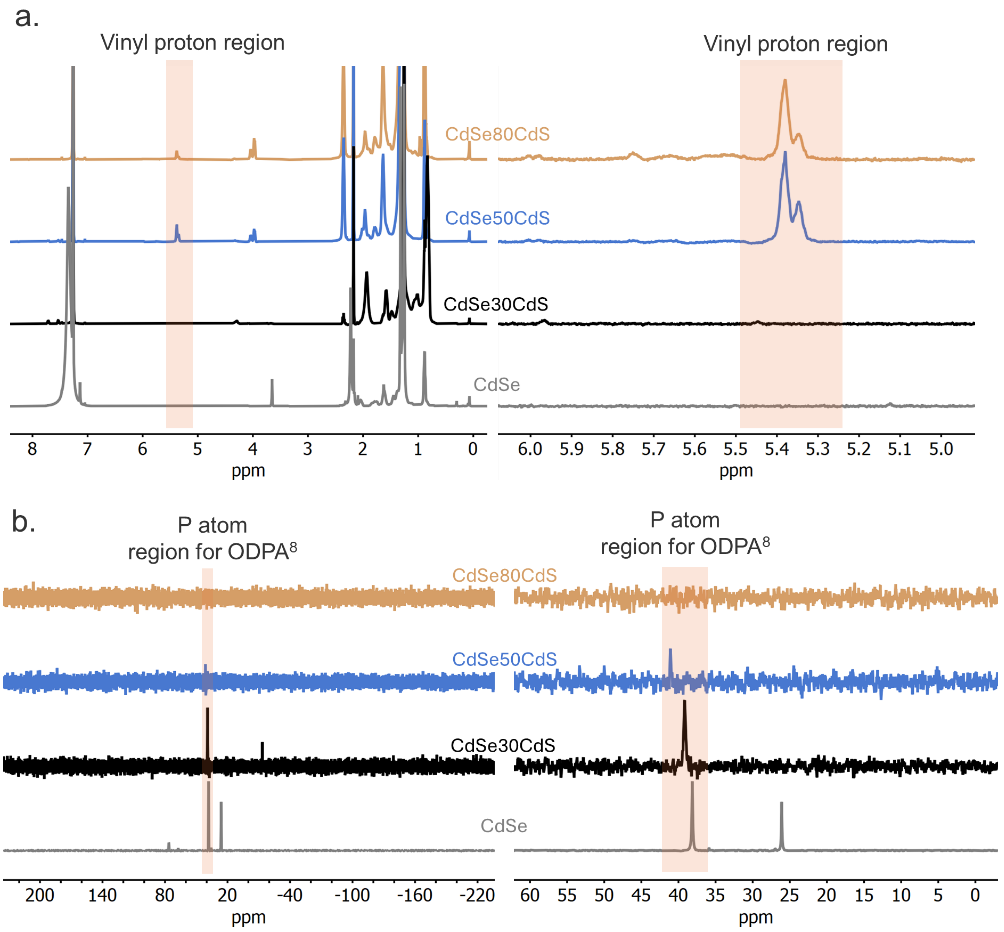

Figure 5.6. Stacked ^{1}H NMR **a.** and ^{31}P NMR **b.** spectra of CdSe cores (gray), CdSe30CdS (black), CdSe50CdS (blue), and CdSe80CdS (yellow) QDs.

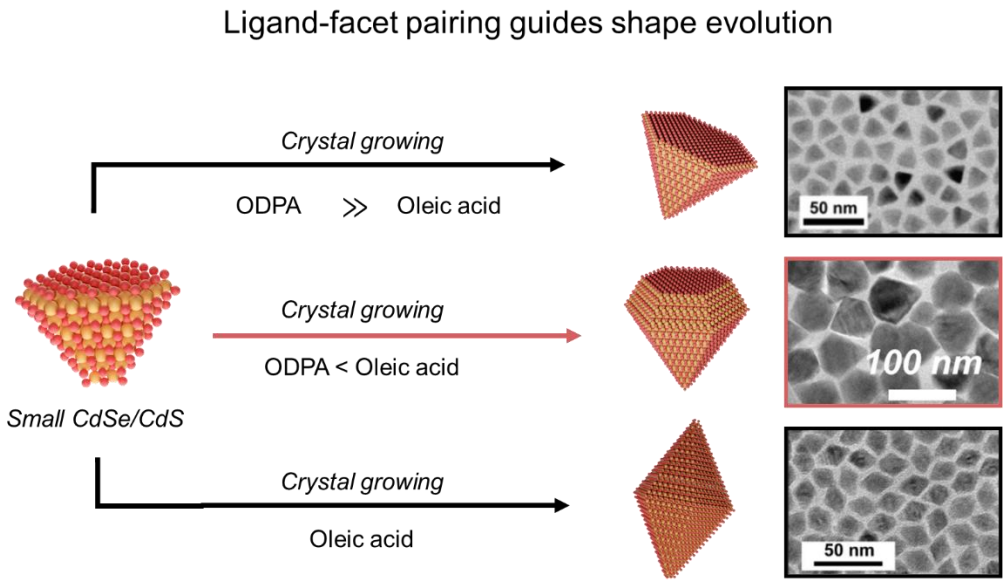

Figure 5.7. Shape evolution from small to giant wurtzite CdSe/CdS QDs governed by ligand ratios while shelling. With ODPA ≫ oleic acid yielding hexagonal pyramids, ODPA < oleic acid hexagonal diamond QDs, while shelling with just oleic acid results in hexagonal bipyramidal QDs. Results and images from the top and bottom cases are from Ou Chen and coworkers.[52]

To examine the morphology and crystal structure of our colossal QDs in greater detail, we performed STEM-HAADF imaging with an atomic resolution. **Figure 5.8** shows CdSe9CdS (obtained by extracting an aliquot during the CdSe30CdS QD synthesis), CdSe30CdS, and CdSe50CdS QDs oriented down well-defined crystallographic directions. The particles are oriented parallel to the [0001] and [1100] directions of the crystal structure, as depicted by the VESTA models. The faceting of these particles from these crystallographic orientations is consistent with the diamond shape from **Figure 5.5** and supports our characterization of the diamond shape as consisting of 12 $\{10\bar{1}1\}$ facets and one (0001) facet. The image of the CdSe9CdS

sample matches well with the structural model. In contrast, in the case of CdSe30CdS and CdSe50CdS, we observe deviations from the model structures, which we interpret as evidence of stacking faults along the c-axis. Stacking faults can be observed directly in the magnified HAADF image in **Figure 5.8.f**. We concluded that the appearance of faint atomic columns in the center of the hexagons in the magnified HAADF image in **Figure 5.8.e** is due to the same type of stacking faults, as discussed in detail in Section S7. The observation of stacking faults in the CdSe30CdS and CdSe50CdS QDs but not in the CdSe9CdS QDs suggests that stacking faults become more common as the shell thickness increases. The stacking faults appear to be relatively concentrated in the shorter [0001] growth direction (**Figure 5.9.a**), consistent with observations of asymmetric concentrations of stacking faults in CdSe nanorods.[62] The asymmetric concentration of stacking faults may also describe patterns observed in the CdSe30CdS QDs oriented down the [0001] direction, as described in more detail in **Figures 5.9**. Asymmetric growth is also observed in Figure 5a, where the shape is nominally hexagonal but some faces are smaller than others. This reduces the symmetry of the structure from 6-fold rotational symmetry to 3-fold rotational symmetry. Overall, atomic resolution STEM-HAADF imaging suggests that colossal CdSe/CdS QDs feature a diamond morphology, with some asymmetry in the growth of the facets.

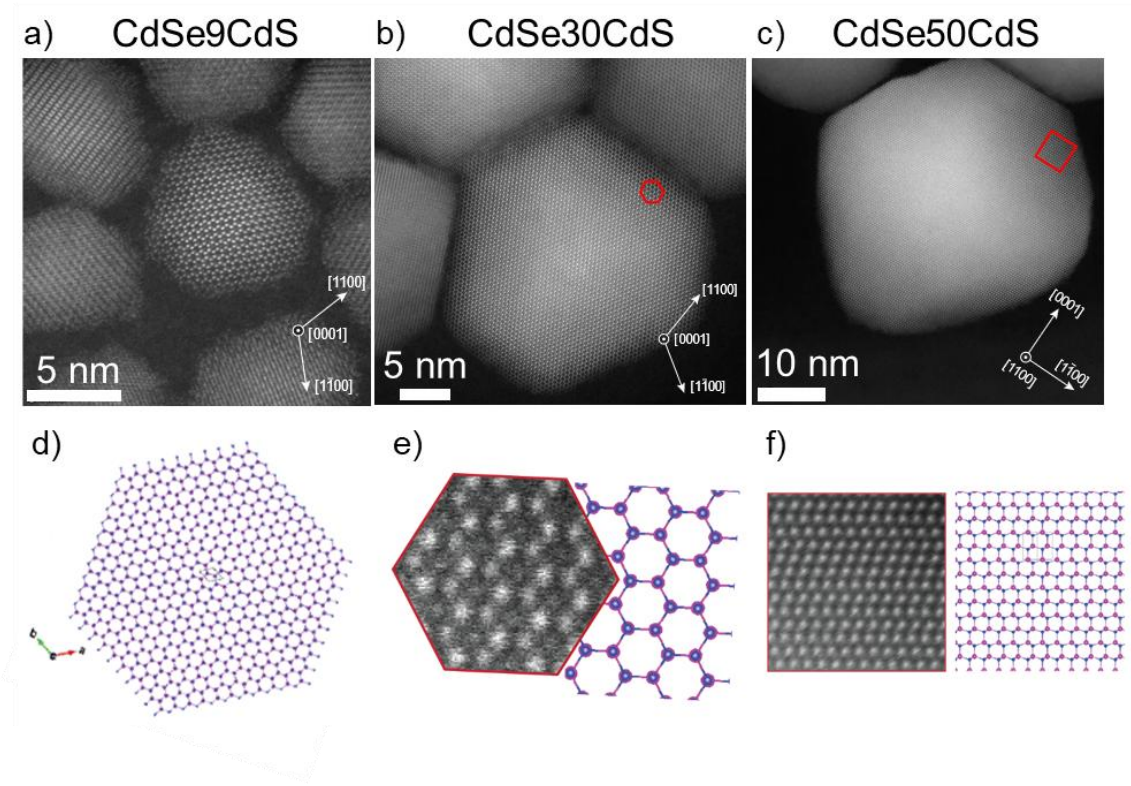

Figure 5.8. Atomic resolution STEM-HAADF images of **a.** CdSe9CdS and **b.** CdSe30CdS oriented looking down the [0001] direction and **c.** CdSe50CdS oriented down the [1100] direction. **d-f.** Structural models generated in VESTA reveal that the atomic structures largely match the expected structure from these orientations. For the thicker shell samples, deviations such as the faint columns in the center of the hexagons in **e.** and stacking faults in **f.** are observed.

Given the somewhat asymmetric growth of the CdS shell, it is worth examining whether the CdSe core is placed in the center of the core/shell structure or biased toward one end. To characterize the position of the CdSe core, we performed energy dispersive X-ray spectroscopy (EDS) in a scanning transmission electron microscope on CdSe9CdS QDs. CdSe9CdS was selected because the shell is thin enough to detect EDS signal from the CdSe core yet large enough to remain sufficiently stable under the electron beam.[40] Visual inspection of the EDS composition

maps in **Figure 5.11.b–d**, as well as line profiles drawn through two particles **Figure 5.11.e, g, & h**, reveals that the CdSe cores are located toward one end of the particle. This is consistent with the asymmetric growth of the CdS shell, which causes the CdSe core to be closer to the slower-growing (0001) facet rather than the faster-growing tip in the $[000\bar{1}]$ direction (**Figure 5.11.f**).

The STEM-HAADF images shown in **Figure 5.11** have deviations from the expected wurtzite structure, which we suspect are stacking faults along the c-axis. **Figure 5.9.a** below shows the rough position of regions with stacking faults. The position of these stacking faults in the [0001] direction describes why deviations are only shown in center, rather than extending fully to the edges of the CdSe30CdS QD oriented down [0001], as shown schematically in **Figure 5.9.b**. To study defects in the CdSe30CdS QD oriented down the [0001] direction, we analyzed the atomic column position and intensity using StatSTEM, which fits the atomic columns as a superposition of 2D Gaussians peaks, each corresponding to a column of atoms.[6] The StatSTEM analysis, shown in **Figure 5.9.c-h**, reveals the interface between the edges of the QD, which show no signs of stacking faults, and the center of the QD, which show signs of stacking faults consistent with the schematic in **Figure 5.9.b**.

We believe that the "filled hexagon" lattice fringe pattern observed in some colossal CdSe/CdS QDs is due to stacking faults. To test this hypothesis, we constructed two model structures (**Figure 5.10**), one without stacking faults and the other with one stacking fault. When viewed down the c-axis, the model without stacking faults, or a purely wurtzite structure, features a hexagonal lattice with no atoms at the center of the hexagons. In the model with one stacking fault, one layer of atoms is shifted such that there are now atoms in the center of the hexagons. Experimentally, we observed that the atoms in the middle of the hexagons had lower HAADF intensity. To compare this with a model structure, we performed multislice STEM simulations of

the two models using the abTEM Python package. The simulated STEM-HAADF image shows that the atoms in the middle of hexagons have lower intensity, in agreement with our experimental observations. Overall, this suggests that the lighter spots at the center of the hexagons are due to stacking faults. Quantitative analysis of the relative intensities of the atomic columns as well as simulation of larger, defective models may enable the stacking fault density to be determined for wurtzite QDs oriented down the [0001] direction.

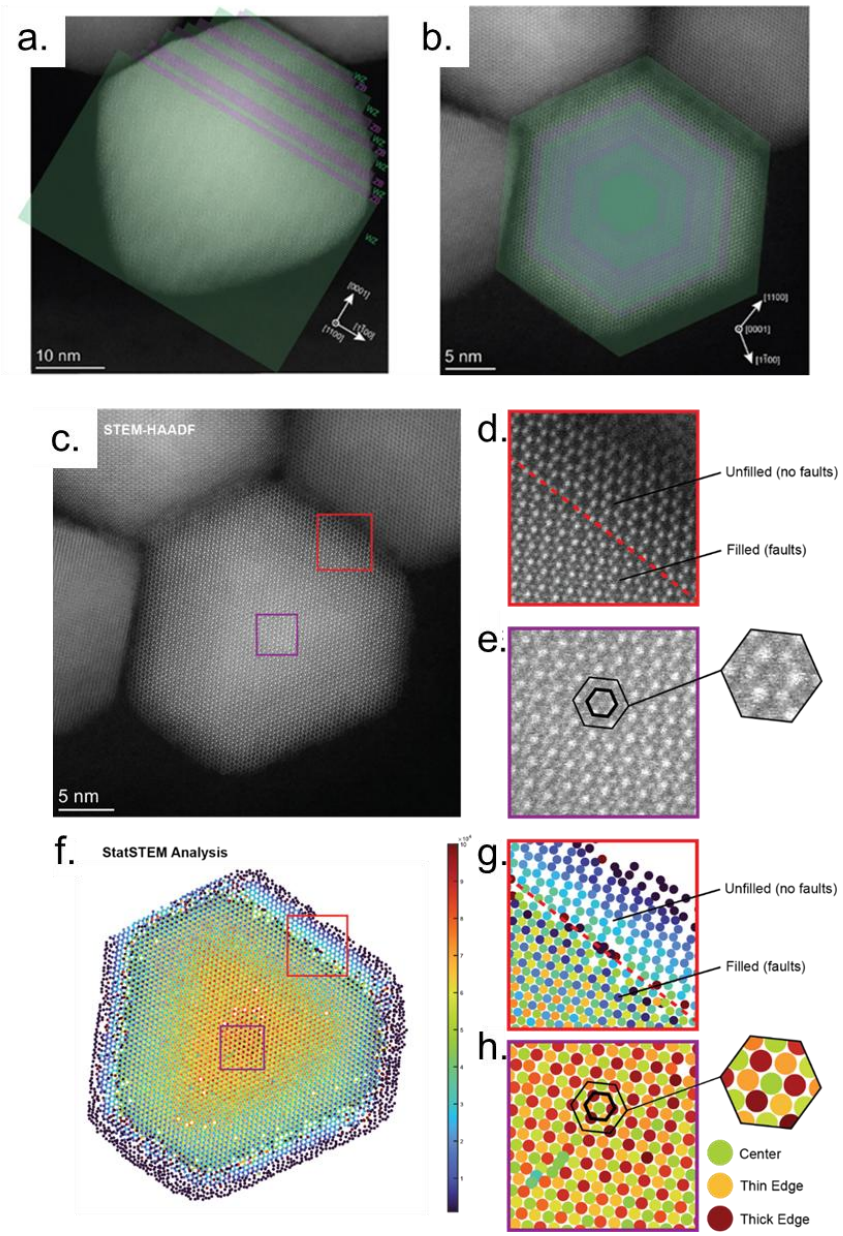

Figure 5.9. Qualitative stacking fault analysis in **a.** CdSe50CdS QD oriented down the [1100] direction and **b.** CdSe30CdS QD oriented down the [0001] direction. Comparison of raw STEM-HAADF images **c-e.** and StatSTEM analysis **f-g.** for a single CdSe/CdS (30ML) QD. **h.** Colormap of StatSTEM volumes – the integrated intensities of the modeled atomic columns – shows the thickness of the columns, where blue is the thinnest and red is the thickest. StatSTEM analysis makes the interface between the stacking fault-free regions (wurtzite) and regions

comprising stacking faults (zinc-blende-like) much clearer (**d.** & **g.**) and also resolves an intensity pattern in the central part of the nanocrystal (**h.**). There are some artifacts at the edges of the modeled particle, as seen in the top right of (**g.**). That is, the StatSTEM model is not fully representative of the STEM-HAADF image but provides a rough sense of the atomic column position and intensity across the QD.

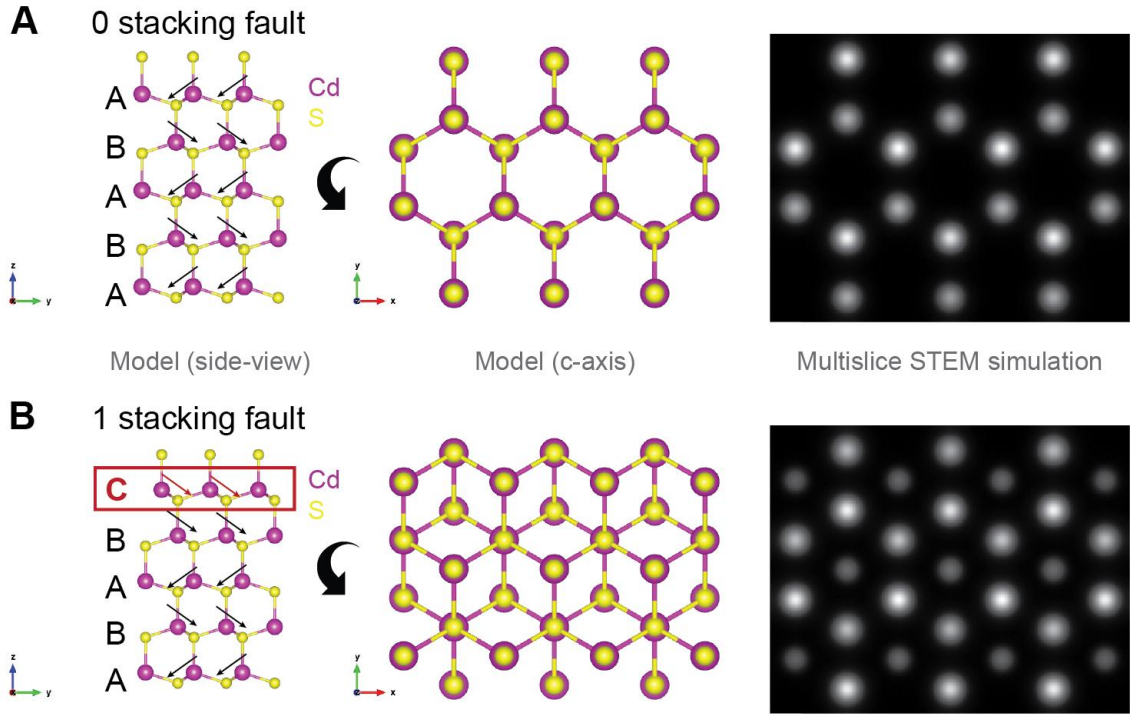

Figure 5.10. Model structures and multislice STEM simulation for wurtzite CdS slab with **a.** no stacking faults and **b.** with one stacking fault. Arrows were added to highlight the Cd-S bond direction, which alternates in direction for the wurtzite structure but becomes locally parallel with the stacking fault. The model structures were visualized in VESTA while the multislice STEM simulation was generated using the abTEM Python package.

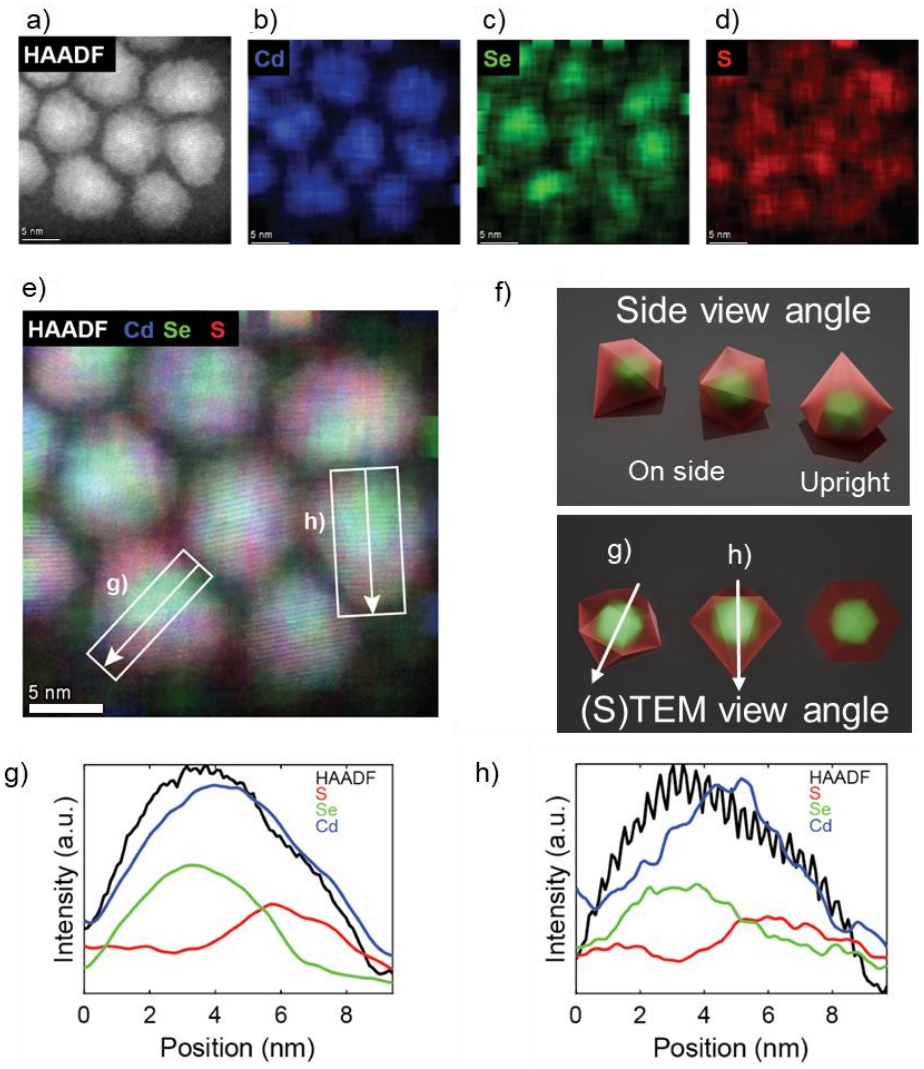

Figure 5.11. STEM-EDS of CdSe9CdS NCs. **a-d.** Isolated HAADF image and Cd, Se, S compositional maps. **e.** Overlay of HAADF with Cd, Se, and S composition maps. Cd, Se, and S signal is averaged to resolve structures more easily. **f.** Schematic of particles illustrating core/shell structure from different orientations. **g, h.** Line profiles showing HAADF and EDS intensity as a function of position for two particles in **e.** To improve the signal-to-noise ratio, the EDS signal was averaged over 28 pixels (2.83 nm).

5.3.2 *Structural Rounding and Flat Facet Reconstruction*

As seen in the TEM images (**Figure 5.1.b–f**), all syntheses consistently yielded particles with sharp corners, except for the CdSe50CdS QDs (**Figures 5.1.d** and **Figure 5.8.c**). Despite all samples in this synthesis series undergoing thermal annealing at high temperatures for several hours after their synthesis, only the CdSe50CdS batch shows rounded facets. Recent studies have revealed that the conversion from faceted CdSe/CdS nanocrystals to their spherical counterparts is independent of particle size[63] and can be driven by factors such as increased annealing temperature and duration,[52,53,64] high concentrations of amine ligands,[52,57,65,66] and selective facet-ligand pairing.[57] In our study, all syntheses included an identical annealing step (280 °C for 4–6h) without adding extra phosphonic acids or amines, yet both faceted and spherical particles were observed in different batches (**Figures 5.1.d** and **Figure 5.12**). Since spherical particles appeared without any deliberate chemistry to induce facet reconstruction, this rounding is likely due to the incomplete formation of CdS MLs on the seeds, followed by atom migration facilitated by the high annealing temperatures. When large particles are shelled, adding an extra ML requires a significant amount of Cd and S atoms to be deposited uniformly onto the particle seed. If the reaction is stopped prematurely or the precursor supply is depleted before a growing ML is complete, subsequent annealing can lead to intraparticle atom migration, resulting in ripening of sharp edges and corners and the formation of thermodynamically favorable rounded particles. Interestingly, this transformation is reversible during the sequential shelling, as demonstrated by the evolution from CdSe50CdS to CdSe80CdS (**Figure 5.1.d–e**)**.** We confirmed this reversibility through a series of experiments where a submonolayer of CdS was added to the rounded CdSe50CdS particles (**Figure 5.13.a**). TEM images of the resulting particles, **Figure 5.13.c-e**, reveal structures with more flat facets and sharper corners than the initially rounded particles (**Figure 5.13.b**). We

used the circularity index (C) to quantitatively assess the roundness of the particle shapes. This index ranges from 0.70 to 0.86 for diamond-like or truncated kite two-dimensional (2D) projections, indicating less rounded shapes, and exceeds 0.9 for hexagonal projections, with values approaching 1.0 as the shapes become more circular (**Figure 5.14.a**). We only applied this measurement to the diamond-like projections to avoid overestimating circularity. Adding less than one CdS ML did not significantly change the overall sizes of the particles but resulted in a noticeable decrease in their C values from 0.84 ± 0.03 to less than 0.80 (**Figure 5.14.b**).

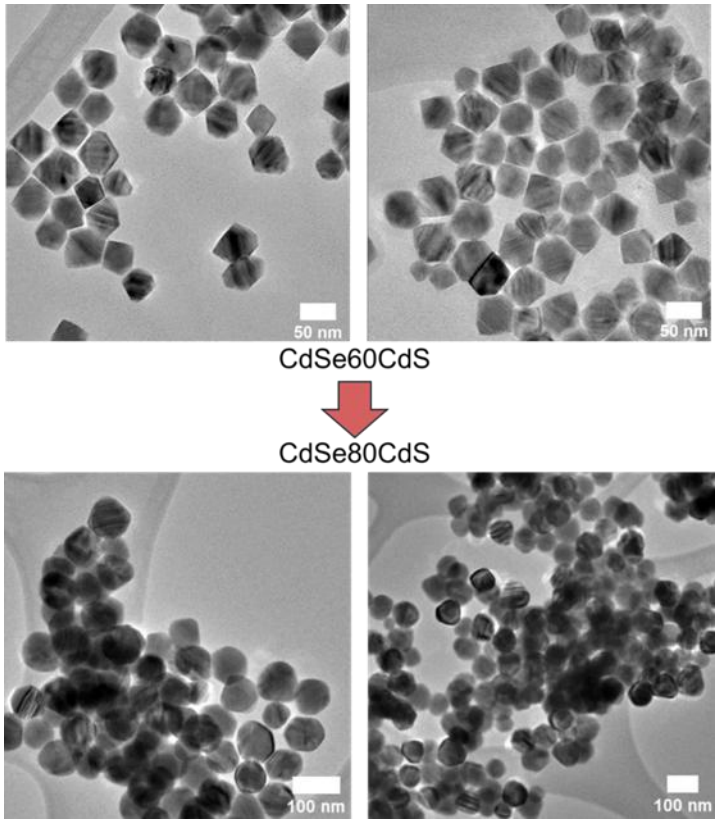

Figure 5.12. TEM images of CdSe60CdS and CdSe80CdS QDs. These QDs were synthesized in a different series from the one in the main text. CdSe60CdS QDs were grown from CdSe40CdS QDs, and CdSe80CdS QDs were grown from CdSe60CdS QDs. CdSe60CdS QDs show flat facets and pointy corners while CdSe80CdS QDs show rounded shapes.

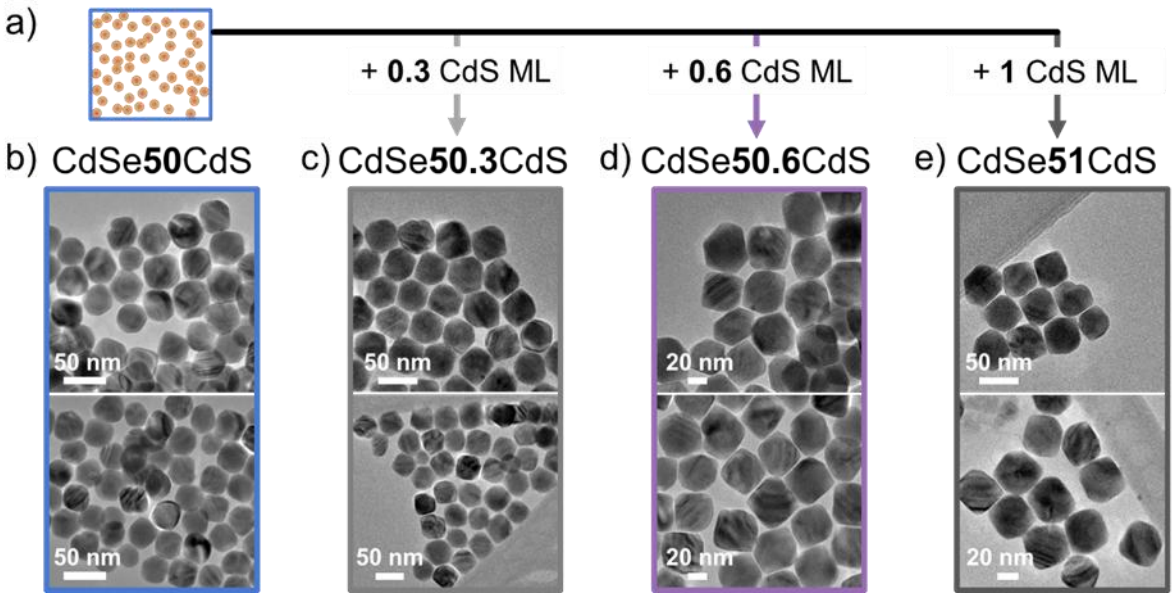

Figure 5.13. TEM images of **a.** CdSe50CdS and the products from flat facet reconstruction achieved by the addition of **b.** 0.3, **c.** 0.6, **d.** and 1 ML of CdS.

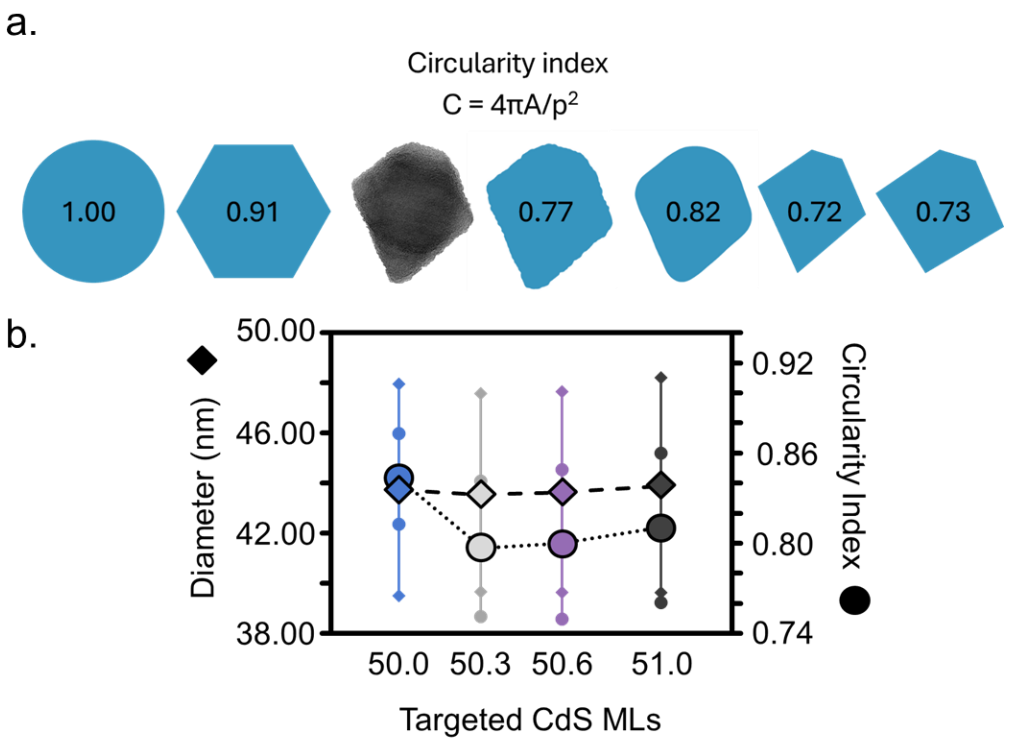

Figure 5.14. a. Different shapes with corresponding circularity index. A circle has C = 1, a perfect hexagon has C = 0.91. Values of C for a diamond-shape similar to the colossal QD shape

range 0.7 to 0.9 depending on the roundness of the shape. **b.** Comparison of particle diameters and average circularity indexes. Only diamond-shape TEM projections were counted for the circularity index assessment. C values above 0.9 and below 0.7 were not included to avoid over- and under-estimations.

5.3.3 *Optical Properties of Colossal QDs*

The ensemble normalized optical absorption and emission spectra of the colossal QD series taken in anhydrous hexane are shown in **Figure 5.15.a**. The CdSe30CdS QDs show typical absorption features for giant CdSe/CdS QDs, where absorption is dominated by the CdS shell, and onset happens around the bulk CdS bandgap energy, 515 nm. The absorption feature of the larger QDs is similar to that of bulk CdS particles (**Figure 5.16**). As the CdS shell thickness and overall particle size increase, significant scattering becomes evident across the visible region and two distinct absorption peaks arise at 487 and 501 nm. Deciphering the origin of these features requires deconvolution of the contributions from absorption, scattering, and refraction, a process that presents significant complexity.[67,68] The emission peaks (**Figure 5.15.a**) of the colossal QDs exhibit a slight blue shift from 642 to 629 nm, likely due to ionic intradiffusion,[69-71] and a line width narrowing as the number of CdS monolayers increases. The PLQYs for all samples are detailed in Table 2, indicating a gradual decrease from 36.8% for CdSe30CdS to 10.5% for CdSe100CdS. Due to significant scattering of the solutions, these values represent a lower bound due to overestimation of the number of photons absorbed by the sample.[72] Even after 4 months of storage in hexane under ambient conditions, the PLQYs remained stable (**Table 5.3**).

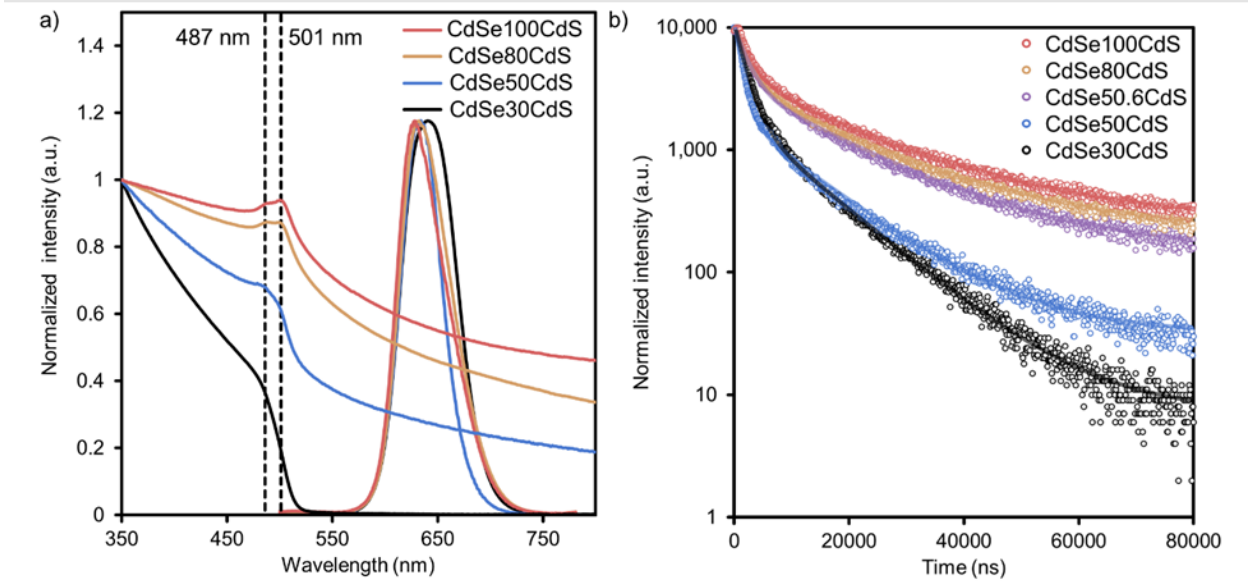

Figure 5.15. a. Solution-phase absorption and PL spectra, and **b.** time-resolved PL decay of CdSe30CdS (black), CdSe50CdS (blue), CdSe50.6CdS (purple), CdSe80CdS (yellow), and CdSe100CdS (red) QDs with excitation wavelength of 525 nm. All data were collected after one centrifugation step with methyl acetate as an antisolvent and hexane as a solvent without size-selective purification.

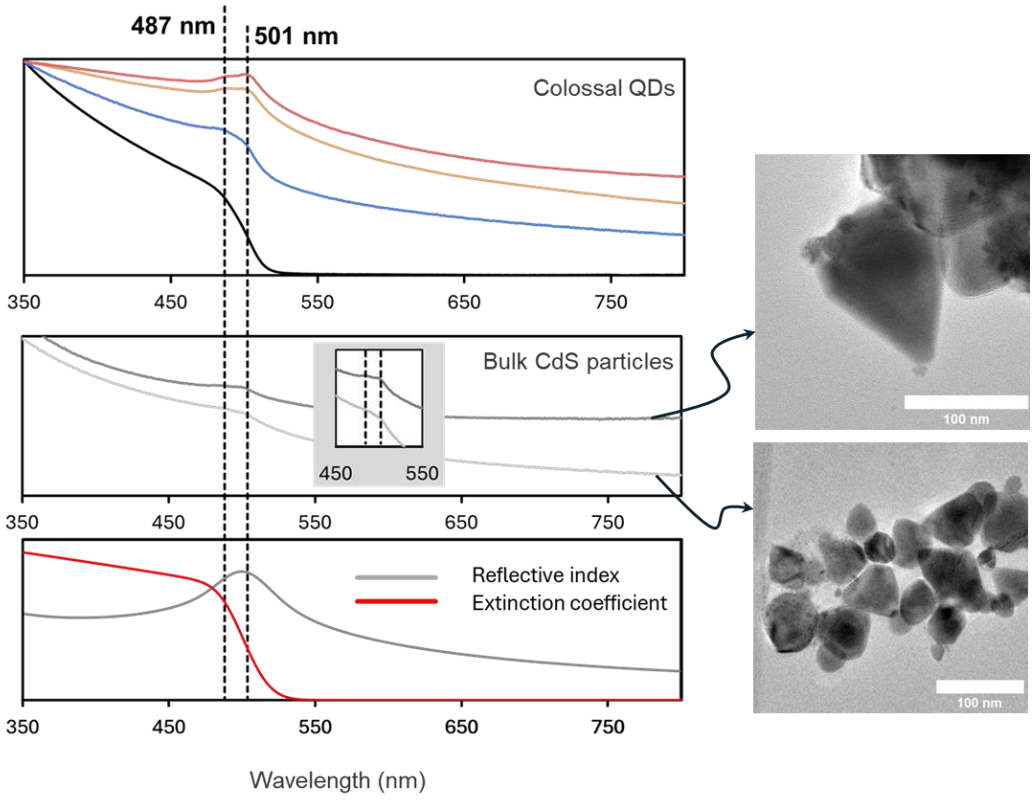

Figure 5.16. (top) Absorption spectra of colossal QDs, (middle) bulk CdS particles synthesized using a procedure from Wang et al., and (bottom) reflective index and extinction coefficient spectra of bulk CdS.

Table 5.3. Summary of PLQY of as-synthesis QDs, QDs stored under ambient conditions after 4 months, and their lifetimes (excited at 525 nm) derived from biexponential fits of time-resolved PL decays.

Samples	**PLQY as-synthesis (%)**	**PLQY after 4 months in air (%)**	**t_1 (µs)**	**A_1**	**t_2 (µs)**	**A_2**	**t_{av} (µs)**
CdSe30CdS	36.8 ± 1.2	34.3 ± 0.7	1.72 ± 0.01	8.44 ± 0.04	10.18 ± 0.15	2.16 ± 0.04	3.45 ± 0.08

CdSe50CdS	30.9 ± 0.8	30.3 ± 0.6	1.21 ± 0.01	8.69 ± 0.04	11.10 ± 0.19	1.90 ± 0.03	2.98 ± 0.08
CdSe50.6CdS	28.1 ± 0.4	27.6 ± 0.8	3.34 ± 0.02	3.34 ± 0.02	15.06 ± 0.15	1.78 ± 0.02	6.54 ± 0.08
CdSe80CdS	15.8 ± 1.0	15.1 ± 0.8	1.90 ± 0.02	3.26 ± 0.02	16.03 ± 0.16	1.79 ± 0.01	6.91 ± 0.08
CdSe100CdS	10.5 ± 0.6	11.2 ± 1.1	2.99 ± 0.02	2.98 ± 0.02	17.00 ± 0.15	1.96 ± 0.01	7.93± 0.07

Figure 5.15.b presents the time-resolved PL decay traces of the QDs at room temperature, and **Table 5.3** lists the decay times derived from biexponential fits, showing average lifetimes of a few microseconds for all samples. These long lifetimes and their correlation with shell thickness are consistent with our understanding that the electron wave function delocalizes into the shell volume in this core–shell system. This delocalization reduces the overlap between electron and hole wave functions, increasing the radiative lifetime.[45,73] Compared to giant QDs with smaller sizes reported in the literature to date, the lifetimes of these colossal QDs are longer (**Table 5.4**), suggesting that the increase in wave function separation with shell thickness has not yet reached a maximum.

Table 5.4. PL Lifetime comparison among giant Cd-based core/shell QDs.

Composition	Particle diameter or	$\lambda_{excitation}$ (nm)	Emission peak (nm)	Lifetime (ns)	Ref.

	longest dimension (nm)				
CdSe80CdS	72	525	630	6910	This work
CdSe80CdS	72	425	630	1436	This work
CdSe100CdS	96	525	630	7930	This work
CdSe100CdS	96	425	630	2327	This work
CdSe20CdS	17	405	650	638	Sapienza & coworkers[89]
CdSe40CdS	40	377	685	4000	Dubertret & coworkers[42]
CdSe16CdS	22	360	~635	242	Chen & coworkers[52]
CdZnSe/CdS	19	445	590	504	Snee & coworkers[90]

Interestingly, the CdSe50CdS QDs with rounded edges have shorter photoluminescence lifetimes (~3 μs), which deviate from the expected trend seen in other samples. In contrast, CdSe50.6CdS QDs with flat facets exhibit significantly longer lifetimes (~6 μs). This observation suggests that subtle changes in particle morphology and surface structure, even in this size regime, can directly and substantially affect the optical properties. Since the primary distinction between the CdSe50CdS and CdSe50.6CdS QDs lies in their surface morphology, we believe that surface strain is a critical parameter. As discussed previously, the rounded facets likely result from surface reconstruction due to an incomplete monolayer, thereby inducing strain similar to that observed in

flat and helical ZnS shells of ZnSe/ZnS nanorods[58] (**Figure 5.17**). We hypothesize that if precursor (Cd and S ions) supply is depleted before an additional CdS ML (n+1th ML) is complete, surface atoms can migrate into thermodynamically stable positions (yellow dashed line) during annealing. We think that this hypothesis is similar to the study by Ji et al.,[58] where the stable morphology is dictated by the balance of the surface energy and surface strain. This balance might be the origin of particle rounding, surface island formation, and particle instability especially when the surface area is high.

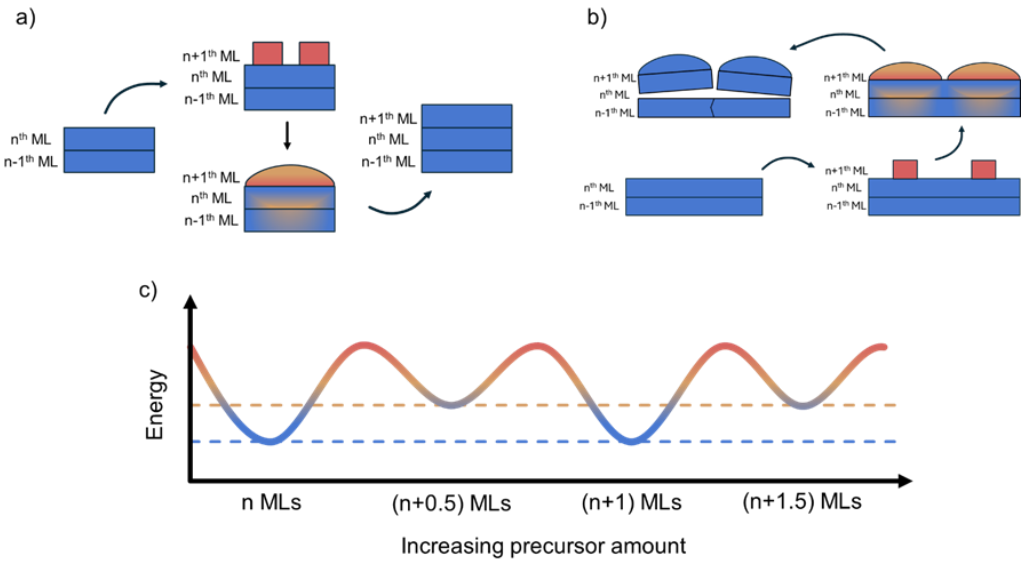

Figure 5.17. Illustration of hypothesis for **a.** strain induced particle rounding and **b.** instability. **c.** Hypothetical energy landscape during shell growth.

To evaluate the blinking behavior of single colossal QDs, we used wide-field PL microscopy to sample hundreds of single QDs. **Figure 5.18.a** illustrates the nonblinking fractions across the samples, with all QDs in the series showing significant nonblinking behavior, typical for thick-shelled CdSe/CdS. To assess QD photobleaching, each single-particle PL trace was fit to a single exponential equation:[74]

$$I(t) = Ae^{-\frac{t}{\tau_{bleach}}} \quad (5.1)$$

where τ_{bleach} is the characteristic time of the QD photobleach and A is an intensity-related prefactor. As the shell thickness increases, the average photobleaching time decreases, with the rounded QDs exhibiting faster bleaching than the similarly sized flat-faceted QDs (**Figure 5.18.b**). Our wide-field PL analysis indicates that there is no definitive trend in blinking behavior as shell thickness increases, despite **Figure 5.18.a** suggesting a decrease in the nonblinking fraction. This is because "blinking" fractions for the larger QDs are primarily reporting on photobleached QDs. Furthermore, single-particle PL comparisons reveal that flat-faceted CdSe50.6CdS QDs exhibit a clearly improved nonblinking fraction and longer photobleaching time compared to the rounded CdSe50CdS QDs (**Figure 5.18.a-b**). This distinction highlights the impact of facet morphology on the QD performance.

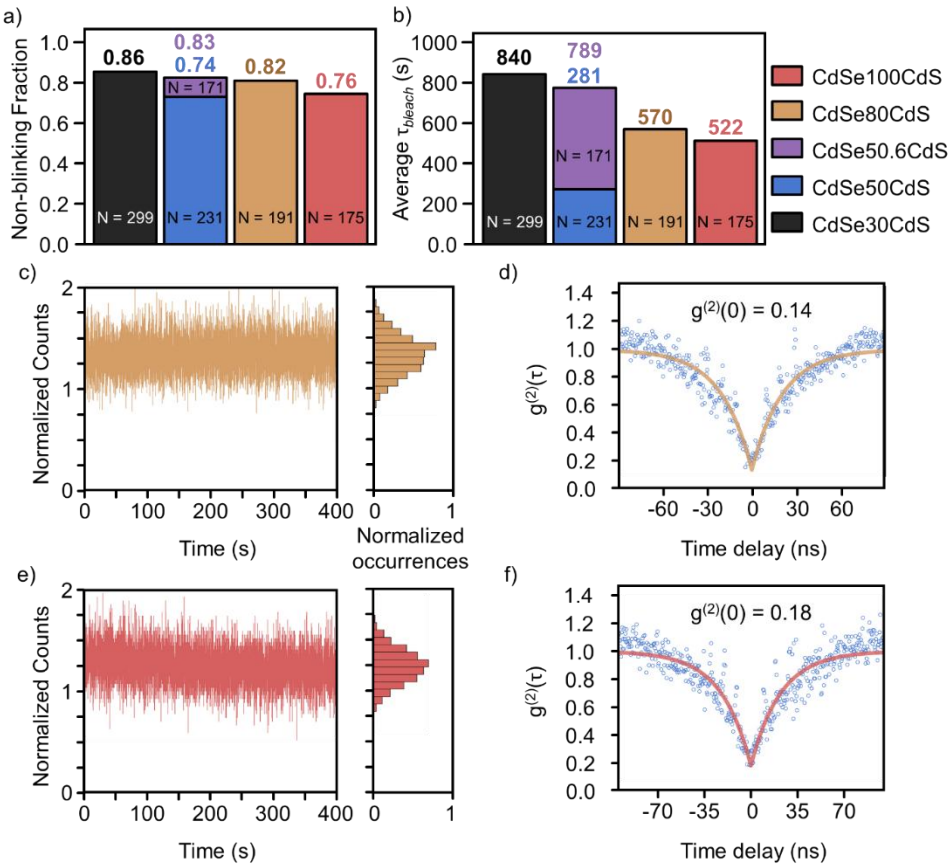

Figure 5.18. a. Non-blinking fractions, and **b.** average photobleaching time constant of colossal QDs. Representative PL traces (**c**, **e**) and second-order autocorrelation function $g^{(2)}(\tau)$ (**d**, **f**) from single CdSe80CdS and CdSe100CdS QDs.

Single-particle PL traces of all colossal QDs showed a stable PL intensity with a unimodal ON state over many minutes of measurement under excitation. **Figure 5.18.c & e** show representative PL traces of a single QD with 80 and 100 CdS ML, respectively. To assess the single-photon emission of colossal QDs, we measured the second-order temporal correlation function ($g^{(2)}(\tau)$) of many single QDs. All measured single QDs, regardless of shell thickness, have a $g^{(2)}(\tau = 0) < 0.4$, which is indicative of a single-photon emitter under continuous-wave excitation without any spectral filtering or background correction. **Figure 5.18.d** & **f** present $g^{(2)}(\tau = 0)$ curves of CdSe80CdS and CdSe100CdS single QDs, respectively, with $g^{(2)}(\tau = 0)$

values below 0.2. In contrast, giant CdSe/CdS QDs with much smaller sizes have been reported with $g^{(2)}(\tau = 0))$ values above 0.3.[48,75] Given that thick CdS shells can efficiently promote recombination of stable multiexcitons[42,48] that are believed to potentially affect the single-photon emission purity, our results imply that this factor either does not scale proportionally with the thickness of the CdS shell or has minimal impact on the single-photon emission from CdSe/CdS QDs.

Compared to the previously reported giant CdSe/CdS QDs (**Table 5.5**), colossal QDs are poised to be highly effective for scalable and deterministic single-particle positioning and ultimately precise coupling with optical cavities using solution-processable techniques, including template-assisted self-assembly,[17] electrohydrodynamic inkjet printing,[76,77] and those that have been used for other particles with sub-100 nm diameters.[78]

Table 5.5. Feature comparison of CdSe/CdS with different shell thickness regimes

Features	**Thin shells**	**Thick shells**	**Colossal shells**
Number of CdS MLs	5 – 10	10 – 30	30 – 100
Diameter	< 10 nm	10 – 20 nm	20 – 100 nm
PLQY	> 90 %[49,53]	< 90 %[39,40]	< 50 %
Emission lifetime	< 100 ns	100 ns – 1 µs	> 1 µs
Blinking	Significant	Highly suppressed	Highly suppressed
Colloidal stability	High	High	Moderate
Single-particle positioning	Random	Random	Large scale & deterministic*

*Large-scale deterministic positioning has been shown for particles with sizes from 50 to 100 nm[17,79,89]

5.4 Deterministic Inkjet Printing of Single Colossal QDs on Nanobeam Cavities

5.4.1 *Deterministic Inkjet Printing of Single QDs*

We developed a novel electrohydrodynamic (EHD) printing regime to achieve deterministic deposition of individual QDs with nanoscale precision, enabling scalable integration of single-photon emitters for quantum photonic applications. The mechanism of the inkjet printing technique can be found on our recent publication.[91] This section focuses on adapting EHD printing to deposit colossal CdSe/CdS QDs. The advantage of using colossal QDs is the large CdS shells, which posses large dipole moments and optical stability ideal for manipulation under nonuniform electric fields. By designing the ink medium to be relatively non-polarizable and exploiting dielectrophoretic (DEP) forces, we selectively extracted and printed single QDs from dilute apolar dispersions (**Figure 5.19**). Using numerical modeling and experimental validation, we determined the interfacial energies, electric field gradients, and particle sizes required to overcome the energy barrier associated with pulling a single particle through a liquid interface. Through optimization of field parameters, we achieved a high single-particle print yield (~50%) without visible solvent wetting or droplet formation, indicating a fundamentally new mechanism of particle transfer (**Figure 5.20**). **R**oom temperature PL spectrum of a single printed QD with an emission peak at 624 nm, and a full-width half-maximum (FWHM) of ~21 nm, consistent with behavior of particles of this composition deposited by conventional drop-casting approaches and measured in solution (**Figure 5.20.d**). Second-order correlation ($g^{(2)}(\tau)$) measurements on the QDs confirm single-photon emission from printed QDs. **Figure 5.20.e** shows an example of a QD maintaining its single-photon emissivity ($g^{(2)}(\tau = 0) < 0.5$) after EHD printing, a critical performance metric for

utilizing these materials as single photon sources in quantum computing or networking technologies. Measuring a sample of the EHD-printed single QDs **Figure 5.20.f** shows a distribution of single-photon emitters, with a mean of $g^{(2)}(\tau = 0)$= 0.33 ± 0.1.

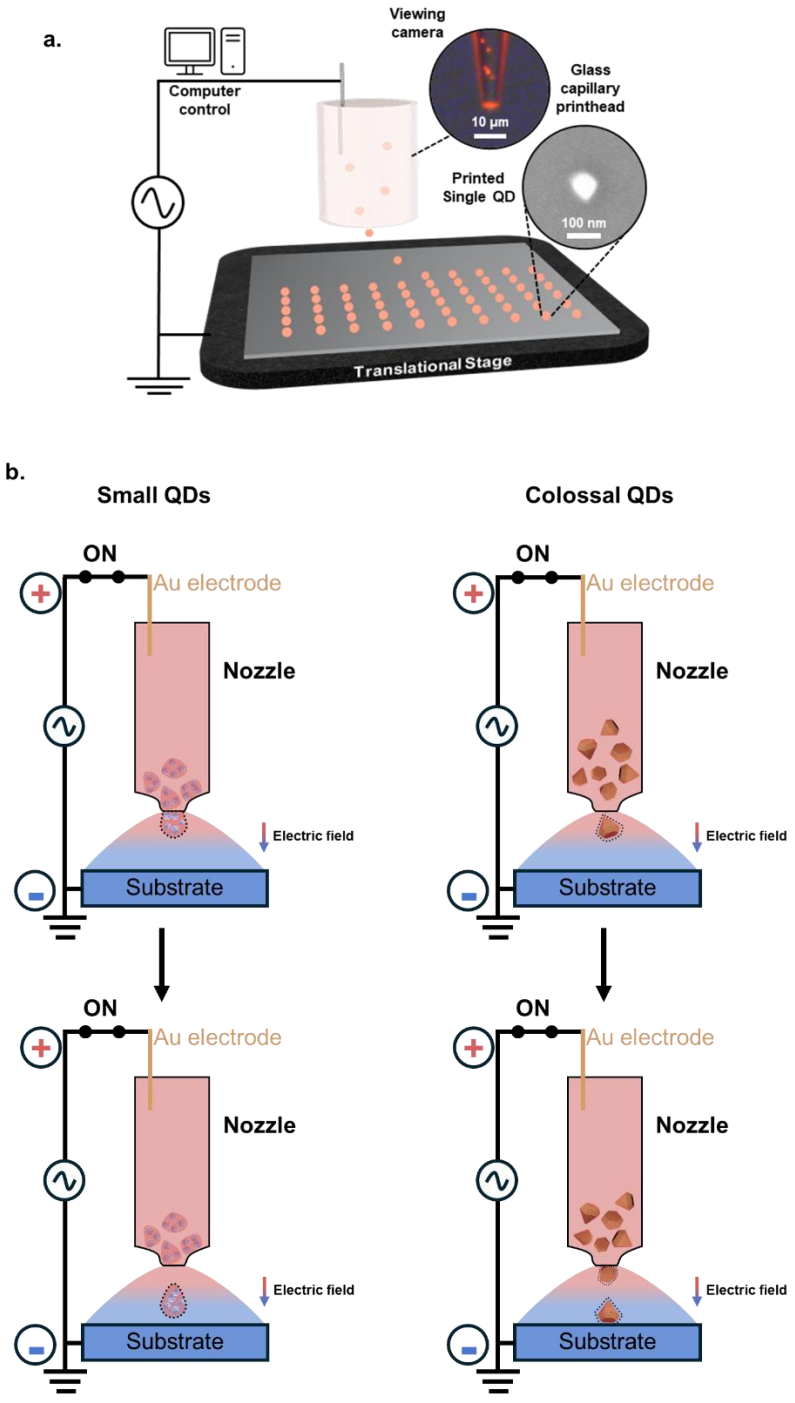

Figure 5.19. a. Schematic diagram of the EHD printing setup used here. Top inset: fluorescence (FL) microscopy of EHD printhead. Bottom inset: Scanning electron microscopy (SEM) of single EHD-printed QD. **b.** illustrations of EHD printheads dielectrophoretically

overcoming surface tension to print droplets of particle ensembles and interfacial forces to print singular particles.

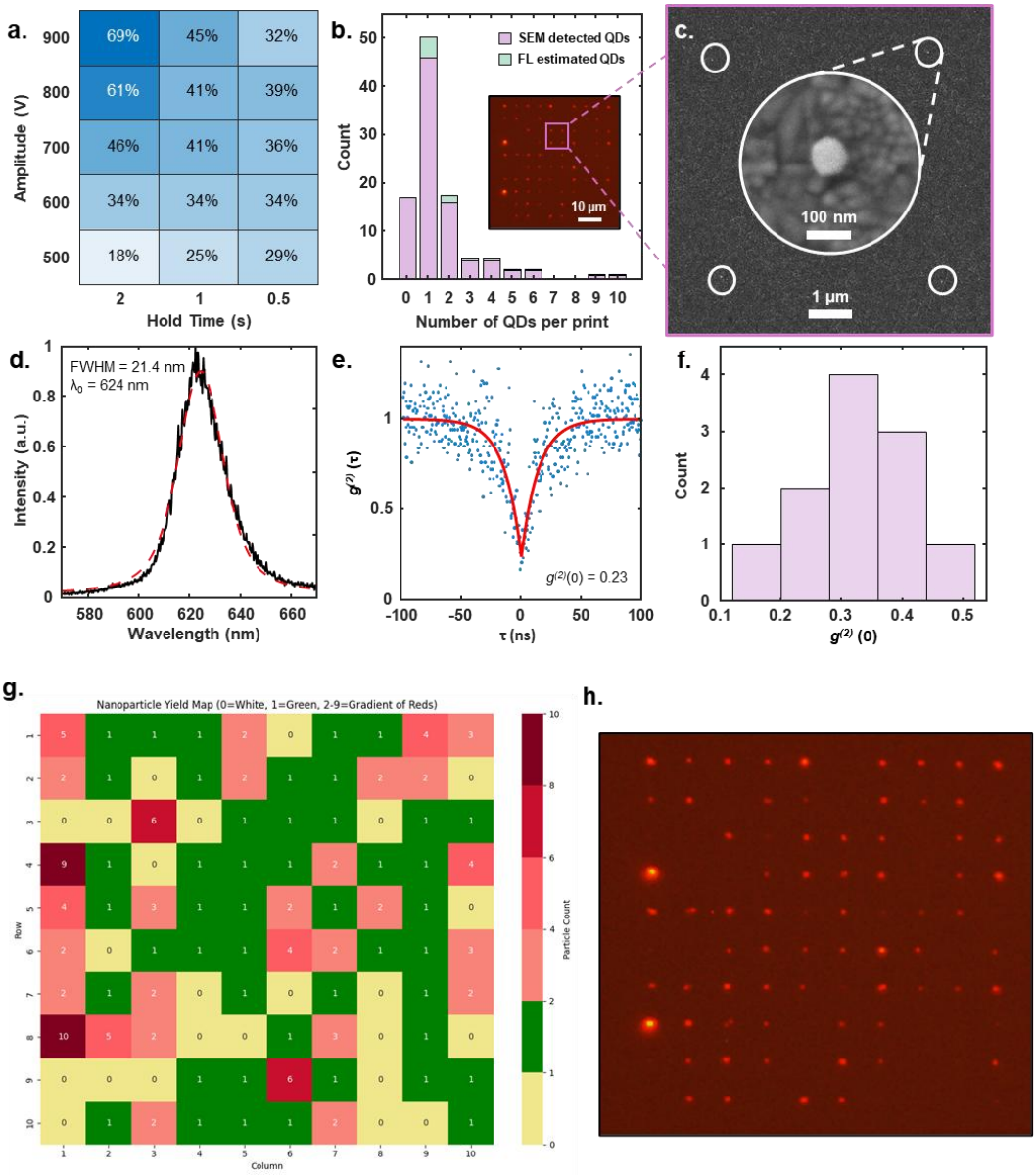

Figure 5.20. Experimental results of EHD printing colossal QDs. **a.** Effect of drive amplitude on FL detected print yield as a heatmap of number of prints detected out of a 10 x 10 array of print attempt sites, per parameter configuration. **b.** Histogram plot of QDs counted per print site for a 10 x 10 array (900 V and 2 s parameter configuration) of attempt sites, as

determined by SEM and FL. Estimated QDs indicate QDs not detected via SEM but were positively-indicated by the FL microscopy (inset). The distribution of estimated QDs is based on the non-zero statistical prevalence QDs per print, per bin. **c.** SEM image of 2 x 2 array of EHD-printed single QDs. White circles indicate single QD positions. Inset: SEM image of single QD. **d.** Plot of single QD emission spectrum (black) and Lorentzian fit (red). **e.** Second-order time correlation plot (blue) and fit (red) of EHD-printed QD showing single-photon emission, measured at room temperature, with 10 μW excitation (**d** and **e**). **f.** Histogram plot of $g^{(2)}(\tau = 0)$ measurements on EHD-printed single QDs (n = 11). **g.** Heatmap of SEM analysis. Plotted heatmap summary of the number of QDs counted per print attempt site, via SEM, for the 900 V and 2 s parameter configuration. **h.** Fluorescent microscopy images of EHDIJ prints in an array of amplitudes and hold times with 5 μm print spacing.

5.4.2 *A Single QD on A Nanobeam Cavity*

To demonstrate the utility of our single QD printing method, we integrated a printed QD into a horseshoe-shaped nanophotonic crystal cavity designed with a resonant frequency of ~614.5 nm. The cavity, featuring a monolithic waveguide and outcoupling gratings, directed emission from the centrally printed QD toward the gratings, as shown by fluorescence microscopy. SEM imaging confirmed the presence of a single colossal QD at the intended print site. Despite the QD not being perfectly aligned with the cavity's field maximum, significant coupling was observed. Photoluminescence spectra at 70 K revealed a broad QD emission coupled with a sharp cavity mode, displaying Fano interference features that were more pronounced at room temperature. A Lorentzian fit of the cavity mode indicated a quality factor of 12,500. Low-temperature measurements (8 K) under variable excitation powers showed distinct excitonic emission, phonon sidebands, and a high-energy multi-excitonic peak, with the latter scaling nonlinearly with power.

Finally, second-order correlation measurements confirmed that the QD maintained single-photon emission after integration with the cavity, underscoring the effectiveness of our approach for deterministic coupling of printed single QDs to photonic structures.

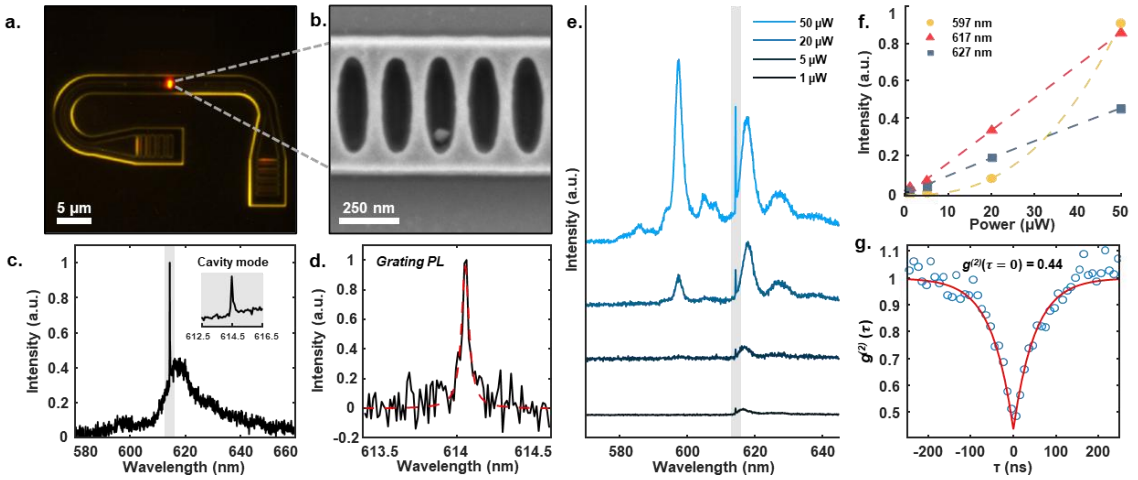

Figure 5.21. Single QD nanophotonic cavity heterointegration. **a.** Fluorescent microscopy of horseshoe-shaped cavity with single EHD-printed QD. **b.** SEM image of the cavity region containing single QD. **c.** Spectrum plot of cavity integrated QD, at 70 K, excited and measured from the top. Inset: Magnified spectrum (shaded) around the cavity mode. **d.** Spectrum of the pure QD-coupled cavity mode PL to the grating (black) and Lorentzian fit (red) when exciting from the top, measured at room temperature with 10 μW excitation (**c** and **d**). **e.** Power-dependent spectra of QD-coupled cavity at 8 K with the cavity mode region shaded (614 nm), excited and measured from the top. **f.** Power dependence of 597 nm (yellow), 617 nm (red), and 627 nm (blue) peak intensities at 8 K, with power-law fits (dashed lines). **g.** Second-order time correlation plot (blue) and fit (red) of cavity-coupled QD, excited (10 μW) and measured from the top at room temperature.

5.5 CONCLUSION

In summary, we have demonstrated that a stepwise HTCI method is essential for synthesizing colossal core–shell CdSe/CdS QDs with diameters of up to 100 nm and size distributions under 10%. This is in contrast to more conventional direct shelling to prepare core/shell QDs of over 50 nm in diameter, which results in instability and independent CdS nucleation. Additionally, pushing the QD size above 100 nm requires careful adjustment of the precursor concentrations. These colossal QDs display a hexagonal diamond shape with the CdSe core situated closer to the particle base. Structural analysis through microscopic techniques confirmed that the particles consist of 12 semipolar $\{10\bar{1}1\}$ facets and one polar (0001) facet. Our observations also revealed that particle rounding occurs during shelling due to incomplete monolayer growth. These rounded QDs can be sharpened by introducing a small amount of shelling precursors to complete the CdS ML.

We have shown that with a significantly large number of CdS shells, the optical properties of colossal QDs remain similar to those of previously reported giant QDs with diameters <20 nm. Additionally, we have confirmed that QD surface morphology can directly affect optical properties, and this could only be observed clearly in the colossal particle size regime. All samples of colossal QDs in this study exhibit long solution-phase PL lifetimes of a few microseconds at room temperature, consistently demonstrate nonblinking fractions above 70%, and maintain low antibunching emission even for QDs with 100 MLs of CdS. The optical properties differ markedly between rounded and flat-faceted particles, with the latter showing enhanced PL lifetime and improved nonblinking behavior.

Our findings regarding particle morphologies and properties throughout the shelling process in this colossal particle size regime provide valuable insights into precision for crystal

growth and size-dependent optical properties. We believe that this synthetic approach will unlock numerous innovative applications for QDs and represents a crucial step toward the practical development of real optoelectronic devices, especially those utilizing single-QD emitters.

To further demonstrate the potential of the colossal QDs synthesized in this work, we applied them in a newly developed electrohydrodynamic (EHD) inkjet printing process capable of deterministically positioning single QDs with nanoscale precision. This printing method, which operates through dielectrophoretic expulsion of highly polarizable particles from a dilute, non-polar solvent, was enabled by the unique physical and dielectric properties of our colloidal QDs. Their large size, faceted morphology, and high polarizability allowed them to overcome interfacial energy barriers and be printed individually onto designated substrate sites without solvent wetting or droplet formation. Using this approach, we achieved single-particle placement into prefabricated nanophotonic structures and confirmed the preservation of single-photon emission after printing. This capability opens a scalable and high-throughput pathway to integrate individual QDs into optical cavities and other quantum photonic components without relying on complex lithography or vacuum processing.

More broadly, the compatibility of these synthetically tailored QDs with a contactless, room-temperature additive nanomanufacturing technique suggests new directions for device-level implementation of colloidal materials. The ability to position individual QDs with sub-micron accuracy expands the toolbox for constructing quantum optoelectronic platforms, including arrays of single-photon sources or integrated photonic circuits. While our study focused on CdSe/CdS core/shell QDs, the printing mechanism is generalizable to other nanoparticle systems with similar dielectric properties, such as halide perovskites and nanodiamonds. Together, this work highlights how advances in colloidal QD synthesis, particularly in accessing the colossal size regime with

controlled morphology and optical stability, can directly enable new applications in additive nanomanufacturing and scalable quantum technologies.

5.6 Experimental Methods

5.6.1 *Materials*

All chemicals listed below were used without further purification, unless stated otherwise. Oleic acid (≥90%), anhydrous methyl acetate (99.5%), selenium powder (99.999%, 100 mesh), cadmium oxide powder (CdO, 99.9%), trioctylphosphine oxide (TOPO, 99%), trioctylphosphine (TOP, 90%), 1-octanethiol (99%), 1-octadecene (ODE, 90%), and anhydrous hexane (95%) were purchased from MilliporeSigma, and n-octadecylphosphonic acid (ODPA, 99%) was purchased from PCI Synthesis. Cadmium oleate was synthesized following a literature procedure.[49]

5.6.2 *Synthesis Wurtzite CdSe QDs*

Wurtzite CdSe QDs were synthesized using an established method with some minor modifications.[54] TOPO (3 g), CdO (0.06 g), ODPA (0.28 g), and a magnetic stir bar were loaded into a 15 mL three-neck round-bottom flask secured with a septum, a thermowell equipped with a thermometer, and a condenser. The flask was heated to 110 °C and put under a vacuum for 30 min. The flask was then refilled with N_2 gas and was heated to 375 °C. While the temperature was ramping up from 320 to 370 °C, TOP (1.5 mL) was added slowly into the reaction. When the temperature was stabilized around 372–375 °C, a solution of Se powder (0.058 g) completely dissolved in TOP (0.4 mL) was quickly injected into the reaction. The reaction temperature fluctuated around 368–370 °C. The heating was stopped 45 s after the Se injection. The flask was quickly cooled to room temperature with forced air to yield QDs with the lowest energy electronic

transition at 560 nm. The product was purified in a glovebox with methyl acetate as antisolvent and hexane as solvent and was stored in a N_2 gas-filled glovebox. Using molar extinction coefficient and sizing curve estimations from the literature,[49,81] the particle diameter was calculated to be 3.5 nm and the concentration of the CdSe QDs in hexane was 1.00×10^{-4} M. Size estimation using a sizing curve equation:

$$D\ (nm) = 59.60816 - 0.54736\lambda + 1.8873 \times 10^{-3}\lambda^2 - 2.85743 \times 10^{-6}\lambda^3 + 1.62974 \times 10^{-9}\lambda^4$$

with $\lambda = 564$ nm in our case, D (nm) = 3.50 nm. The molar extinction coefficient was estimated using equation: $\varepsilon_{1S} = 155507 + 6.67054 \times 1013 \times \exp(E_{1S}/0.10551)$, with $E_{1S} = 1239.8 / \lambda = 2.19822695$ eV. The half-width-half-max (HWHM) of the absorption lowest excitonic energy transition was determined by fitting the absorption feature with a Gaussian curve, which yielded HWHM = 0.0638 eV. The absorbance at 564 nm is 0.1342 for a cuvette sample containing 20 µL of the CdSe QD solution and 3 mL of hexane. The concentration of the stock CdSe QD solution using Beer's law is calculated as below:

$$[CdSe]\ (M) = (\text{ Absorbance }) / (\ \varepsilon_{1S}\, l\ ) \times (\text{ HWHM } / 0.06) = 1.00 \times 10^{-4}\ M$$

where l = 1 cm is the light path and (HWHM / 0.06) is the correction factor compensating for size distribution of QDs.

5.6.3 *Direct Shelling of CdSe with CdS*

ODE (6 mL) was added into a 25 mL three-neck round-bottom flask secured with a septum, a thermowell equipped with a thermometer, and a condenser. The flask was heated to 110 °C and put under a vacuum for 60 min. The flask was refilled with N_2 gas and a desired amount of CdSe core in hexane (typically 5–100 nmol of QD or 0.0048–0.96 mL of the solution) was added to the reaction solution. The reaction solution was put under vacuum for 30 min to remove all hexane and then was refilled with N_2 gas. The flask was heated to 310 °C. When the temperature was at

260 °C, 0.2 M $Cd(Oleate)_2$ and 0.2 M 1-octanethiol solutions with amounts calculated based on the CdSe core amount and the desired number of CdS ML or final size, both in ODE, were injected into the reaction flask using a dual-syringe pump with the rate of 3 mL/h. Usually, the temperature reaches 310 °C 5 min after injection starts. When the injection was completed, the reaction mixture was kept at 310 °C for 10 min and then at 280 °C for at least 4 h. The flask was quickly cooled to room temperature with forced air and was brought into a glovebox for purification with methyl acetate/hexane.

5.6.4 *Stepwise Shelling of CdSe with CdS*

The schematic stepwise shelling process for the samples in our study is described in **Figure 5.1.a**. Initially, CdSe cores were shelled with 30 monolayers (MLs) of CdS using the direct shelling method outlined previously. After the reaction was cooled to 85 °C, a portion of the reaction was transferred to a separate N_2 gas-filled three-neck round-bottom flask, which was subsequently heated to 310 °C. This procedure was replicated to add an additional 30 CdS MLs, resulting in CdSe80CdS QDs, and once more to add 20 CdS MLs, resulting in CdSe100CdS QDs. The sample portions that were not used for stepwise shelling were brought into a glovebox for purification with methyl acetate/hexane and characterization.

As an example, we show here the calculations of Cd and S precursor amounts for shelling CdSe30CdS prepared previously with 20 more CdS MLs to achieve CdSe50CdS QDs.

From the calculation above, the final volume in the flask is 21.1 mL × 2 + 6 mL = 48.2 mL. We used 10 mL of this CdSe30CdS QD solution for the next shelling step.

Dilution factor or volume ratio of the portion used for the next shelling step to the final volume of the previous step, $\alpha_{<30\text{-}50>} = 10 / 48.2 = 0.207$

Injection volume, $V_{injection<30\ to\ 50>} = (V_{injection<0\ to\ 50>} - V_{injection<0\ to\ 30>}) \times \alpha_{<30\text{-}50>} = 12.53$ mL = $(81.624 - 21.11) \times 0.207 = 12.53$ mL.

with $V_{<0\ to\ 50>}$ being the amount needed to direct shell CdSe core with 50 ML of CdS, calculated as above.

A portion (10 mL) of the freshly made and warm (85 °C) CdSe30CdS QD solution was transferred into a separate flask, which was degassed for 1 h and refilled with N_2 gas. The solution was heated to 310 °C. Upon reaching 260 °C, solutions of Cd and S precursors, intended for an additional 20 CdS MLs, were injected into the flask at a rate of 3 mL/h using a dual-syringe pump. Following the completion of the injection, the reaction mixture was maintained at 310 °C for 30 minutes and then at 280 °C for a minimum of 2 hours to synthesize CdSe50CdS QDs. The yellow precipitate was washed 5 times with hexane, then dispersed and stored in hexane inside a glovebox. Similarly, calculations of the injection volume needed to shell CdSe50CdS with 30 CdS MLs to produce CdSe80CdS, and the injection volume needed to shell CdSe80CdS with 20 CdS MLs to produce CdSe100CdS, were done below:

$V_{injection<50\ to\ 80>} = ((V_{injection<0\ to\ 80>} - V_{injection<0\ to\ 30>}) \times \alpha_{<30\ to\ 50>} - V_{injection<30\ to\ 50>}) \times \alpha_{<50\ to\ 80} =$ $((300.365 - 21.1)*0.207 - 12.528) \times 0.428 = 19.38$ mL

$V_{injection<80\ to\ 100>} = (((V_{injection<0\ to\ 100>} - V_{injection<0\ to\ 30>}) \times \alpha_{<30\ to\ 50>} - V_{injection<30\ to\ 50>}) \times \alpha_{<50\ to\ 80>} - V_{injection<50\ to\ 80>}) \times \alpha_{<80\ to\ 100>} = (((565.52 - 21.1)*0.207 - 12.528) \times 0.428 - 19.38) \times 0.5 = 11.75$ mL

Table 5.6. Precursor amounts and QD concentration throughout stepwise shelling

Steps	Added Vol (mL)	Injection Vol (mL)	Total Vol (L)	Dilution Factor	Cummulative Dilution Factor	Mol	[QD] (mol/L)
0-30	6	21.1	0.0482	1	1	0.00000003	6.22407E-07
30-50	10	12.528	0.035056	0.207	0.207	0.00000003	1.77145E-07
50-80	15	19.38	0.05376	0.428	0.088596	0.00000003	4.94397E-08
80-100	27	11.75	0.0505	0.5	0.044298	0.00000003	2.63156E-08

It is important to estimate the final volume of the reaction to decide the flask volume to use for each shelling step. It is also important to estimate the injection time to avoid Cd(oletate)$_2$ from solidifying in the syringe and to avoid letting the reaction at a high temperature for a long time.

5.6.5 *(Scanning) Transmission Electron Microscopy ((S)TEM)*

TEM imaging was done on an FEI Tecnai G2 F20 SuperTwin microscope operated at 200 kV by using bright field imaging. Samples were prepared in a nitrogen glovebox by drop-casting 5 μL of dilute QD suspensions in toluene onto a suspended ultrathin carbon film on a lacey carbon support film, 400 mesh, copper grids purchased from Ted Pella Inc., allowed to dry fully (10 min), and then placed under vacuum overnight. TEM size analysis, including size measurements and circularity index assessment, was performed using manual analysis in ImageJ over at least 150 particle diameter measurements per sample.

STEM was performed with a Thermo Scientific Titan Themis operated at an accelerating voltage of 300 kV. Samples were prepared by drop-casting solutions of the QDs onto TEM grids (Ted Pella, Prod#01824; ultrathin carbon film on lacey carbon support film, 400 mesh, Cu). Samples were dried under a vacuum. Excess ligands were removed from the CdSe50CdS, CdSe80CdS, and CdSe100CdS samples by submerging the grids in ethanol over activated carbon, adapting a procedure from Li et al.[82] Prior to imaging, samples were further dried under a vacuum at 120 °C overnight. Energy dispersive X-ray spectroscopy (EDS) was performed with a Super-X quad EDS detector. Tilt series were acquired from roughly −70 to 70° using a Gatan Elsa Cryo-Transfer Holder with an ultralow-profile tip at room temperature. To accommodate a wide range of angles for the tilt series, the samples were drop-cast onto 200 mesh TEM grids (Ted Pella, Prod no. 01841; carbon film on 200 mesh, Cu). Samples were cleaned by the same process as that described before.

EDS analysis was performed with Thermo Scientific Velox software.

Tilt series images were aligned in ImageJ using the TomoJ plugin.[83] The aligned tilt series were cropped, and then tomographic reconstruction was performed with TomoJ. The resulting image stack was thresholded and exported using the 3D Viewer plugin and visualized in Microsoft PowerPoint.[84]

Analysis of atomic column intensity and position was performed with StatSTEM.

Model structures were constructed in VESTA.[60] To construct a model with stacking faults, the model was exported from VESTA into MATLAB. A stacking fault was induced by reflecting and shifting the coordinates of atoms in the outermost {0001} plane. Atoms outside of certain bounds were deleted to make a well-defined slab for easier comparison with other slabs.

Multislice STEM simulations were performed with the ab TEM Python Package.

5.6.6 *Solution UV–Visible Absorption and PL Measurements*

Ultraviolet–visible (UV–vis) spectra were collected on a Cary 5000 spectrophotometer from Agilent. Steady-state PL measurements were taken on a HORIBA Jobin Yvon FluoroMax-4 fluorescence spectrophotometer, and quantum yield measurements were taken with a Hamamatsu C9920–12 integrating sphere with a Hamamatsu C10027–01 photonic multichannel analyzer. All PLQY measurements were taken in triplicate. Time-resolved photoluminescence decay was measured using an Edinburgh FLS 1000 Fluorimeter located in the University of Washington's MEM-C shared user facility. The excitation wavelength is 525 nm.

5.6.7 *Single-Particle PL, Wide-Field PL, and $g^{(2)}$ Measurements for Colossal QDs*

Low fluorescence glass coverslips (VistaVision#1.5 22 mm × 22 mm, VWR) were cleaned via sequential sonication in soap solution, deionized water (×2), acetone, and IPA with each

sonication lasting 10 min. Immediately prior to sample deposition, each side of the coverslips was UV-ozone cleaned for 23 min.

Low-concentration QD solutions were prepared in hexanes via serial dilution. The solutions were diluted by a factor of 1000 to 100,000 and sonicated for 10 min. Single-QD films were then prepared via spin coating. 60 μL of solution was deposited onto the cleaned coverslips and spun at 2000 rpm for 40 s. The films were measured immediately after spin coating.

Wide-field microscopy measurements were performed on a Nikon TE2000 inverted optical microscope using a CFI Super Fluor 40× Oil immersion objective (NA = 1.3) with an Olympus F immersion oil. The illumination source was a 415 nm light-emitting diode (LED) (SOLIS-415C, Thor Laboratories) at a power density of 47 mW/cm^2. The following filters were used for the measurement: FF02–650/100 (AVR Optics), FF01–424/SP-25 (Semrock), and ZT488rdc (Chroma) mounted in Chroma Laser TIRF for Nikon TE2000/T filter cube. Videos of the sample photoluminescence over time were collected on a Prime 95B (Photometrics) camera. Videos consisted of 8000 images with an integration time of 50 ms. Individual QD photoluminescence traces were extracted from the videos using a custom-built Python package for selecting bright objects from a dark background and analyzed using a custom Python package for Change Point Analysis.[87,88] More details describing the Change Point Analysis and particle selection code and performance can be found elsewhere. Our particle selection and CPA code is publicly available at: https://github.com/GingerLabUW/Widefield-CPA.

Single-particle spectroscopy was performed in ambient conditions with a home-built scanning PL setup. QDs were spin-coated on a Si/SiO_2 substrate. 532 nm continuous-wave laser light (Laserglow Technologies 532 nm DPSS Laser) was focused on the sample using a 100× (NA 0.95) dry objective lens. The typical excitation power was 5 μW as measured before the objective

lens. The position of the excitation/collection spot was controlled by a fast-steering mirror (Newport FSM-300–01). The collected PL was filtered through a 580 nm long-pass filter and fiber-coupled either to a spectrometer to collect the PL spectrum or through a 50:50 fiber splitter to a pair of avalanche photodiodes MPD-plasma desorption mass (MPD-PDM) to collect the $g^{(2)}(\tau)$ spectrum. For the $g^{(2)}(\tau)$ spectra, the time correlation was performed by a time tagger (PicoQuant TimeHarp 260). The PL time traces were collected in parallel with the $g^{(2)}(\tau)$ spectra. Custom software was used to map a specific area of the sample first and allow us to select specific spots for all measurements. PL counts were displayed live during the measurement. We considered emitters that appeared as isolated spots in the PL map and showed a PL count larger than 3000 and less than 50 k.

5.6.8 *QD Ink Preparation for Inkjet Printing*

The QD ink was prepared by evaporating a hexane-based QD solution under vacuum at 100 °C for 30 min, yielding ~3 mg of bright yellow QD powder. The resulting powder was subsequently dispersed in 10 mL of a 1:1 octane:hexadecane mixture through stirring at 80 °C for 1 h, followed by sonication 1 h.

5.6.9 *Electrohydrodynamic Inkjet Printing*

Electrohydrodynamic inkjet printing was conducted by loading the prepared CdSe/CdS ink into pulled borosilicate glass capillary pipettes with a tip internal nozzle diameter of ~5 μm. These printheads were manufactured with a tungsten electrode filament integrated inside this pipette. After mounting the printhead into the printer and placing the substrate on a grounded stage vacuum chuck, printing could be initiated. For the nanophotonic cavity, an alignment process was used to map the designed printing pattern to the orientation of the target substrate. Upon completion,

printing was initiated with the following parameters: bias: 1000 V, amplitude: 900-1000 V, frequency: 1 kHz, hold time 1-2 seconds.

5.6.10 *Photoluminescence Characterization of Bare Substrate QD*

Single-particle characterization was performed in air using a custom-built scanning PL set-up. A 532 nm continuous-wave laser (Laserglow Technologies 532 nm DPSS Laser) was focused on the particles with a 100× (NA 0.95) dry objective lens with a typical excitation power of 10 μW. The laser spot position was controlled via a steering mirror (Newport FSM-300–01). The collected PL was filtered through both a 550 nm long-pass filter and a bandpass filtered centered on 618 nm with 50 nm bandwidth. The collected PL was fiber-coupled either to a spectrometer (Princeton Instruments Isoplane 100) to collect the single-particle spectrum or through a 50:50 fiber splitter to a pair of avalanche photodiodes (MPD-PDM) to collect the $g^{(2)}(\tau)$ spectrum. For the $g^{(2)}(\tau)$ spectra, the time correlation was performed via a time tagger (PicoQuant TimeHarp 260).

5.6.11 *Nanophotonic Cavity Fabrication*

The SiN nanobeam cavities were designed for operation on a SiO_2 substrate with no top cladding in 220 nm thick SiN. The cavity was formed by punching a one-dimensional array of elliptical holes in a 550 nm wide SiN waveguide. The dimensions of the elliptical holes were fixed to a major diameter of 411 nm and a minor diameter of 98 nm. Each half of the cavity consisted of 10 elliptical holes that quadratically tapered from a period of 184 nm to 190 nm. An additional 20 elliptical holes with a period of 193 nm were placed on either end to form the cavity mirrors. According to FDTD simulations, this resulted in a cavity mode at 618 nm with quality factor ~4 x 105 and mode volume ~ 2 $(\lambda/n)^3$. To fabricate the nanobeam cavities, 100 kV ebeam-lithography

was used to transfer the pattern to a positive-tone e-beam resist. The pattern was then etched into the SiN thin film using a fluorine-based plasma etch.

5.6.12 *Photoluminescence Characterization of Cavity-Integrated QD*

Measurements were performed in a confocal setup operating in ambient conditions. Green continuous wave 532 nm laser light (LaserQuantum opus532) was passed through a 532 dichroic mirror (Chroma ZT532RDC) focused onto the center of the cavity using a 40x/0.6 NA Olympus objective, with a 1 μm spot size. A 580LP was used to filter out excitation light and PL went to a Princeton Instruments 300 grooves/mm grating spectrometer (SpectraPro HRS-750) coupled to a Pixis CCD (PIXIS: 100BR_eXcelon). Confocal scans were performed using a SPCM (Excelitas SPCM-AQ4C) coupled to a NIDAQ (BNC-2110). $g^{(2)}(\tau)$ was measured by going through a 40:60 fiber beam splitter and a timetagger (Swabian Instruments Timetagger Ultra). All low temperature measurements were done with a Montana cryostat (cryostation S-series) operating at 8K. Peaks were integrated and fit to a power law $I = aPb$, with the emission intensities scaling with excitation power (P) : excitonic (P^1), multi-excitonic (P^2 or higher), and phononassisted (P^1 or higher).

5.7 REFERENCES

(1) Aharonovich, I.; Englund, D.; Toth, M. Solid-State Single-Photon Emitters. *Nat. Photonics* **2016**, *10*, 631–641. https://doi.org/10.1038/nphoton.2016.186.

(2) Reimer, M. E.; Cher, C. The Quest for a Perfect Single-Photon Source. *Nat. Photonics* **2019**, *13*, 734–736. https://doi.org/10.1038/s41566-019-0544-x.

(3) Zhong, H.-S.; Wang, H.; Deng, Y.-H.; Chen, M.-C.; Peng, L.-C.; Luo, Y.-H.; Qin, J.; Wu, D.; Ding, X.; Hu, Y. Quantum Computational Advantage Using Photons. *Science* **2020**, *370*, 1460–1463. https://doi.org/10.1126/science.abe8770.

(4) Walker, T.; Kashanian, S. V.; Ward, T.; Keller, M. Improving the Indistinguishability of Single Photons from an Ion-Cavity System. *Phys. Rev. A* **2020**, *102*, 032616. https://doi.org/10.1103/PhysRevA.102.032616.

(5) Darquié, B.; Jones, M. P. A.; Dingjan, J.; Beugnon, J.; Bergamini, S.; Sortais, Y.; Messin, G.; Browaeys, A.; Grangier, P. Controlled Single-Photon Emission from a Single Trapped Two-Level Atom. *Science* **2005**, *309*, 454–456. https://doi.org/10.1126/science.1113394.

(6) Abe, N.; Mitsumori, Y.; Sadgrove, M.; Edamatsu, K. Dynamically Unpolarized Single-Photon Source in Diamond with Intrinsic Randomness. *Sci. Rep.* **2017**, *7*, 46722. https://doi.org/10.1038/srep46722.

(7) Mizuochi, N.; Makino, T.; Kato, H.; Takeuchi, D.; Ogura, M.; Okushi, H.; Nothaft, M.; Neumann, P.; Gali, A.; Jelezko, F. Electrically Driven Single-Photon Source at Room Temperature in Diamond. *Nat. Photonics* **2012**, *6*, 299–303. https://doi.org/10.1038/nphoton.2012.75.

(8) Gao, T.; von Helversen, M.; Antón-Solanas, C.; Schneider, C.; Heindel, T. Atomically-Thin Single-Photon Sources for Quantum Communication. *Npj 2D Mater. Appl.* **2023**, *7*, 4. https://doi.org/10.1038/s41699-023-00366-4.

(9) Gupta, S.; Wu, W.; Huang, S.; Yakobson, B. I. Single-Photon Emission from Two-Dimensional Materials, to a Brighter Future. *J. Phys. Chem. Lett.* **2023**, *14*, 3274–3284. https://doi.org/10.1021/acs.jpclett.2c03674.

(10) Zhang, L.; Yu, Y.-J.; Chen, L.-G.; Luo, Y.; Yang, B.; Kong, F.-F.; Chen, G.; Zhang, Y.; Zhang, Q.; Luo, Y. Electrically Driven Single-Photon Emission from an Isolated Single Molecule. *Nat. Commun.* **2017**, *8*, 580. https://doi.org/10.1038/s41467-017-00681-7.

(11) Toninelli, C.; Gerhardt, I.; Clark, A. S.; Reserbat-Plantey, A.; Götzinger, S.; Ristanović, Z.; Colautti, M.; Lombardi, P.; Major, K. D.; Deperasińska, I. Single Organic Molecules for Photonic

Quantum Technologies. *Nat. Mater.* **2021**, *20*, 1615–1628. https://doi.org/10.1038/s41563-021-00987-4.

(12) Thomas, S. E.; Wagner, L.; Joos, R.; Sittig, R.; Nawrath, C.; Burdekin, P.; de Buy Wenniger, I. M.; Rasiah, M. J.; Huber-Loyola, T.; Sagona-Stophel, S. Deterministic Storage and Retrieval of Telecom Light from a Quantum Dot Single-Photon Source Interfaced with an Atomic Quantum Memory. *Sci. Adv.* **2023**, *10*, eadi7346. https://doi.org/10.1126/sciadv.adi7346.

(13) Michler, P.; Imamoğlu, A.; Mason, M. D.; Carson, P. J.; Strouse, G. F.; Buratto, S. K. Quantum Correlation among Photons from a Single Quantum Dot at Room Temperature. *Nature* **2000**, *406*, 968–970. https://doi.org/10.1038/35023100.

(14) Chen, Y.; Sharp, D.; Saxena, A.; Nguyen, H.; Cossairt, B. M.; Majumdar, A. Integrated Quantum Nanophotonics with Solution-Processed Materials. *Adv. Quantum Technol.* **2022**, *5*, 2100078. https://doi.org/10.1002/qute.202100078.

(15) Kagan, C. R.; Bassett, L. C.; Murray, C. B.; Thompson, S. M. Colloidal Quantum Dots as Platforms for Quantum Information Science. *Chem. Rev.* **2021**, *121*, 3186–3233. https://doi.org/10.1021/acs.chemrev.0c00831.

(16) Uppu, R.; Midolo, L.; Zhou, X.; Carolan, J.; Lodahl, P. Quantum-Dot-Based Deterministic Photon–Emitter Interfaces for Scalable Photonic Quantum Technology. *Nat. Nanotechnol.* **2021**, *16*, 1308–1317. https://doi.org/10.1038/s41565-021-00965-6.

(17) Nguyen, H. A.; Sharp, D.; Fröch, J. E.; Cai, Y.-Y.; Wu, S.; Monahan, M.; Munley, C.; Manna, A.; Majumdar, A.; Kagan, C. R.; Cossairt, B. M. Deterministic Quantum Light Arrays from Giant Silica-Shelled Quantum Dots. *ACS Appl. Mater. Interfaces* **2023**, *15*, 4294–4302. https://doi.org/10.1021/acsami.2c18475.

(18) Utzat, H.; Sun, W.; Kaplan, A. E. K.; Krieg, F.; Ginterseder, M.; Spokoyny, B.; Klein, N.

D.; Shulenberger, K. E.; Perkinson, C. F.; Kovalenko, M. V.; Bawendi, M. G. Coherent Single-Photon Emission from Colloidal Lead Halide Perovskite Quantum Dots. *Science* **2019**, *363*, 1068–1072. https://doi.org/10.1126/science.aau7392.

(19) Becker, M. A.; Scarpelli, L.; Nedelcu, G.; Rainò, G.; Masia, F.; Borri, P.; Stöferle, T.; Kovalenko, M. V.; Langbein, W.; Mahrt, R. F. Long Exciton Dephasing Time and Coherent Phonon Coupling in $CsPbBr_2Cl$ Perovskite Nanocrystals. *Nano Lett.* **2018**, *18*, 7546–7551. https://doi.org/10.1021/acs.nanolett.8b03027.

(20) Nguyen, H. A.; Dixon, G.; Dou, F. Y.; Gallagher, S.; Gibbs, S.; Ladd, D. M.; Marino, E.; Ondry, J. C.; Shanahan, J. P.; Vasileiadou, E. S. Design Rules for Obtaining Narrow Luminescence from Semiconductors Made in Solution. *Chem. Rev.* **2023**, *123*, 7890–7952. https://doi.org/10.1021/acs.chemrev.3c00097.

(21) Song, Y.; Liu, R.; Wang, Z.; Xu, H.; Ma, Y.; Fan, F.; Voznyy, O.; Du, J. Enhanced Emission Directivity from Asymmetrically Strained Colloidal Quantum Dots. *Sci. Adv.* **2022**, *8*, eabl8219. https://doi.org/10.1126/sciadv.abl8219.

(22) Geiregat, P.; Van Thourhout, D.; Hens, Z. A Bright Future for Colloidal Quantum Dot Lasers. *NPG Asia Mater.* **2019**, *11*, 41. https://doi.org/10.1038/s41427-019-0141-y.

(23) Saxena, A.; Chen, Y.; Ryou, A.; Sevilla, C. G.; Xu, P.; Majumdar, A. Improving Indistinguishability of Single Photons from Colloidal Quantum Dots Using Nanocavities. *ACS Photonics* **2019**, *6*, 3166–3173. https://doi.org/10.1021/acsphotonics.9b01481.

(24) Zhu, C.; Marczak, M.; Feld, L.; Boehme, S. C.; Bernasconi, C.; Moskalenko, A.; Cherniukh, I.; Dirin, D.; Bodnarchuk, M. I.; Kovalenko, M. V.; Rainò, G. Room-Temperature, Highly Pure Single-Photon Sources from All-Inorganic Lead Halide Perovskite Quantum Dots. *Nano Lett.* **2022**, *22*, 3751–3760. https://doi.org/10.1021/acs.nanolett.2c00756.

(25) Hsu, B.-W.; Chuang, Y.-T.; Cheng, C.-Y.; Chen, C.-Y.; Chen, Y.-J.; Brumberg, A.; Yang, L.; Huang, Y.-S.; Schaller, R. D.; Chen, L.-J. Very Robust Spray-Synthesized $CsPbI_3$ Quantum Emitters with Ultrahigh Room-Temperature Cavity-Free Brightness and Self-Healing Ability. *ACS Nano* **2021**, *15*, 11358–11368. https://doi.org/10.1021/acsnano.1c00733.

(26) Park, Y.-S.; Guo, S.; Makarov, N. S.; Klimov, V. I. Room Temperature Single-Photon Emission from Individual Perovskite Quantum Dots. *ACS Nano* **2015**, *9*, 10386–10393. https://doi.org/10.1021/acsnano.5b04584.

(27) O'Brien, J. L.; Furusawa, A.; Vučković, J. Photonic Quantum Technologies. *Nat. Photonics* **2009**, *3*, 687–695. https://doi.org/10.1038/nphoton.2009.229.

(28) Gupta, S.; Waks, E. Spontaneous Emission Enhancement and Saturable Absorption of Colloidal Quantum Dots Coupled to Photonic Crystal Cavity. *Opt. Express* **2013**, *21*, 29612–29619. https://doi.org/10.1364/OE.21.029612.

(29) Jun, S.; Kim, J.; Choi, M.; Kim, B. S.; Park, J.; Kim, D.; Shin, B.; Cho, Y.-H. Ultrafast and Bright Quantum Emitters from the Cavity-Coupled Single Perovskite Nanocrystals. *ACS Nano* **2024**, *18*, 1396–1403. https://doi.org/10.1021/acsnano.3c06760.

(30) Chen, Y.; Ryou, A.; Friedfeld, M. R.; Fryett, T.; Whitehead, J.; Cossairt, B. M.; Majumdar, A. Deterministic Positioning of Colloidal Quantum Dots on Silicon Nitride Nanobeam Cavities. *Nano Lett.* **2018**, *18*, 6404–6410. https://doi.org/10.1021/acs.nanolett.8b02764.

(31) Schell, A. W.; Kewes, G.; Schröder, T.; Wolters, J.; Aichele, T.; Benson, O. A Scanning Probe-Based Pick-and-Place Procedure for Assembly of Integrated Quantum Optical Hybrid Devices. *Rev. Sci. Instrum.* **2011**, *82*, 073709. https://doi.org/10.1063/1.3615629.

(32) Kim, J.-H.; Aghaeimeibodi, S.; Richardson, C. J. K.; Leavitt, R. P.; Englund, D.; Waks, E. Hybrid Integration of Solid-State Quantum Emitters on a Silicon Photonic Chip. *Nano Lett.* **2017**,

17, 7394–7400. https://doi.org/10.1021/acs.nanolett.7b03220.

(33) Barth, M.; Schietinger, S.; Fischer, S.; Becker, J.; Nüsse, N.; Aichele, T.; Löchel, B.; Sönnichsen, C.; Benson, O. Nanoassembled Plasmonic-Photonic Hybrid Cavity for Tailored Light-Matter Coupling. *Nano Lett.* **2010**, *10*, 891–895. https://doi.org/10.1021/nl903555u.

(34) Choi, M.; Lee, M.; Park, S.-Y. L.; Kim, B. S.; Jun, S.; Park, S. I.; Song, J. D.; Ko, Y.-H.; Cho, Y.-H. Single Quantum Dot Selection and Tailor-Made Photonic Device Integration Using a Nanoscale-Focus Pinspot. *Adv. Mater.* **2023**, *35*, 2210667. https://doi.org/10.1002/adma.202210667.

(35) Xie, W.; Gomes, R.; Aubert, T.; Bisschop, S.; Zhu, Y.; Hens, Z.; Brainis, E.; Van Thourhout, D. Nanoscale and Single-Dot Patterning of Colloidal Quantum Dots. *Nano Lett.* **2015**, *15*, 7481–7487. https://doi.org/10.1021/acs.nanolett.5b03068.

(36) Reiss, P.; Protière, M.; Li, L. Core/Shell Semiconductor Nanocrystals. *Small* **2009**, *5*, 154–168. https://doi.org/10.1002/smll.200800841.

(37) Nann, T.; Mulvaney, P. Single Quantum Dots in Spherical Silica Particles. *Angew. Chem., Int. Ed.* **2004**, *43*, 5393–5396. https://doi.org/10.1002/anie.200460752.

(38) Sampat, S.; Karan, N. S.; Guo, T.; Htoon, H.; Hollingsworth, J. A.; Malko, A. V. Multistate Blinking and Scaling of Recombination Rates in Individual Silica-Coated CdSe/CdS Nanocrystals. *ACS Photonics* **2015**, *2*, 1505–1512. https://doi.org/10.1021/acsphotonics.5b00423

(39) Chen, Y.; Vela, J.; Htoon, H.; Casson, J. L.; Werder, D. J.; Bussian, D. A.; Klimov, V. I.; Hollingsworth, J. A. Giant" Multishell CdSe Nanocrystal Quantum Dots with Suppressed Blinking. *J. Am. Chem. Soc.* **2008**, *130*, 5026–5027. https://doi.org/10.1021/ja711379k.

(40) Singh, A.; Majumder, S.; Orfield, N. J. T.; Sarpkaya, I.; Nordlund, D.; Bustillo, K. C.; Ciston, J.; Nisoli, V.; Ivanov, S. A.; Bowes, E. G. From Inside Out: How the Buried Interface,

Shell Defects, and Surface Chemistry Conspire to Determine Optical Performance in Nonblinking Giant Quantum Dots. *Small Sci.* **2023**, *3*, 2300092. https://doi.org/10.1002/smsc.202300092.

(41) Bladt, E.; van Dijk-Moes, R. J. A.; Peters, J.; Montanarella, F.; de Mello Donega, C.; Vanmaekelbergh, D.; Bals, S. Atomic Structure of Wurtzite CdSe (Core)/CdS (Giant Shell) Nanobullets Related to Epitaxy and Growth. *J. Am. Chem. Soc.* **2016**, *138*, 14288–14293. https://doi.org/10.1021/jacs.6b06443.

(42) Nasilowski, M.; Spinicelli, P.; Patriarche, G.; Dubertret, B. Gradient CdSe/CdS Quantum Dots with Room Temperature Biexciton Unity Quantum Yield. *Nano Lett.* **2015**, *15*, 3953–3958. https://doi.org/10.1021/acs.nanolett.5b00838.

(43) Galland, C.; Ghosh, Y.; Steinbrück, A.; Hollingsworth, J. A.; Htoon, H.; Klimov, V. I. Lifetime Blinking in Nonblinking Nanocrystal Quantum Dots. *Nat. Commun.* **2012**, *3*, 908. https://doi.org/10.1038/ncomms1916.

(44) García-Santamaría, F.; Chen, Y.; Vela, J.; Schaller, R. D.; Hollingsworth, J. A.; Klimov, V. I. Suppressed Auger Recombination in "Giant" Nanocrystals Boosts Optical Gain Performance. *Nano Lett.* **2009**, *9*, 3482–3488. https://doi.org/10.1021/nl901681d.

(45) Pal, B. N.; Ghosh, Y.; Brovelli, S.; Laocharoensuk, R.; Klimov, V. I.; Hollingsworth, J. A.; Htoon, H. Giant' CdSe/CdS Core/Shell Nanocrystal Quantum Dots As Efficient Electroluminescent Materials: Strong Influence of Shell Thickness on Light-Emitting Diode Performance. *Nano Lett.* **2012**, *12*, 331–336. https://doi.org/10.1021/nl203620f.

(46) Diroll, B. T.; Hua, M.; Guzelturk, B.; Pálmai, M.; Tomczak, K. Long-Lived and Bright Biexcitons in Quantum Dots with Parabolic Band Potentials. *Nano Lett.* **2023**, *23*, 11975–11981. https://doi.org/10.1021/acs.nanolett.3c04361.

(47) Matsuzaki, K.; Vassant, S.; Liu, H.-W.; Dutschke, A.; Hoffmann, B.; Chen, X.;

Christiansen, S.; Buck, M. R.; Hollingsworth, J. A.; Götzinger, S.; Sandoghdar, V. Strong Plasmonic Enhancement of Biexciton Emission: Controlled Coupling of a Single Quantum Dot to a Gold Nanocone Antenna. *Sci. Rep.* **2017**, *7*, 42307. https://doi.org/10.1038/srep42307.

(48) Park, Y.-S.; Malko, A. V.; Vela, J.; Chen, Y.; Ghosh, Y.; García-Santamaría, F.; Hollingsworth, J. A.; Klimov, V. I.; Htoon, H. Near-Unity Quantum Yields of Biexciton Emission from CdSe/CdS Nanocrystals Measured Using Single-Particle Spectroscopy. *Phys. Rev. Lett.* **2011**, *106*, 187401. https://doi.org/10.1103/PhysRevLett.106.187401.

(49) Hanifi, D. A.; Bronstein, N. D.; Koscher, B. A.; Nett, Z.; Swabeck, J. K.; Takano, K.; Schwartzberg, A. M.; Maserati, L.; Vandewal, K.; van de Burgt, Y. Redefining Near-Unity Luminescence in Quantum Dots with Photothermal Threshold Quantum Yield. *Science* **2019**, *363*, 1199–1202. https://doi.org/10.1126/science.aat3803.

(50) Hollingsworth, J. A. Heterostructuring Nanocrystal Quantum Dots Toward Intentional Suppression of Blinking and Auger Recombination. *Chem. Mater.* **2013**, *25*, 1318–1331. https://doi.org/10.1021/cm304161d.

(51) Ghosh, Y.; Mangum, B. D.; Casson, J. L.; Williams, D. J.; Htoon, H.; Hollingsworth, J. A. New Insights into the Complexities of Shell Growth and the Strong Influence of Particle Volume in Nonblinking "Giant" Core/Shell Nanocrystal Quantum Dots. *J. Am. Chem. Soc.* **2012**, *134*, 9634–9643. https://doi.org/10.1021/ja212032q.

(52) Tan, R.; Yuan, Y.; Nagaoka, Y.; Eggert, D.; Wang, X.; Thota, S.; Guo, P.; Yang, H.; Zhao, J.; Chen, O. Monodisperse Hexagonal Pyramidal and Bipyramidal Wurtzite CdSe-CdS Core–Shell Nanocrystals. *Chem. Mater.* **2017**, *29*, 4097–4108. https://doi.org/10.1021/acs.chemmater.7b00968.

(53) Chen, O.; Zhao, J.; Chauhan, V. P.; Cui, J.; Wong, C.; Harris, D. K.; Wei, H.; Han, H.-S.;

Fukumura, D.; Jain, R. K.; Bawendi, M. G. Compact High-Quality CdSe–CdS Core–Shell Nanocrystals with Narrow Emission Linewidths and Suppressed Blinking. *Nat. Mater.* **2013**, *12*, 445–451. https://doi.org/10.1038/nmat3539.

(54) Cirillo, M.; Aubert, T.; Gomes, R.; Van Deun, R.; Emplit, P.; Biermann, A.; Lange, H.; Thomsen, C.; Brainis, E.; Hens, Z. "Flash" Synthesis of CdSe/CdS Core–Shell Quantum Dots. *Chem. Mater.* **2014**, *26*, 1154–1160. https://doi.org/10.1021/cm403518a.

(55) Christodoulou, S.; Vaccaro, G.; Pinchetti, V.; De Donato, F.; Grim, J. Q.; Casu, A.; Genovese, A.; Vicidomini, G.; Diaspro, A.; Brovelli, S. Synthesis of Highly Luminescent Wurtzite CdSe/CdS Giant-Shell Nanocrystals Using a Fast Continuous Injection Route. *J. Mater. Chem. C* **2014**, *2*, 3439–3447. https://doi.org/10.1039/c4tc00280f.

(56) Wang, X.; Liu, M.; Zhou, Z.; Guo, L. Toward Facet Engineering of CdS Nanocrystals and Their Shape-Dependent Photocatalytic Activities. *J. Phys. Chem. C* **2015**, *119*, 20555–20560. https://doi.org/10.1021/acs.jpcc.5b07370.

(57) Lei, H.; Li, T.; Li, J.; Zhu, J.; Zhang, H.; Qin, H.; Kong, X.; Wang, L.; Peng, X. Reversible Facet Reconstruction of CdSe/CdS Core/Shell Nanocrystals by Facet–Ligand Pairing. *J. Am. Chem. Soc.* **2023**, *145*, 6798–6810. https://doi.org/10.1021/jacs.2c13500.

(58) Ji, B.; Panfil, Y. E.; Waiskopf, N.; Remennik, S.; Popov, I.; Banin, U. Strain-Controlled Shell Morphology on Quantum Rods. *Nat. Commun.* **2019**, *10*, 2. https://doi.org/10.1038/s41467-018-07837-z.

(59) Kong, X.; Yu, F.; Zhang, H.; Lv, F.; Wang, Y.; Yin, L.; Huang, J.; Feng, Q. Synthesis and Study of Morphology Regulation, Formation Mechanism and Photocatalytic Performance of CdS. *Appl. Surf. Sci.* **2022**, *576*, 151817. https://doi.org/10.1016/j.apsusc.2021.151817

(60) Momma, K.; Izumi, F. VESTA3 for Three-Dimensional Visualization of Crystal,

Volumetric and Morphology Data. *J. Appl. Crystallogr.* **2011**, *44*, 1272–1276. https://doi.org/10.1107/S0021889811038970.

(61) Rempel, J. Y.; Trout, B. L.; Bawendi, M. G.; Jensen, K. F. Properties of the CdSe(0001), $(000\bar{1})$, and $(11\bar{2}0)$ Single Crystal Surfaces: Relaxation, Reconstruction, and Adatom and Admolecule Adsorption. *J. Phys. Chem. B* **2005**, *109*, 19320–19328. https://doi.org/10.1021/jp053560z.

(62) Hughes, S. M.; Alivisatos, A. P. Anisotropic Formation and Distribution of Stacking Faults in II–VI Semiconductor Nanorods. *Nano Lett.* **2013**, *13*, 106–110. https://doi.org/10.1021/nl3036417.

(63) Alpay, D.; Peng, L.; Marks, L. D. Are Nanoparticle Corners Round? *J. Phys. Chem. C* **2015**, *119*, 21018–21023. https://doi.org/10.1021/acs.jpcc.5b07021.

(64) Coropceanu, I.; Bawendi, M. G. Core/Shell Quantum Dot Based Luminescent Solar Concentrators with Reduced Reabsorption and Enhanced Efficiency. *Nano Lett.* **2014**, *14*, 4097–4101. https://doi.org/10.1021/nl501627e.

(65) Zhou, X.; Pu, C. Proton Shuttle-Assisted Surface Reconstruction toward Nonpolar Facets-Terminated Zinc-Blende CdSe/CdS Core/Shell Quantum Dots. *J. Am. Chem. Soc.* **2023**, *145*, 26287–26295. https://doi.org/10.1021/jacs.3c09413.

(66) Zhou, J.; Pu, C.; Jiao, T.; Hou, X.; Peng, X. A Two-Step Synthetic Strategy toward Monodisperse Colloidal CdSe and CdSe/CdS Core/Shell Nanocrystals. *J. Am. Chem. Soc.* **2016**, *138*, 6475–6483. https://doi.org/10.1021/jacs.6b00674.

(67) Xu, J. X.; Yuan, Y.; Liu, M.; Zou, S.; Chen, O.; Zhang, D. Quantification of the Photon Absorption, Scattering, and On-Resonance Emission Properties of CdSe/CdS Core/Shell Quantum Dots: Effect of Shell Geometry and Volumes. *Anal. Chem.* **2020**, *92*, 5346–5353.

https://doi.org/10.1021/acs.analchem.0c00016.

(68) Piri, N.; Shams-Nateri, A.; Mokhtari, J. The Relationship between Refractive Index and Optical Properties of Absorbing Nanoparticle. *Color Res. Appl.* **2016**, *41*, 477–483. https://doi.org/10.1002/col.21983.

(69) Cho, J.; Jung, Y. K.; Lee, J.-K.; Jung, H.-S. Highly Efficient Blue-Emitting CdSe-Derived Core/Shell Gradient Alloy Quantum Dots with Improved Photoluminescent Quantum Yield and Enhanced Photostability. *Langmuir* **2017**, *33*, 3711–3719. https://doi.org/10.1021/acs.langmuir.6b04333.

(70) Bae, W. K.; Nam, M. K.; Char, K.; Lee, S. Gram-Scale One-Pot Synthesis of Highly Luminescent Blue Emitting $Cd_{1-x}Zn_xS$/ZnS Nanocrystals. *Chem. Mater.* **2008**, *20*, 5307–5313. https://doi.org/10.1021/cm801201x.

(71) Singh, R.; Akhil, S.; Dutt, V. G. V.; Mishra, N. Shell Thickness Dependent Photostability Studies of Green-Emitting "Giant" Quantum Dots. *Nanoscale Adv.* **2021**, *3*, 6984–6991. https://doi.org/10.1039/D1NA00663K.

(72) Würth, C.; Resch-Genger, U. Determination of Photoluminescence Quantum Yields of Scattering Media with an Integrating Sphere: Direct and Indirect Illumination. *Appl. Spectrosc.* **2015**, *69*, 749–759. https://doi.org/10.1366/14-07679.

(73) García-Santamaría, F.; Brovelli, S.; Viswanatha, R.; Hollingsworth, J. A.; Htoon, H.; Crooker, S. A.; Klimov, V. I. Breakdown of Volume Scaling in Auger Recombination in CdSe/CdS Heteronanocrystals: The Role of the Core–Shell Interface. *Nano Lett.* **2011**, *11*, 687–693. https://doi.org/10.1021/nl103801e.

(74) Qin, H.; Meng, R.; Wang, N.; Peng, X. Photoluminescence Intermittency and Photo-Bleaching of Single Colloidal Quantum Dot. *Adv. Mater.* **2017**, *29*, 1606923.

https://doi.org/10.1002/adma.201606923.

(75) Fisher, B.; Caruge, J. M.; Zehnder, D.; Bawendi, M. Room-Temperature Ordered Photon Emission from Multiexciton States in Single CdSe Core-Shell Nanocrystals. *Phys. Rev. Lett.* **2005**, *94*, 087403. https://doi.org/10.1103/PhysRevLett.94.087403.

(76) Cohen, T. A.; Sharp, D.; Kluherz, K. T.; Chen, Y.; Munley, C.; Anderson, R. T.; Swanson, C. J.; De Yoreo, J. J.; Luscombe, C. K.; Majumdar, A. Direct Patterning of Perovskite Nanocrystals on Nanophotonic Cavities with Electrohydrodynamic Inkjet Printing. *Nano Lett.* **2022**, *22*, 5681–5688. https://doi.org/10.1021/acs.nanolett.2c00473.

(77) Guymon, G. G.; Sharp, D.; Cohen, T. A.; Gibbs, S. L.; Manna, A.; Tzanetopoulos, E.; Gamelin, D. R.; Majumdar, A.; MacKenzie, J. D. Electrohydrodynamic Printing-Based Heterointegration of Quantum Dots on Suspended Nanophotonic Cavities. *Adv. Mater. Technol.* **2024**, *9*, 2301921. https://doi.org/10.1002/admt.202301921.

(78) Barad, H.-N.; Kwon, H.; Alarcón-Correa, M.; Fischer, P. Large Area Patterning of Nanoparticles and Nanostructures: Current Status and Future Prospects. *ACS Nano* **2021**, *15*, 5861–5875. https://doi.org/10.1021/acsnano.0c09999.

(79) Shulevitz, H. J.; Huang, T.-Y.; Xu, J.; Neuhaus, S. J.; Patel, R. N.; Choi, Y. C.; Bassett, L. C.; Kagan, C. R. Template-Assisted Self-Assembly of Fluorescent Nanodiamonds for Scalable Quantum Technologies. *ACS Nano* **2022**, *16*, 1847–1856. https://doi.org/10.1021/acsnano.1c09839.

(80) Greybush, N. J.; Pacheco-Peña, V.; Engheta, N.; Murray, C. B.; Kagan, C. R. Plasmonic Optical and Chiroptical Response of Self-Assembled Au Nanorod Equilateral Trimers. *ACS Nano* **2019**, *13*, 1617–1624. https://doi.org/10.1021/acsnano.8b07619.

(81) Jasieniak, J.; Smith, L.; van Embden, J.; Mulvaney, P.; Califano, M. Re-Examination of the Size-Dependent Absorption Properties of CdSe Quantum Dots. *J. Phys. Chem. C* **2009**, *113*, 19468–19474. https://doi.org/10.1021/jp906827m.

(82) Li, C.; Tardajos, A. P.; Wang, D.; Choukroun, D.; Van Daele, K.; Breugelmans, T.; Bals, S. A Simple Method to Clean Ligand Contamination on TEM Grids. *Ultramicroscopy* **2021**, *221*, 113195. https://doi.org/10.1016/j.ultramic.2020.113195.

(83) Messaoudi, C.; Boudier, T.; Sorzano, C. O. S.; Marco, S. TomoJ: Tomography Software for Three-Dimensional Reconstruction in Transmission Electron Microscopy. *BMC Bioinf.* **2007**, *8*, 288. https://doi.org/10.1186/1471-2105-8-288.

(84) Schmid, B.; Schindelin, J.; Cardona, A.; Longair, M.; Heisenberg, M. A High-Level 3D Visualization API for Java and ImageJ. *BMC Bioinf.* **2010**, *11*, 274. https://doi.org/10.1186/1471-2105-11-274.

(85) De Backer, A.; van den Bos, K. H. W.; Van den Broek, W.; Sijbers, J.; Van Aert, S. StatSTEM: An Efficient Approach for Accurate and Precise Model-Based Quantification of Atomic Resolution Electron Microscopy Images. *Ultramicroscopy* **2016**, *171*, 104–116. https://doi.org/10.1016/j.ultramic.2016.08.018.

(86) Madsen, J.; Susi, T. The ab TEM Code: Transmission Electron Microscopy from First Principles. *Open Res. Eur.* **2021**, *1*, 124. https://doi.org/10.12688/openreseurope.13015.2.

(87) Yaman, M. Y.; Guye, K. N.; Ziatdinov, M.; Shen, H.; Baker, D.; Kalinin, S. V.; Ginger, D. S. Alignment of Au Nanorods along de Novo Designed Protein Nanofibers Studied with Automated Image Analysis. *Soft Matter* **2021**, *17*, 6109–6115. https://doi.org/10.1039/D1SM00645B.

(88) Gallagher, S.; Kline, J.; Jahanbakhshi, F.; Sadighian, J. C.; Lyons, I.; Shen, G.; Rappe, A.

M.; Ginger, D. S. Ligand Equilibrium Influences Photoluminescence Blinking in $CsPbBr_3$: A Change Point Analysis of Widefield Imaging Data. *ACS Nano* **2024**, *18*, 19208–19219. https://doi.org/10.1021/acsnano.4c04968.

(89) Morozov, S.; Vezzoli, S.; Myslovska, A.; Di Giacomo, A.; Mortensen, N. A.; Moreels, I.; Sapienza, R. Purifying Single Photon Emission from Giant Shell CdSe/CdS Quantum Dots at Room Temperature. *Nanoscale* **2023**, *15*, 1645–1651. https://doi.org/10.1039/D2NR04744F.

(90) Pálmai, M.; Beckwith, J. S.; Emerson, N. T.; Zhao, T.; Kim, E. B.; Yin, S.; Parajuli, P.; Tomczak, K.; Wang, K.; Sapkota, B.; et al. Parabolic Potential Surfaces Localize Charge Carriers in Nonblinking Long-Lifetime "Giant" Colloidal Quantum Dots. *Nano Lett*. **2022**, *22*, 9470–9476. https://doi.org/10.1021/acs.nanolett.2c03563.

(91) Guymon, G. G., Nguyen, H. A., Sharp, D., Nguyen, T., Lei, H., Ginger, D. S., Fu, K.-M. C., Majumdar, A., Cossairt, B. M., MacKenzie, J. D. Deterministic Printing and Heterointegration of Single Colloidal Quantum Dot Photon Sources. *In Review* **(April 10, 2025)**.

Chapter 6. CONCLUSIONS AND OUTLOOKS

The work in this dissertation has advanced both the synthesis and integration of colloidal QDs for quantum photonic applications by addressing two central challenges: achieving deterministic single-photon emission and understanding the impact of particle composition, shape, and size on optical properties. Through targeted materials development and device-level integration, this work demonstrates how colloidal QDs can evolve from chemically tunable emitters into scalable quantum light sources.

6.1 KEY FINDINGS

I explored two synthetic frontiers: silica shelling and colossal CdSe/CdS core/shell growth. Each approach advances the QD toolbox in unique, complementary ways. Silica shelling enables physical enlargement of QDs, transforming ~10 nm particles into ~100 nm structures while preserving their optical activity. These silica-encased QDs withstand mechanical and chemical handling steps that would typically damage native QDs, making them ideal candidates for deterministic placement. Although the shelling doesn't reduce blinking and in fact often introduces more optical instability, it allows the emitters to survive nanofabrication processes that are essential for device integration. Meanwhile, I tried to pushed the CdSe/CdS QD growth to new extremes, creating "colossal" particles >90 nm across with pristine optical performance. Unlike the silica-shelled counterparts, these giants exhibit dramatically reduced blinking and photobleaching, along with single-photon purity. Synthesized through a precise stepwise method, they maintain crystallinity, while also revealing fascinating structure–property relationships. Subtle morphological features, such as facet development and roundness, correlating directly with emission dynamics, opening the door to tunable QD behavior via nanoscale architecture.

The other half of the story is deterministic positioning. With wonderful collaborators, we have achieved single particle patterning and integration with two methods: Using template-assisted self-assembly, large silica shelled QDs were placed into ordered arrays and cavity sites with high single-particle fidelity. A major advance of this work lies in the deployment of single QDs via high precision electrohydrodynamic printing. This method enabled direct, residue-free deposition of individual QDs onto both conductive and dielectric substrates with yields approaching 50%, verified by fluorescence microscopy and SEM. Importantly, printed QDs retained single-photon emission characteristics ($g^2(0) < 0.5$), establishing the first additive manufacturing strategy for deterministic quantum emitters. We further applied this technique to heterointegrate single QDs into prefabricated high-Q nanophotonic cavities with sub-wavelength accuracy. We showed the cavity-enhanced emissions of single QDs and maintained quantum purity under ambient conditions.

6.2 OUTLOOKS

Looking ahead, our work opens several exciting directions for advancing quantum photonics and colloidal nanomaterials. Improving printing yield through better QD dispersity in ink formulations will enhance array uniformity and scalability. Extending emission wavelengths, particularly toward the telecom C-band, by adapting colossal shelling strategies to alternative core compositions could broaden the impact of this platform in quantum communication. Further exploration of QD-cavity coupled systems promises deeper insights into engineered light–matter interactions at the single-emitter level.

Beyond emission control, shape anisotropy offers a pathway to add complexity to superstructures and tune optical responses via engineered morphology. Meanwhile, the large size of these QDs presents unique opportunities for studying cathodoluminescence behavior and exploring alternative integration strategies across nanophotonic or electronic systems. One such

application has been realized in nanocavity-enhanced second-harmonic generation (SHG), where integrating colossal CdSe/CdS QDs with silicon nitride nanobeam cavities yielded over 2000-fold SHG enhancement (**Figure 6.1**).[1] SHG is a nonlinear optical process in which two photons at a fundamental frequency combine to generate a single photon at twice the energy (half the wavelength), enabling frequency conversion for applications such as on-chip lasers and quantum light sources. The large size and high polarizability of colossal QDs enhance their second-order nonlinear susceptibility, making them particularly effective for SHG. Coupling these QDs to high-Q cavities further concentrates the electromagnetic field, amplifying the SHG response at low input powers. This marks the first demonstration of cavity-enhanced nonlinear optics using colloidal QDs and underscores their potential for low-power, scalable photonic devices.

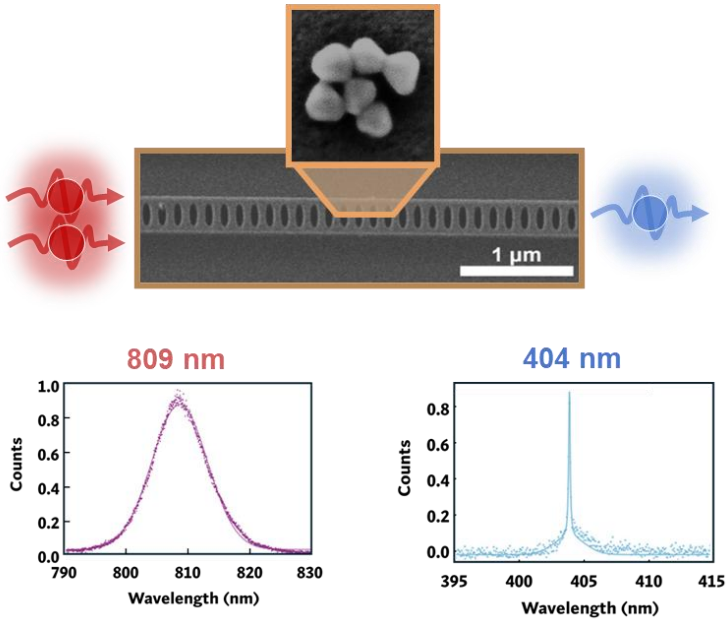

Figure 6.1. Spectrum of the ultrafast pump laser centered at 808.7 nm with a Gaussian line shape (red) and QD-cavity SHG spectrum (blue).

Together, these efforts will expand the functional capabilities of single-QD devices and help push forward the additive manufacturing of quantum materials for future quantum technologies. By enabling precise control over QD placement, emission, and nonlinear optical

behavior, this work lays the foundation for scalable integration of quantum emitters into photonic circuits—advancing applications in quantum communication, sensing, and information processing.

6.3 REFERENCES

(1) Sharp, D.; Kala, A.; Rarick, H.; Nguyen, H. A.; Skytte, E.; Cossairt, B. M.; Majumdar, A. Nanocavity-Enhanced Second-Harmonic Generation from Colossal Quantum Dots. *ACS Photonics*, **2025**

APPENDIX A: A SUMMER RESEARCH PROGRAM FOR COMMUNITY COLLEGE STUDENTS LED BY GRADUATE STUDENTS AT THE UNIVERSITY OF WASHINGTON

I started my academic career at Pierce College in Puyallup, Washington in 2016. During my time here, although I had wonderful teachers and friends, I struggled to find chemistry research opportunities as a community college student. This created many difficulties for me later when I transferred to Texas A&M University to complete my bachelor's degree in chemistry, where I often got rejected from research labs and scholarships due to the lack of previous research experience and research achievements. Going into my PhD program at the University of Washington, I promised myself that I will commit to help community college students to achieve their academic goals by mentoring, sharing connections and resources, and ultimately creating a solid opportunity for community college students. This is the motivation that urged me to create the summer research program for community college students (SCROCCS). This section aims to the design, execution, evaluations, and results of SCROCCS over its first two years (2022 and 2023).

Components of this chapter were republished with permission of the American Chemical Society, from "*A Summer Research Program for Community College Students Led by Graduate Students at the University of Washington*", Hao A. Nguyen*, Emily Miura-Stempel, Christine M. Morrison, Grant Dixon, Micaela K. Homer, Florence Y. Dou, Alyssia Snow, Matthew R. Golder, and Brandi M. Cossairt; *Journal of Chemical Education,* **2024**, *101, 7,* 2693–2702; Copyright 2025 American Chemical Society.

A1. Introduction

Community colleges play a pivotal role in the United States education system, providing accessible and affordable higher education entry points to a diverse population, particularly for underrepresented and low-income students. According to a Community College Research Center (CCRC) analysis of National Center for Education Statistics (NCES) data, community colleges serve approximately 41% of all undergraduates in the United States, translating to 8.9 million students in the 2020-2021 academic year.[1] Data from the 2016 National Postsecondary Student Aid Study shows that community colleges, compared to their four-year counterparts, cater to a more varied demographic with nearly half of the student population falling in the 25-59 age bracket and a significant number of first-generation students and those juggling academic commitments with parenthood.[2] Moreover, the National Science Foundation reports that 44% of students receiving a science or engineering bachelor's or master's degree at the beginning of the 21st century attended a community college during their education.[3] These institutions are essential pathways for students looking to transfer to four-year colleges or universities and those who wish to gain additional skills and knowledge for job qualifications.[4,5]

Despite their important roles, most community colleges do not offer their students hands-on undergraduate research opportunities, which are critical for students' learning and career development.[6] Engaging in research projects helps students apply theory to real-world issues, enhancing their understanding, critical thinking, and problem-solving abilities. These experiences also develop communication and teamwork skills through collaboration with peers and mentors. Furthermore, undergraduate research assists in clarifying career goals, preparing students for advanced studies or chemical industry roles. Additionally, these experiences strengthen students' competitiveness for scholarships, internships, and jobs, showcasing their dedication and practical

skills in their field.[7–11] Consequentially, lack of undergraduate research experience during the first two years of college can be disadvantageous for community college students when they transition to their next educational destinations.[12,13]

Recently, many community colleges have started to recognize the importance of undergraduate research and many undergraduate research initiatives at these institutions have been founded.[7,14–19] Schauer classified approaches to implementing undergraduate research at community colleges into two models: traditional research model and curricular research model.[20] The traditional model research closely resembles undergraduate research experience at R-1 universities, where students work under mentors on a research project outside of the students' curriculum. The main downside of this approach is that the faculty are the only mentors at community colleges, which makes this model almost impossible since community college faculty often have heavy teaching loads, grading responsibilities without teaching assistant support, and significant advising commitments. The curricular research model embeds research components directly within the chemical education curriculum, either through individual experiments, or a series of investigative laboratory exercises, or a research-based capstone course. This approach poses some unique challenges including lack of diversity in research topics, high demand in advising, and the research timeline being strictly tied to the academic schedule.

Although external research programs for undergraduate students, such as Research Experiences for Undergraduates (REU), exist and encourage community college students to apply, these students may not be aware of such opportunities and often face heightened competitiveness since they often have to juggle multiple responsibilities, such as work, childcare, and financial constraints, making it challenging and impractical for them to allocate time and effort to research endeavors.[6,16] Hence, it is imperative to establish summer research initiatives that specifically

welcome community college students and cater to their distinct educational trajectories. An example of such initiatives is the Research Experience for Community College Students (RECCS), an REU program in environmental and geosciences in Colorado, funded by the National Science Foundation (NSF). In a recent study assessing the feedback from RECCS alumni, the authors show that program significantly enhances students' scientific and professional skills, fosters a scientific identity, boosts interest in pursuing graduate studies, and increases confidence in their scientific capabilities[21]. In an effort to bring similar research experience to community college students, who have interest in chemistry specifically, we have established an initiative: the Summer Chemistry Research Opportunities for Community College Students (SCROCCS) program at the University of Washington (UW). Chemistry majors transferring from community colleges typically join research labs later than their traditional students who start directly at four-year institutions, resulting in less time and experience to prepare for internships or graduate school. **Figure A1** shows that a typical chemistry major transferring from a community college to a university faces a constrained timeline, with just one year available to gain research experience for their graduate school applications. Since the best time for undergraduates to undertake internships is the summer after their third year, and internship applications typically open early in that year, transfer students without prior research experience from their community colleges find themselves at a significant disadvantage, often having minimal practical skills when applying for these important internships. To address this gap, SCROOCS offers community college students early access to research opportunities at an R-1 university, aligning their experience with that of traditional first-year university students[14]

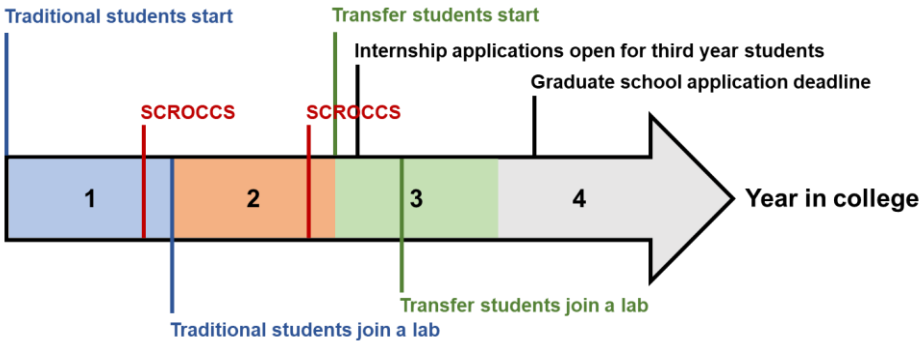

Figure A1. A comparative timeline between traditional students and transfer students, delineating key stages such as entry into research laboratories, opening of internship applications, deadlines for graduate school applications, and potential junctures for community college students to engage in hands-on research experiences via SCROCCS.

A2. Program Description

SCROCCS is designed to be an annual 9-week summer program similar to existing REU programs. The program at UW in Seattle targets local community college students in the Greater Puget Sound area. The first two years of SCROCCS, summer 2022 and 2023, admitted two students each year. Each participating student conducted hands-on research in a chemistry lab at UW and attended workshops and events organized by graduate student organizers. Participants were offered stipends provided by the lab hosts. Details about program organizing, including a timeline for SCROCCS organizers (**Table S1**), can be found in Section S1.

2a. Recruitment

The organizing team reached out to community colleges in the Greater Puget Sound area, distributing program advertisements and online application forms. We communicate with chemistry professors at these colleges through emails and online meetings to advertise SCROCCS and request them to promote the program in their classrooms or at career fairs and science events held at their institution. Establishing and maintaining relationships with community college

representatives, particularly science professors, is crucial for the success of our program. A strategic approach to make these connections involves having graduate or undergraduate students who previously attended local community colleges in our organizing team. For instance, in our first year, two graduate students from UW, both alumni of nearby community colleges, proactively engaged with their former chemistry professors, effectively introducing the SCROCCS program to them and advertising the program to community college students. Furthermore, we often provide updates to these community college professors, especially when their students participate in SCROCCS to ensure a continuous and meaningful dialogue between the program and the community colleges. In total, we contacted seven community colleges and received more than 15 applications each year (2022 and 2023). See application questions in Section S2. The applications were reviewed by the organizing team, who created a list of top candidates. The participating faculty then selected their preferred students based on the participant interest and compatibility with the lab host. The application process was designed to be straightforward and efficient. Applicants were assessed based on their motivation to participate, clarity of career goals, and eagerness to engage in scientific pursuits. An example of our application can be found in the Supporting Information. It is important to note that the number of student admissions is based on the available labs in the department. For example, the organizing team approached four chemistry labs at UW in 2022 and there were two labs agreeing to host a SCROCCS student. The availability of a lab host can be varied year by year due to a number of factors including the financial and graduate student mentor capacities.

2b. Activities

The main focus of SCROCCS was on research activities. At the beginning of the program, usually in the first week, students meet with their graduate student mentors and faculty advisors to

define research goals, establish expectations, and plan their schedules. They then engaged in research alongside their mentors in a traditional research fashion. Mentors and advisors set a primary goal for the program, along with short-term milestones involving reading and hands-on activities, to guide students through the research process step by step. An example of this planning document is included in the Supporting Information.

Table A1. List of SCROCCS activities and their objectives

Activities	**Objectives**
Campus tour	Familiarize participants with the university environment and resources
Interdisciplinary research lab visits	Expose participants to diverse scientific fields and career paths
Tips for transferring workshop	Provide insights and strategies for successful university transfer
Science communication workshop	Develop effective research presentation and discussion skills
Reading and writing a research paper workshop	Enhance critical analysis and scientific writing abilities
Weekly journal club	Foster critical thinking, analytical skills, and scientific curiosity
Grad student panel/Grad school information	Offer insights into graduate school life, application processes, and career opportunities

Final presentation	Showcase research findings, build confidence in scientific work, receive feedback, and improve presentation skill

Furthermore, a key component of the SCROCCS program is the variety of engaging activities offered to participants besides research activities, including campus tours, interdisciplinary research lab visits, workshops, and presentation opportunities (**Table A1**). These activities are frequently organized in collaboration with other REU programs or campus organizations to create opportunities for SCROCCS participants to interact and engage with a wider student community on campus. On the first week of the program, we introduced students to UW campus with a campus tour that enabled them to explore the campus and learn about the school's offerings. Free campus tours are often offered by most universities to provide a general overview of academic and student life. In our program, the organizers contacted UW office of administration to schedule the tour.

Although SCROCCS is a chemistry-focused program, the participants may not have a clear vision about their interests in future majors and research topics due to their lack of exposure. Therefore, the interdisciplinary research lab tour was intended to let students explore a diverse range of labs across various departments at UW. SCROCCS lab tour consisted of five 30-minute visits to labs in different departments. During each visit, representatives from the lab explained their scientific field, introduced their research projects, and showcased the instruments and products of their research. These tours not only provided students with a broader perspective on their intended majors, but also inspired them to explore new scientific disciplines and appreciate cutting-edge research. To organize the tours, the graduate student team contacted labs with

different scientific research topics and scheduled all lab tours into a one-day event. Lab selection was done based on two main factors: (1) the overall diversity of science topics, and (2) the possibility for short hands-on activities offered by the lab. For example, in 2023, the Yankowitz lab in the Physics department at UW offered SCROCCS students a hands-on demonstration where the students conducted a short graphene exfoliation experiment and looked at the graphene layers under an optical microscope, while the Stromberg lab in the Biology department let the students observe and touch plant and animal macrofossils. **Figure A2** shows the 2023 SCROCCS lab tour schedule and description.

Summer Chemistry Research Opportunity for Community College Students

Lab Tours

July 11th, 2023

Lab 1: The Pozzo Lab (1:00-1:30 PM)

The Pozzo Research Group focuses on the control and optimization of material structures for applications in alternative energy, synthesis, separations, medicine, and more. They employ machine learning, high throughput analysis, automation of laboratory procedures, and advanced characterization techniques using small angle x-ray and neutron scattering to accelerate the discovery and screening of novel materials.

Lab 2: The Baker Lab (1:40-2:10 PM)

The Baker Lab develops protein design software and utilizes it to create molecules that address challenges in medicine, technology, and sustainability. By constantly iterating between computation and laboratory experiments, they continually improve their protein design methods.

Lab 3: The Stromberg Lab (2:20-2:50 PM)

The Stromberg Lab investigates the evolution of grasses and the assembly of grassland ecosystems. They explore questions such as the origin and diversification of grasses, the emergence and spread of grasslands, and the influence of grasses on faunas and faunal evolution. Their research spans multiple regions and continents to gain a comprehensive understanding of the evolutionary history of grasses and the formation of grassland ecosystems.

Lab 4: The Yankowitz Lab (3:00-3:30 PM)

The Yankowitz Lab is an experimental condensed matter physics laboratory at the University of Washington in Seattle. They specialize in the investigation and control of novel electronic states in quantum materials, particularly atomically-thin van der Waals materials and heterostructures. Their research involves characterizing devices at low temperatures and in high magnetic fields using electrical transport measurements and scanning probe microscopy.

Lab 5: The Majumdar Lab (3:40-4:10 PM)

The Majumdar Lab focuses on the synergy of fundamental physics and intelligent engineering in technological advancements. They study light-matter interaction at the Integrated Quantum Optoelectronics lab, addressing challenges such as changing the amplitude, phase, and frequency of light with lower energy, faster speed, smaller size, and reduced cost. Their research aims to develop scalable nanophotonic systems and explore new applications in optical computing, communication, imaging, sensing, and quantum information science.

Figure A2. SCROCCS lab tour schedule for the 2023 program.

In addition to the tours, participants engaged in career development workshops that covered crucial topics including reading and writing research articles, designing, and presenting research posters or presentations, and communicating effectively to a variety of audiences. These

workshops were designed by the graduate student organizers. For "reading and writing a research paper" workshop, SCROCCS participants learned to classify different types of articles i.e. review articles vs. research articles, identify journals and their scopes, apply the "three-pass method for reading research papers" introduced by Keshav[22] and other active reading strategies[23], use writing strategies established by the Whitesides' group[24], and to effectively utilize available tools such as Google, ChatGPT, and Zotero for active reading and writing.[25,26] For the "Science communication workshop", we invited a graphic designer with expertise in scientific communication to give a talk titled "Design Eye for the Scientist", where students learnt the significance of scientific presentations, rules for effective communication through graphics, how to design chemistry posters and slides, and how to present science to a targeted audience. The outline for these workshops are available in the Supporting Information.

The above workshops worked synergistically with the "weekly journal club" activity as it presents a good introduction for practicing scientific literacy every week and is advised to be held earlier in the program. The weekly journal club, organized in collaboration with the IMOD REU program, served as a platform for students to learn essential skills such as using journal databases like SciFinder to find research papers, comprehending research papers, and crafting and delivering scientific presentations. Mentors worked alongside students to select a research paper that aligns with their summer project. Together, they delved into the paper's content to ensure a clear understanding of the core findings and concepts. Students then created a 10-minute PowerPoint presentation, summarizing their chosen paper and offering suggestions for improvement. This is followed by a presentation to their peers at the journal club, during which they address questions for roughly 5 minutes. This process boosts students' confidence in several key skills, including a

more profound understanding of their research project, critical reading, presentation creation, and public speaking.

SCROCCS also offered a "Tips for Transferring" workshop designed to assist students in transferring to a 4-year university. Graduate students who previously attended community colleges were invited to share their perspectives, discuss challenges they faced during the transfer process, and provide tips on crafting compelling applications, including personal statements and resumes. Students were also introduced to university resources that help transfer students such as the career center and the university office of admission.

With the goal of introducing participants to graduate school as a post-college pathway, SCROCCS held a graduate student panel event where they invited a group of graduate students from different UW departments. During the session, these panelists not only shared their firsthand experiences working as researchers in the lab but also offered insights into their journey through graduate school, detailing their decisions to pursue advanced studies and discussing various career opportunities.

In the last week of the program, participants were asked to submit a research summary and give a formal presentation about their research to a group of graduate students and professors. The final presentation provides a crucial avenue for community college students to showcase their summer research. It is also a chance to apply communication skills learned from workshops hosted by SCROCCS. This presentation, along with the research summary, encapsulates their scientific journey, offering a chance for reflection and demonstrating the practical application of skills acquired, serving as invaluable experiences for their academic and professional growth in the field of chemistry.

2c. Cost and Resources

The operational expenses of the SCROCCS program encompass student stipends, transportation assistance, and costs associated with organizing social events. For the 2022 and 2023 SCROCCS programs, we offered approximately $600 per week in stipend, which was comparable to most STEM REU programs at UW. Depending on the participant's situation and the local public transportation rate, we offered transportation assistance from none to $200 per program duration. Primary financial support for the program was derived from participating faculty, who allocated funds for summer student positions in their grant proposals or by directly requesting supplemental undergraduate funding from their program managers. To minimize costs, the program capitalized on the university's available resources, such as campus and lab tours, workshops led by departmental graduate students, and events sponsored by established research centers across the university. By utilizing the available resources, we did not have to raise more funds for our first two years of SCROCCS.

2d. Roles of Organizers, Mentors and Research Advisors and Their Experience

The SCROCCS program was led entirely by graduate students. They encompassed a diverse array of responsibilities. These included program development and promotion, engagement with chemistry faculty, application processing, continuous communication with students, mentors, and advisors, logistical arrangements for meetings, orchestrating career workshops and social gatherings, and adeptly managing unforeseen schedule adjustments. Overall, the SCROCCS organizers perceived the program as a practical opportunity to cultivate leadership skills while actively contributing to the community.

Mentors guided a related side-project throughout the program, collaborating with the SCROCCS student daily to enhance their confidence and knowledge in chemistry research. Before each program began, mentors and mentees met to discuss project overviews, set goals, and

establish expectations regarding communication and safety. The initial week was dedicated to safety training and lab procedures, while the following weeks focused on learning fundamental research skills. To ensure a productive mentor-mentee relationship, we recommend establishing a mentorship agreement (the detailed agreement can be found in the Supporting Information), collaboratively completed by both parties during an in-person meeting. This process, particularly beneficial for community college students new to one-on-one academic mentorship, helps mitigate potential tension arising from mismatched expectations. Ultimately, the mentorship in SCROCCS equips students to navigate the challenges of a research-intensive environment, offering insights on transitioning to a four-year institution or pursuing a career in STEM fields. Within the lab, mentors helped SCROCCS students familiarize themselves with the social dynamics of working in a research lab. This integration allowed them to feel more welcome and supported by peers while engaging in both science and non-science related topics. Additionally, students were encouraged to present their research updates at regular meetings with other group members. Receiving suggestions, asking for help troubleshooting, and navigating questions from peers are essential skills to practice when conducting chemistry research. Graduate student mentors reported significant benefits to their own graduate studies by partaking in the SCROCCS program. Mentors appreciated the opportunity to improve their time management and communication skills while broadening their scientific and academic perspectives.

Research advisors oversaw research projects and ensured participants receive a meaningful educational experience. Their main responsibilities include project design and approval, resource allocation, progress monitoring, quality assurance, and networking and collaboration. They ensured that research conducted adheres to high standards and helped community college students expand their professional networks. Moreover, interspersed 1-on-1 meetings between the

SCROCCS student and the research advisor were a valuable opportunity for the student to present specific research updates, re-evaluate their research goals, and discuss any outstanding questions or concerns regarding the program or their relationship with their graduate student mentor. The purpose of these meetings is open-ended, primarily serving as a private space for the student to communicate directly with the faculty.

Following the initial two years, SCROCCS garnered favorable feedback from engaged mentors and faculty. Notably, the original involvement of two chemistry faculty members in the inaugural SCROCCS program led to their commitment for two additional years.

A3. SCROCCS Program Outcomes

After each program concluded, we sent out an exit survey to the student participants to assess their experience with the program. Four students from the first two SCROCCS cohorts, 2022 and 2023, provided positive feedback on the valuable learning opportunities and social connections offered by the program. We divided the results from the survey into two categories: quantitative and qualitative findings.

3a. Quantitative Findings

We asked the participants to give scores to statements reflecting their experience with SCROCCS. The list of statements in our exit survey was created to align with the program's objectives and motivations. We aimed to evaluate the effectiveness of the program's activities and to determine whether the students' experiences aligned with the anticipated outcomes we envisioned during the program's development. The scale for the scoring is from 0 to 10, where 0 is extremely disagree and 10 is extremely agree. In **Figure A3**, the bar graph presents the average scores from four students, reflecting their responses to a series of statements about their experiences in the SCROCCS program. All the statements received high ratings, with averages

ranging from 8.5 to 10. This indicates a general satisfaction with various aspects of the program, such as mentor communication and the lab environment, and a significant improvement in students' confidence in key academic and professional skills, including reading scientific papers and public speaking. The average scores above 9.5 for statements about (1) increased interest in pursuing a study in STEM, (2) increased interest in doing scientific research, satisfaction in (3) lab and department environment, (4) hands-on research experience, and (5) feeling comfortable to communicate with mentors highlight the program's impact in enhancing both the skill set and the scientific enthusiasm for its participants.

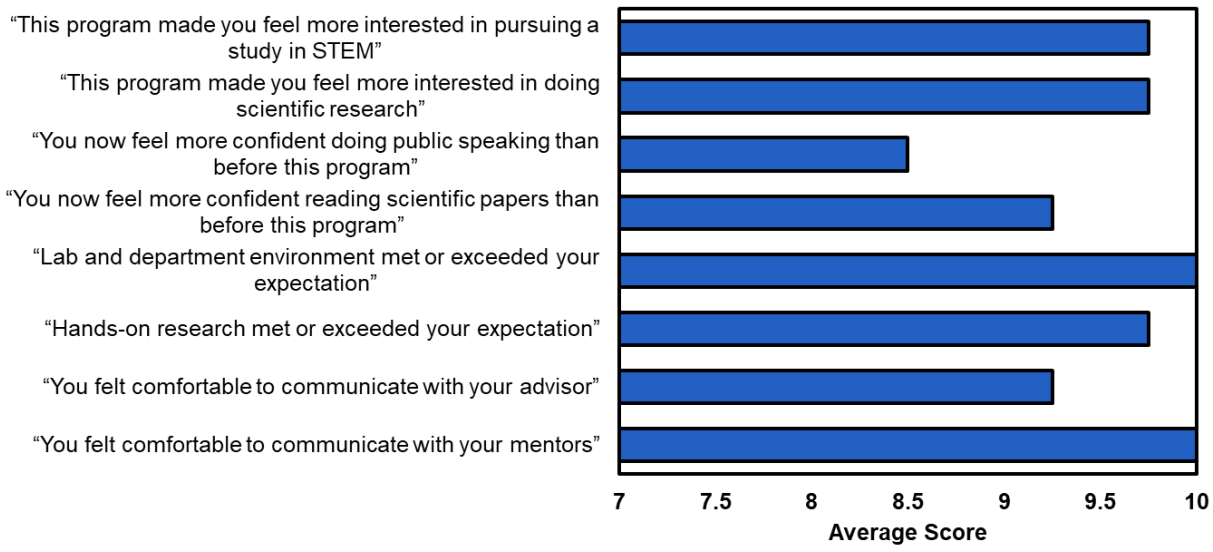

Figure A3. Student Ratings of SCROCCS Program Experience and Impact on STEM Motivation.

Figure A4 shows average scores from student evaluations of various activities at SCROCCS. The data reveals a uniformly high level of satisfaction across all activities, with scores ranging from 9 to 10. Notably, the Lab Tours and Final Presentation each achieved a perfect score of 10, reflecting their exceptional impact and popularity among the students. Additionally, the Reading and Writing a Research Paper Workshop closely followed with an impressive average of 9.75, indicating its significant value in enhancing students' academic skills. Other activities,

including the Journal Club, Campus Tour, Science Communication Workshop, and Tips for Transferring Workshop, also received scores above 9. These results collectively underscore the effectiveness and appeal of the SCROCCS program's diverse and enriching activities in fostering a comprehensive and engaging learning experience for the students

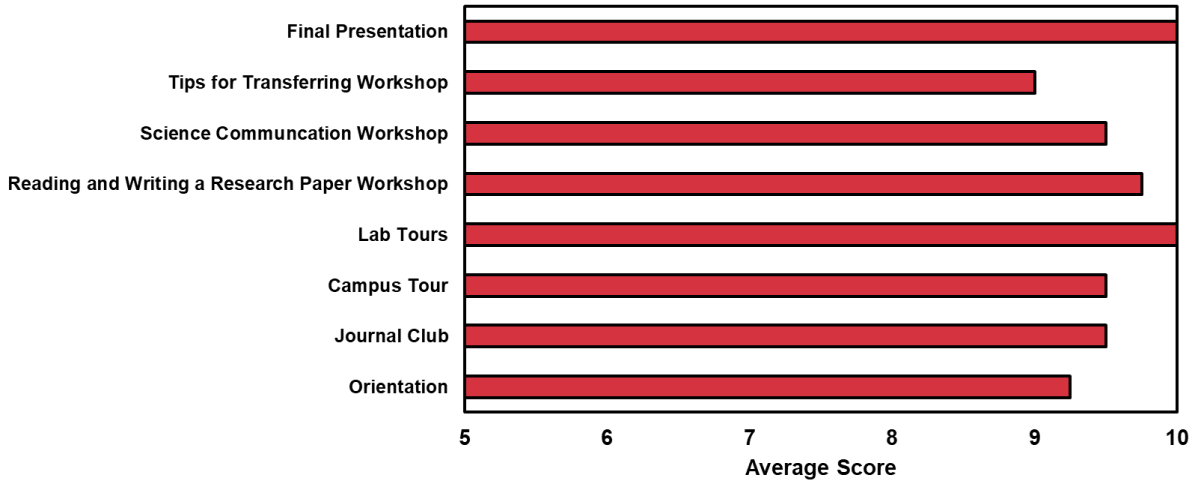

Figure A4. Average scores for SCROCCS activities at summer 2022 and 2023 programs from participants.

3b. Qualitative Findings

As of 2023, SCROCCS had a total of four participants, making the quantitative data less impactful for drawing broad statistical conclusions. Therefore, we place a stronger emphasis on the qualitative findings to highlight the individual experiences and outcomes of our participants. The program provided a unique environment for education and discovery, effectively combining detailed academic study with a supportive community atmosphere. Responding to the exit survey, students shared their experience that highlights both personal growth and collective achievements. One participant, who had only taken two quarters of General Chemistry courses at her community college, described the initial apprehension and subsequent comfort:

"I wanted to share how at first, I was slightly nervous and intimidated about how it was going to be, but from the moment I arrived, I was welcomed into a very friendly and supportive environment. I learned how to handle different instruments and different experimental techniques and also incredibly enjoyable with the people I was working with."

This sense of a welcoming environment and excitement for learning, exploring different instruments, and experimental techniques alongside new friends underscored the welcoming and supportive spirit of SCROCCS. This student continued working as an undergraduate researcher at the research lab after the summer and has already presented her research work with SCROCCS at three symposiums including the University of Washington Undergraduate Research Symposium, the American Chemical Society (ACS) Younger Chemists Committee's Pa' Adelante y ARRIBA (Onwards and Upwards) symposium, and the 2024 ACS National Meeting Undergraduate Research in Catalysis Symposium. The student also shared her insights on how SCROCCS influenced her career trajectory:

"As someone who is still exploring potential careers in the field of chemistry, my participation in the SCROCCS program allowed me to apply chemistry concepts in a real-world research project, offering insight into the kind of research I might want to pursue in possible graduate studies and beyond. This experience helps me boost my confidence in my academic abilities and also improved my critical and analytical thinking skills in a science setting, which I can apply to any future opportunities and programs, and in the career, I will ultimately decide to pursue."

Another student shared insights into his transformative journey, emphasizing the shift from initial uncertainty to a distinct and forward-looking trajectory:

> *"This has been a phenomenal experience and [I] will pursue doing more research during my undergrad and possibly beyond. [...] I felt very comfortable approaching my mentors and other labmates with questions or help."*

He expressed enthusiasm for learning advanced techniques such as air-free synthesis and NMR, especially when engaging in discussions with graduate students on topics that were once beyond his understanding. His involvement in summer research led to his contribution as a co-author on a research paper, and he successfully transferred to a R-1 university, where he continues to participate in undergraduate research projects.

Further emphasizing the program's practical benefits, another participant, who had a strong background in chemistry from taking Organic Chemistry courses and working as a Chemistry Stockroom assistant, appreciated the independence in conducting experiments and acquiring new skills during SCROCCS. She expressed her enthusiasm:

> *"I enjoyed being able to set up my own experiments while learning new techniques."*

With an eye on graduate school, she used her free time to gather insights, saying,

> *"I spent my free time learning about everyone's experiences and why they chose to pursue grad school, which gave me a lot to consider about my future plans."*

Reflecting on her SCROCCS experience, she highlighted its impact on her academic and professional trajectory:

> *"I know the experience I gained through SCROCCS will qualify me for more opportunities that I otherwise would not be able to pursue. I plan to continue being involved with*

research while finishing my bachelor's, and my involvement in this program will make me a more competitive student."

Her journey has now led her to UW, where she is preparing to apply to the School of Dentistry after her undergraduate studies.

All students valued the connections made with their mentors, graduate students, and peers, which not only enriched their learning experience but also helped their career trajectory. Students commented on the experience:

"Lots of highlights: making connections with other grad students and professors, getting lab experience at an R1 school and learning directly from grad students, having fun in lab, understanding the environment and daily life of a grad student."

"I also felt like I really connected with my mentor. She even helped me write a CV to apply for more research opportunities."

"Some highlights were meeting and working with lots of great people, making friends with other undergrads from different places. Working and learning with a great mentor."

These comments capture the comprehensive and engaging nature of the SCROCCS program, which ultimately leads to the student success.

A4. How to Start a SCROCCS at Your Institution

To establish a SCROCCS program at your university, we suggest following the steps in **Table A2** below.

Table A2: Suggested steps to start a SCROCCS program at your institution including resources and possible outcomes.

Steps	Resources	Outcomes

1. Assemble a team of organizers	Graduate students and faculty in the department, especially those who have experience working with or attending community colleges	This team coordinates all aspects of the program, from planning to execution, ensuring a broad range of skills and perspectives are utilized in developing the program
2. Identify funding sources, lab host availability, and target community colleges in the area	This work (**Section 2c**), other similar works, faculty, existing university and departmental programs and organizations	Transparent funding sources enable the program to offer high-quality resources and support to participants while clear community college targets help identify needs and demands
3. Develop a recruitment plan, including advertisements such as a website or flyers and application materials	For website: Free and user-friendly website development services such as Wix.com or Google Slides. For recruitment plans and application materials: this work (**Section S1 and 2a**), other similar works,	Early recruitment and strong advertising plans increase the program's visibility within the target community colleges, leading to a diverse and motivated pool of applicants. The program website can also help archive past cohorts, showcase program highlights,

	university and departmental REU program coordinators	and increase program credibility
4. Design and identify organizing timeline, program schedule, and possible activities	This work (**Table S1, and Section 2b**), other similar works, university and departmental REU program coordinators	Clear organizing timeline and program plan help run the program smoothly
5. Make connections with local community college science professors	Local community colleges	Strong and long-lasting connections with local community college professors ensure successful advertising and recruitment of the program. They also help identify needs from community college students in terms of research opportunities

A5. Challenges and How to Overcome Them

Running the SCROCCS program comes with various challenges that need to be tackled to ensure a successful experience for community college students. One crucial concern is the potential for low applicant turnout from these students, which might be due to limited awareness or perceived barriers to participation. Organizers should be proactive in advertising the program

many months in advance. Additional efforts to create flyers or use social media to increase reach to local communities can be very helpful in promoting the program. Obtaining sufficient funding to support student stipends and program activities can be demanding. We have experienced situations where university faculty were not willing to host SCROCCS students due to lack of grant funding. Directly discussing the financial availability of prospective lab hosts in the department should be the first thing organizers consider when starting the program.

Moreover, some participants may not actively engage in communication or attend events, or fully commit to research plans. Hence, it's crucial for organizers, mentors, and advisors to establish robust communication practices with all participants. This involves organizers reaching out to admitted students prior to the program's commencement to ensure their commitment, while advisors and mentors play a pivotal role in crafting comprehensive research plans, schedules, and guiding participants to adhere to the outlined schedule. Organizers must also remain adaptable in the face of unforeseen circumstances, such as changes in university regulations, lab availability, or participant needs. Ultimately, ensuring the long-term success and growth of SCROCCS requires continuous effort, dedication, and support from university stakeholders and graduate students. By addressing and overcoming these challenges, organizers can create a valuable and rewarding research experience for community college students.

A6. Vision

SCROCCS is unique among other REU programs in three ways: (1) it directly provides students from local community colleges with a traditional hands-on research experience on cutting-edge science and an opportunity to work with graduate students, post-docs, and faculty at the host university; (2) it does not require resources from community colleges and their faculty; and (3) while NSF-funded programs like RECCS requires a university faculty to initiate,

SCROCCS is led entirely by graduate students at the host university, providing graduate students themselves with opportunities to improve their leadership, management, and organizational skills. This structure also ensures the adaptability of the program and allows for flexible adjustments in alignment with the available resources and needs of the host university, thereby enhancing the program's efficacy and reach.

As the program continues to grow and evolve, we envision a future where this initiative expands into a national network of SCROCCS programs at universities across the United States. This network will facilitate collaboration and resource sharing, promoting best practices in supporting community college students seeking research opportunities in chemistry and other STEM fields. In addition to offering summer research experiences, we anticipate extending the program to provide research opportunities during the academic year, further enhancing community college students' access to hands-on research experiences.

To promote seamless integration with existing undergraduate research initiatives, we envision a collaboration with existing programs focusing on research for community college students such as the Louis Stokes Alliances for Minority Participation (LSAMP), the course-based undergraduate research experiences (CUREs)[27,28], and the Community College Undergraduate Research Initiative (CCURI). LSAMP programs significant initiatives aimed at increasing the quality and quantity of underrepresented minority students successfully transitioning from community colleges to four-year degree programs in STEM fields by providing academic support, mentoring, and research opportunities. CUREs are educational programs that integrate research experiences into the curriculum, allowing students to engage in scientific investigation as part of their coursework.[27,28] CCURI, on the other hand, uses an inquiry-based teaching approach, where students start with real-world science case studies in their introductory courses and then move on

to hands-on research related to those cases.[29] By working in conjunction with these programs, SCROCCS aims to provide community college students with comprehensive research experiences that span classroom and laboratory settings. Furthermore, we intend to expand the SCROCCS program's scope beyond chemistry to include other STEM disciplines, offering a more diverse array of research opportunities for participating students.

In comparison to established undergraduate research programs such as CUREs[28], SCROCCS operates on a smaller scale, which offers distinct advantages and challenges. The intimate size of SCROCCS cohorts can significantly boost student confidence and enhance teamwork skills, akin to the benefits observed in Peer-Led Team Learning programs.[30] This small group setting allows for greater flexibility, enabling organizers to tailor the program to meet participants' needs annually. However, the smaller scale presents challenges in program evaluation and establishing a consistent program structure. Unlike CUREs, which have defined upper and lower-division courses for varying levels of research involvement,[28] SCROCCS occasionally includes students at disparate levels of their academic journey, from those who have not taken general chemistry to those who have completed organic chemistry. Despite these challenges, SCROCCS's focus on individual development provides a unique, personalized research experience for each participant.

Ultimately, our vision for the SCROCCS program is to create an inclusive, supportive, and interconnected ecosystem that empowers community college students to excel in their chosen fields. By cultivating a rich network of research experiences and fostering collaborations among students, mentors, and institutions, we believe that SCROCCS can become a cornerstone for promoting equity and inclusivity in STEM education on a national scale.

A7. Supplemental Information

S1. Organizing SCROCCS

The programs in 2022 and 2023 were orchestrated and carried out by a group of graduate students with a general timeline described in **Table 1**. For a SCROCCS program starting in mid-June, the organizing team was formed in November to discuss recruitment and program structure. In collaboration with department faculty members, the organizing team identified laboratory positions and funding sources for participating students by the end of December. Subsequently, they worked closely with the department's human resources to handle the hiring process for summer students, taking into account factors such as funding sources, university hiring regulations, and state employment laws, which may have implications for the eligibility of international students or individuals below a certain age. Upon gathering the necessary information, the organizing team proceeded to create a website,

https://sites.google.com/view/scroccs/home,

which hosted both promotional information about the program and the application form.

In late January or early February, the team contacted chemistry faculty at local community colleges to promote the program and to distribute the online applications. The submission deadline was set for late March or early April. This timeline allowed students sufficient time to apply, while enabling organizers to process applications and finalize the hiring process. Upon completing the recruitment process, the organizing team collaborated with the university student center and other organizations to identify and schedule workshops and events. For example, the team partnered with an on-campus science center, NSF Center for Integration of Modern Optoelectronic Materials on Demand – IMOD, which has its own summer REU program to form joint activities and

networking opportunities. The organizing team subsequently selected workshops for the program and invited guest speakers before the program started.

Table S1. Timeline for SCROCCS organizers.

	Tasks
November	• Form a graduate student organizing team • Begin planning the program structure and logistics
December	• Approach faculty members to inquire about hosting student researchers • Consult with the HR department to gather information on hiring procedures and regulations • Finalize available research positions in faculty labs
January	• Develop application forms and other necessary materials
February	• Distribute advertisements and application forms to local community colleges • Communicate with chemistry departments and professors at local community colleges to promote the program
April	• Application deadline • Process applications and create a list of top candidates • Send decision letters to applicants • Initiate the hiring process for selected students
May	• Finalize the program schedule, including research activities, career development workshops, and social events
June	• SCROCCS program commences

August	• SCROCCS program concludes

S2. Example of the program application template.

Summer Chemistry Research Opportunity for Community College Students at the University of Washington

Application Deadline:

Decisions will be sent out no later than

Requirements:

(1) Must be a student currently registered at a community college located in the Greater Seattle area.

(2) While previous research experience is not necessary, applicants are expected to possess basic skills in Word, PowerPoint, Excel, and Algebra.

(3) Must have finished high school or currently enrolled in a Running Start program.

About SCROCCS:

SCROCCS was established by graduate students at the University of Washington in Seattle in 2022. This year, the program is offering a Chemistry Summer Research opportunity to community college students, with the aim of providing them with practical experience in chemistry and helping them prepare for future careers, including the potential to transfer to a 4-year university.

The program is specifically designed for students who have limited access to research

opportunities and are looking to gain more experience in the field of chemistry over the summer. It is supported by chemistry laboratories at the University of Washington, and successful applicants will have the opportunity to work alongside graduate students and researchers in a chemistry lab from [ ] to [ ], with a weekly stipend of [ ] .

This year's program will be hosted by two chemistry labs: the [ ] laboratory, led by Professor [ ], which focuses on the synthesis and application of nanocrystals, and the [ ] laboratory, led by Professor [ ], which studies organic synthesis and polymer chemistry. For more information about the labs and their research, please visit their websites: [ ]

Notes for applicants:

Our assessment of applicants is based on their motivation for participating in the program and the potential for the program to enhance their future career prospects. In addition, we take into account applicants' academic accomplishments and their eagerness to engage in scientific pursuits.

Contact**:** For more information, please email [ ].

How did you hear about this summer research program?

1. Please provide your full name:
2. Date of birth:
3. Expected graduation from your current institution (mm/yyyy):
4. Current institution:
5. Are you an international student?
6. Please write a brief statement about why you are interested in this summer research program and how this program would help you achieve your educational or career

goals. Include any experience in chemistry laboratories or/and chemistry courses you have taken (300-500 words):

7. Do you have a preference of which research lab you are interested in?
8. Describe how you will commute to the UW during the program period:
9. If you are admitted to this program, how can we best assist you to come to work and learn at UW? (Include any accommodation request for disability, medical condition, transportation, etc. Put N/A if you do not need any assistance):
10. Upload your CV or resume here. Must include a listing of all education, training, and work experience and your unofficial transcript. Please combine into one PDF file named "Lastname_CV.pdf".

S3. Suggested admission rubric for organizers.

1. Eligibility: This assesses whether the applicant meets the basic requirements of the program, including being currently registered at a community college in the Greater Seattle area, having finished high school or enrolled in a Running Start program.

2. Motivation and Interest (50%): This is based on the applicant's response to why they are interested in the program and how they believe it will help them achieve their educational or career goals. This includes a demonstration of interest in chemistry and the specific research labs offered.

3. Previous Experience (20%): This assesses the applicant's current level of exposure to chemistry laboratory, taking into account any laboratory experiences or chemistry courses mentioned in their application. While prior lab experience is not a requirement, it's noted for context. This category aims to identify those who stand to benefit the most from the lab experiences provided by the SCROCCS program. Applicants are evaluated holistically,

and both those with limited lab exposure and those with more extensive experience are encouraged to apply, as we value diverse backgrounds and perspectives in our program. For example, applicants with little to no lab experience but show strong evidence of how this opportunity can advance their career are prioritized.

4. Academic Achievement (15%): This looks at the applicant's academic accomplishments, including their performance in relevant coursework, as reflected in their unofficial transcript included in the CV or resume.

5. Personal Circumstances (5%): This includes the consideration of the applicant's commuting plan and any assistance required to participate in the program, such as accommodation for disabilities or medical conditions.

6. Presentation (10%): This assesses the overall quality of the application, including clarity, organization, and professionalism in the presentation of the CV or resume and the written responses.

Please note that this rubric is just one possible way to evaluate applications, and the weightings of each category can be adjusted based on the specific priorities and objectives of the SCROCCS program.

S4. Example of milestones and goals for a SCROCCS participant.

Research Goals and Milestones for A--- (Summer 2023)

Summer research goal: Understanding the effect of gadolinium (III) as a dopant into cerium oxide (CeO_2) nanoparticles for DMNP hydrolysis catalytic activity.

Milestone 1: Complete synthesis of CeO_2 nanoparticles (NPs) (control + Gd-dopant) with mentor shadowing

Important resource: “Controlled Synthesis and Self-Assembly of CeO_2 Nanocubes” (https://pubs.acs.org/doi/10.1021/ja063359h)

Target completion date: June 30, 2023

Milestone 2: Review the literature provided by mentor to plan an experiment based on reading

(1) Identify a base procedure to modify experimental parameters, important resource: “Hydrothermal synthesis and characterization of rare earth doped ceria nanoparticles” (https://www.sciencedirect.com/science/article/pii/S0921509307004078)

(2) Identify which experimental parameters to modify and how we want to modify them

Target completion date: July 7, 2023

Milestone 3: Complete training of relevant instruments at UW and characterization of NPs using 1H NMR spectroscopy, powder XRD, XPS/TEM (this will be done with mentor)

Target completion date: July 7, 2023

Milestone 4: Perform ligand exchange on CeO_2 NPs (undoped and doped) with 6-nitrodopamine

Successfully purify and characterize each reaction.

Target completion date: July 21, 2023

Milestone 5: Conduct doping reaction of CeO2 with Gd, perform catalysis studies with the doped products, and analyze catalysis results

Target completion date: July 28, 2023

Milestone 6: Present research progress at XXX Lab Group Meeting

(1) Compile a research presentation with introduction, results/discussion, conclusions/future directions

(2) Compile a written research summary including the same information

Target completion date: August 11, 2023 / August 18, 2023

S5. Reading and writing a research paper workshop outline.

I. Introduction

Welcome and overview of the workshop's objectives

Importance of understanding academic articles in chemistry research

II. Understanding Academic Articles

IIa. Types of Academic Articles

Differentiating between research articles, review articles, and news articles

Importance of each type in academic research and understanding

IIb. Identifying Relevant Journals

Overview of prominent chemical journals

Discussing the scope and specialization of various journals

Resources and strategies for finding suitable journals for specific research purposes

III. Effective Reading Strategies

IIIa. The Three-Pass Method by Keshav[31]

Pass 1: Grasping the Overall Content

Techniques and tips to understand the article's context and purpose

Identifying key objectives and hypotheses

Pass 2: Comprehending Figures and Content

Strategies to interpret figures, tables, and graphical representations

Extracting the core story and key findings

Pass 3: Questioning the Authors

Analyzing methodology and rationale behind the authors' choices

Encouraging critical thinking and formulating pertinent questions

IIIb. Active Reading Techniques (adapted from the University of Washington Department of Chemistry)[32]

How to Read Actively:

Step 1: Preview the assigned passage (5-10 min)

Read the section headings, boldface and italicized print, and any tables or figures contained in the reading assignment. What words or phrases do you notice?

Step 2: Develop a list of questions (2-5 min)

Determine the purpose of the reading. Based on the words and phrases you noted in Step 1, what questions do you expect the reading to answer for you?

Step 3: Read and paraphrase the passage, one paragraph at a time (variable)

Read the first paragraph, then paraphrase it in your own words. Read the next paragraph and paraphrase it in your own words, *but fold in the information from the previous paragraph as well*. After reading the third paragraph, your paraphrase will contain all information from the *previous two paragraphs*. Continue in this fashion until you have read the entire passage.

It might seem like this will take much longer than simply reading the passage straight through, but consider this: is it easy to read a textbook passage straight through and fully retain all the information in one try? Chances are you said no. Your brain gets distracted during the middle of a paragraph, you get to the end realizing you didn't remember any of it, and you have to start over from the top.

By paraphrasing each paragraph as you go, you will retain *much more* information. You will use your limited time *far more* efficiently, because you are only moving in one direction through the passage. In addition, you will have created a robust set of notes that you can use when reviewing for quizzes and exams.

IMPORTANT: Don't skip the worked examples!

The worked example problems in the reading assignments contain crucial information about how to apply the concepts and techniques you are reading about. If you skip over these, you are skipping some of the most important content in the reading!

Step 4: Reflect (5-10 min)

When you have finished reading and paraphrasing, ask yourself: Have all the questions I created in Step 2 been answered? Did the reading inspire any additional questions that I can bring to class or office hours?

IV. Practical Application

Identifying Main Points in a Research Paper

Group exercises and activities for participants to practice identifying and summarizing main points

Tips for effectively extracting essential information from research papers

V. Modern Writing Tools

V.a Utilizing ChatGPT in Writing

Introduction to AI-based writing tools like ChatGPT for drafting and refining scientific content

Best practices for using AI tools effectively in academic writing[33,34]

Vb. Managing Papers and References with Zotero

Introduction to Zotero as a reference management tool

Demonstrations on how to organize papers, create citations, and manage references using Zotero

VI. Writing Strategies for Research Papers

Whitesides Group Writing Approach

Step-by-step guidance for organizing thoughts and concepts before writing

Addressing essential questions for structuring a research paper (e.g., objectives, results, conclusions)

Emphasizing adaptability and flexibility in research objectives and conclusions

VII. Conclusion and Q&A

Recap of key takeaways from the workshop

Encouraging questions and discussions from participants

Providing additional resources and support for further learning

S6. Science communication workshop outline (adapted from the presentation *Design Eye for the Scientist* from Dan Morton)

1. Introduction

Overview of the importance of design in scientific communication.

Objectives of the presentation.

2. Principles of Scientific Design

Key design principles for scientific presentations.

Balancing aesthetics and functionality.

3. Visual Elements in Science

Role of visuals in scientific explanation.

Types of visual elements (graphs, charts, diagrams).

4. Designing Scientific Posters

Best practices for poster layout and design.

Case studies or examples of effective posters.

5. Scientific Presentations

Tips for creating engaging and informative slides.

Using visuals effectively in presentations.

6. Data Visualization

Techniques for representing data clearly and accurately.

Common pitfalls in data visualization.

7. Design Tools and Software

Overview of useful tools for scientific design.

Brief tutorials or demonstrations.

8. Case Studies

Analysis of well-designed scientific materials.

Discussion on what makes them effective.

9. Conclusion

Summary of key takeaways.

Encouragement for applying design principles in scientific work.

10. Q&A Session

Open floor for questions and discussions.

S7. Suggested template for a mentor – mentee contract.

The contract below is adapted from: Branchaw, J. L., Pfund, C., and Rediske, R. (2010) Entering Research Facilitator's Manual: Workshops for Students Beginning Research in Science, Freeman & Company.

Mentee Name _____ Mentor Name _____

This contract outlines the parameters of our work together on this research project.

1. Our major goals are:

A. research project goals, and technical skills expected to gain during the research –

B. mentee's personal and/or professional goals (motivations for research, career goals)–

C. mentor's areas most able to provide support on the above--

2. Our shared vision of success in this summer research experience is:

3. The mentorship relationship will continue as long as both parties feel comfortable with its productivity. We agree to work together on this project for at least _____. However, if either party finds the mentoring relationship unproductive and requests that it be terminated, we agree to honor that individual's decision.

4. The mentee will work _____ hours per week in the summer.

A. The mentee will propose their weekly schedule to the mentor by _____

B. If the mentee must deviate from this schedule, then they will communicate this to the mentor at least _____ (weeks / days / hours) before the change occurs.

C. Procedure if either party gets sick/has communicable illness:

5. Communication:

A. On a daily basis, our primary means of communication will be through (circle):

face-to-face / phone / email / instant messaging / texting

B. How do we define a timely response?

C. What times do we prefer to not communicate?

6. When learning new techniques and procedures, the mentor will train the mentee using the following procedure(s) (e.g. write out directions, hands-on demonstration, verbally direct as mentee does procedure, etc.):

7. We will strive for the mentee to gain research independence.

Once trained on basic techniques, the mentee will gain independence by

The mentor will assist gaining independence by

8. If the mentee gets stuck while working on the project (e.g. has questions or needs help with a technique or data analysis) the procedure to follow will be:

9. Other mentoring relationships: are there others in the group who can serve as good secondary mentors? What will the role of the PI be in the mentorship of the mentee?

10. The standard operating procedures for working in our research group, which all group members must follow, and the mentee agrees to follow, include (e.g. wash your own glassware, attend weekly lab meeting, reorder supplies when you use the last of something, etc.):

11. How will these other research skills be developed?

A. Laboratory notebook

B. Reading literature

C. Planning experiments

D. Accepting and utilizing constructive criticism

12. Other issues not addressed above that are important to our work together:

By signing below, we agree to these goals, expectations, and working parameters for this research project.

Mentee's signature: _____ Date: _____

Mentor's signature: _____ Date: _____

References

(1) Jenkins, D.; Fink, J. *How Will COVID-19 Affect Community College Enrollment? Looking to the Great Recession for Clues*. https://ccrc.tc.columbia.edu/easyblog/covid-community-college-enrollment.html (accessed 2023-04-06).

(2) Beer, A. Diversity of Community College Students in 7 Charts. *Association of Community College Trustees*. https://perspectives.acct.org/stories/diversity-of-community-college-students-in-7-charts.

(3) Foley, D.; Milan, L.; Hamrick, K. *The Increasing Role of Community Colleges among Bachelor's Degree Recipients: Findings from the 2019 National Survey of College Graduates*; NSF 21-309; National Center for Science and Engineering Statistics, 2021. https://ncses.nsf.gov/pubs/nsf21309 (accessed 2023-04-06).

(4) Community Colleges Provide a Crucial Bridge to Chemical and Biotech Industries. *CEN Glob. Enterp.* **2022**, *100* (32), 24–27. https://doi.org/10.1021/cen-10032-cover3.

(5) Bragg, D. D. Community College Access, Mission, and Outcomes: Considering Intriguing Intersections and Challenges. *Peabody J. Educ.* **2001**, *76* (1), 93–116. https://doi.org/10.1207/S15327930PJE7601_06.

(6) Freeman, S.; Pape-Lindstrom, P.; Casper, A.; Eddy, S. Community College Students Rise to the Challenge. Meeting the Time Demands of Highly Structured Courses. *J. Coll. Sci. Teach* **2020**, *49* (15).

(7) Craney, C. L.; DeHaan, F. P. A Collaborative Summer Research Program for Community College Students. *J. Chem. Educ.* **1991**, *68* (11), 904. https://doi.org/10.1021/ed068p904.

(8) Leonetti, C. T.; Lindberg, H.; Schwake, D. O.; Cotter, R. L. A Call to Assess the Impacts of Course-Based Undergraduate Research Experiences for Career and Technical Education, Allied Health, and Underrepresented Students at Community Colleges. *CBE—Life Sci. Educ.* **2023**, *22* (1), ar4. https://doi.org/10.1187/cbe.21-11-0318.

(9) Wenzel, T. J.; Larive, C. K.; Frederick, K. A. Role of Undergraduate Research in an Excellent and Rigorous Undergraduate Chemistry Curriculum. *J. Chem. Educ.* **2012**, *89* (1), 7–9. https://doi.org/10.1021/ed200396y.

(10) Schowen, B. Research as a Critical Component of the Undergraduate Educational Experience. In *Assessing the Value of Research in the Chemical Sciences: Report of a Workshop*; National Research Council (US) Chemical Sciences Roundtable; National Academies Press (US), 1998.

(11) Brown, D. R. Undertaking Chemical Research at a Community College. *J. Chem. Educ.* **2006**, *83* (7), 970. https://doi.org/10.1021/ed083p970.

(12) Fechheimer, M.; Webber, K.; Kleiber, P. B. How Well Do Undergraduate Research Programs Promote Engagement and Success of Students? *CBE—Life Sci. Educ.* **2011**, *10* (2), 156–163. https://doi.org/10.1187/cbe.10-10-0130.

(13) Eagan, M. K.; Hurtado, S.; Chang, M. J.; Garcia, G. A.; Herrera, F. A.; Garibay, J. C. Making a Difference in Science Education: The Impact of Undergraduate Research Programs. *Am. Educ. Res. J.* **2013**, *50* (4), 683–713. https://doi.org/10.3102/0002831213482038.

(14) Reeves, A. G.; Bischoff, A. J.; Yates, B.; Brauer, D. D.; Baranger, A. M. A Pilot Graduate Student-Led Near-Peer Mentorship Program for Transfer Students Provides a Supportive Network at an R1 Institution. *J. Chem. Educ.* **2023**, *100* (1), 134–142. https://doi.org/10.1021/acs.jchemed.2c00427.

(15) Zhao, M. Summer Science Academy in Chemistry as a Gateway to STEM for Matriculating First-Generation and Other Underrepresented Students. *J. Chem. Educ.* **2022**, *99* (2), 759–767. https://doi.org/10.1021/acs.jchemed.1c00950.

(16) Burchett, S.; Hayes, J. L. Development of a Pre-Professional Program at a Rural Community College. In *Strategies Promoting Success of Two-Year College Students*; ACS Symposium Series; American Chemical Society, 2018; Vol. 1280, pp 83–90. https://doi.org/10.1021/bk-2018-1280.ch005.

(17) *Chemistry Research Opportunities for Community College Students*,. https://www.odu.edu/academics/research-experiences/reu/chemistry (accessed 2023-10-09).

(18) *Stanford Summer Community College Research Program (SSCCrP)*. https://med.stanford.edu/odme/pre-med-students/commmunity-college-student-summer-research.html (accessed 2023-10-09).

(19) *Climate and Sustainability Research in Nanotechnology and Electrochemical Devices for Community College Students*. https://reu.rice.edu/nanotechnology (accessed 2023-10-09).

(20) Schauer, D. J. Identifying, Recruiting, and Motivating Undergraduate Student Researchers at a Community College. In *Strategies Promoting Success of Two-Year College Students*; ACS Symposium Series; American Chemical Society, 2018; Vol. 1280, pp 145–154. https://doi.org/10.1021/bk-2018-1280.ch009.

(21) Okochi, C.; Gold, A.; Christesen, A.; Batchelor, R. L. Early Access to Science Research Opportunities: Growth within a Geoscience Summer Research Program for Community College Students. *PLOS ONE 18* (12), e0293674. https://doi.org/doi.org/10.1371/journal.pone.0293674.

(22) Keshav, S. How to Read a Paper. *SIGCOMM Comput. Commun. Rev. 37* (3). https://doi.org/10.1145/1273445.1273458.

(23) *Active Reading*. https://chem.washington.edu/active-reading (accessed 2023-11-12).

(24) Whitesides, G. M. Whitesides' Group: Writing a Paper. *Adv. Mater.* **2004**, *16* (15), 1375–1377. https://doi.org/10.1002/adma.200400767.

(25) Humphry, T.; Fuller, A. L. Potential ChatGPT Use in Undergraduate Chemistry Laboratories. *J. Chem. Educ.* **2023**, *100* (4), 1434–1436. https://doi.org/10.1021/acs.jchemed.3c00006.

(26) Buriak, J. M.; Akinwande, D.; Artzi, N.; Brinker, C. J.; Burrows, C.; Chan, W. C. W.; Chen, C.; Chen, X.; Chhowalla, M.; Chi, L.; Chueh, W.; Crudden, C. M.; Di Carlo, D.; Glotzer, S. C.; Hersam, M. C.; Ho, D.; Hu, T. Y.; Huang, J.; Javey, A.; Kamat, P. V.; Kim, I.-D.; Kotov, N. A.; Lee, T. R.; Lee, Y. H.; Li, Y.; Liz-Marzán, L. M.; Mulvaney, P.; Narang, P.; Nordlander, P.; Oklu, R.; Parak, W. J.; Rogach, A. L.; Salanne, M.; Samorì, P.; Schaak, R. E.; Schanze, K. S.; Sekitani, T.; Skrabalak, S.; Sood, A. K.; Voets, I. K.; Wang, S.; Wang, S.; Wee, A. T. S.; Ye, J. Best Practices for Using AI When Writing Scientific Manuscripts. *ACS Nano* **2023**, *17* (5), 4091–4093. https://doi.org/10.1021/acsnano.3c01544.

(27) Provost, J. J. Developing Course Undergraduate Research Experiences (CUREs) in Chemistry. *J. Chem. Educ.* **2022**, *99* (12), 3842–3848. https://doi.org/10.1021/acs.jchemed.2c00390.

(28) Watts, F. M.; Rodriguez, J.-M. G. A Review of Course-Based Undergraduate Research Experiences in Chemistry. *J. Chem. Educ.* **2023**, *100* (9), 3261–3275. https://doi.org/10.1021/acs.jchemed.3c00570.

(29) *Community College Undergraduate Research Initiative*. https://www.ccuri.us/ (accessed 2024-05-15).

(30) Wilson, S. B.; Varma-Nelson, P. Small Groups, Significant Impact: A Review of Peer-Led Team Learning Research with Implications for STEM Education Researchers and Faculty. *J. Chem. Educ.* **2016**, *93* (10), 1686–1702. https://doi.org/10.1021/acs.jchemed.5b00862.

(31) Keshav, S. How to Read a Paper. *SIGCOMM Comput. Commun. Rev. 37*. https://doi.org/10.1145/1273445.1273458.

(32) *Active Reading*. https://chem.washington.edu/active-reading (accessed 2023-11-12).

(33) Humphry, T.; Fuller, A. L. Potential ChatGPT Use in Undergraduate Chemistry Laboratories. *J. Chem. Educ.* **2023**, *100*, 1434–1436. https://doi.org/10.1021/acs.jchemed.3c00006.

(34) Buriak, J. M.; Akinwande, D.; Artzi, N.; Brinker, C. J.; Burrows, C.; Chan, W. C. W.; Chen, C.; Chen, X.; Chhowalla, M.; Chi, L.; Chueh, W.; Crudden, C. M.; Di Carlo, D.; Glotzer, S. C.; Hersam, M. C.; Ho, D.; Hu, T. Y.; Huang, J.; Javey, A.; Kamat, P. V.; Kim, I.-D.; Kotov, N. A.; Lee, T. R.; Lee, Y. H.; Li, Y.; Liz-Marzán, L. M.; Mulvaney, P.; Narang, P.; Nordlander, P.; Oklu, R.; Parak, W. J.; Rogach, A. L.; Salanne, M.; Samorì, P.; Schaak, R. E.; Schanze, K. S.; Sekitani, T.; Skrabalak, S.; Sood, A. K.; Voets, I. K.; Wang, S.; Wang, S.; Wee, A. T. S.; Ye, J. Best Practices for Using AI When Writing Scientific Manuscripts. *ACS Nano* **2023**, *17*, 4091–4093. https://doi.org/10.1021/acsnano.3c01544.

APPENDIX B: SCIENCE ARTS AND STORIES

Inspired by the stunning science visuals from Ella Maru Studio, Kurzgesagt – In a Nutshell, CGFigures, and Ryo Mizuta Graphics, I set out to create eye-catching scientific illustrations of my own to sharpen my science communication skills. Already pretty handy with PowerPoint, I started teaching myself Adobe Illustrator, and later, Blender, during my second year of Ph.D.

Since then, I've created a wide range of graphics: from research figures and presentation visuals to journal covers and Table of Contents artwork—not just for my own papers, but also for my friends, labmates, and advisors. Each figure or TOC has a story behind it, sometimes thoughtful, sometimes ridiculous, and this gallery is a peek into those moments. If you scroll through in order, you'll also see how my design skills evolved over time. Enjoy the ride!

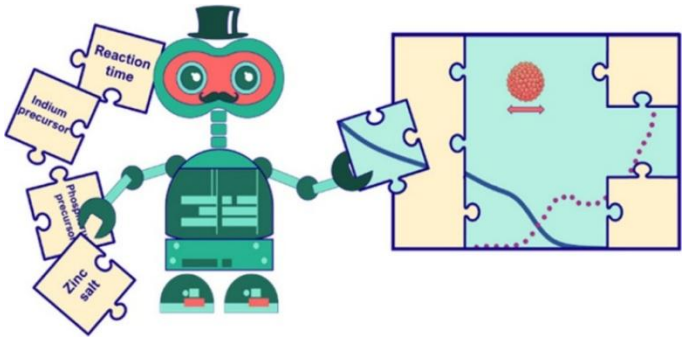

Starting with this robot—my very first science graphic, built entirely in PowerPoint for my first paper with the Cossairt lab. The paper, titled "Predicting Indium Phosphide Quantum Dot Properties from Synthetic Procedures Using Machine Learning", was published in Chemistry of Materials (*Chem. Mater.* **2022**, *34, 14*, 6296–6311), and this little robot made it to the Table of Contents. QD synthesis is full of puzzling variables, and the robot was my way of showing a machine-learning helper trying to piece everything together.

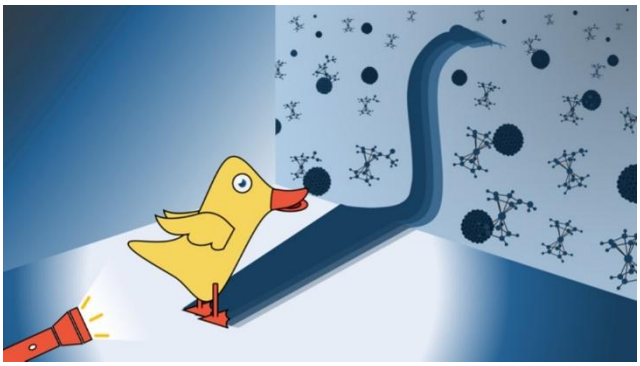

While working with my lab mate Micaela Homer, I whipped up this graphic in PowerPoint for her paper, "Photoinduced Charge Transfer from Quantum Dots Measured by Cyclic Voltammetry Phosphide Surfaces", published in JACS (*J. Am. Chem. Soc.* **2022**, *144, 31*, 14226–14234). The duck? That's a nod to the classic cyclic voltammetry shape, but flip on the light, and something weird starts to happen. Bonus joy: my advisor, Professor Brandi Cossairt, still calls this TOC graphic her favorite and loves to show it off during talks and conferences. It always makes me smile.

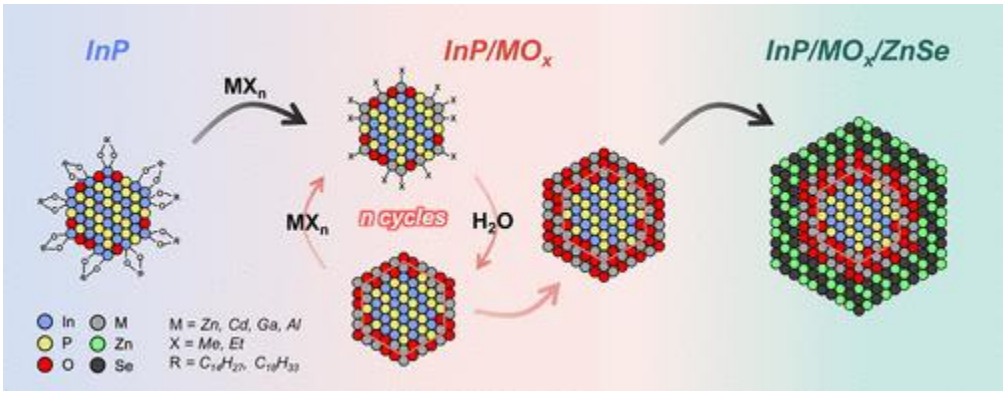

This graphic was created in PowerPoint for my lab mate Nayon Park's paper, "Colloidal, Room-Temperature Growth of Metal Oxide Shells on InP Quantum Dots", published in Inorganic Chemistry (*Inorg. Chem.* **2023**, *62, 17*, 6674–6687). It illustrates the elegance and precision of Nayon's work—improving the surface of InP quantum dots one delicate layer at a time.

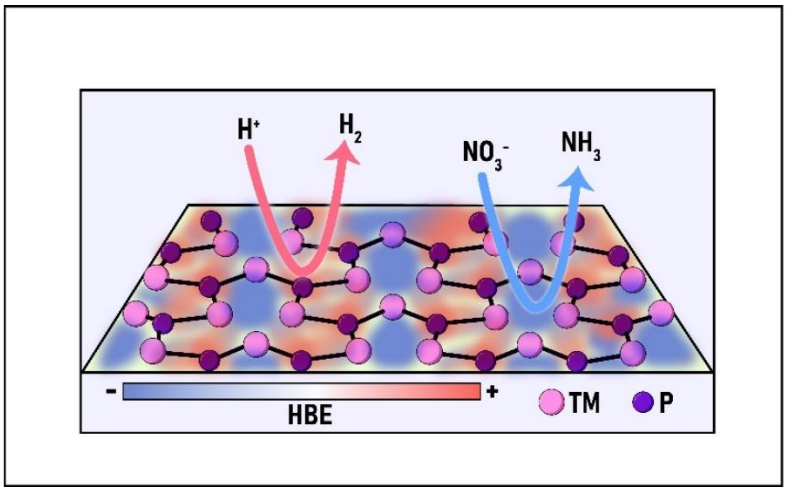

When postdoc Ding-Yuan Kuo asked if I could make a TOC graphic for a viewpoint article he was preparing, I saw it as the perfect excuse to finally dive into Adobe Illustrator. This simple illustration became my first published artwork using the tool, featured as the TOC graphic for his article, "The Role of Hydrogen Adsorption Site Diversity in Catalysis on Transition-Metal Phosphide Surfaces", published in ACS Catalysis (*ACS Catal*. **2023**, *13*, *1*, 287–295). A small step in design, one giant leap in Illustrator confidence!

In 2022, I attended the NSF/DOE Quantum Science Summer School (QS3) in sunny Santa Barbara, where I met some amazing friends and inspiring leaders in the quantum world. One of

the highlights for me? Winning the T-shirt design competition, which, hilariously enough, meant going head-to-head with none other than the program director himself, Columbia professor Cory Dean. (Plot twist: I found out three years later from my Graduate Student Representative, professor Matthew Yankowitz, at my Ph.D. defense that Cory is a fellow Blender nerd!) If you ever spot someone rocking that shirt, tell them this story; they probably won't remember me, but they'll definitely know Cory Dean.

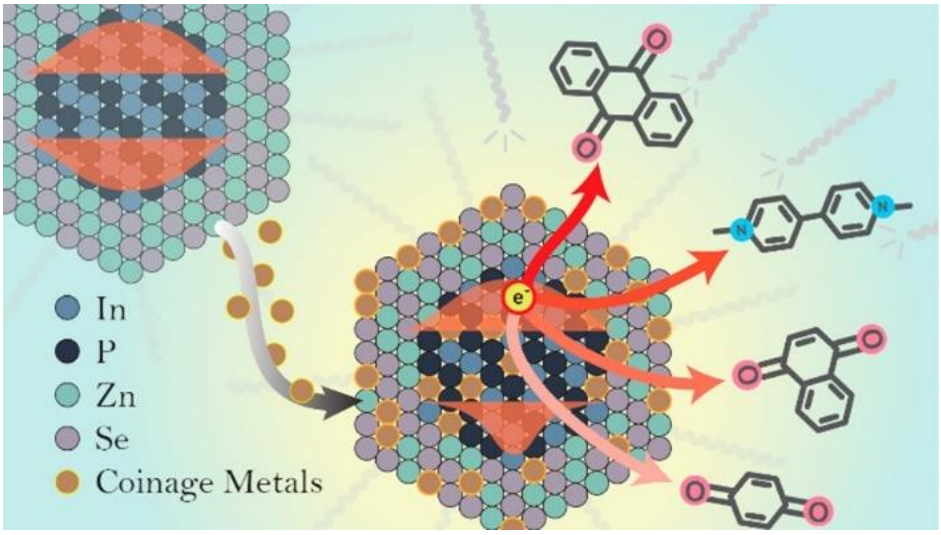

Another PowerPoint creation—this time for my lab mate Forrest Eagle, to highlight his work on doping quantum dots with coinage metals. The graphic was published as the TOC for his paper, "Enhanced Charge Transfer from Coinage Metal Doped InP Quantum Dots", in ACS Nanoscience Au (*ACS Nanosci. Au* **2023**, *3*, *6*, 451–461). Forrest's science dives deep into boosting charge transfer, and this graphic gave me a fun excuse to play with metallic flair.

ACS APPLIED MATERIALS & INTERFACES

January 25, 2023
Volume 15
Number 3
pubs.acs.org/acsami

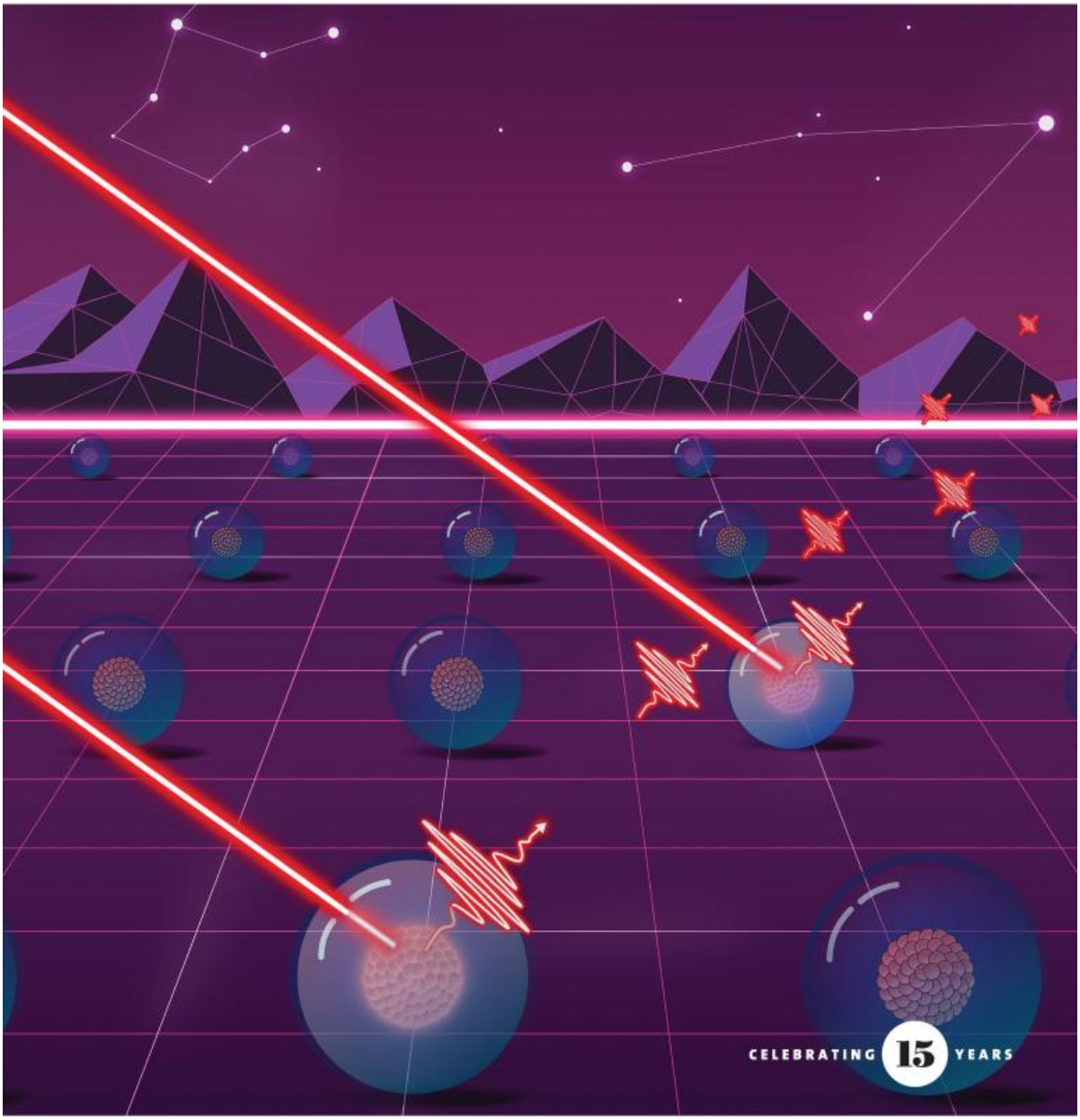

ACS Publications
Most Trusted. Most Cited. Most Read.

www.acs.org

This was my first-ever journal cover, created for my own paper, “Deterministic Quantum Light Arrays from Giant Silica-Shelled Quantum Dots”, published in ACS Applied Materials & Interfaces (*ACS Appl. Mater. Interfaces* **2023**, *15*, 4294−4302). Inspired by that bold, retro-futuristic neon aesthetic of the '80s, I designed the artwork using Adobe Illustrator. And while I don’t believe in astrology… if you look closely at the stars in the top left corner, you might spot my zodiac sign shining through. The first draft of this figure is shown below.

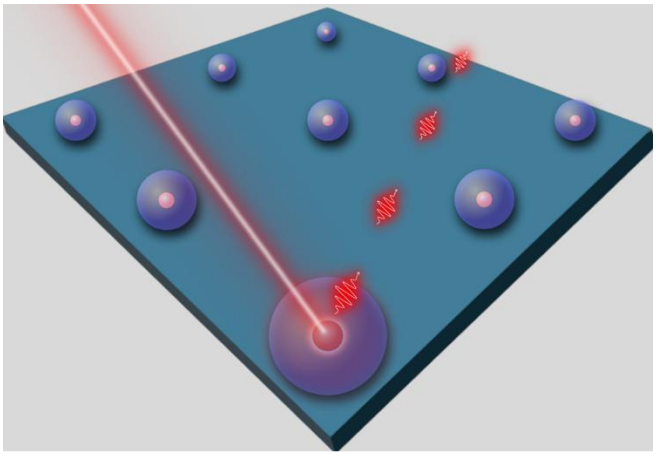

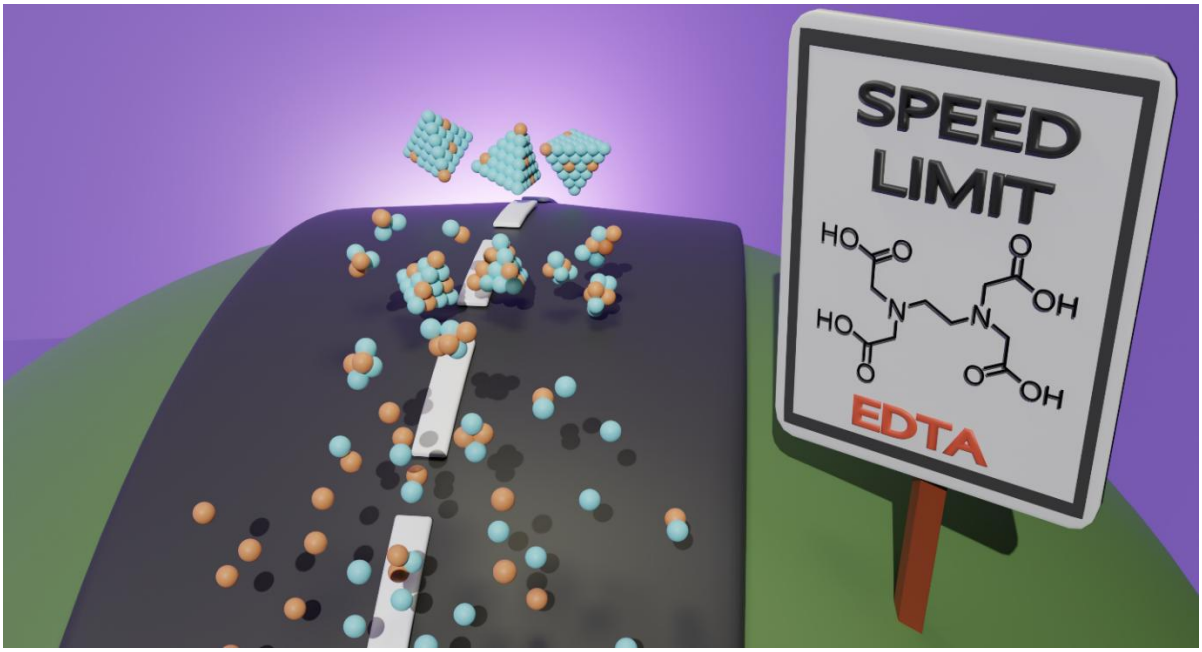

My first-ever Blender-made TOC graphic was for my labmate Helen Larson's paper, "Indium–Poly(carboxylic acid) Ligand Interactions Modify InP Quantum Dot Nucleation and Growth", published in Chemistry of Materials (*Chem. Mater.* **2023**, *35, 15*, 6152–6160). As you can see, every nanoparticle nucleation process has its limits, and Helen pushed those boundaries to test just how far InP nucleation can go. The first draft of this TOC from Helen is shown below.

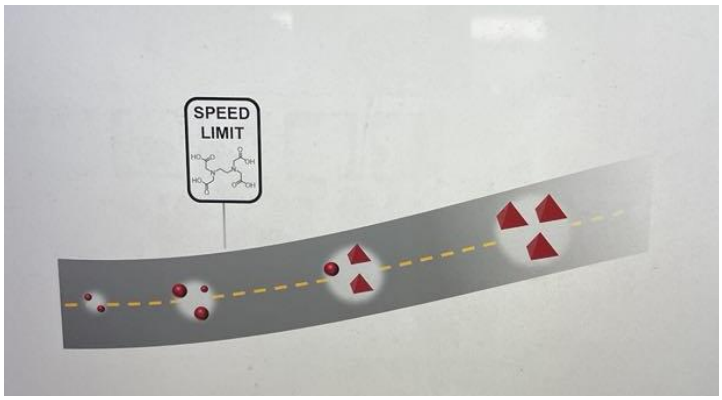

The next two posters were created as part of my capstone project for the Clean Energy Institute fellowship, designed to explain cutting-edge materials for clean energy in a way that anyone can understand. The first poster focuses on colloidal quantum dots, and the second on carbon nanotubes.

This is where I really began to appreciate the power of visuals in science. I've always been inspired by the incredible graphics I've seen in YouTube videos and conference posters—secretly dreaming of becoming one of those creators whose work makes science both beautiful and accessible. So it meant a lot when Professor Jacob Olshansky reached out to ask if he could use my quantum dot poster. I was flattered, and honestly kind of giddy, that my graphic might end up on a wall that isn't just mine.

QUANTUM DOTS

Nanomaterials for Clean Energy Project

Quantum dots are nanoscale particles, typically between 2 and 10 nanometers in diameter. Thousands of quantum dots could fit across the width of a human hair. They are made from semiconductor materials and have unique optical and electronic properties due to their size and quantum confinement effects.

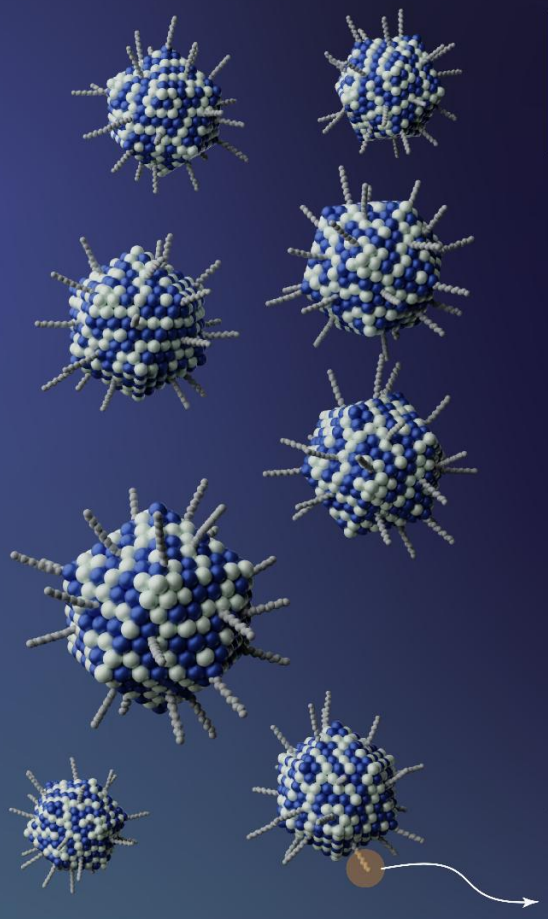

QUANTUM CONFINEMENT EFFECTS

These effects describe how an electron's behavior changes when it is squeezed into a tiny space, like in a quantum dot. Just like you would move differently in a small room compared to a wide field, the electron's energy levels become distinct, not continuous. Because of this effect, the size and shape of the quantum dot control these energy levels, which is key for electronics and photonics.

LIGHT EMISSION

Quantum dots can emit light in different colors. When energy (from light or electricity) is given to these dots, it gets absorbed by the electrons in the dot. These excited electrons then drop back to their original energy level, releasing the extra energy as light. The color of the light depends on the size of the dot - smaller dots give off bluer (higher energy) light, while larger dots emit redder (lower energy) light.

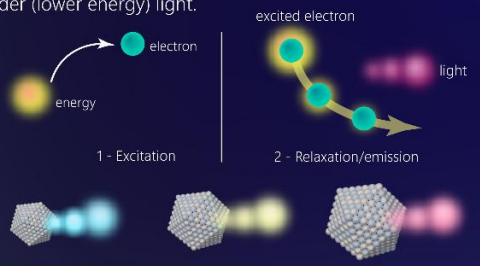

COMPOSITION

A quantum dot can be made of one, two, or more elements. These elements arrange in a specific way to construct the structure, shape, and size of the quantum dot. Typical types of quantum dots are cadmium selenide, cadmium telluride, indium phosphide, lead sulfide, and lead selenide. Quantum dots can be dispersed in solution, similar to dissolving salt or sugar in water. The surface of a quantum dot is covered by ligands, which are molecules that help stabilize the quantum dot in solution. Below is a typical ligand called oleate.

CLEAN ENERGY APPLICATIONS

Quantum dots are versatile tiny tools in clean energy. Their ability to absorb different colors of sunlight and customizable properties make solar panels more efficient, generate energy from sunlight, and make better displays.

Solar cells

Quantum dots can soak up different colors of sunlight and create more power-packed particles, helping solar cells to use more of the sun's energy and work better.

Display technology

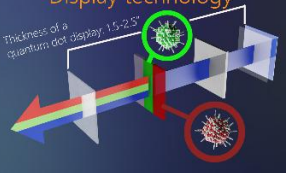

Quantum dots make screens for TVs and smartphones brighter and more colorful while using less energy, resulting in stunning displays and longer battery life.

Photocatalysis

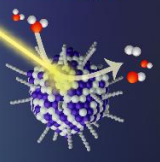

Quantum dots can act like tiny solar-powered factories. When they absorb light, they can help break down abundant molecules to create more useful molecules.

Creator: Hao Nguyen @nguyen_anh_hao

UNIVERSITY of WASHINGTON

CLEAN ENERGY INSTITUTE

Jacob Olshansky <jolshansky@amherst.edu> Tue, Aug 22, 2023, 10:42 AM

to me

Hello Hao,

I noticed that you made a very nice quantum dot educational poster. Would you be ok if I printed out a copy and hung it near my lab at Amherst College (it would of course have your information on it for credit).

If yes, would you be able to send me a hi-resolution version?

Thank you!
Jacob

CARBON NANOTUBES

Nanomaterials for Clean Energy Project

Carbon nanotubes are tube-shaped molecules consisting solely of carbon atoms. They can be incredibly tiny, with a diameter typically varying from 0.4 to 40 nanometers, which is about 2500 times smaller than the diameter of a single strand of a spider's silk. As for their length, they can range vastly from a minuscule 0.14 nanometers, all the way up to more than 50 centimeters. Carbon nanotubes are fascinating because of their unique combination of strength, flexibility, and conductivity. They're at the cutting edge of nanotechnology, promising to revolutionize fields from electronics to materials science.

ALLOTROPES

Allotropes are different forms of the same element due to variations in arrangement of atoms, each with unique properties. Carbon nanotubes, diamonds, graphite, and graphene are some allotropes of carbon. Diamonds are extremely hard due to their three-dimensional atomic network. Graphite, soft and slippery, consists of layers of carbon atoms in a hexagonal pattern. Graphene, a single two-dimensional layer of carbon atoms, is renowned for its strength and conductivity

Diamond Graphene Graphite

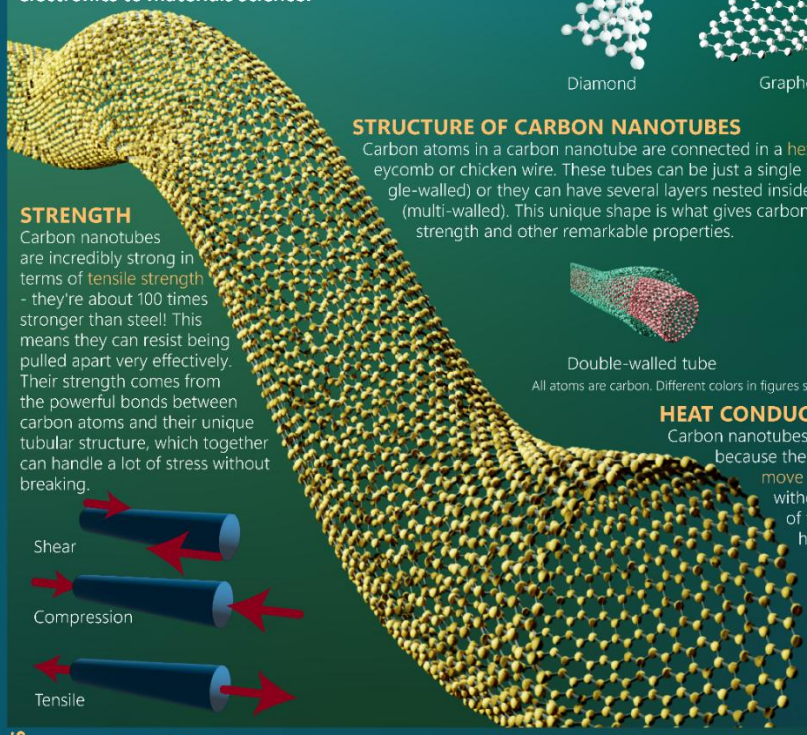

STRUCTURE OF CARBON NANOTUBES

Carbon atoms in a carbon nanotube are connected in a hexagonal pattern, similar to a honeycomb or chicken wire. These tubes can be just a single layer of atoms thick (single-walled) or they can have several layers nested inside each other like Russian dolls (multi-walled). This unique shape is what gives carbon nanotubes their exceptional strength and other remarkable properties.

Double-walled tube Triple-walled tube

All atoms are carbon. Different colors in figures simply distinguish between layers, or 'walls'.

STRENGTH

Carbon nanotubes are incredibly strong in terms of tensile strength - they're about 100 times stronger than steel! This means they can resist being pulled apart very effectively. Their strength comes from the powerful bonds between carbon atoms and their unique tubular structure, which together can handle a lot of stress without breaking.

HEAT CONDUCTION

Carbon nanotubes are amazing at transferring heat because the energy vibrations (phonons) can move smoothly along their length without getting interrupted. Because of this, they could be crucial in helping high-powered electronics from getting too hot.

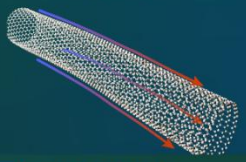

CLEAN ENERGY APPLICATIONS

HYDROGEN STORAGE

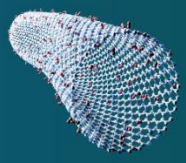

Carbon nanotubes, with their high surface area, can store hydrogen gas efficiently. This could advance fuel cell technology, a potential clean energy source.

WATER FILTRATION

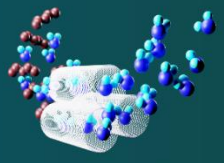

Carbon nanotubes can purify water, trapping impurities while water flows through. This could revolutionize water purification, ensuring cleaner water globally.

COMPOSITE MATERIALS

When mixed into plastics or metals, they create stronger but lighter composites, ideal for fields like aerospace engineering.

Creator: Hao Nguyen @nguyen_anh_hao

UNIVERSITY of WASHINGTON

CLEAN ENERGY INSTITUTE

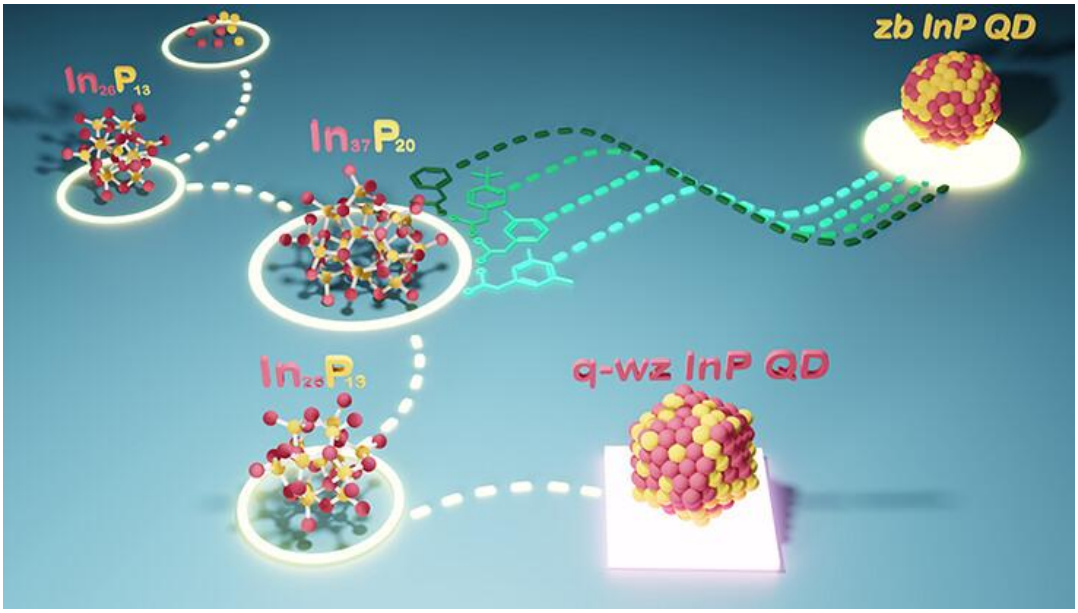

This TOC graphic was created for my labmate Soren Sandeno's first paper, "Ligand Steric Profile Tunes the Reactivity of Indium Phosphide Clusters", published in JACS (*J. Am. Chem. Soc*. **2024**, *146, 5,* 3102–3113). It was a fun challenge for me—my first time working with crystal structures in Blender. These clusters turned out to be more than just visually striking; they gave us valuable insight into the formation of quantum dots, or should I say "the formation before the formation of the quantum dots"? Below is the first draft.

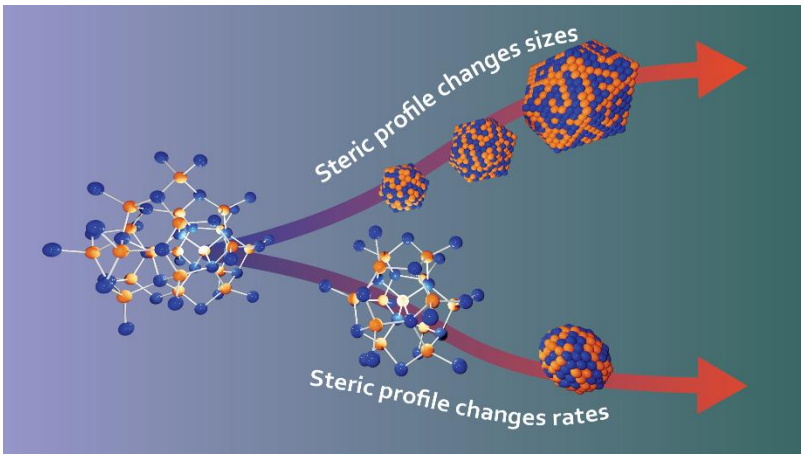

ACS Publications
Most Trusted. Most Cited. Most Read.

www.acs.org

I had the incredible opportunity to co-author a massive review article titled "Design Rules for Obtaining Narrow Luminescence from Semiconductors Made in Solution" (*Chem. Rev.* **2023**, *123*, *12*, 7890–7952), and naturally, I volunteered to create most of the artwork. While I did hit the usual writing blocks along the way, the real challenge turned out to be... design block, especially when it came to the journal cover.

Then, inspiration struck, completely by chance, during a meeting with Christopher Arnette, a Program Director for Supporting and Broadening Participation at the NSF Center for Integration of Modern Optoelectronic Materials on Demand, which I'm part of. In his office, I noticed a shelf full of snow globes from every city he'd visited. That gave me the idea: what if each snow globe held a tiny world of colloidal nanocrystals? And that's how the cover design was born. It ended up being selected as the journal cover for Chemical Reviews, a surreal full-circle moment of turning creative block into something beautiful.

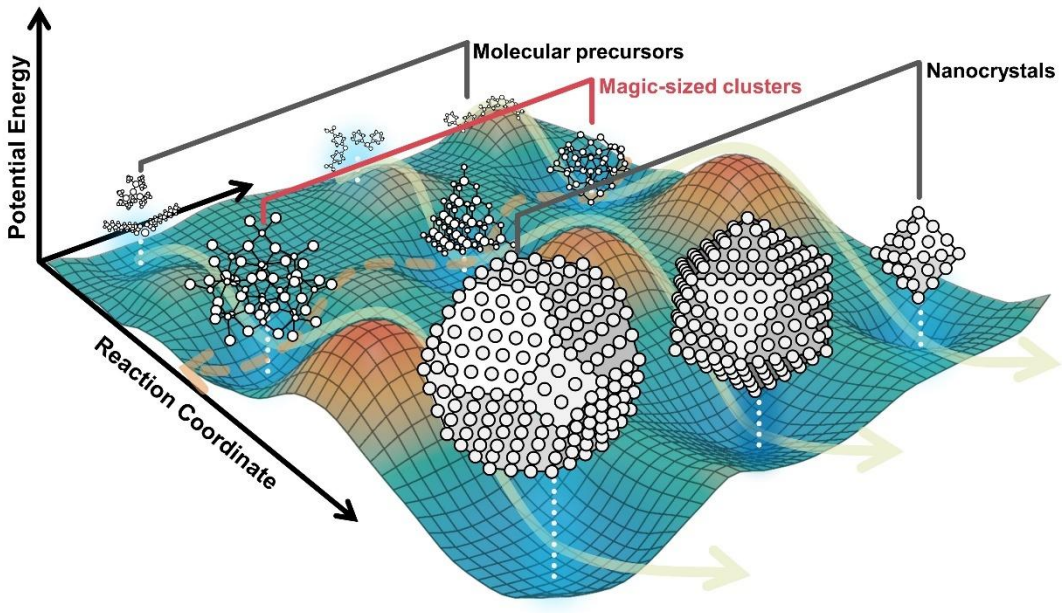

The figure above was featured as the TOC graphic for our review article, "Structure and Reactivity of II–VI and III–V Magic-Sized Clusters: Understanding and Expanding the Scope of Accessible Form and Function", published in Accounts of Materials Research (*Acc. Mater. Res.* **2024**, *5*, *6*, 726–738). Since clusters are my advisor Professor Brandi Cossairt's absolute favorite topic, I definitely felt the pressure to make this one shine. The catch? I had just three weeks to design this graphic, along with four others for the article. To save time (and my sanity), I combined my skills in PowerPoint and Blender to bring this piece together. In the end, it turned out quite nicely! Below, you'll see another figure from the same article, a timeline capturing the discovery milestones of CdSe and InP clusters.

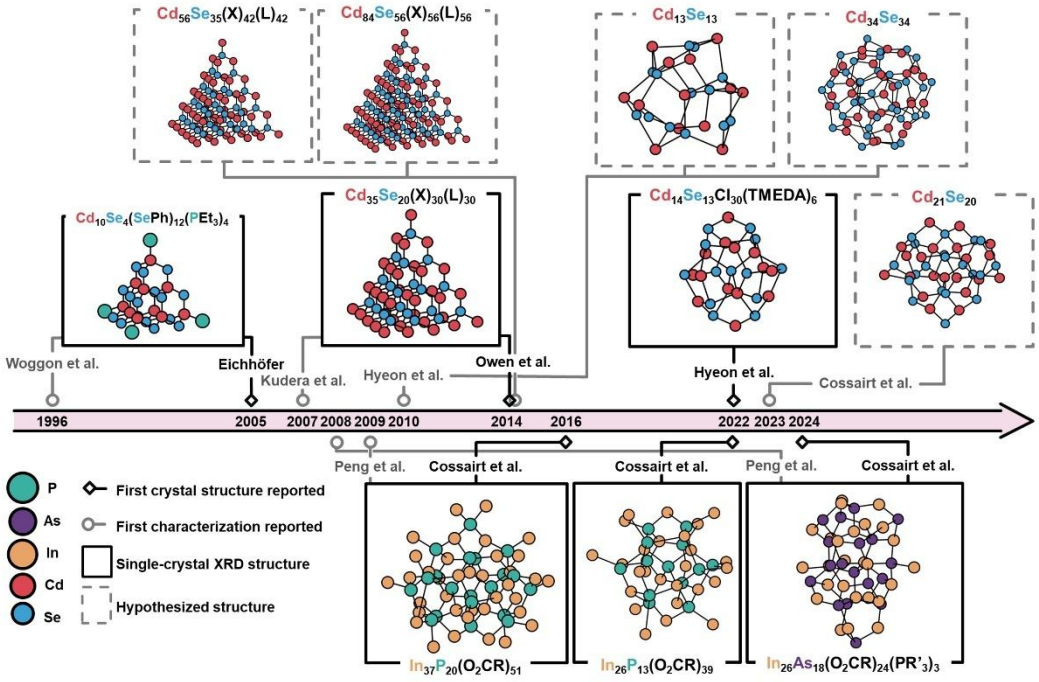

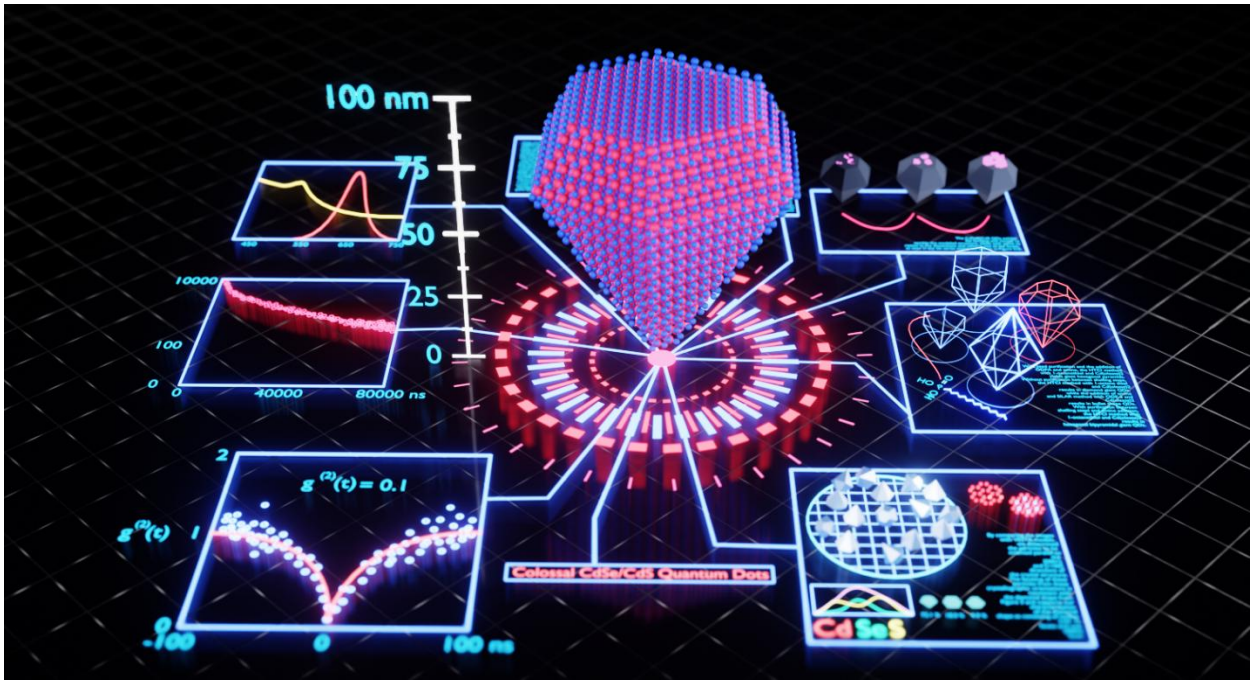

This TOC is hands down my favorite—not just because it's the cover for my own paper, "Colossal Core/Shell CdSe/CdS Quantum Dot Emitters", published in ACS Nano (ACS Nano **2024,** *18, 31,* 20726–20739), but because it continues the retro neon aesthetic that's become a bit of a theme in my Ph.D. journey. If you've ever wondered about the tiny glowing blue words scattered throughout the design… well, some of them are lines pulled straight from the paper. But others? They're lyrics from my favorite Taylor Swift songs. If you look closely at the bird's-eye view below, you'll spot *August* in the top left square and *Love Story* in the top right. A little science, a little sparkle, and a lot of fun.

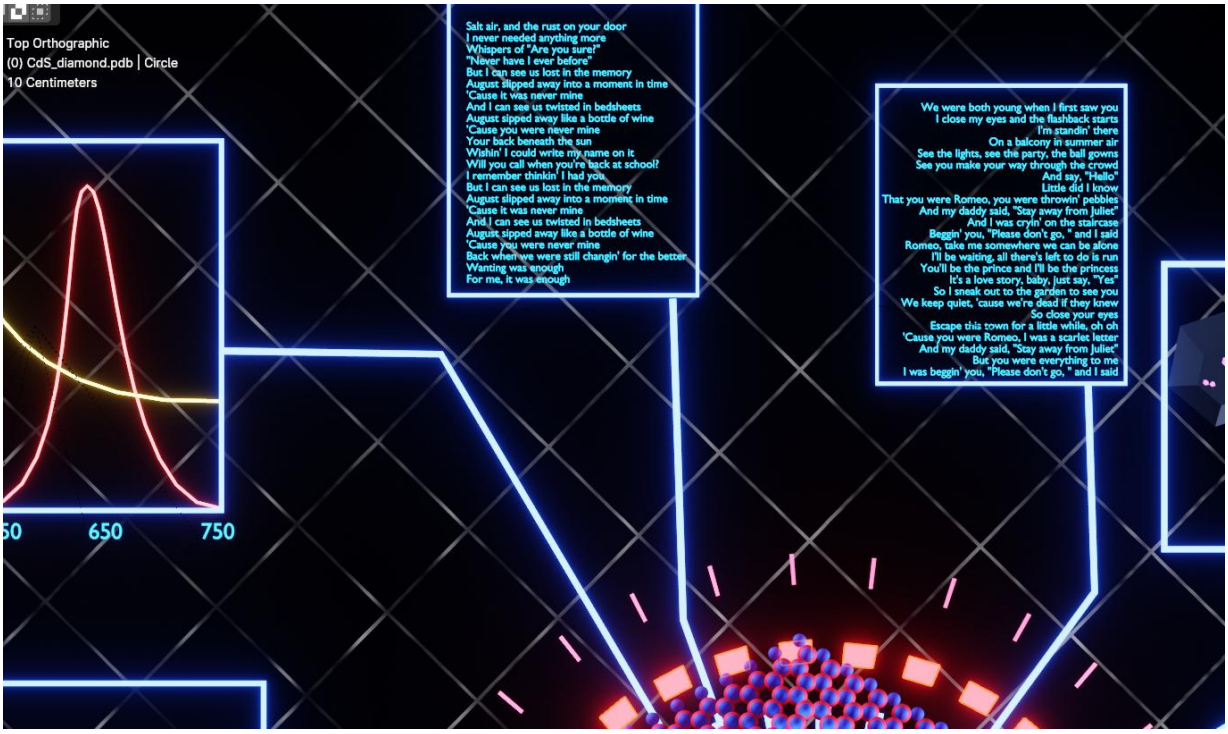

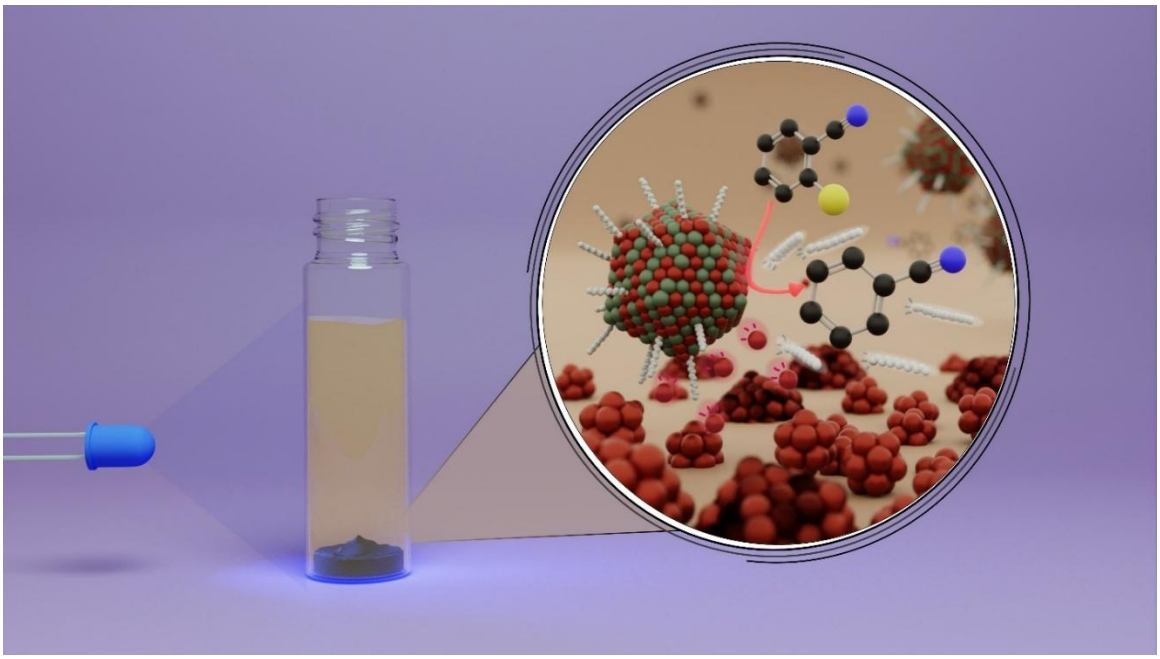

This next one was made for my lab mate Florence Dou's paper, "*Pathways of CdS Quantum Dot Degradation during Photocatalysis: Implications for Enhancing Stability and Efficiency for Organic Synthesis*", published in ACS Applied Nano Materials (*ACS Appl. Nano Mater.* **2024**, *7*,

13, 15781–15785). This project taught me an important lesson: the creator's favorite isn't always the client's favorite. I personally liked the figure below way more, but Florence was all in on the top one. Sometimes, you just have to let go and trust the process (and your collaborator's taste).

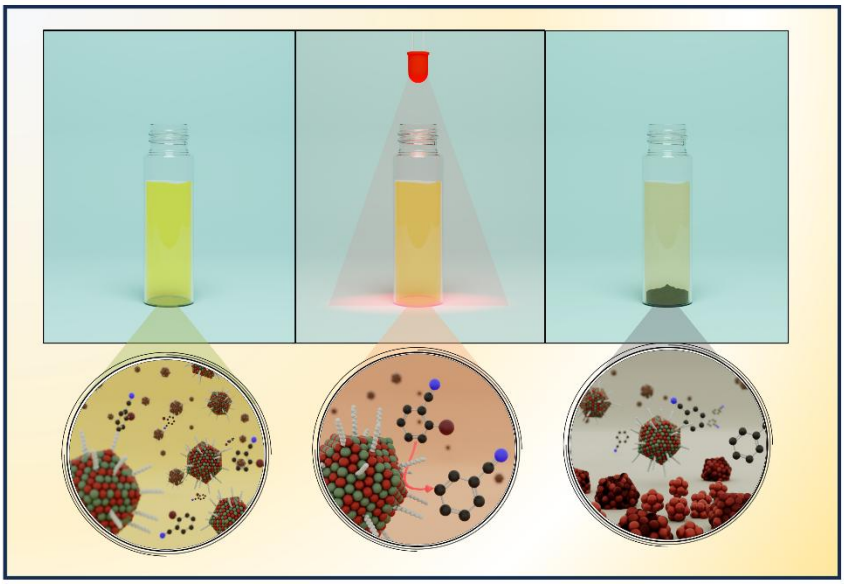

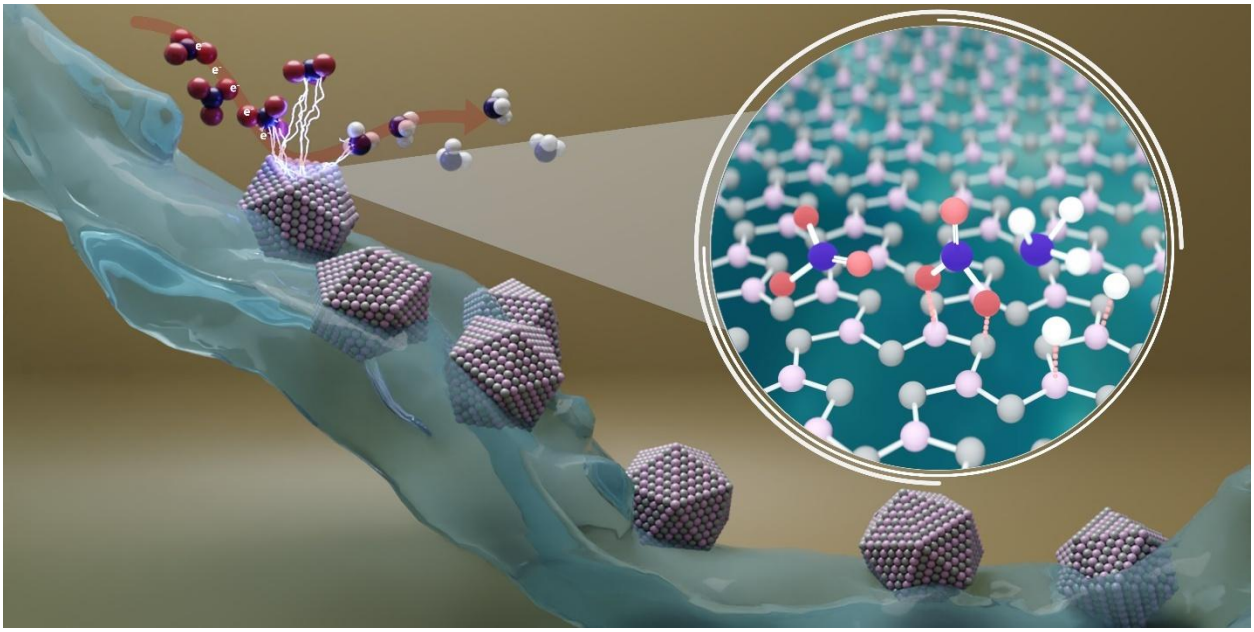

Emily Nishiwaki was my best friend during my Ph.D., so I was so excited to make this TOC graphic for her. She handed me a draft (below) and had just one request: "Make it feel like

Avatar: The Last Airbender." Challenge accepted. The graphic above was my take on that vibe of elemental, bold, and a little mystical. Her paper, "Ni_2P Active Site Ensembles Tune Electrocatalytic Nitrate Reduction Selectivity", was published in Chemical Communications (*Chem. Commun.*, **2024**, *60*, 6941-6944). Making this for her was one of the most fun (and nerdy) collaborations I've had.

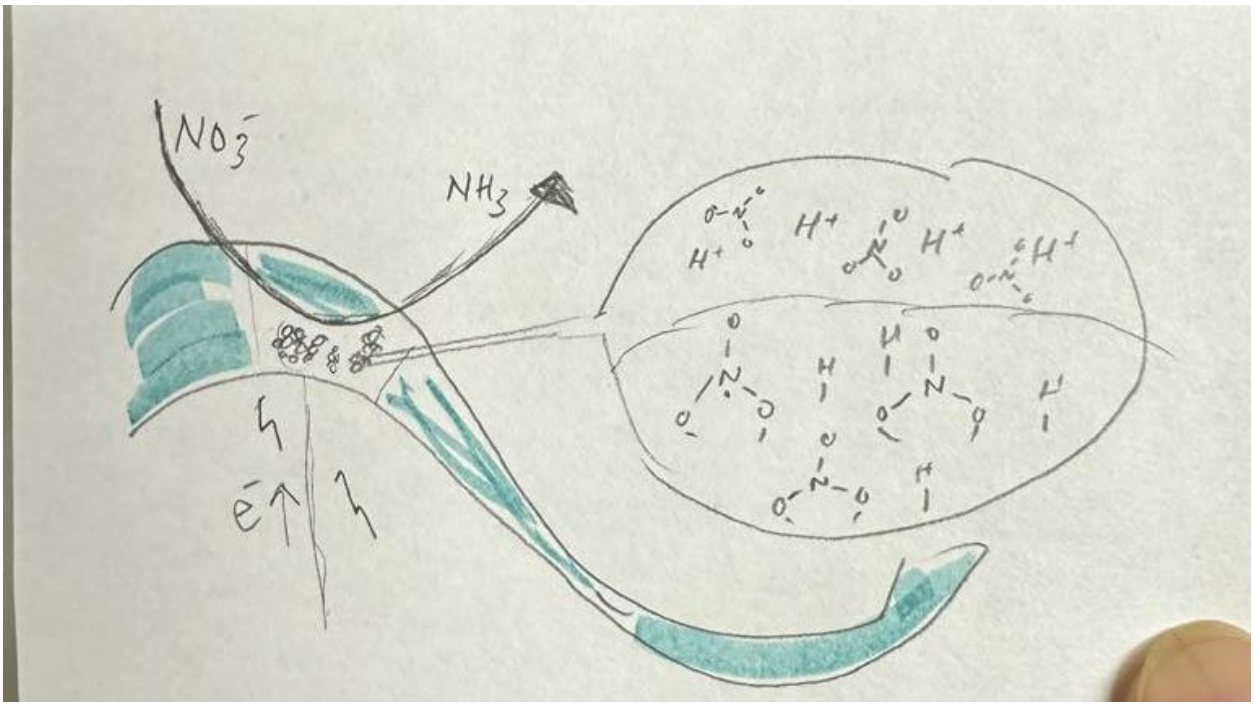

VITA

Hao A. Nguyen is originally from Tân Hiệp, Kiên Giang, Vietnam. He earned an Associate of Sciences degree from Pierce College Puyallup in Washington State in 2018 before transferring to Texas A&M University, where he completed his Bachelor of Science in Chemistry with a minor in Mathematics in 2020, graduating Magna Cum Laude. During his undergraduate studies, he conducted research in the laboratories of Professors Donald Darensbourg, working on biomimetic hydrogenation catalysis inorganic chemistry under Dr. Trung Le's direct mentorship, as well as in Professor Dunbar's group on single-molecule magnets under Dr. Brian Dolinar's direct mentorship.

In Fall 2020, Hao began his Ph.D. in Chemistry at the University of Washington, Seattle, where he worked under the supervision of Professor Brandi Cossairt. His doctoral research focused on the synthesis, processing, and deterministic integration of colloidal quantum dots for use in quantum photonics and optoelectronic devices. His efforts included the development of large, silica-shelled CdSe/CdS quantum dots and colossal CdSe/CdS quantum dots, engineering high-precision placement using inkjet printing and lithographic templating, and applying atomic layer deposition techniques to control shell morphology and emitter stability. He has extensive experience in nanoparticle synthesis, spectroscopy, electron microscopy, and nanofabrication, and has contributed to over 20 peer-reviewed publications, several as first author.

Beyond research, Hao is committed to leadership, mentorship, and outreach. He organized a major symposium at the 2024 Materials Research Society (MRS) Spring Meeting in Seattle, bringing together over 500 participants and 40 international speakers. He also founded and led SCROCCS, a summer research program that supported community college students' entry into

research careers at the University of Washington. He has served as a teaching assistant in five chemistry courses and mentored multiple undergraduate and graduate students in research.

Hao's achievements have been recognized with numerous honors, including the Best Dissertation Award (UW Chemistry Department, 2025), the Langmuir Graduate Student Award (American Chemical Society, 2024), the Chemistry Merit Award (UW Chemistry Department, 2024), and the Husky 100 distinction (UW, 2025). He won first place at The Royal Society of Chemistry Global Poster Competition in 2024. He was also awarded the Clean Energy Institute Fellowship in 2022-2023 and selected for the MIT Quantum Science Summer School in 2022.

Looking ahead, Hao plans to continue working at the intersection of materials chemistry and semiconductor technology. His career goal is to translate fundamental insights in nanomaterials and photonics into scalable, impactful technologies for computing, energy conversion, and next-generation communication systems.